Washington University in St. Louis
Washington University Open Scholarship

McKelvey School of Engineering Theses & Dissertations | McKelvey School of Engineering

Winter 12-15-2014

Aerosol Techniques for Deposition and Characterization of Biological and Biomimetic Sensitizers for Solar Devices

Vivek B. Shah
Washington University in St. Louis

Follow this and additional works at: https://openscholarship.wustl.edu/eng_etds

 Part of the Engineering Commons

Recommended Citation

Shah, Vivek B., "Aerosol Techniques for Deposition and Characterization of Biological and Biomimetic Sensitizers for Solar Devices" (2014). *McKelvey School of Engineering Theses & Dissertations*. 75.
https://openscholarship.wustl.edu/eng_etds/75

This Dissertation is brought to you for free and open access by the McKelvey School of Engineering at Washington University Open Scholarship. It has been accepted for inclusion in McKelvey School of Engineering Theses & Dissertations by an authorized administrator of Washington University Open Scholarship. For more information, please contact digital@wumail.wustl.edu.

WASHINGTON UNIVERSITY IN ST. LOUIS

School of Engineering and Applied Science

Department of Energy, Environmental and Chemical Engineering

Dissertation Examination Committee:
Pratim Biswas, Chair
Robert Blankenship
Dewey Holten
Cynthia Lo
Palghat Ramachandran
Venkat Subramanian

Aerosol Techniques for Deposition and Characterization of Biological and Biomimetic Sensitizers for Solar Devices

by

Vivek B. Shah

A dissertation presented to the
Graduate School of Arts and Sciences
of Washington University in St. Louis
in partial fulfillment of the
requirements for the degree
of Doctor of Philosophy

December 2014
Saint Louis, Missouri

© 2014, Vivek B. Shah

Contents

List of Figures

List of Tables

Acknowledgments

I thank my advisor Prof. Biswas for providing me opportunities to be part of his group and work on interesting projects. Prof. Biswas has been very supportive and a great mentor. Over the last five years I have learnt a lot of things in and outside the lab. He has helped me improve not only in research but also other aspects, which I feel have played a significant role in shaping my personality. I feel confident to work on challenging problems as and when I encounter them.

I thank Prof. Holten for introducing me to self-assembly and for numerous discussions relating to it. I thank Prof. Blankenship for discussions on photosynthesis and light harvesting complexes. I thank Prof. Lo, Prof. Ramachandran and Prof. Subramanian for the inputs in improving the thesis.

I acknowledge the funding and support from the McDonnell Internationals Scholars Academy for fellowship. I would like to acknowledge funding from Photosynthetic Antenna Research Center (PARC), an Energy Frontier Research Center funded by the U.S. Department of Energy, Office of Science, Office of Basic Energy Sciences under Award Number DE-SC0001035 and Solar Energy Research Institute for India and the United States, funded jointly by the U.S. Department of Energy (Office of Science, Office of Basic Energy Sciences, and Energy Efficiency and Renewable Energy, Solar Energy Technology Program, under Subcontract DE-AC36-08GO28308.

I am thankful to Dr. Woo-Jin An for mentoring me when I joined the lab. Dr. An has been instrumental and highly supportive in guiding me through the initial stages of my research. I joined lab with little background in performing experiments. I thank Dr. Lying Zhu for

introducing me to electrospray setup and Dr. Weining Wang for teaching me the basics of experimental design and performing experiments. I thank the current AAQRL members Tandeep Chadha, Sameer Patel and Jiaxi Fang for fruitful discussions and EECE friends, without whom the time in St. Louis would have been difficult. Apart from the people in lab, AAQRL alumni – Dr. Soubir Basak, Dr. Manoranjan Sahu, Dr. Elijah Thimsen and Dr. Chris Hogan - have been very kind to help when asked for.

Most of the work in this thesis would be hard to accomplish without the help of wonderful collaborators at Washington University. I would like to acknowledge the help of Joseph Springer from Holten Lab for assisting me with analysis and characterization. I would like to thank Gregory Orf from Blankenship Lab for the discussions and collaborative experiments. I thank Haijun Liu for insightful discussions on PSI and its working. I thank Ray Henson for his contribution for the PSI study as a co-author.

I thank my friends for making my stay in St. Louis enjoyable. I am indebted to my friends Venkat, Phani, Kshamta and Piyush who have been a great source of support and help during my critical years. They have stuck with me through tough times and have been extremely kind.

I thank my parents, sister and other family members for their unconditional love and support through the years. I am extremely grateful to them

Vivek B. Shah

Washington University in St. Louis
December 2014

...to my parents

and

grandparents

ABSTRACT OF THE DISSERTATION

Aerosol Techniques for Deposition and Characterization of Biological and Biomimetic Sensitizers for Solar Devices

by

Vivek Shah

Doctor of Philosophy in Energy, Environmental and Chemical Engineering

Washington University in St. Louis, 2014

Professor Pratim Biswas, Chair

Nano-structured columnar films synthesized by the aerosol chemical vapor deposition (ACVD) system are unique, and have proved to be useful for fabricating solar cells and in other applications. The film formation by ACVD process involves three main phenomenon - aerosol formation and growth, deposition, and restructuring. In this work, thin film formation by the ACVD process is simulated by combining three models – (A) particle formation in gas phase by atrimodal model, (B) particle deposition onto heated substrate by a Brownian dynamics model and (C) sintering on the heated substrate by a multi-particle geometric sintering model (MPGSM). Modelling and simulation done in this work gives insights into working of the ACVD. Analysis suggests that a balance between arrival rate and sintering rate must be maintained to obtain the desired morphology by the ACVD process.

Since the titanium dioxide films synthesized by ACVD cannot absorb light in visible regions, various biological and biomimetic sensitizers have been explored. Natural sensitizers and reaction centers, which have high absorption coefficient and remarkable quantum efficiency, have been characterized in this work by electrospray-scanning mobility particle sizer (ES-SMPS) and deposited. The stability and retention of the photoactivity for the same has been

demonstrated in this work. PSI which is a light harvesting complex with reaction center has been deposited by electrospray onto nanostructured TiO_2 columns, synthesized by ACVD. The deposited PSI adheres due to dissolution of surfactant in the electrolyte and the performance is characterized using a photoelectrochemical cell. The orientation of PSI, due to linker free deposition and adhesion, has resulted in the highest photo-current observed for PSI based photoelectrochemical cells.

In order to improve the biological sensitizer chlorosome, mimics of chlorosomes are synthesized by self-assembly of synthetic and natural dyes in aerosolized droplet. We have developed a single-step method for the self-assembly of synthetic chlorin molecules (analogs of native bacteriochlorophyll *c*) in aerosolized droplets, containing a single solvent and two solvents, to synthesize bio-mimetic light harvesting structures. In the single-solvent approach, assembly is promoted by a concentration driven process due to evaporation of the solvent. Although assembly is thermodynamically favorable, the kinetics of self-assembly play an important role and this was demonstrated by varying the initial concentration of the pigment monomer. The kinetic limitations can be overcome by the use of a two solvent technique, which can also alter the size of self-assembled structures. The self-assembly of dye in aerosolized droplets has been extended to the naturally occurring bacteriochlorophyll *c*. The absorption and fluorescence of the assembled BChl *c* were demonstrated to be comparable to the naturally occurring chlorosomes. Finally the films were characterized by GISAXS and they show a scattering pattern characteristic of lamellar structures, which are present in chlorosomes. This technique of aerosol based assembly will enable the use of these materials as biomimetic sensitizers for solar cells.

Chapter 1 Introduction

1.1 Introduction

Energy is required for human development and improving the standard of living. Energy requirements will increase due to growing population and rise in per capita consumption of energy in the developing countries. It is projected that the global energy requirement will reach 25 TW by 2035 from 17.8 TW in 2011.[1] Out of the total energy consumed in 2011, fossil fuels contributed 83.7%. Continued consumption of fossil fuels at this rate will result in extremely high concentrations of CO_2 in atmosphere (~450 ppm from existing 390 ppm). High concentrations of CO_2 in atmosphere will result in global warming with damaging effects. This has accelerated the need to shift to carbon free energy sources. There are various options for energy sources such as nuclear, wind, solar and geothermal. Out of these sources, solar energy is the most abundant source with ~100,000 TW[2] incident on the earth. Moreover solar energy is available in most parts of the earth and is important from the perspective of attaining energy independence for many countries which are dependent on imported oil. Thus utilizing solar energy, which is free and abundant, is a promising alternative. Existing solar cells are made out of high grade crystalline silicon which has high production costs. This results in higher cost of electricity generated by solar cells compared to other sources. Only low cost solar devices will enable large scale implementation of solar projects to meet the increasing energy requirements and reduce CO_2 emissions.

Third generation solar cells, made out of non-toxic and abundant material such as TiO_2, are deemed to be a cheaper alternative. Solar energy can be utilized by photolysis to synthesize hydrogen from water or by converting it to electricity. Fujishima and Honda first demonstrated that it is possible to split water into hydrogen and oxygen using TiO_2 as a photoanode.[3] Gratzel

showed that it is possible to mimic photosynthesis by using nano-structured TiO_2 film coated with a dye to form a solar cell.[4] The main requirements of TiO_2 based photo-electrode for good performance is high surface area, anatase phase and single crystal structure. Although various techniques[5-7] exist for making TiO_2 based photo-electrode, they either involve multiple steps or are difficult to scale up. Aerosol chemical vapor deposition (ACVD) is a one-step scalable process to deposit thin films of TiO_2.[8] The films deposited by ACVD consist of single crystal columnar structures which are good for electron transport in solar cells.[9] The morphology of the film such as columnar, granular and dense structured films can be controlled by changing process parameters depending on the final application. It is essential to scale up the thin film synthesis to reduce the production costs. Although there is qualitative understanding of the process, there is a need to model the ACVD process for scale up and extension to other metal oxides.

TiO_2 is preferred as a photo-electrode because it is a semiconductor and does not photo corrode. However, only 4% of the solar spectrum is absorbed by TiO_2 since it is a wide band gap (3-3.2ev) semiconductor. In order to extend the coverage of the solar spectrum, TiO_2 based photo-electrode is sensitized with materials that absorb in visible and near infrared (NIR) region such as quantum dots,[10, 11] dyes,[12] quantum wires[13] and plasmonic materials.[14] State of the art ruthenium dye based solar cells have 11% energy conversion efficiency.[15] The efficiency of the dye sensitized solar cell needs to be improved further to 15 % in order to make it economically attractive. For this purpose more incident solar energy needs to be harvested. However, so far no sensitizer has been fabricated which spans the complete solar spectrum. Co-sensitizing involves using two dyes, which have different absorption spectrum, to sensitize titanium dioxide. This has

resulted in improved efficiency, however the improvement in efficiency is not proportional to increased absorption because of charge recombination between the two dyes.[16] Thus there is a need for novel sensitizers which can absorb light and efficiently separate charge to improve the performance of titanium dioxide based solar cells.

Photosynthetic organisms have evolved over billions of years to harvest solar energy efficiently. Natural organisms have separate light absorption and reaction centers (to separate charge). The light-harvesting complexes (LHCs) contain systematically arranged dyes to maximize light absorption. The absorbed light is funneled to the reaction center by energy transfer processes, where it undergoes charge separation to drive bio-chemical processes. There are various architectures in nature for light-harvesting antennas, compared to reaction center. Various LHCs such as Fenna-Mathew-Olson (FMO) complex, LH2 and phycobilisomes have a protein network which holds the pigments in specific orientation for improving absorption and efficiently transferring energy. Chlorosomes on the other hand have a tightly stacked network of

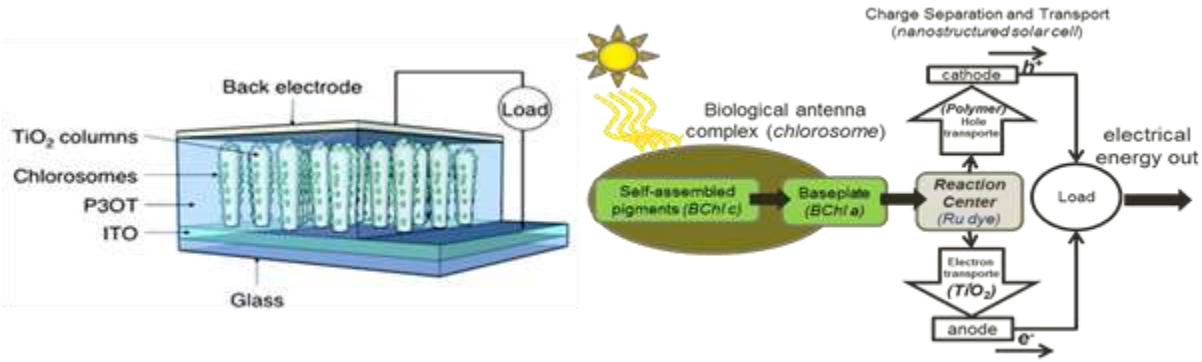

Figure 1–1: Schematic of titanium dioxide based solar cell with chlorosomes as sensitizer. Reproduced from Modesto et. al. 2011[17]

dyes with minimal protein network.[17] Light-harvesting complexes (LHCs), present in photosynthetic organisms, are being studied to understand the process of photosynthesis and to

utilize them in making useful bio-hybrid and artificial devices. LHCs and reaction center have been incorporated in various bio-hybrid and bio-chemical devices to improve performance. One such example is use of chlorosomes to transfer energy to reaction center in the ruthenium based dye sensitized solar cell.[18] The schematic of the device is shown in Figure 1–1. The device consists of nanostructured columnar TiO_2 deposited by the ACVD process. Chlorosomes were deposited by electrospray and then polymer (P3OT) was deposited to complete the device fabrication. In order to fabricate biohybrid devices using LHCs it is important to characterize the LHCs and immobilize them on a nanostructured surface.

Chlorosomes, present in bacteria, are one of the biggest and most efficient antennas present in nature. Chlorosomes consist of self-assembled dye molecules (Bacteriochlorophyll *c/d/e*) with minimal or no protein network.[17] This results in highest density of dyes among the natural light-harvesting complexes. These self-assembled dyes results in red-shift in peak absorbance compared to monomeric dyes, allowing bacteria to absorb in NIR region. Self-assembled structures contain carotenoids along with the dye molecules for photo-protection. Carotenoids also extend the absorption spectrum by absorbing light in visible region and transferring energy to BChl *c*. The light energy absorbed by self-assembled dye molecules is transferred to the baseplate and then to FMO by Förster resonance energy transfer (FRET). The absorption spectrum of baseplate and FMO are successively red shifted resulting in funneling effect. Thus all the light absorbed by chlorosomes is transferred to the reaction center. Chlorosomes are ellipsoidal in shape and depending on the species and growth conditions its size varies. The natural light-harvesting antennas cannot be tuned with respect to its size, absorption spectra or composition. In addition, it is cumbersome to extract the light-harvesting antennas

from the living organism. In order to control the size, absorption spectrum and composition of the chlorosomes like antennas they need to be synthesized synthetically.

In summary, to develop low cost next generation solar technology it is essential to have a scalable and economical method to make a TiO_2 photo-electrode. This wide band gap photo-electrode needs to be sensitized with novel sensitizers to improve the efficiency of the solar cell. Nature has perfected the architecture for light-harvesting by separating the light absorption and charge separation centers. Novel sensitizers, biological and synthetically made, with potential to improve the efficiency of the solar cell are characterized and deposited.

1.2 Objectives

Based on the motivation and research gaps described, the overarching goals of the PhD are three fold: to model the aerosol methodology for synthesis of 1-D, single crystal nanostructures which have proven to be very effective; to characterize various biological sensitizers and incorporate them to build solar cells; and, to develop a robust methodology for synthesis of biomimetic sensitizers. The specific objectives are:

1. To simulate morphology of thin films formed by aerosol methods – to understand the effect of sintering rate, particle size, and deposition rate on the morphology of nanostructured thin films of TiO_2 fabricated by ACVD
2. To characterize various biological light-harvesting complexes (LHC) and reaction centers using electrospray-mobility methods in flight and after deposition; to synthesize PSI based photoelectrochemical cells

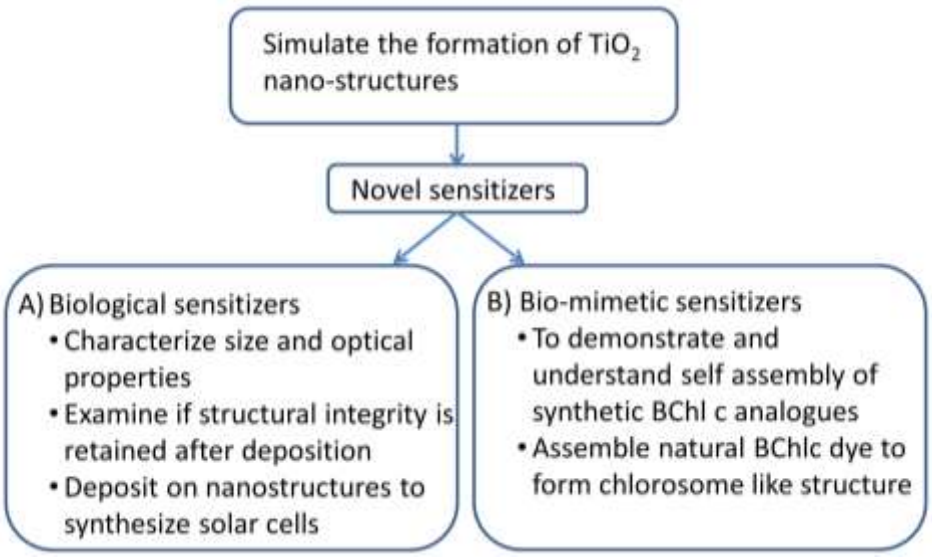

Figure 1–2: Flowchart representing the logical approach for the research objectives

3. To synthesize size tunable mimics of chlorosomes by promoting self-assembly via aerosol routes using synthetic and natural molecules

1.3 Outline

The thesis is broadly classified into two parts modelling and experiments. Chapter 2 describes the modelling of the ACVD system and supporting chapters in Appendix A and B. The experimental part involves use of electrospray for synthesis and/or deposition of the biological or biomimetic sensitizers. Chapter 3 and 4 describe the characterization of sensitizer and deposition to fabricate a solar cell. Chapter 5 and 6 describe the one step assembly in sprayed droplet for BChl *c* and its artificial analog.

In Chapter 2 the three models – Trimodal model, Brownian dynamics models and multiparticle sintering model are integrated to simulate the film formed by the ACVD process and study the effects of particle size, deposition rates, and sintering rates on morphology. ACVD involves deposition of particles to synthesize films with different morphologies. The trimodal

model is used to estimate the size of particles formed in the ACVD system. The deposition of these particles onto a substrate is simulated by the Brownian dynamics model. Since the substrate is heated the particles sinter after deposition, this is simulated by the Multi-particle Geometric Sintering Model. The results from these models are combined to give the morphology of the deposited film.

In Chapter 3 various LHCs such as chlorosome, FMO protein, phycobilisome, and LH2complex are characterized using ES-SMPS. These LHCs are deposited onto a conducting substrate by electrospray without being damaged, and the fluorescence and absorption spectra results are presented. In Chapter 4, a photoanode is fabricated by directed assembly after spraying PSI, which is a reaction center, onto nanostructured TiO_2 columns deposited by ACVD. On characterizing the photoelectrochemical performance, highest photocurrents for PSI based solar cells were obtained.

In chapter 5, molecular self-assembly inside an aerosolized droplet is demonstrated. The underlying mechanism of self-assembly is explained with help of single solvent technique and two solvent technique. Using two solvent technique, the control over the size of self-assembled structure is demonstrated. Chapter 6 extends the results for self-assembly in aerosolized droplet, demonstrated in previous chapter, to the naturally occurring bacteriochlorophyll *c*. A detailed comparison for the effect of concentration and droplet size on self-assembly are presented. Finally the self-assembled structures are characterized with GISAXS to get an understanding of their internal structure.

Chapter 7 lists the conclusions and the future work that can be done to gain better understanding of existing systems and enable new work.

The Appendix A lists the detailed derivation for the trimodal model and Appendix B gives the detailed derivation for multi-particle sintering model, both of them are used for the simulating films deposited by ACVD in Chapter 2. Appendix C lists the derivation for maximum flow rate that can be obtained by electrospray under an applied potential.

1.4 References

1. International Energy Outlook 2011 (Http://Www.Eia.Gov/Forecasts/Ieo/Pdf/0484%282011%29.Pdf).

2. Gratzel, M. Photovoltaic and Photoelectrochemical Conversion of Solar Energy. *Philosophical Transactions of the Royal Society a-Mathematical Physical and Engineering Sciences* **2007**, *365*, 993-1005.

3. Fujishima, A.; Honda, K. Electrochemical Photolysis of Water at a Semiconductor Electrode. *Nature* **1972**, *238*, 37.

4. O'Regan, B.; Gratzel, M. A Low-Cost, High-Efficiency Solar Cell Based on Dye-Sensitized Colloidal TiO_2 Films. *Nature* **1991**, *353*, 737-740.

5. Ito, S.; Chen, P.; Comte, P.; Nazeeruddin, M. K.; Liska, P.; Péchy, P.; Grätzel, M. Fabrication of Screen-Printing Pastes from TiO_2 Powders for Dye-Sensitised Solar Cells. *Progress in Photovoltaics: Research and Applications* **2007**, *15*, 603-612.

6. Su, Y. F.; Chou, T. C.; Ling, T. R.; Sun, C. C. Photocurrent Performance and Nanostructure Analysis of TiO_2/ITO Electrodes Prepared Using Reactive Sputtering. *J. Electrochem. Soc.* **2004**, *151*, A1375-A1382.

7. Allam, N. K.; Shankar, K.; Grimes, C. A. A General Method for the Anodic Formation of Crystalline Metal Oxide Nanotube Arrays without the Use of Thermal Annealing. *Adv. Mater.* **2008**, *20*, 3942-3946.

8. An, W.-J.; Thimsen, E.; Biswas, P. Aerosol-Chemical Vapor Deposition Method for Synthesis of Nanostructured Metal Oxide Thin Films with Controlled Morphology. *J. Phys. Chem. Lett.* **2010**, *1*, 249-253.

9. An, W.-J.; Jiang, D. D.; Matthews, J. R.; Borrelli, N. F.; Biswas, P. Thermal Conduction Effects Impacting Morphology During Synthesis of Columnar Nanostructured TiO_2 Thin Films. *J. Mater. Chem.* **2011**, *21*, 7913-7921.

10. Kamat, P. V. Quantum Dot Solar Cells. Semiconductor Nanocrystals as Light Harvesters†. *J. Phys. Chem. C* **2008**, *112*, 18737-18753.

11. Zhu, L.; An, W.-J.; Springer, J. W.; Modesto-Lopez, L. B.; Gullapalli, S.; Holten, D.; Wong, M. S.; Biswas, P. Linker-Free Quantum Dot Sensitized TiO_2 Photoelectrochemical Cells. *Int. J. Hydrogen Energy* **2012**, *37*, 6422-6430.

12. Kay, A.; Graetzel, M. Artificial Photosynthesis. 1. Photosensitization of Titania Solar Cells with Chlorophyll Derivatives and Related Natural Porphyrins. *J. Phys. Chem.* **1993**, *97*, 6272-6277.

13. Chen, H. N.; Zhu, L. Q.; Wang, M.; Liu, H. C.; Li, W. P. Wire-Shaped Quantum Dots-Sensitized Solar Cells Based on Nanosheets and Nanowires. *Nanotechnology* **2011**, *22*.

14. Brown, M. D.; Suteewong, T.; Kumar, R. S. S.; D'Innocenzo, V.; Petrozza, A.; Lee, M. M.; Wiesner, U.; Snaith, H. J. Plasmonic Dye-Sensitized Solar Cells Using Core-Shell Metal-Insulator Nanoparticles. *Nano Lett.* **2011**, *11*, 438-445.

15. Chen, C.-Y.; Wang, M.; Li, J.-Y.; Pootrakulchote, N.; Alibabaei, L.; Ngoc-le, C.-h.; Decoppet, J.-D.; Tsai, J.-H.; Graetzel, C.; Wu, C.-G.; Zakeeruddin, S. M.; Graetzel, M. Highly Efficient Light-Harvesting Ruthenium Sensitizer for Thin-Film Dye-Sensitized Solar Cells. *ACS Nano* **2009**, *3*, 3103-3109.

16. Clifford, J. N.; Forneli, A.; Chen, H.; Torres, T.; Tan, S.; Palomares, E. Co-Sensitized Dscs: Dye Selection Criteria for Optimized Device Voc and Efficiency. *J. Mater. Chem.* **2011**, *21*.

17. Blankenship, R. E.; Olson, J. M.; Miller, M., Anoxygenic Photosynthetic Bacteria. Blankenship, R. E.; Madigan, M. T.; Bauer, C. E., Eds. Kluwer Academic Publishers, The Netherlands: 1995; pp 399–435.

18. Modesto-Lopez, L. B.; Thimsen, E. J.; Collins, A. M.; Blankenship, R. E.; Biswas, P. Electrospray-Assisted Characterization and Deposition of Chlorosomes to Fabricate a Biomimetic Light-Harvesting Device. *Energy Env. Sci.* **2010**, *3*, 216-222.

Chapter 2 Simulation of Morphology of Nanostructured Thin Films Synthesized via Aerosol Processes

To be submitted to Aerosol Science and Technology, September, 2014

2.1 Abstract

A comprehensive model is built to simulate the morphology of films formed by any aerosol deposition process. The film formation by any aerosol deposition process involves three main parts - aerosol formation and growth, deposition, and restructuring. In this work, the film formed by Aerosol Chemical Vapor Deposition (ACVD) process is simulated by combining three models – (A) particle formation in gas phase by Trimodal model, (B) particle deposition onto heated substrate by Brownian dynamics model and (C) sintering on the heated substrate by a Multi-Particle Geometric Sintering Model (MPGSM). The simulated films have been characterized by their height, surface area and spread index. The Trimodal model and newly developed MPGSM have been validated with results reported in literature. Simulations using the integrated model have been performed to study the growing structure, and to understand the influence of sintering and deposition rates. It is shown that it is possible to get films of different heights and spread index by varying the sintering rate keeping everything else constant. Moreover, similar morphology variation can also be obtained by just changing the deposition rate. A balance between arrival rate and sintering rate must be maintained to obtain the desired morphology.

Keywords:

Multiparticle sintering, Aerosol deposition, Thin films, Simulation of morphology

2.2 Introduction

Nano-structured thin films have a variety of applications such as corrosion protection agents,[1-3] self-cleaning materials,[5] thin film transistors,[6] solar cells,[7-9] CO_2 reduction[10] and water purification.[11] Thin films have properties that are similar to that of bulk material for surface reactions. In addition, lower material requirements for fabrication of thin films reduce the production costs. There is a wide range of aerosol-based processes for film deposition such as electrospray deposition,[12, 13] aerosol chemical vapor deposition (ACVD, An et al. 2010), flame aerosol reactor system for deposition,[14] pulsed laser deposition[15] and thermal plasma based synthesis.[16] Apart from the simplicity and the control that aerosol based process offer, major benefits of using aerosol methods are solvent free processing, and ease of scale up. For example, ACVD is a process, offering a one-step approach that is easy to scale-up. This process can be used to deposit films of varying morphology and thickness by changing process conditions such as concentration and time of deposition. This method has previously demonstrated the capability of fabricating single crystal thin films of TiO_2 with 1D structures for water splitting[4] and photovoltaic applications.[8]

There are various physical characteristics of thin films such as thickness, porosity, surface area, morphology, and crystallinity that determine the performance and application. Each application requires a specific morphology, for example, a highly porous morphology is preferred for sensors to reduce the gas phase mass transfer coefficient.[17] On the other hand, for solar application crystalline material with 1D structure and high surface area would be preferential.[4, 9, 18] In contrast to previous two cases, corrosion protection requires a thin film with a flat morphology and low porosity.[1] In order to generate films with tailored characteristics a

detailed understanding of the effect of process parameters on film morphology is imperative. Apart from experiments, which result in qualitative understanding, comprehensive model and simulations are necessary for scale up.[19]

Thin film formation by aerosol process mainly involves deposition on particles onto a substrate. However most aerosol processes to form thin films[13-15] not only involve deposition of particles, but also their formation and restructuring after deposition. For example, films deposited by flame aerosol reactor[14] involves particle formation and growth, deposition, and sintering after deposition which take place on a millisecond time scale. Since these processes take place over a short time and distance, the models for aerosol formation and growth, and film restructuring need to be combined along with the deposition models for simulations.

There is a wide range of approaches for modeling aerosol formation and particle growth, ranging from approximate modal models[20, 21] to very accurate models such as Discrete Sectional.[22-24] As the objective of this paper is to simulate using integrated model, a computationally manageable trimodal model is used for modeling particle formation in gas phase. Moreover, the trimodal model is used because this can be applied to any system which has nucleation or multiple components, unlike other simpler unimodal[20] and bimodal model.[25]

One of the initial studies on particle deposition was conducted by Tassopoulos et al.[26] in which space and time were discretized to simulate deposition. The discretized space restricts the movement of particles to a grid, unlike real scenarios, thus limiting its ability to predict properties accurately. Kulkarni and Biswas[27] simulated the deposition of particles in a continuum space using Brownian dynamics model and studied effect of various forces such as van der

Waals, thermophoretic and electrostatic forces. Mädler et al.[28] extended the simulations to the deposition of fractal aggregates.

After deposition of particles restructuring takes place due to sintering or annealing as a result of thermal treatment. Thermal treatment is an important factor that alters the properties of a thin film.[9] With the exception of Kulkarni and Biswas,[29] none of the previous studies considered the effect of sintering on the evolution of the morphology of the thin films. The aforementioned study incorporated a sintering model which involved increasing size of one particle and decreasing size of the other particle such that the volume was conserved, and reducing the net area of two particles in contact. However, the sintering model was not physically correct and their simulation study was limited to deposition of few particles to form film. Sintering is a microscopic phenomenon and depends strongly on the local environment such as number of neighbors and their positions. Most of the existing models[30, 31] have been developed for sintering which involves particle-particle interaction in the gas phase. They track reduction of total surface area and conserve mass, without taking into account the local factors such as positions and re-arrangement of particles. This limits their use in simulating film morphology. Other works involving molecular dynamics based simulations,[32] or surface energy reduction methods[33, 34] give an accurate description of the geometry of sintering particles. However, these models are computationally intensive and cannot be applied to large number of particles present in the film. Two particle geometric sintering model which described physics accurately as well as being computationally simple was developed by Cho and Biswas.[35] Later, it was extended to particles of unequal size by Xie.[36] However, so far the geometric sintering model has been applicable for only two particles. To simulate sintering in a film there is a need

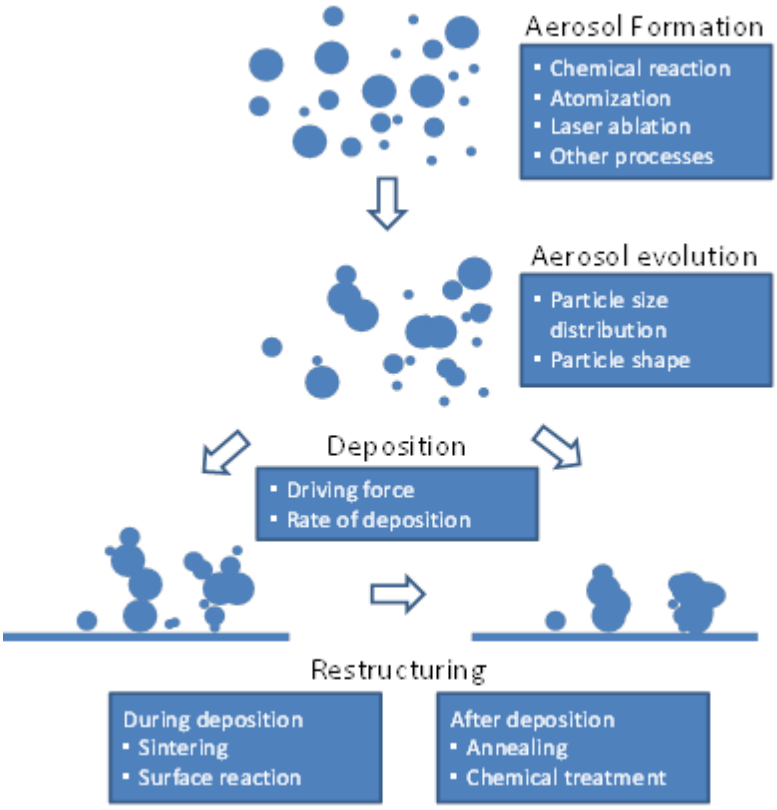

Figure 2–1: Schematic of film formation by deposition of aerosols

to extend the model to account for interaction of multiple particles. To the best of our knowledge multi-particle sintering has not been used before for simulating the morphology of deposit with large number of particles (>10000).

The objective of this work is to validate the newly developed models, then integrate them to simulate the film deposition by any aerosol process. The trimodal model, which is simple model for aerosol evolution, is verified using experimental data. A multiparticle geometric sintering model, newly developed, is compared with KFM to demonstrate the advantages. These models are then applied to ACVD process to simulate the morphology of the nanostructured film. In this work, the entire ACVD process is modeled in three parts. First, the formation of

particles in the gas phase is modeled with computationally simple trimodal model. Second, the deposition of particles onto the substrate is modeled with Brownian dynamics model. Third, new multi-particle geometric sintering model (MPGSM) is developed to model sintering of the deposited particles. The effects of particle size, deposition rates, and sintering rates on morphology have been studied and shown to influence the morphology of film significantly.

2.3 Modeling approach

The thin film formation by aerosol process can be divided into three parts namely, aerosol formation and growth, deposition to form a film, and restructuring. Figure 2–1 depicts these three parts and the main factors affecting them are also listed. The process of film deposition begins with the formation of aerosols. Aerosols can be formed by various methods[37] such as chemical reactions, atomization, or condensation. The aerosols then evolve depending on the initial size distribution, number concentration, temperature, the residence time and other conditions. Trimodal model is used to simulate the evolution of the particle size distribution of the aerosols. The model helps to estimate the size distribution and the shape of particles, which are the important factors that affect the characteristics of the deposited film. These particles are then deposited onto a surface under various driving forces such as gravity, thermophoresis, electrostatic forces or concentration gradients. The deposition process is modeled with the Brownian dynamics model, which takes into account the effect of various forces. This model gives the morphology of the deposit. Deposition rate which depends on driving force and fluid flow is the input to Brownian dynamic model. The film can then undergo restructuring simultaneously with deposition, or after deposition is complete. This restructuring can be due to

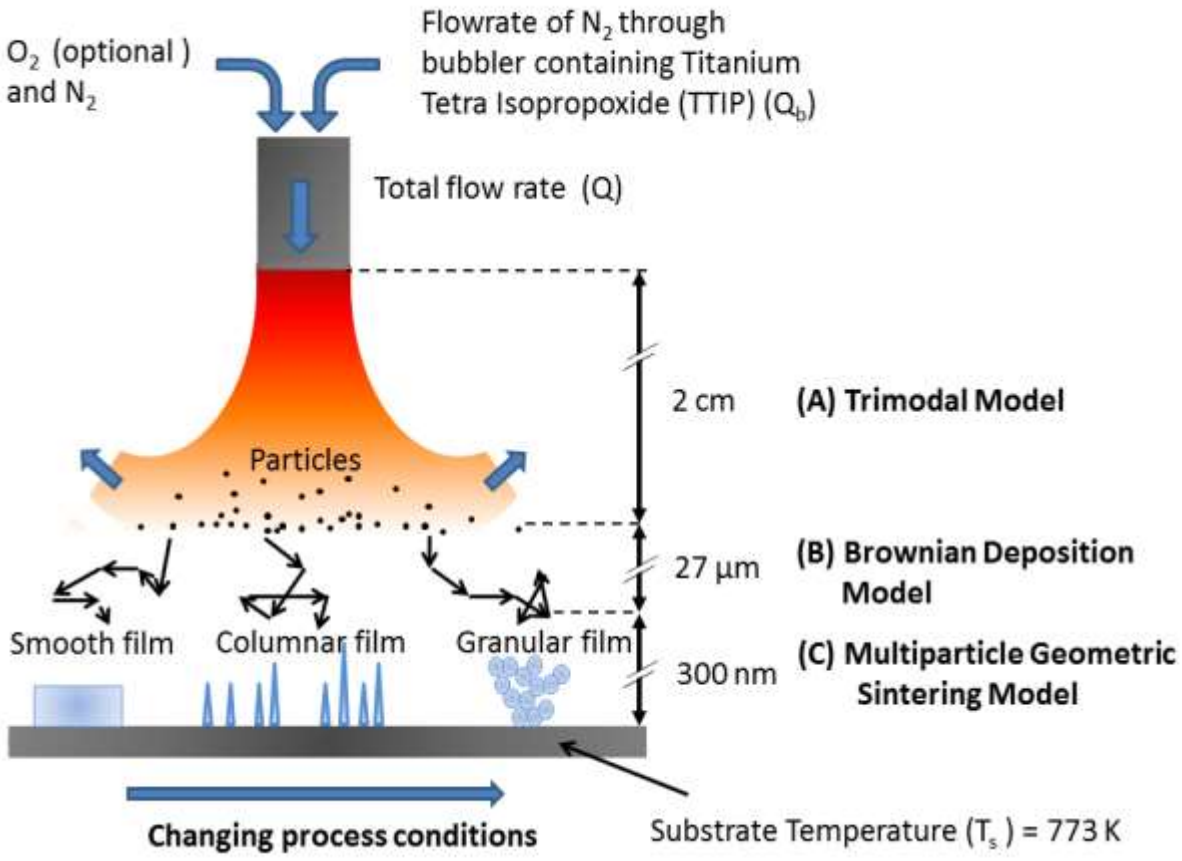

Figure 2–2: Schematic of ACVD reactor depicting the regions and the various models used to simulate film formation. Trimodal is used to model particle formation and evolution of aerosol, Brownian dynamics model for deposition and multi-particle geometric sintering model (MPGSM) is used to model sintering. The experimental conditions for the film deposition are listed in Table 2-2. The figure is adopted from An et. al.[4]

physical factors such as sintering or annealing as a result of high temperature, or chemical factors such as surface reaction or post deposition chemical treatment.

2.4 Methodology

First the overview of the ACVD process is given and the various models used are listed. The models are then described in detail individually. The models have been formulated so that

they can be applied to any aerosol deposition system. Finally the tools used to characterize the simulated film are described.

2.4.1 Model formulation

The schematic of the Aerosol Chemical Vapor Deposition (ACVD) process is shown in Figure 2–2. The substrate is heated to 773K and the region above it (Figure 2–2) acquires an elevated temperature through heat transfer. The precursor, in this case titanium tetra isopropoxide (TTIP), is fed into the reactor by a multi nozzle inlet. The TTIP precursor decomposes to form TiO_2 monomers. The monomers of TiO_2 combine to form larger particles due to the low vapor pressure of TiO_2.[38] These particles then grow by collision. The formation of particles from the vapor precursor and their growth is modeled by the Trimodal model. The Trimodal model gives the size distribution of particles and their shape. The particles along with vapor are carried convectively until they enter the boundary layer. The particles are deposited onto the substrate due to driving force such as van der Waals and concentration gradient. The important factors for deposition are driving force and rate of deposition. The deposition rate used in this work is obtained from the experimental measurements. In the boundary layer, the particle motion is dominated by diffusion hence a Brownian dynamics model is used to simulate the motion of particle. The deposited particles sinter to form nano-structures since the substrate is hot; sintering between nanoparticles is modeled using the MPGSM. Further experimental details and operating conditions are given elsewhere.[4] The formulation of each model (A) Trimodal model, (B) Brownian dynamics model and (C) MPGSM is described in detail as follows.

Trimodal model - Formation of particles in gas phase

The formation of particles in the gas phase is described using the Trimodal model. A constant temperature profile and a plug flow are assumed within the reactor between nozzle and substrate. The TTIP precursor introduced in the reactor decomposes to form TiO_2 molecules according to following first order process,

$$I = kc_p = kNAc_{p0}e^{-k(l/v)} \tag{2.1}$$

where c_{p0} is the initial precursor concentration, *t* is the residence time in reactor and *k* is the rate constant for decomposition given by Okuyama et al.,[39]

$$k = 3.96\times10^5 \exp\left(-\frac{70.5kJ\,/\,mole}{R_gT}\right)s^{-1} \tag{2.2}$$

The formation of larger TiO_2 particles from molecules and their subsequent growth is governed by collision. The particle formation is modeled using Trimodal model which consists of three size bins (characteristic modes). The three size bins, typically represent molecular size (mode 0), nucleation size (mode 1), and size of final particle (mode 2). However in the case of TiO_2, the nucleation size is molecular size.[40] Since this is a special case where no nucleation takes place, mode 1 has been chosen to represent a size twice that of mode 0. Condensation term has been replaced by a collision term, since the nucleation size for TiO_2 particles is the size of a monomer. The general dynamic equation written in discretized form, thus number concentration at each mode is expressed in terms of number concentrations of each modes. The number balance on the mode 0 gives,

$$\frac{dN_0}{dt} = I_0 - \beta_{01}N_0N_1 - \beta_{02}N_0N_2 - \frac{1}{2}\beta_{00}N_0^2\times2 + \frac{1}{2}\beta_{00}N_0^2\frac{m_1-2}{m_1-1} \tag{2.3}$$

where, I_0 is monomer generation rate from precursor, v_0 is monomer volume, v_1 is volume of particle in mode 1, $m_1 = v_1/v_0$ ratio of volume in mode 1 to mode 0, N_i is the number concentration of mode i, and β_{ij} is coagulation coefficient between mode i and j. When particles are formed by collision the resulting particle may or may not belong to either of the modes. In order to conserve the mass in the system the particles are apportioned between the two consecutive nodes using method described by Jeong and Choi.[25] This is accounted by using a correction factor, and for mode 0 it is $\frac{1}{2}\beta_{00}N_0^2\frac{m_1-2}{m_1-1}$.

Similarly by applying number balance on mode 1,

$$\frac{dN_1}{dt} = \frac{1}{2}\beta_{00}N_0^2\frac{1}{m_1-1} - \frac{1}{2}\beta_{11}N_1^2\frac{m_2}{m_2-1} + \frac{1}{m_1}\beta_{01}N_oN_1 - \beta_{12}N_1N_2 \tag{2.4}$$

where m_2 is the ratio of the volume of mode 2 to the volume of mode 1. Using an approach described earlier, the total number concentration, volume, and area for mode 2 are,

$$\frac{dN_2}{dt} = \frac{1}{2}\beta_{11}N_1^2\frac{1}{m_2-1} - \frac{1}{2}\beta_{22}N_2^2 \tag{2.5}$$

$$\frac{dV_2}{dt} = \frac{1}{2}\beta_{11}N_1^2\frac{m_2}{m_2-1}\upsilon_1 + \beta_{12}N_1N_2\upsilon_1 + \beta_{02}N_oN_2\upsilon_o \tag{2.6}$$

and

$$\frac{dA_2}{dt} = \frac{1}{2}\beta_{11}N_1^2\frac{m_2}{m_2-1}a_1 + \beta_{12}N_1N_2a_1 + \beta_{02}N_oN_2a_o \tag{2.7}$$

where N_2, V_2 and A_2 are total number concentration, volume and area of mode 2, respectively. a_i denotes the surface area of mode i. There are three equations for three unknowns in the mode 2, namely number concentration, size of particle and the fractal dimension which can be calculated from surface area. The resulting five ordinary differential equations (3-7) are solved using

Runge-Kutta method. The size of particles in mode 2, which represents the size of particles formed, is chosen as the size of particles getting deposited.

Brownian dynamics model - Deposition of particles on substrate

The motion of particle as it approaches the substrate is simulated with a Brownian dynamics model. A particle is dropped into a box which is 100 nm in height and has a square base in x-y plane of length 300 nm. The particle in the box follows a trajectory governed by the Langevin equation[41]

$$\hat{r}(t+\delta t) = \hat{r}(t) + \left(\frac{D}{kT} F_{ext}(t) \right) \delta t + \delta \hat{r}_g \tag{2.8}$$

$\hat{r}(t)$ is the position of the particle before random displacement, $\hat{r}(t+\delta t)$ gives the position of the particle after it has moved, $\hat{F}_{ext}(t)$ is the external force acting on the particle, and $\delta \hat{r_g}$ is the random displacement with zero mean over time and $2D\delta t$ variance. The diffusivity of the particle is dependent on the radius of depositing particle. The radius of particle is obtained from Trimodal model. Since this region is very close to the substrate, the residence time of particle is very small and the number concentration of particles is very low. Hence the particle is assumed to have the same size during deposition. If the particle goes out of the box in the 'z' direction a new particle is introduced. Periodic boundary conditions are applied on the other sides in the 'x' and the 'y' directions. The depositing particle is attracted to other deposited particles (P-P) and the substrate (P-S) due to van der Waals forces. Following equations are used for van Der Waals forces[42]

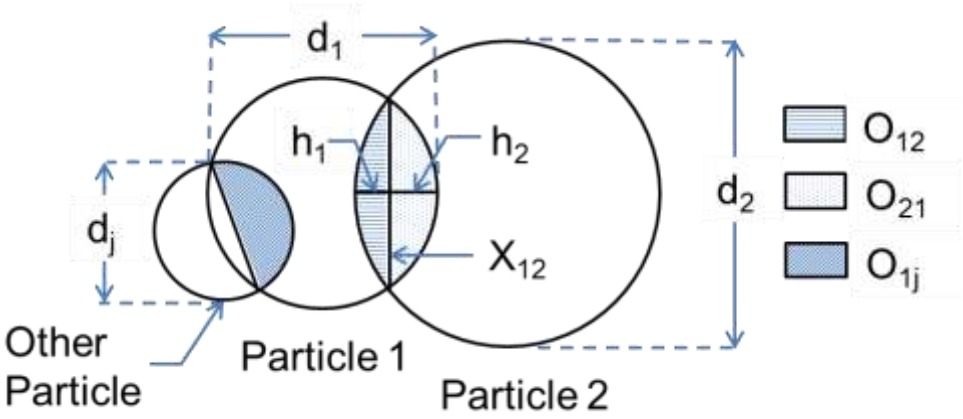

Figure 2–3: A two dimensional sketch depicting three sintering particles with diameter d_j, d_1 and d_2. The neck diameter is denoted by X_{12}, h_1 is the height of the spherical cap and O_{12} denotes the fraction of overlap volume between particles 1 and 2 which is in contiguous with particle 1.

$$F_{pp}^{VDS}(x,r,ri) = -\frac{H}{3}\left(\frac{2xrr_i}{\left(x^2-(r+r_i)^2\right)^2}+\frac{2xrr_i}{\left(x^2-(r+r_i)^2\right)^2}-\frac{x}{x^2-(r+r_i)^2}+\frac{x}{x^2-(r+r_i)^2}\right)\hat{e}_{r_{pp}} \quad (2.9)$$

$$F_{ps}^{VDS}(x,r) = -\frac{H}{6}\left(\frac{r}{(x-r)^2}+\frac{r}{(x+r)^2}+\frac{1}{x-r}-\frac{1}{x+r}\right)\hat{e}_{r_x} \quad (2.10)$$

here x is the center to center distance between particles or the normal distance between the deposition plane and the center of the particle, H is the Hamaker constant, and r_i is the radius of deposited particles. After the particle is deposited a new particle is introduced after a time interval determined by deposition rate. Sequential deposition is used because the time taken for deposition is shorter than the time after which the next particle is introduced in the box. The deposited particle starts sintering with the deposit. The height at which the particle is dropped is increased so as to maintain 100 nm distance between the highest particle in the deposit and new particle dropped. The particle transport rate from gas phase to film is obtained from experimental measurements. The weight of the film is measured at the start and at end of the experiments.

Since the size and density of particles is known, the flux of particles deposited from gas phase can be calculated.

Multiparticle geometric sintering model - Sintering of deposited particles on substrate

At high temperatures sintering affects the morphology of film. Sintering can also affect the porosity and surface area of the deposit. Since ACVD involves high temperature it is important to model sintering in order to accurately simulate the deposited film. The sintering begins as soon as the depositing particle comes in contact with other particles on the hot substrate.

A new multi-particle geometric sintering model (MPGSM), which is an extension of the model built by Cho and Biswas[35] and Xie,[36] is described in this section. Consider two particles of diameter d_1 and d_2 as shown in Figure 2–3. Let their initial diameter be d_{1i} and d_{2i}. These particles come in contact with each other at time $t = 0$ at temperature T. The particle center to center distance is given by D_{12}. This inter-particle distance will keep on reducing throughout the process and reduce to zero when the particles have fully sintered or coalesced. The rate of sintering depends on the size of particle, the type of material, its shape, the temperature, the neck diameter (labeled X_{12} in Figure 2–3) and the orientation of the grain boundary.[43] It is assumed that TiO_2 is a homogeneous material with no dependence on grain boundary orientation and that it is always a part of a sphere in the process of sintering.

The neck diameter is X_{12} at any given time, and h_1 and h_2 denote the heights of the spherical caps O_{12} of particles 1 and O_{21} of particle 2 respectively. By using simple geometrical considerations the neck diameter can be expressed as,

$$X_{12} = d_2\sqrt{1-(1-h_2)^2} = d_1\sqrt{1-(1-h_1)^2} \tag{2.11}$$

The diameter of particle 2, which is in contact with multiple particles changes, not only from sintering to particle 1, but also from sintering to other particles with which it is in contact. In the case of multiple particles in contact with one particle, two particles are selected at a time and the two particle sintering model[36] is applied after changing the initial diameter of the particle. To conserve the volume of the system the initial diameter of the particle, which is constant in two particle geometric sintering model, is modified at each time step to account for the overlap volume of the parent sphere with all other spheres except the one with which it is sintering. The initial diameter to be used in the two particle geometric sintering model is given by equation,

$$d_{s1} = \frac{6}{\pi}\left(V_1^0 + \sum_{j\neq 2} O_{1j}\right)^{1/3} \tag{2.12}$$

Here V_1^0 is the volume of the particle 1 prior to sintering, and O_{1j} denotes the volume overlap between 1 and j. Similarly,

$$d_{s2} = \frac{6}{\pi}\left(V_2^0 + \sum_{k\neq 1} O_{2k}\right)^{1/3} \tag{2.13}$$

where d_{s1} and d_{s2} denote the apparent initial diameter of the particles while sintering. This apparent initial diameter d_{s1} is different from d_1. d_1 shall be obtained after solving equations for two particle sintering model. The overlap volume between particle 1 and 2 belonging to particle 1 is given by,

$$O_{12} = \pi h_1^2\left(\frac{d_1}{2} - \frac{h_1}{3}\right) \tag{2.14}$$

The equations (2.13) and (2.14) simplifies to initial diameter of each particle for two particle sintering since the volume overlap with other particles is zero. After plugging in the apparent initial diameter into the two particle geometric sintering model which is given by,

$$X_2 = \frac{64\gamma D\Omega}{kTd_1}t \tag{2.15}$$

The actual diameter d_1 and the neck diameter X are obtained at various time. The new area, distance between the centers, and the volume overlap between particles can then be calculated. The two particle sintering model is applied to all the particles pairwise, and all the particles are rearranged according to the new distance between them. The particles in contact with the surface are rearranged first, followed by rearrangement of other particles on top of them. When the sintering is complete, the distance between two particles is zero. All the particles which were in contact with particles 1 or 2 are in contact with just one new particle of combined volume following merger. The time step is then increased and procedure is continuously repeated. The time step is chosen to be less than the sintering time constant.

Another way in which deposited film is affected is surface reaction. The undecomposed TTIP will decompose on the surface of deposited TiO_2 nano-structured film. The reaction rate constant is given by $k_s \approx 1\times10^{11}\exp(-15155.16/T)$.[44] In a case, where there are no mass transfer limitations, the reaction takes place on surface of the deposit. The maximum growth rate calculated is 0.06 nm/s at experimental conditions of 773K. The growth due to surface reaction is about 3.5 nm for simulation time of 1 min considered in this work. Since the growth due to surface reaction is less than the film thickness, growth due to surface reaction is not considered.

However, it could be incorporated by accounting for the material generated by surface reaction. This can be done by changing the initial diameter of the sintering particle.

2.4.2 Film Analysis

The simulated film is characterized by its height (h_{rms}), surface area and spread index. The height of the deposit is given by the volume weighted root mean square of the positions of the particles.

$$h_{rms} = \sqrt{\sum_{i=1}^{n} v_i z_i \Big/ \sum_{i=1}^{n} v_i} \tag{2.16}$$

here h_{rms} is the root mean square height of the deposit, v_i is the volume of particle before it starts sintering, and z_i is the position of the particle in z direction. A weighted average is taken because all particles are of different sizes. Thin film deposits can result in significant increase in area of a substrate for small mass deposited on it. The total surface area is calculated by adding up the exposed surface area of each particle calculated by MPGSM. The spread of a 'unit' in simulated deposit is calculated to provide insight into the morphology and porosity of the film. A unit is defined as all particles that are in mutual contact. First, the radius of gyration about the center of mass of a single unit is calculated. The spread index is calculated by normalizing the radius of gyration of a unit with the radius of gyration of the cylinder with equivalent volume and height given by equation (2.16).The weighted average across all units in the deposited film is taken to get a spread index for the simulated deposit. The spread index for a perfect sphere is about 1.6, and for a cylinder it is 1. Since a porous or branched deposit has particles spread out its spread index will be greater than 1.6.

2.5 Results and Discussion

A list of all simulations performed is summarized in Table 2-2. Section 2.5.1 presents the results for these simulations performed using the individual models, and their comparisons with other results in literature are discussed. In section 2.5.2, simulation results for integrated models are discussed.

2.5.1 Validation of models used

In this section the Trimodal model is validated with conditions for formation of particles in Flame Aerosol Reactor because experimental measurements are available and MPGSM has been compared with Koch and Friedlander model (KFM) and modified KFM.

Results from the Trimodal model and deposition rates calculation

In order to validate the Trimodal model two cases from Thimsen and Biswas[14] have been simulated. Thimsen and Biswas[14] used a premixed flame aerosol reactor (FLAR) to synthesize particles, which are deposited to form film. Two cases for TTIP flow rate of 0.059 mmol/hr and 0.55 mmol/hr were simulated. The size obtained from simulations was 1.83 nm and 4.41 nm in

Table 2-2: List of simulation for validating models and for the ACVD deposition system

Serial no.	Objective	Models used for simulations[a]	Description	Results
1	Model validation and results	A	Compare to experimental results from Thimsen and Biswas, 2007 and results for ACVD	Table 2-2
2	Model validation	B	Compare to KFM and Modified KFM	Figure 2–5
3	Growth of deposit	B, C	10 nm particles are deposited on substrate at 1173K	Figure 2–6
4	Sintering rate	A, B, C	4.7 nm particles obtained from Trimodal model for granular case are deposited	Figure 2–7
5	Deposition rate	A, B, C	4.7 nm particles obtained from Trimodal model for granular case are deposited	Figure 2–8

[a]A - Trimodal model, B - Brownian dynamics model and C – Multiparticle geometric sintering model (MPGSM)

Table 2-1: Experimental conditions for the ACVD reactor[a], simulation parameters and results obtained from the Trimodal model

	Experimental Process Parameters[b]			Experimental Results	Simulations Parameters		Simulation results		
Types of Morphologies[c]	Bubbler temperature (K)	Gas flow through bubbler (lpm)	Total gas flowrate (lpm)	Rate of deposition (mg/s)	Residence time (ms)	Concentration of precursor (mmol/m3)	Arrival Rate (#/s on 300x300 nm region)	Maximum radius (nm)	Percent of precursor decomposed
Dense	296	0.55	2	0.9	8.94	0.29	79237	0.6	5.9
Columnar	303	0.47	0.9	1	19.88	0.42	4422	1.57	12.6
Granular	303	0.47	0.47	0.8	38.08	3.23	215	4.3	22.8

[a]The distance between the nozzle and substrate is 2cm. The area of the nozzle is 14.9 mm^2

[b]Experimental conditions taken from An et. al.[4]

[c]As classified by An et. al.[4]

diameter, respectively. The sizes measured by author were 4.5 nm and 8 nm in diameter by TEM. The difference in the simulated values and measured values is mainly due to mixing in the flame. This mixing may lead to vigorous collisions between particles, resulting in accelerated growth.

The size of particles formed in ACVD is simulated using Trimodal model. The parameters used for simulations calculated from experimental conditions are given in Table 2-1. The simulated radius of the particles formed by the decomposition of TTIP in ACVD process is summarized in the table. It is observed that only 5.9% of TTIP gets decomposed in dense case because of low residence time. The time constant τ_{col} for collisional growth is given by Friedlander.[45]

$$\tau_{col} = \frac{2}{\beta N_0} \tag{2.17}$$

here N_0 is the number concentration of the aerosol and β is the collision frequency which is constant for particular size. Low number concentration of TiO_2 monomers formed in case of dense morphology increases the time constant for collision as shown in (2.17). This results in fewer collisions before deposition leading to formation of very small particles. Particles of size 0.6 nm in radius are formed for the case of dense morphology. In case of columnar morphology, longer residence time results in more TTIP decomposing than the previous case. Higher concentration of precursor and longer residence time compared to case of dense morphology, result in high number concentration of TiO_2 molecules and hence lower collision time constant. The particles formed are of radius 1.57 nm which is larger than in case of dense morphology. On further increasing the residence time and concentration of precursor, in case of granular morphology, larger particles which are 4.7 nm in radius are obtained. Hence under constant

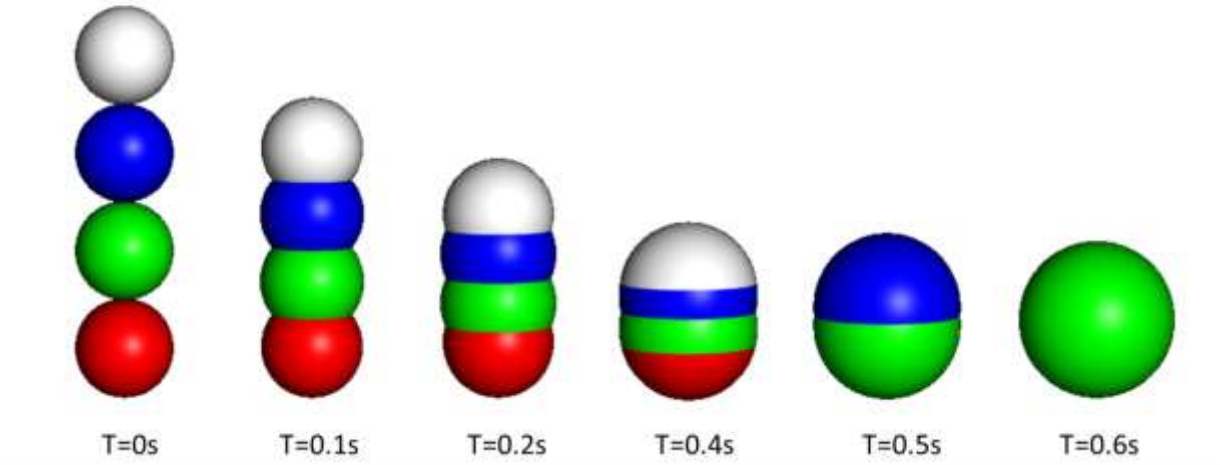

Figure 2–4: Sequential representation of four 5 nm radius particles sintering over time, as predicted by the multi-particle geometric sintering model (MPGSM)

temperature assumption, concentrations of TTIP and residence time are the two important parameters that control the size of particles. Since the mass of the film deposited is constant for all the morphologies, the particle deposition rate is inversely proportional to size of particles. This means smaller particles have larger deposition rate or more frequency of deposition. In case of dense morphology which has smallest particle size, 79000 particles/s are deposited while in granular case only 215 particles/s are deposited.

Comparison of MPGSM with other models

Figure 2–4 shows the sequential representation of shape of the four particles, with radius 5 nm, undergoing sintering according to MPGSM at 1173 K. The radius of particle, the distance between them and their surface area has been compared for three different models Koch and Friedlander model (KFM), modified KFM and MPGSM. In the modified KFM model the time constant for sintering changes with the change in radius. Following values were used in all the

sintering models for the calculations γ = 0.6 J/m^2, $D = 1.086 \times 10^{-2}\, exp\left(-\frac{323kJ/mole}{RT}\right)$ and Ω = 1.57×10^{-29} m^3.[35, 43]

The normalized radius of particles undergoing sintering with three different models is

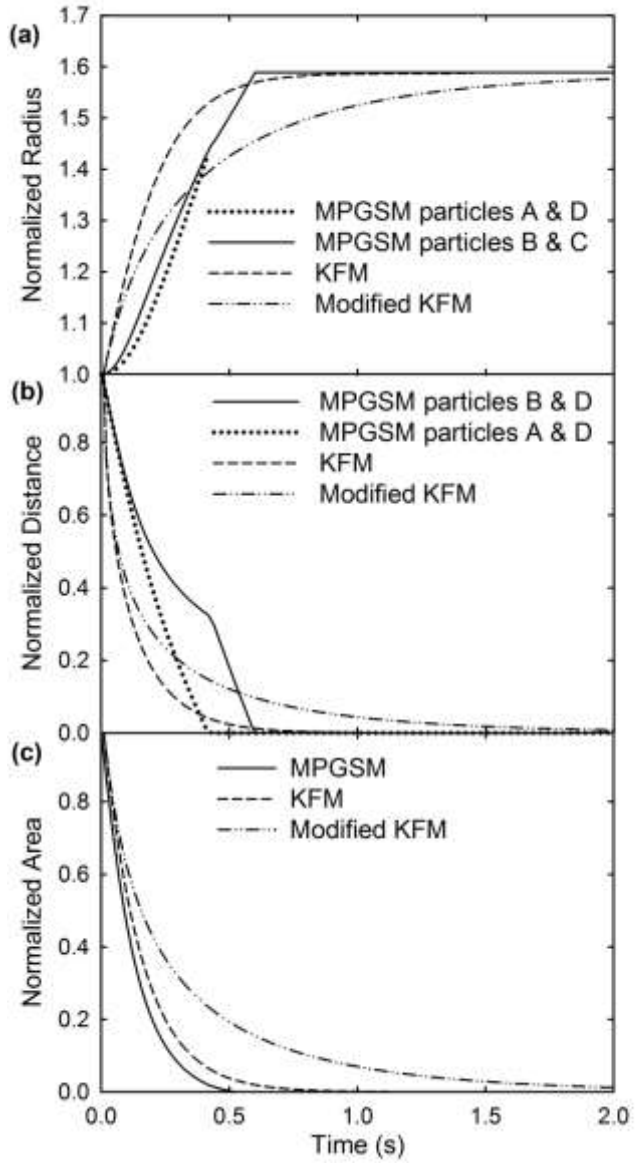

Figure 2–5: Comparison of a) normalized radius b) normalized distance between particles and c) normalized total surface area predicted by multi-particle geometric sintering model (MPGSM), Koch and Friedlander model (KFM) and modified KFM for four 5 nm radius particles undergoing sintering with time constant 0.14 seconds. The arrangement of particles and their labels are shown in Figure 2–4

shown in Figure 2–5a. It is possible to get radius of each and every particle involved in the process of sintering using MPGSM, unlike KFM since each particle is tracked. The radius of particles B & C is shown as dotted lines and A & D is shown as solid lines in the MPGSM model. The curve representing radius of particles as predicted by MPGSM are continuous at the time of merger and also have same slope. After the sintering is over, their radius is constant. The KFM and modified KFM predict a very quick increase in the radius of the particle; moreover there is no way to distinguish one particle from rest of the particles. So all the four particles have same radius in KFM and modified KFM model, which implies that the way in which particles are arranged does not affect the sintering rate.

The distance between particles also decreases quickly for the KFM and modified KFM, compared to the MPGSM (Figure 2–5b). Particles A & B and C& D merge when the distance between them goes to zero. After the merger of particles, the slope of curve representing the distance between particles B and C changes indicating there is slower rate of increase in size. This is because they have just one particle in contact now compared to two particles earlier. The area for KFM does not decrease as quickly as the MPGSM (Figure 2–5c). Cho and Biswas[35] compared the KFM model with GSM. They observed that the rate of decrease of area is higher for KFM than for GSM. This is contrary to current results. Since there are three pairs of particles, the rate of decrease of area in MPGSM is three times higher, where as in KFM the rate is independent of number of particles involved. Thus MPGSM is more accurate and used in this work for simulations.

2.5.2 Integrated simulations

Simulating film formation by deposition of particles taking place inside a reactor requires coupling of multiple models to simulate it. Hence in this section two or more models have been

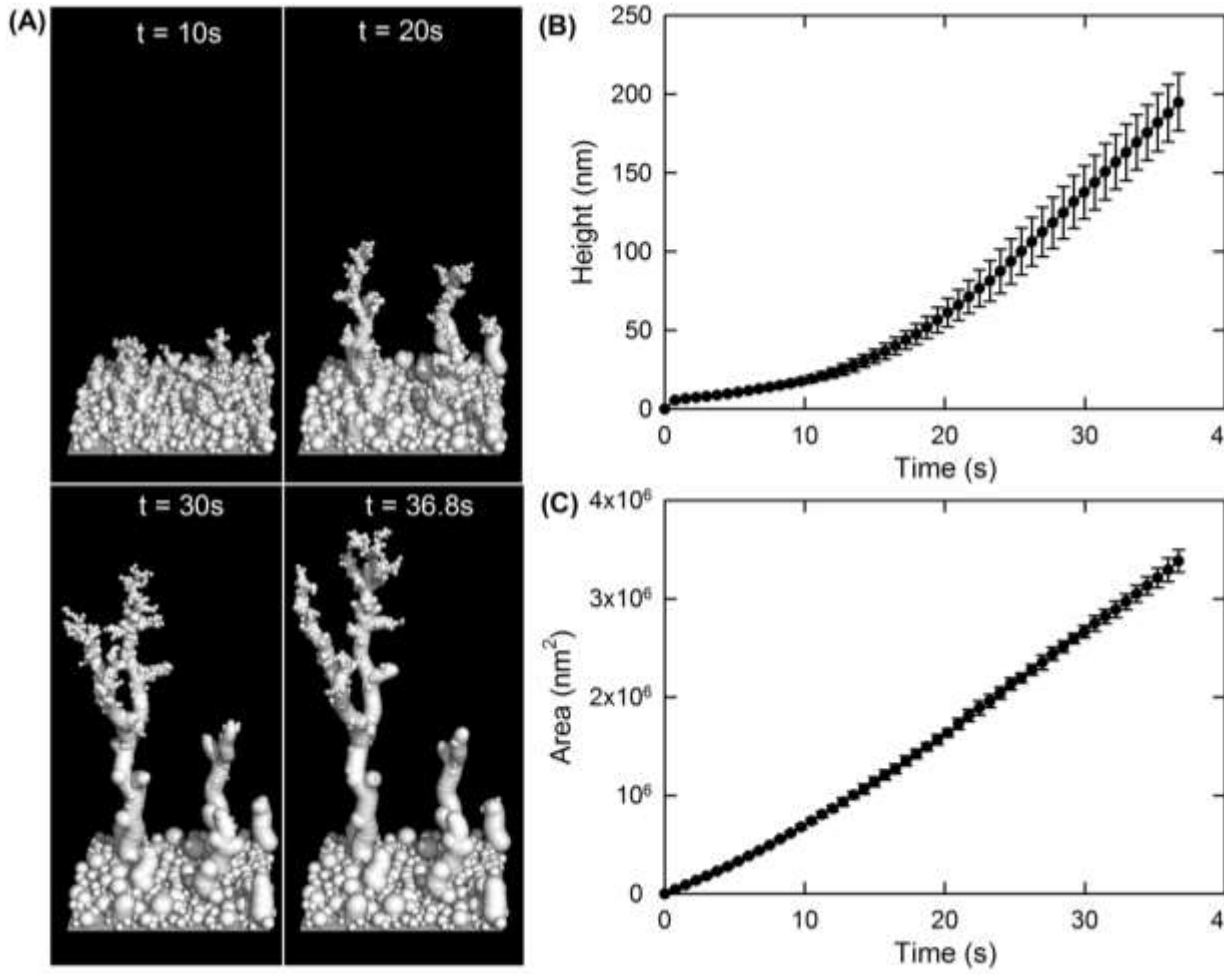

Figure 2–6: (a) Representations of the growing structure formed by 4nm particles depositing on the substrate at 1173 K at 10 s, 20 s, 30 s and 36.8 s. (b) The corresponding surface area of the growing structure and (c) height of the growing structure, as a function of time

integrated to study how both sintering rate and deposition rate influence the film morphology formed by ACVD. First the growth of film is simulated by coupling the models. Then the effect of sintering rate and deposition rate on the film characteristics is studied.

Growth of film

Figure 2–6a shows the growing deposit formed by 4 nm particles depositing on substrate at 1173 K averaged for 5 different runs. Since the substrate is hot, the particles start sintering with each other. It is seen that small structures are formed at 20 seconds. It is not possible to see

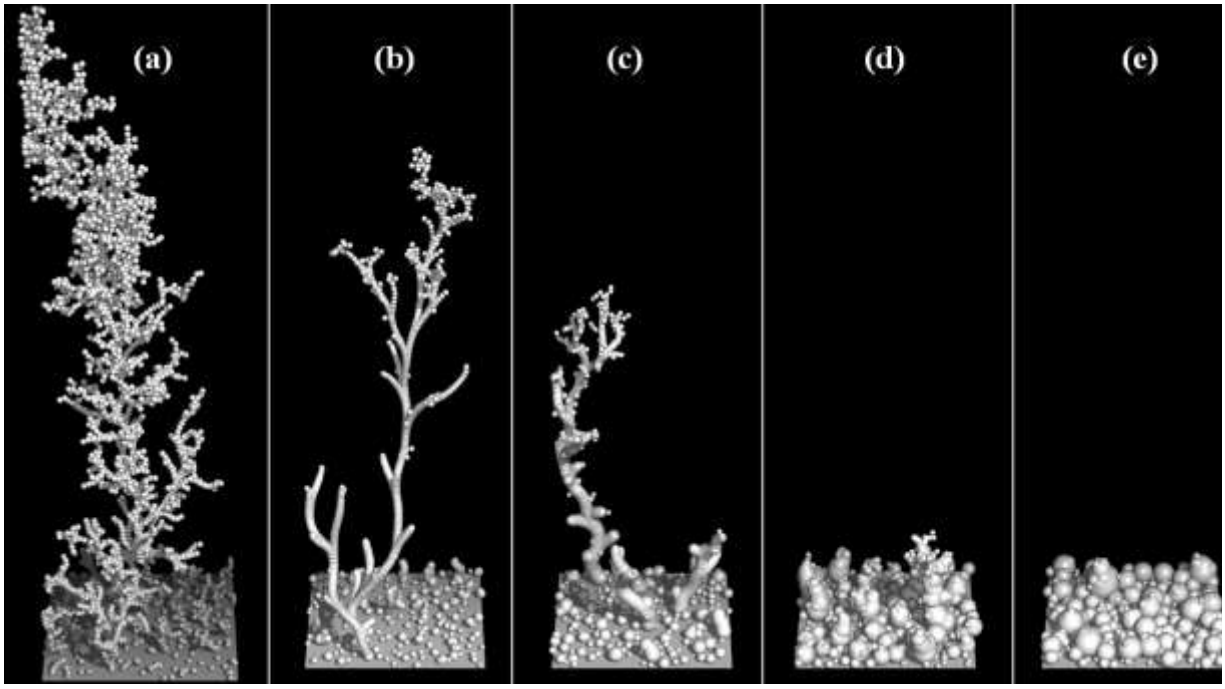

Figure 2–7: Effect of temperature of substrate, which affects the sintering rate, on morphology of film formed on deposition of 4.7 nm radius particles at substrate temperatures of a) 1047 K b) 1096 K c) 1150 K d) 1209 K e) 1276 K

individual particles close to substrate because they have sintered with other particles. The newly deposited particles are visible on the upper part of columnar structure at 30 seconds. These particles have not sintered to the main structure, hence they are distinctly visible. Figure 2–6b & c show the height and total area of the deposit respectively. The increase in height of the film is slow initially because particles get deposited all over the substrate. After some time the columnar structures start forming. The particles are intercepted by these structures and do not reach the substrate.[29] Hence the height increases at a higher rate. On the other hand the total surface area increase is linear. The surface area increases as new particles deposited particles, yet there are no differences in increase in surface area with time. The sintering rate is not affected by the differences in location of deposited particles, unlike the height of deposit. This is evident from the standard deviation in area which is very less compared to standard deviation in height.

Table 2-3: Properties of the simulated deposit formed at different substrate temperatures[a]

Temperature of susbstrate (K)	Sintering time constant (s)	Maximum height (nm)	Spread Index
1047	23.8	1055.4	21.2
1096	4.76	850.5	14.7
1150	0.95	562.9	4.5
1209	0.19	184.7	1.4
1276	0.04	83.1	1.4

[a]The radius of particle is 4.7nm, equivalent deposition time is 24.3s and rate of deposition is 164 particles/s

Effects of rate of sintering on the morphology of the simulated film

Figure 2–7 shows the different morphologies formed by changing sintering rate. The film is formed by the depositing 4.7 nm particles, which is the simulated size of particles formed in conditions for granular case. The sintering rates are varied by changing the temperature of the substrate in experiments. The time constants for sintering and other details are summarized in Table 2-3. The spread index for lowest temperature of substrate is 21.26, which means a highly porous and spread out structure is formed. The particles are loosely attached to each other as shown in Figure 2–7a and since they do not sinter the height of deposit is very high. As the temperature of the substrate goes on increasing, the sintering rate increases and the spread index goes down. The structures that are formed are less spread-out finally reaching a minimum at 1209 K and then rising again because of spherical particles. The spread index suggests that columnar morphology is formed at higher temperature (1209 K) and branched morphology at lower temperatures which is in agreement with observations by An et al.[8] The deposits formed are more compact at higher temperature because of sintering as indicated by the height of film.

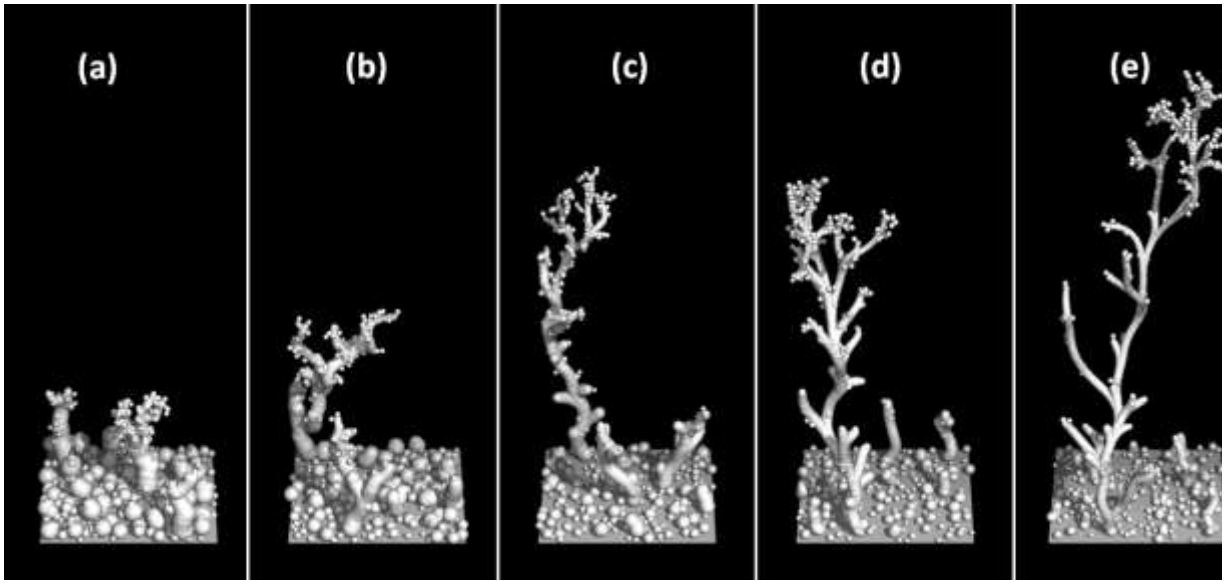

Figure 2–8: Effect of deposition rate on the morphology of the film. The particles of radius 4.7 nm are deposited at 1150 K. The deposition rate is 0.25, 0.5, 1, 2 and 4 times the rates obtained from experiment.

The substrate temperature used for observing variation in morphology using simulations in higher compared to experiments of An et al.[8] This is due to higher sintering rate of particles smaller than 10 nm compared to sintering rate predicted by empirical models for sintering.[46]

Effect of the rate of deposition on the morphology of the simulated film

Figure 2–8 shows the effect of the change of flux on the morphology of the deposit. The 4.7 nm particles are deposited on substrate at 1173 K. The deposition rate has been varied from 0.25, 0.5, 1, 2, and 4 times the rate of deposition obtained from experiments. The properties of the deposit are summarized in Table 2-4. The particles sinter quickly to form very compact structures when the deposition rate is low. On the other hand at very high deposition rate the structure grows big very quickly. The big structure intercepts all the depositing particles. The particles depositing at higher rate do not sinter completely and hence form highly branched and porous structure. This can also be compared using the spread index which is 19 and the height of the film which is 834.7 nm when deposition rate is high. On the other extreme, when deposition

Table 2-4: Properties of the simulated deposit formed at varying deposition rates[a]

Deposition rate (#/s)	Spread index	Average height (nm)
41.2	1.7	215.2
82.3	6.1	348.0
164.6	4.6	563.0
329.2	4.6	661.2
658.4	19.0	831.7

[a]The radius of particle is 4.7, number of particles deposited is 4000 and the temperature of sintering in 1150 K

rate is lowest, the spread index is 1.7 (close to that of sphere) and height is 215 nm. Thus the rate of deposition of the particles is important in determining the morphology of the deposit.

Comparison between sintering rates and arrival rate

The morphology of the film is dependent not only on the rate of sintering but also on number deposition rate of particles. However when we are comparing particles of different sizes a better metric is required. A new term 'arrival rate' is defined to aid the analysis. Arrival rate is the rate at which a particle will hit an already deposited particle. Keeping the amount of deposited material constant, we vary the particle size to see the effect of arrival rate. This variation results in change in number of particles arriving per unit time mainly because number of particles arriving scales as inverse of d^3 and probability of hitting the already deposited particle decreases by inverse of d^2. Figure 2–9a shows three possible scenarios for the depositing particle 'a'. The particles in the film can exist as (i) totally sintered, (ii) partially sintered or (iii) two separate particles. The condition of the deposited particles depends on the time interval after which particle 'a' arrives. Average of this time interval is called arrival time constant (τ_a). A highly granular structure is obtained if particle 'b' does not sinter to particle 'c' when particle 'a' deposits; or arrival time constant is higher than time constant for sintering: $\tau_a >> \tau_s$. In third case,

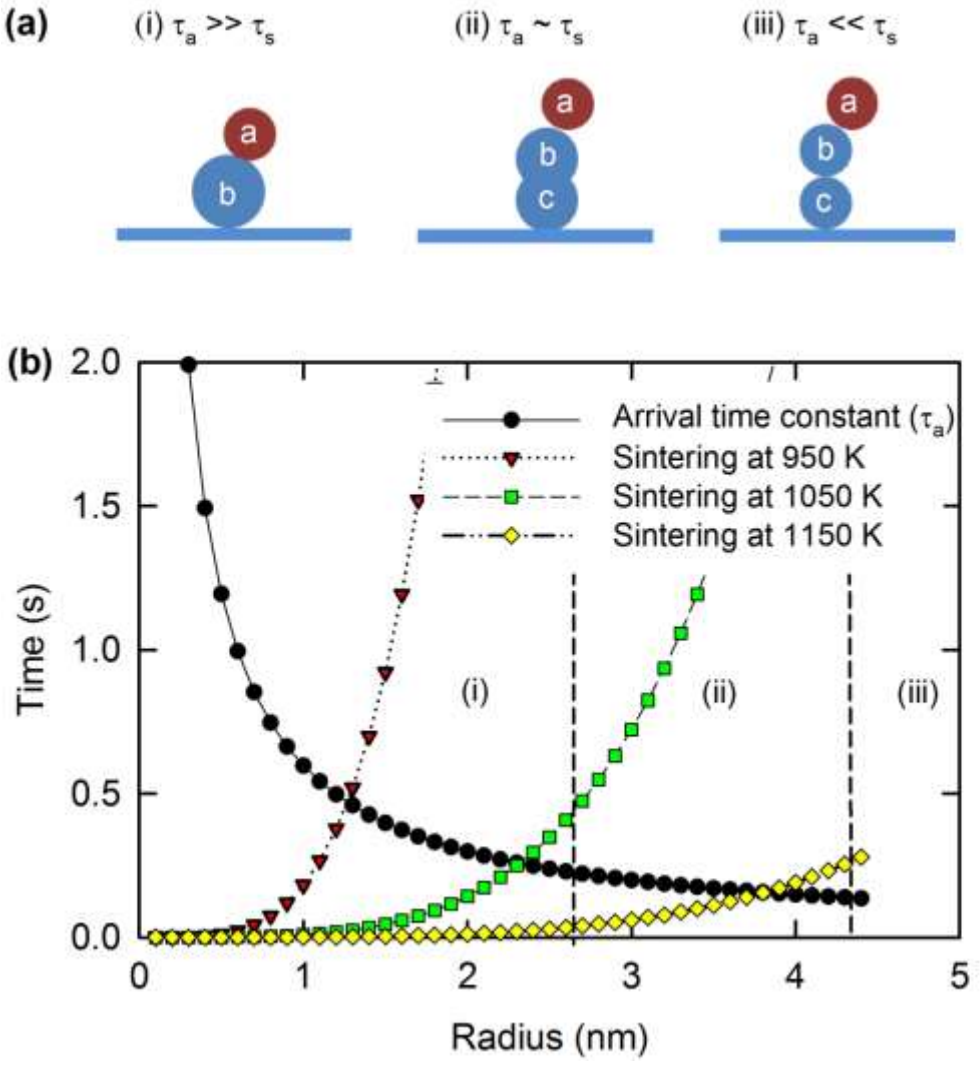

Figure 2–9: (a) Various scenarios possible for the depositing particle 'a' (i) on completely sintered particles (ii) on partially sintered particle (iii) non-sintered particles (b) Values of arrival time constant and sintering time constant for previously described cases with deposition rates held constant (sintering time constant from Kobata et al., 1991)

the particles 'b' and 'c' have merged completely before particle 'a' deposits, that is $\tau_s >> \tau_a$. This means particles get sintered as soon as they are deposited. When the $\tau_s \sim \tau_d$, columnar morphology will be formed because the new particle will be deposited on the partially sintered structure. These morphologies can be predicted by calculating time constants from sintering equation and calculated arrival rates. Figure 2–9b shows the comparison of the time constant for sintering and arrival time constant for deposition at 1150 K. The three regimes discussed

previously are depicted on the graph. A dense film is formed on the left when $\tau_d >> \tau_s$ and on the other extreme a porous film is formed when $\tau_d << \tau_s$. Particles of optimal size in region (ii) will be needed to grow columnar structure. The size of particle forming the columnar structure will grow bigger as the temperature for sintering increases (Figure 2–9b) if the amount of deposited material is held constant. This analysis is important from the perspective of scale-up, increasing just the number of particles getting deposited may increase the growth rate of film but it will also affect the morphology of the film. An et al.[8] attributes changes in morphology primarily to thermal conduction effects and sintering, but changes in arrival rates which is dependent on multiple factors such as fluid flow and driving force also needs to be taken into accounted.

2.6 Conclusions

Three models – Trimodal model, Brownian dynamics model and MPGSM have been coupled to simulate the film formed by ACVD process. The radius of particles depositing is largest for the granular case (4.7 nm), followed by columnar (1.57 nm) and smallest particles for dense film (0.6 nm). These particles are deposited on surface by diffusion and van Der Waals force. A computationally efficient MPGSM has been built for simulating sintering in the deposit. The film is characterized by its height, surface area and spread index. Spread index can be used as an objective indicator for the morphology of the film. Sintering rate, which can be controlled by changing the substrate temperature, is an important parameter that affects the morphology of the film. Apart from sintering, deposition rate plays an important role in determining the morphology of the film. Balance between the rate of deposition and sintering needs to be maintained to obtain a particular morphology. The temperature of substrate had to be increased to change sintering rate in simulations because particles below 10 nm have higher sintering rate

than predicted by current sintering expression.[46] A phenomenological model for sintering of particles smaller than 10 nm needs to be developed in order to improve the simulations.

A wide range of surface area enhancements, height of the film and morphology can be obtained by controlling the process parameters in ACVD. This simulation approach can be used for any aerosol based deposition process forming thin films, especially for films formed at high temperatures. In future other parameters like electrical conductivity, thermal conductivity and crystallinity could be incorporated to help tailor thin films for specific applications.

2.7 Nomenclature

a area of particle (nm^2)

c_p precursor concentration (M)

c_{p0} initial precursor concentration (M)

d diameter of particle (nm)

h height of overlap volume (nm)

k reaction rate constant (mols/s)

k_s rate constant for surface reaction (m/s)

m ratio of volume

v volume of particle (nm^3)

t time (s)

A area of all particles (nm^2)

C_c Cunningham slip correction factor

D diffusion coefficient (m^2/s)

D_{ij} distance between two particles (nm)

H Hamaker constant

I rate of generation of monomers (mols/s)

N number concentration (#/m^3)

N_A Avogadro number (#/mol)

O_{ij} Volume overlap between two spheres i and j (nm^3)

R_g Universal gas constant (J/(mol.K))

R Radius of particle (nm)

T Temperature (K)

V volume of all particles (m^3, nm^3)

X_{ij} neck radius between particle i and j (nm)

Greek Alphabets

β Collision frequency (m^3/s)

γ surface tension (kg/s^2)

η viscosity of air (Pa.s)

τ time constant (s)

Ω molecular volume (m^3)

2.8 References

1. Yang, G. X.; Biswas, P.; Boolchand, P.; Sabata, A. Deposition of Multifunctional Titania Ceramic Films by Aerosol Routes. *J. Am. Ceram. Soc.* **1999**, *82*, 2573-2579.

2. Hubler, R.; Cozza, A.; Marcondes, T. L.; Souza, R. B.; Fiori, F. F. Wear and Corrosion Protection of 316-L Femoral Implants by Deposition of Thin Films. *Surface & Coatings Technology* **2001**, *142*, 1078-1083.

3. Wang, D.; Ni, Y.; Huo, Q.; Tallman, D. E. Self-Assembled Monolayer and Multilayer Thin Films on Aluminum 2024-T3 Substrates and Their Corrosion Resistance Study. *Thin Solid Films* **2005**, *471*, 177-185.

4. An, W.-J.; Thimsen, E.; Biswas, P. Aerosol-Chemical Vapor Deposition Method for Synthesis of Nanostructured Metal Oxide Thin Films with Controlled Morphology. *J. Phys. Chem. Lett.* **2010**, *1*, 249-253.

5. Nakajima, A.; Hashimoto, K.; Watanabe, T.; Takai, K.; Yamauchi, G.; Fujishima, A. Transparent Superhydrophobic Thin Films with Self-Cleaning Properties. *Langmuir* **2000**, *16*, 7044-7047.

6. Carcia, P. F.; McLean, R. S.; Reilly, M. H.; Nunes, G. Transparent ZnO Thin-Film Transistor Fabricated by Rf Magnetron Sputtering. *Appl. Phys. Lett.* **2003**, *82*, 1117-1119.

7. Pavasupree, S.; Ngamsinlapasathian, S.; Nakajima, M.; Suzuki, Y.; Yoshikawa, S. Synthesis, Characterization, Photocatalytic Activity and Dye-Sensitized Solar Cell Performance of Nanorods/Nanoparticles TiO_2 with Mesoporous Structure. *J. Photochem. Photobiol. A: Chem.* **2006**, *184*, 163-169.

8. An, W.-J.; Jiang, D. D.; Matthews, J. R.; Borrelli, N. F.; Biswas, P. Thermal Conduction Effects Impacting Morphology During Synthesis of Columnar Nanostructured TiO_2 Thin Films. *J. Mater. Chem.* **2011**, *21*, 7913-7921.

9. Thimsen, E.; Rastgar, N.; Biswas, P. Nanostructured TiO_2 Films with Controlled Morphology Synthesized in a Single Step Process: Performance of Dye-Sensitized Solar Cells and Photo Watersplitting. *J. Phys. Chem. C* **2008**, *112*, 4134-4140.

10. Liu, S. H.; Zhao, Z. H.; Wang, Z. Z. Photocatalytic Reduction of Carbon Dioxide Using Sol-Gel Derived Titania-Supported Copc Catalysts. *Photochemical & Photobiological Sciences* **2007**, *6*, 695-700.

11. Fernandez, A.; Lassaletta, G.; Jimenez, V. M.; Justo, A.; GonzalezElipe, A. R.; Herrmann, J. M.; Tahiri, H.; AitIchou, Y. Preparation and Characterization of TiO_2 Photocatalysts Supported on Various Rigid Supports (Glass, Quartz and Stainless Steel). Comparative Studies of Photocatalytic Activity in Water Purification. *Applied Catalysis B-Environmental* **1995**, *7*, 49-63.

12. Lopez, L. B. M.; Pasteris, J. D.; Biswas, P. Sensitivity of Micro-Raman Spectrum to Crystallite Size of Electrospray-Deposited and Post-Annealed Films of Iron-Oxide Nanoparticle Suspensions. *Appl. Spectrosc.* **2009**, *63*, 627-635.

13. van Zomeren, A. A.; Kelder, E. M.; Marijnissen, J. C. M.; Schoonman, J. The Production of Thin Films of $LiMn_2O_4$ by Electrospraying. *25* **1995**, *6*.

14. Thimsen, E.; Biswas, P. Nanostructured Photoactive Films Synthesized by a Flame Aerosol Reactor. *AlChE J.* **2007**, *53*, 1727-1735.

15. Matsumura, M.; Camata, R. P. Pulsed Laser Deposition and Photoluminescence Measurements of ZnO Thin Films on Flexible Polyimide Substrates. *Thin Solid Films* **2005**, *476*, 317-321.

16. Girshick, S. L.; Hafiz, J. Thermal Plasma Synthesis of Nanostructured Silicon Carbide Films. *Journal of Physics D-Applied Physics* **2007**, *40*, 2354-2360.

17. Thybo, S.; Jensen, S.; Johansen, J.; Johannessen, T.; Hansen, O.; Quaade, U. J. Flame Spray Deposition of Porous Catalysts on Surfaces and in Microsystems. *J. Catal.* **2004**, *223*, 271-277.

18. Mor, G. K.; Shankar, K.; Paulose, M.; Varghese, O. K.; Grimes, C. A. Use of Highly-Ordered TiO_2 Nanotube Arrays in Dye-Sensitized Solar Cells. *Nano Lett.* **2006**, *6*, 215-218.

19. Li, Y. M.; Somorjai, G. A. Nanoscale Advances in Catalysis and Energy Applications. *Nano Lett.* **2010**, *10*, 2289-2295.

20. Kruis, F. E.; Kusters, K. A.; Pratsinis, S. E.; Scarlett, B. A Simple Model for the Evolution of the Characteristics of Aggregate Particles Undergoing Coagulation and Sintering. *Aerosol Sci. Technol.* **1993**, *19*, 514-526.

21. Lee, S. R.; Wu, C. Y. Size Distribution Evolution of Fine Aerosols Due to Intercoagulation with Coarse Aerosols. *Aerosol Sci. Technol.* **2005**, *39*, 358-370.

22. Gelbard, F.; Seinfeld, J. H. Simulation of Multicomponent Aerosol Dynamics. *J. Colloid Interface Sci.* **1980**, *78*, 485.

23. Yu, S.; Yoon, Y.; Muller-Roosen, M.; Kennedy, I. M. A Two-Dimensional Discrete-Sectional Model for Metal Aerosol Dynamics in a Flame. *Aerosol Sci. Technol.* **1998**, *28*, 185-196.

24. Wu, C. Y.; Biswas, P. Study of Numerical Diffusion in a Discrete-Sectional Model and Its Application to Aerosol Dynamics Simulation. *Aerosol Sci. Technol.* **1998**, *29*, 359-378.

25. Jeong, J. I.; Choi, M. A Simple Bimodal Model for the Evolution of Non-Spherical Particles Undergoing Nucleation, Coagulation and Coalescence. *J. Aerosol Sci.* **2003**, *34*, 965-976.

26. Tassopoulos, M.; Obrien, J. A.; Rosner, D. E. Simulation of Microstructure Mechanism Relationships in Particle Deposition. *AlChE J.* **1989**, *35*, 967-980.

27. Kulkarni, P.; Biswas, P. A Brownian Dynamics Simulation to Predict Morphology of Nanoparticle Deposits in the Presence of Interparticle Interactions. *Aerosol Sci. Technol.* **2004**, *38*, 541-554.

28. Madler, L.; Roessler, A.; Pratsinis, S. E.; Sahm, T.; Gurlo, A.; Barsan, N.; Weimar, U. Direct Formation of Highly Porous Gas-Sensing Films by in Situ Thermophoretic Deposition of Flame-Made Pt/SnO_2 Nanoparticles. *Sensors and Actuators B-Chemical* **2006**, *114*, 283-295.

29. Kulkarni, P.; Biswas, P. Morphology of Nanostructured Films for Environmental Applications: Simulation of Simultaneous Sintering and Growth. *J. Nanopart. Res.* **2003**, *5*, 259-268.

30. Koch, W.; Friedlander, S. K. The Effect of Particle Coalescence on the Surface Area of a Coagulating Aerosol. *J. Colloid Interface Sci.* **1990**, *140*, 419-427.

31. Schmid, H.-J.; Tejwani, S.; Artelt, C.; Peukert, W. Monte Carlo Simulation of Aggregate Morphology for Simultaneous Coagulation and Sintering. *J. Nanopart. Res.* **2004**, *6*, 613-626.

32. Raut, J. S.; Bhagat, R. B.; Fichthorn, K. A. Sintering of Aluminum Nanoparticles: A Molecular Dynamics Study. *Nanostruct. Mater.* **1998**, *10*, 837-851.

33. Ch'ng, H. N.; Pan, J. Sintering of Particles of Different Sizes. *Acta Mater.* **2007**, *55*, 813-824.

34. Eggersdorfer, M. L.; Kadau, D.; Herrmann, H. J.; Pratsinis, S. E. Multiparticle Sintering Dynamics: From Fractal-Like Aggregates to Compact Structures. *Langmuir* **2011**, *27*, 6358-6367.

35. Cho, K.; Biswas, P. A Geometrical Sintering Model (GSM) to Predict Surface Area Change. *J. Aerosol Sci.* **2006**, *37*, 1378-1387.

36. Xie, H. A Geometrical Model for Coalescing Aerosol Particles. *J. Aerosol Sci.* **2008**, *39*, 277-285.

37. Friedlander, S. K. *Smoke, Dust, and Haze: Fundamental of Aerosol Dynamics*. Second ed.; Oxford University Press: New York, 2000.

38. Yang, G. X.; Zhuang, H. R.; Biswas, P. Characterization and Sinterability of Nanophase Titania Particles Processed in Flame Reactors. *Nanostruct. Mater.* **1996**, *7*, 675-689.

39. Okuyama, K.; Ushio, R.; Kousaka, Y.; Flagan, R. C.; Seinfeld, J. H. Particle Generation in a Chemical Vapor-Deposition Process with Seed Particles. *AlChE J.* **1990**, *36*, 409-419.

40. Kodas, T. T.; Hampden-Smith, M. *Aerosol Processing of Materials*. Wiley-VCH: New York, 1999.

41. Ermak, D. L. Computer-Simulation of Charged-Particles in Solution .1. Technique and Equilibrium Properties. *J. Chem. Phys.* **1975**, *62*, 4189-4196.

42. Parsegian, V. A. *Van Der Waals Forces : A Handbook for Biologists, Chemists, Engineers, and Physicists*. Cambridge University Press: New York, 2006; p xv, 380 p.

43. Astier, M.; Vergnon, P. Determination of the Diffusion Coefficients from Sintering Data of Ultrafine Oxide Particles. *J. Solid State Chem.* **1976**, *19*, 67-73.

44. Battiston, G. A.; Gerbasi, R.; Porchia, M.; Gasparotto, A. Metal Organic CVD of Nanostructured Composite TiO_2-Pt Thin Films: A Kinetic Approach. *Chem. Vap. Deposition* **1999**, *5*, 13-20.

45. Friedlander, S. K. *Smoke, Dust and Haze*. Wiley: New York, 1977.

46. Buesser, B.; Grohn, A. J.; Pratsinis, S. E. Sintering Rate and Mechanism of TiO_2 Nanoparticles by Molecular Dynamics. *J. Phy. Chem. C* **2011**, *115*, 11030-11035.

Chapter 3 Characterization and Deposition of Various Light-Harvesting Antenna Complexes by Electrospray Atomization

The results reported in this chapter were published in - Shah, V. B.; Orf, G. S.; Reisch, S.; Harrington, L. B.; Prado, M.; Blankenship, R. E.; Biswas, P. Characterization and Deposition of Various Light-Harvesting Antenna Complexes by Electrospray Atomization. Anal. Bioanal. Chem. 2012, 404, 2329-2338.

3.1 Abstract

Photosynthetic organisms have light-harvesting complexes that absorb and transfer energy efficiently to reaction centers. Light-harvesting complexes (LHCs) have received increased attention in order to understand the natural photosynthetic process, and also to utilize their unique properties in fabricating efficient artificial and bio-hybrid devices to capture solar energy. In this work, LHCs with different architectures, sizes and absorption spectra, such as chlorosomes, FMO protein, LH2 complex and phycobilisome have been characterized by an electrospray-scanning mobility particle sizer system (ES-SMPS). The size measured by ES-SMPS for FMO, chlorosomes, LH2 and phycobilisome were 6.4 nm, 23.3 nm, 9.5 nm and 33.4 nm respectively. These size measurements were compared to values measured by dynamic light scattering and those reported in the literature. These complexes were deposited onto a transparent substrate by electrospray deposition. Absorption and fluorescence spectra of the deposited LHCs were measured. It was observed that the LHCs have light absorption and fluorescence spectra similar to that in solution, demonstrating the viability of the process.

Keywords:

Electrospray-Scanning mobility particle sizer (ES-SMPS), Electrospray deposition, Light-harvesting complexes (LHCs)

3.2 Introduction

Solar energy harvesting is receiving considerable attention because it is a carbon neutral and a renewable source of energy. Photosynthetic organisms have evolved over billions of years to harvest this energy efficiently. Light-harvesting complexes (LHCs), present in photosynthetic organisms, are key to absorption of sunlight and converting it to chemical energy. The LHCs are being studied to understand the process of photosynthesis and to utilize them in making useful bio-hybrid and artificial devices to harvest solar energy.[1-6]

The light-harvesting complexes contain systematically arranged dye molecules to maximize light absorption. The absorbed light is converted to exciton and transferred to the reaction center by energy transfer processes. In the reaction center, the exciton undergoes charge separation, which drives biochemical processes. Photosystem II (PSII), from cyanobacteria and plants, has been used for making bio-sensors to detect pollutants.[1] Reaction centers such as PSII,[2] bacteriorhodopsin,[3] Photosystem I[4] and light-harvesting antenna complexes or their parts such as C-phycocyanin[5] and chlorosomes[6] have been used in fabricating bio-hybrid solar devices.

LHCs need to be characterized in order to understand their functionality and fabricate a biohybrid device. Since LHCs from different organisms have different architectures, they have different sizes, shapes, and absorption spectra. Various methods such as atomic force microscopy,[7, 8] Small Angle Neutron Scattering (SANS)[9] and X-Ray crystallography[10] have been used for size measurement and characterization of LHCs. SANS is an advanced technique that has been recently used to probe the structure of light-harvesting complexes.[9] This technique provides information about the periodic structures that can be used to estimate the size of LHCs

as well as the organization of pigment and protein. However, it requires specialized equipment and measurements cannot be done in real time. In-flight real-time characterization by electrical mobility measurements can be used for quick determination of size distribution with sub-nanometer precision. Unlike ESI-MS,[11, 12] where electrospray is mainly used to generate ions, in this work electrospray is used to atomize the solution and scanning mobility particle sizer (SMPS) is used for size measurement of particles. This method of characterization requires minimal sample preparation and low volume. Moreover, size measurement by ES-SMPS is non-destructive, which allows it to be coupled to any other analytical technique such as AFM, mass spectrometry or electron microscopy. For example, TEM analysis can be done after ES-SMPS characterization by depositing size-selected material on a substrate.[13] ES-SMPS has been widely used to characterize various biological complexes such as proteins,[14, 15] oligonucleotides,[16] and viruses.[17] Dynamic light scattering (DLS) gives quick real-time measurement of the size of particles in solution. While DLS is good for measuring the size of monodisperse particles, it cannot effectively resolve closely spaced peaks of bimodal or multimodal distributions. On the other hand, ES-SMPS can measure broad multimodal distributions and generate quantitative information about number concentration of particles in solution. In this work, LHCs are characterized by an ES-SMPS system. To the best of our knowledge, photosynthetic antenna complexes have not previously been characterized by aerosol techniques, with the exception of chlorosomes.[6, 18]

In solar cells, using a combination of natural antenna complexes and an artificial reaction center is attractive because a suitable reaction center for separating electron and hole can be used. One such example[6] uses chlorosomes as antenna and dye as reaction center to fabricate TiO_2 based dye-sensitized solar devices. This device has shown 30 times higher incident photo

conversion efficiency than devices using a photo-electrode without chlorosomes. In order to fabricate such devices, a LHC must be immobilized on the surface. Various techniques have been developed to achieve this goal, such as layer by layer deposition,[19, 20] His-Tag affinity[2, 4, 21] and electrospray deposition.[6] Electrospray deposition is a particularly attractive method to construct bio-hybrid devices because it can be used on a variety of conducting and semi-conducting substrates, without any need to modify the substrate or the LHC. Electrospray deposition has been used to fabricate thin films of various materials such as proteins[22] and inorganic materials.[23] However, in the case of biological samples, electrospray can cause damage to the sprayed sample.[17] For devices to be functional, it is essential that the LHCs retain their light-harvesting abilities after being subjected to the high charge and impact involved in electrospray deposition. If the protein environment around the pigment is altered or denatured, the LHC will absorb and fluoresce differently.

The objective of this paper is to characterize and deposit natural LHCs with broad absorption such as chlorosomes, Fenna-Matthews-Olson (FMO) protein, phycobilisomes,[24] and LH2 using electrospray techniques. The sizes of LHCs in flight and in solution were characterized with ES-SMPS and Dynamic Light Scattering (DLS) respectively. The absorption and fluorescence spectra of the LHCs were measured after depositing them onto a slide to ensure that they retain their light-harvesting ability. This characterization is important for understanding the physical properties of various LHCs. This research is also an important step for enabling the development of robust bio-hybrid and bio-mimetic devices such as solar cells that absorb energy over a broad range of wavelengths.

3.3 Experimental methods and characterization

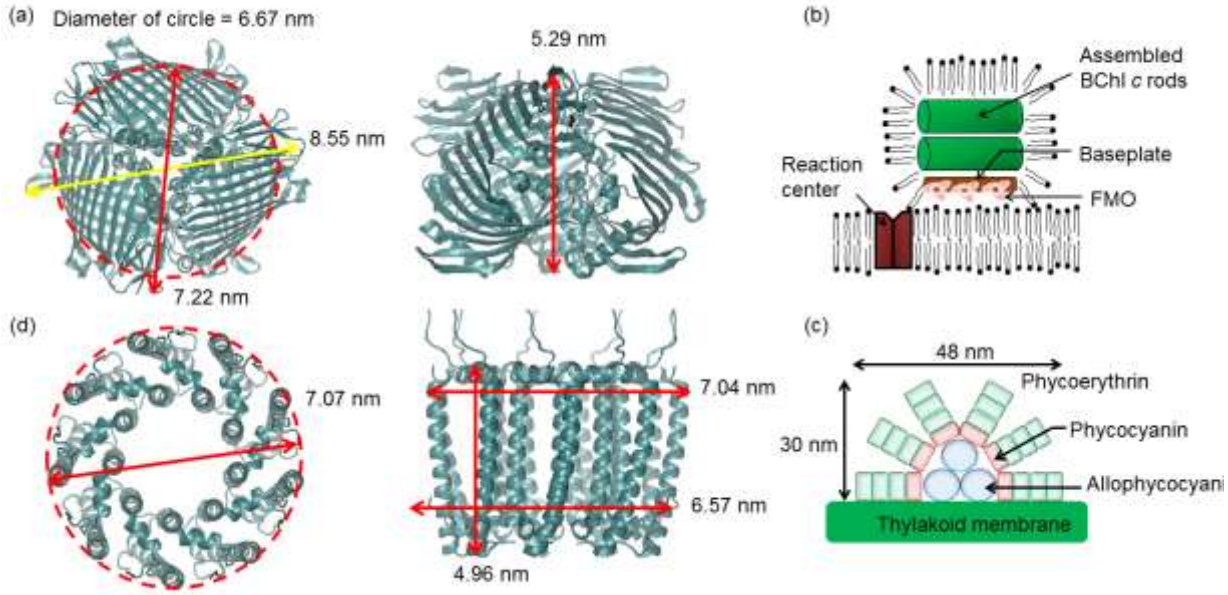

Figure 3–1: Illustration of various light-harvesting complexes characterized and deposited by electrospray (a) top view and front view of FMO (PDB: 3ENI), (b) a model of chlorosomes adapted from Tang et al. 2011,18 (c) model of phycobilisome adapted from MacColl, 1998,[24] and (d) top view and front view of LH2 (PDB: 1NKZ)

Various LHCs characterized in this work of different shapes and sizes are illustrated in Figure 3–1. Two different techniques, ES-SMPS and DLS were used to measure the size of LHCs. In order to ensure that size measured by SMPS is that of intact LHC, these LHCs were deposited onto fluorine doped tin oxide (FTO) slides using electrospray deposition. The UV-vis spectrum of the LHCs after deposition was compared to UV-vis absorption in solution. The fluorescence measurements were done to determine if the LHCs retained capacity to transfer energy after the process of electrospray deposition. The UV-vis and fluorescence measurements were done within 2 hours of LHC deposition.

3.3.1 Extraction and purification of light-harvesting complexes

Chlorosomes were extracted from the green sulfur bacterium *Chlorobaculum tepidum* (formerly *Chlorobium tepidum*) by a previously used method[25] with minor modifications. Cells

were resuspended in 20 mM Tris-HCl buffer (pH 8.0) and 2 M NaSCN, homogenized, and broken by a French press at 20,000 psi. Cell debris was pelleted via low-speed centrifugation. The resulting supernatant was fractionated by a 20%-50% (w/v) linear sucrose gradient in the same resuspension buffer centrifuged at 125,000 x g for 16 hours at 4°C. Chlorosomes were extracted from a layer comprising of approximately 35% sucrose. The sample was further purified via gel-filtration chromatography on a S-300 Sephacryl column using 20 mM Tris-HCl (pH 8.0) buffer for elution. Pure chlorosomes were buffer-exchanged using Amicon 100 MWCO spin filters into 20 mM ammonium acetate buffer for further study.

The FMO protein was purified from *Chlorobaculum tepidum* by a previously used method[26] with minor modifications. Cells were resuspended in 20 mM Tris-HCl buffer (pH 8.0), homogenized, and broken by sonication. A solution of 3.5 M Na_2CO_3 was added to the lysate until the CO_3^{2-} concentration reached 0.2 M. The lysate was stirred overnight at 4°C in the dark, then centrifuged at a low-speed to pellet debris. The supernatant was collected, the CO_3^{2-} concentration was increased to 0.4 M, and the lysate was stirred again overnight in the dark at 4°C. The lysate was then ultracentrifuged at 158,000 x g for 2 hours at 4°C to pellet additional debris. The supernatant was dialyzed against 100 times volume of 20 mM Tris-HCl buffer (pH 8.0) to remove residual CO_3^{2-}. The FMO protein was purified from this solution via a first round of ion-exchange chromatography (DEAE Sepharose Fast-Flow), a round of gel-filtration chromatography (G-200 Sephadex), and a final round of ion-exchange chromatography (Q-Sepharose). The protein was considered pure when the ratio of absorbance at 267 nm to absorbance at 371 nm was less than 0.6. Pure FMO protein was buffer-exchanged using Amicon 30 MWCO spin filters into 20 mM ammonium acetate buffer for further study.

LH2 was purified from the purple bacterium *Rhodobacter sphaeroides*, by a previously used method[27] with minor modifications. Anaerobically grown cells were broken by sonication and membranes were pelleted by ultracentrifugation. After resuspension of the membrane pellet in 20mM Tris-HCl (pH 8.0) with 1 mM EDTA (Buffer A), the membranes were solubilized by stirring in the dark at 4°C for 1 hour with 1% (w/v) LDAO. The extracted membranes were then applied to a step sucrose gradient (Buffer A with 0.1% (w/v) LDAO and 0.2-1.2 M sucrose in 0.2 M sucrose steps) for crude separation of the LH2 from the LH1 and LH1-RC. This was followed by loading the upper red band (0.4-0.6 M sucrose) onto a DEAE Sepharose Fast Flow anion exchange column. Following loading the sample onto the column, the buffer was exchanged to Buffer A with 0.1% (w/v) n-Dodecyl β-D-maltoside (DDM) after which the LH2 was eluted with a linear gradient from 0-400 mM NaCl. All fractions with a ratio of absorbance at 850 nm to the absorbance at 280 nm above 3.7 were pooled. Pure LH2 was buffer-exchanged using Amicon 50 MWCO spin filters into 20 mM ammonium acetate buffer with 0.01% DDM for further study.

Phycobilisomes were purified from the cyanobacterium *Synechocystis* PCC 6803 by previously used method[28] with some modifications due to the use of a different organism. The modifications are mainly related to the number of sucrose gradients and the concentrations used. Cells were resuspended and homogenized in 0.9 M phosphate buffer and broken by vortexing with sharp silicon carbide beads. The broken cells were centrifuged at low speed to pellet cells debris. The pellet was collected, resuspended in 0.9 M potassium phosphate buffer (pH 7.0) with 2% Triton X-100 detergent, and incubated for 1 hour at 4°C. The solution was centrifuged again at low speed to pellet debris. The supernatant was collected and ultracentrifuged at 310,000 x g for 2 hours to pellet the blue phycobilisomes. The pellet was resuspended in 0.9 M potassium phosphate and subjected to a step sucrose gradient (0.5 M, 0.6 M, and 0.75 M sucrose in 0.9 M

potassium phosphate), ultracentrifuged at 310,000 x g for 3 hours at 4°C. The blue phycobilisome band was collected and applied to another step sucrose gradient (1 M, 1.125 M, and 1.25 M sucrose in 0.9 M potassium phosphate) and centrifuged for 18 hours in the same centrifuge conditions as the first. The blue, pure phycobilisome band was collected and buffer-exchanged to 0.9 M potassium phosphate buffer using Amicon 100 MWCO spin filters for further study.

3.3.2 Dynamic light scattering (DLS)

The hydrodynamic diameters of the various LHC's were estimated with dynamic light scattering (ZetaSizer Nano ZS, Malvern Instruments Inc., UK). All measurements were made at 25°C with 173 degree back angle scattering. The DLS measures the diffusivity of the particle (D) and uses the Einstein equation: $d_H = kT/3\pi\eta D$, where k is the Boltzmann constant, T is the absolute temperature (K), and η is the viscosity of the solution to get d_H, the size of the particles. In case of non-spherical particles, the hydrodynamic diameter from DLS measurements is the diameter of a hypothetical solid sphere having the same diffusion coefficient as the observed particles. This is assuming that there is no particle solvent or particle-particle interaction.

3.3.3 General principles of ES-SMPS

Figure 3–2a shows the schematic of the ES–SMPS system. Electrospray produces monodisperse droplets over a wide size range.[29] The size of the droplets formed depends on the conductivity and flow-rate of the solution.[30, 31] One particle per droplet can be obtained by changing the aforementioned parameters or by diluting the spray solution. Upon spraying the LHC solution, the solvent evaporates, leaving behind highly charged particles of photosynthetic complexes. The charge on the particles is reduced to Fuch's charge distribution by subjecting it to bipolar ions from radioactive material Po^{210}. These particles are then passed through a DMA

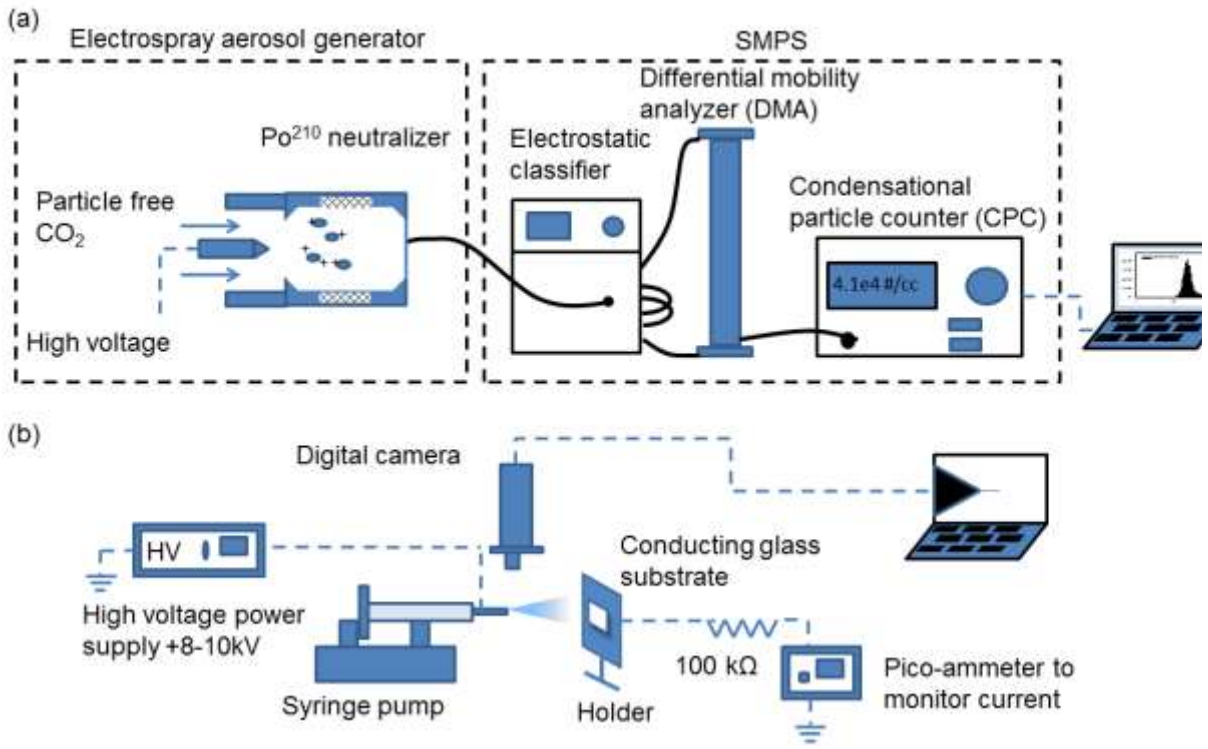

Figure 3–2: (a) Schematic for charge reduced size measurement of light-harvesting complexes by electrospray-SMPS system. (b) Schematic for deposition of the light-harvesting complex onto a conducing substrate by electrospray is shown

(Differential Mobility Analyzer) and subjected to a radial electric field at atmospheric pressure. The particles move under the electric field and only particles with specific mobility exit the DMA. The particles of a specific mobility are counted by a condensation particle counter (CPC). The electric field inside the DMA is varied by changing applied voltage to get a distribution of electrical mobility, which is converted to size of particles. It should be noted that the mobility-based measurements are independent of the density of particles, but depend only on size and shape. In the case of irregularly shaped particles, the size obtained is the size of sphere with the same mobility as that of the test particle. This method can also be used to measure the size of cylindrical particles by appropriate corrections.[32] It has been shown that ES-SMPS can be used for cylindrical particles with volume average diameter less than 100 nm by applying a shape correction factor to calculate mobility of such particles.[13]

3.3.4 Operating conditions for ES – SMPS

The Electrospray Aerosol Generator (EAG - model 3480, TSI inc., Shoreview, MN) produces monodisperse aerosols for size characterization when operated in a cone-jet mode. Radioactive Po^{210} (5 mC activity) was used to reduce the charge on particles before they were introduced into the electrostatic classifier. An Electrostatic Classifier (TSI inc., model 3080) along with a DMA was used for size classification followed by a CPC (TSI inc., model 3776) for particle counting. A Nano DMA (TSI inc., model 3085) was used to characterize FMO and LH2 with aerosol and sheath flow rates of 0.3 and 6 $Lmin^{-1}$ respectively. A Long DMA (TSI inc., model 3081) was used for chlorosomes and phycobilisomes, which are relatively large, with an aerosol flow rate of 1.5 $Lmin^{-1}$ and sheath flow rate of 15 $Lmin^{-1}$. A 40 µm diameter capillary was used for LH2 and FMO, while a 100 µm diameter capillary was used with chlorosomes and phycobilisomes to avoid the blocking of a capillary. Ammonium acetate was used to vary the conductivity of the sprayed solutions. The water from the sprayed droplets evaporates, leaving LHCs suspended in air, which are characterized by SMPS.

3.3.5 Electrospray deposition

A laboratory-made setup as shown in Figure 3–2b was used to deposit various LHCs onto a transparent conducting fluorine-doped tin oxide (FTO) substrate. In this instrument, a tapered needle, 125 µm inner diameter attached to a syringe, is used to spray the LHC solution. A syringe pump (Pump 22, Harvard Apparatus, South Natick, MA, USA) is used to create a 1 µL/min flow of solution. The substrate is placed at a distance of 12 mm from the needle and is grounded. High voltage (8-10kV) is applied between the needle and the substrate. A sheath flow of 2 $Lmin^{-1}$ particle free CO_2 is used to suppress corona formation around the needle tip. The cone jet is ascertained by monitoring the current by an ammeter (6485 Picoammeter, Keithley,

Cleveland, OH) and visually monitoring using a digital optical microscope (QX5, Digital Blue, Atlanta, GA, USA). 10% ethanol (Anhydrous, Sigma Aldrich, MO) was added to reduce the surface tension of the LHC spray solution. DLS and UV-vis measurements were performed to ensure there is no degradation or aggregation in the solution before each spray.

3.3.6 UV-Visible absorption spectrum

The UV-vis absorption spectra of LHCs in solution and after deposition on fluorine tin oxide (FTO) slide were measured using a UV-Visible spectrophotometer (Cary 100, Agilent Technologies, CA) in transmission mode. All measurements were done under ambient conditions.

3.3.7 Fluorescence

Fluorescence emission spectra were obtained in a manner similar to that used by Modesto-Lopez et al. 2010.[6] A custom fluorometer setup (Photon Technology International, NJ) consisting of a Xe excitation lamp, excitation monochromator, emission monochromator, signal chopper, lock-in amplifier, and avalanche photodiode detector was employed. FTO slides containing electrospray-deposited LHC's were mounted using a custom slide holder in the sample compartment at a 50-60° angle to the incident light to maximize absorption cross-section. Placing the slide at an angle greater than 45 degrees to incident light ensures that there is no incident light reflected into the detector. The detector was placed at an angle of 90° to the incident light. Band-pass and long-pass filters were used to eliminate second-order diffraction and scattering from the FTO slide. Chlorosome samples (consisting mostly of BChl *c*) were excited using 450 nm light, while the FMO and LH2 (consisting of BChl *a*) samples were excited using 371 nm light. Phycobilisome samples (containing phycocyanin) were excited using 590 nm light. The conditions for fluorescence measurements after deposition and in solution are

given in Table 3-1 and Table 3-2 respectively. Comparison of absolute fluorescence efficiency could not be accomplished due to the variability of slide orientation during measurement and differences in deposition areas across samples.

Table 3-1: Experimental conditions for fluorescence measurement after electrospray deposition of the LHC

LHC -	Other additives	UV-visible absorbance of solution using 2 mm path length cuvette	Deposition time min	Flowrate µL/min
FMO	20mM Ammonium Acetate	0.3 at 808 nm	15	1
Chlorosomes	20mM Ammonium Acetate	0.3 at 747 nm	40	1
Phycobilisome*	0.9M phosphate, 2mM EDTA	1.1 at 642nm	-	-
LH2	50mM Am Ac, DDM 0.01% v/v	0.4 at 848 nm	20	1

*10µL of Phycobilisome was drop coated on a slide

Table 3-2: Experimental conditions for fluorescence measurement of LHCs in solution

LHC	Other additives	UV-vis absorbance in 1cm path length cuvette
Chlorosomes	20 mM Tris-HCl (pH 8.0)	<0.1 at 808 nm
FMO	20 mM Tris-HCl (pH 8.0)	<0.1 at 747 nm
Phycobilisome	0.9M phosphate, 2mM EDTA	<0.1 at 642nm
LH2	20 mM Tris-HCl (pH 8.0) + 1 mM EDTA + 0.1% DDM	<0.1 at 848 nm

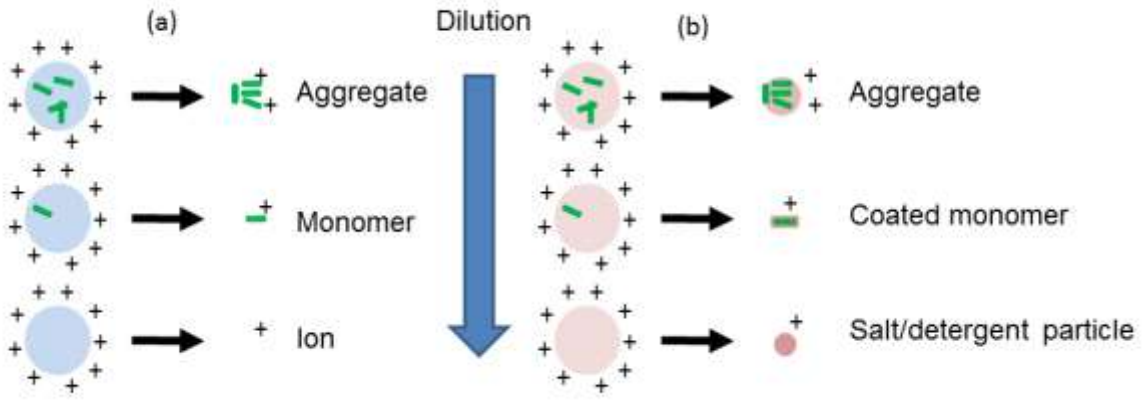

Figure 3–3: Effect of dilution on the formation of particles from droplets sprayed by electrospray. Possible scenarios on evaporation of solvent for droplet containing particles in (a) volatile solution, for example, ammonium acetate in water and (b) non-volatile solution such as buffer salt or detergent

3.4 Results and discussion

The size distributions of LHCs measured by ES-SMPS system are shown in Figure 3–4. All the sizes measured by ES-SMPS and DLS, along with the measurements in previous works for various LHCs are summarized in Table 3-3. Thin films of LHCs were deposited onto the conducting fluorine tin oxide (FTO) slide by electrospray deposition. The flow rate of the solution was different in both cases. Thus, the size of the droplet formed for deposition was different from droplet size in the characterization setup and LHCs deposited were agglomerates. Figure 3–5 shows the comparison between the absorption spectrum of the electrospray deposited LHCs and their absorption in solution. The fluorescence spectra of the deposited LHCs are shown in Figure 3–6. This was used to verify that LHCs are not damaged by electrospray.

3.4.1 Size measurement by ES-SMPS and DLS

Figure 3–3 depicts the various possible scenarios for formation of particles from the sprayed droplet. In the first scenario depicted in Figure 3–3a, the droplet contains solution with a

Table 3-3: List of various light-harvesting complexes characterized and deposited using electrospray - their source species, and size measurements from electrospray-SMPS and DLS

Light-harvesting complex	Source organism	Shape from literature	Dimensions from literature (nm)	Diameter from DLS (nm)	Size from Electrospray (nm)
FMO protein	*Chlorobaculum tepidum* (formerly *Chlorobium tepidum*)	Frustum of cone	(h×d) 5×8[33]	7.9±0.7	6.4
Chlorosomes	*Chlorobaculum tepidum* (formerly *Chlorobium tepidum*)	Ellipsoidal	(l×b×h) - 174×91.4×10.86[7]	77.9±4.1	23.3
LH2 complex	*Rhodobacter spheroids*	Cylindrical	(d×h) - 6×7[21]	11.3±1.1	9.5
Phycobillisome	*Synechocystis* 6803	Hemidiscoidal	(d×w×h) - 48×30×15[34, 35]	NA[a]	33.4

[a]Measurement was not possible since phycobilisome fluoresces at DLS laser wavelength (632.2 nm)

volatile solute such as ammonium acetate. The solution will evaporate completely, forming an aggregate of LHCs present inside the droplet. The spray solution can be diluted so that each droplet contains one or no LHC. The droplets that do not contain any LHCs will evaporate completely and no particles will be measured by the SMPS. The droplets containing one LHC will form a single highly charged complex after evaporation of solvent and SMPS will measure its size. Thus, the size of the LHCs can be measured by diluting the spray solution. Some LHCs, such as phycobilisomes and LH2, are stable only in presence of buffer salts or detergents. Figure 3–3b shows various possibilities for formation of particles due to presence of non-volatile solutes in droplets. Upon evaporation of the solvent, an aggregate containing LHCs and non-volatiles will be formed. Dilution of the spray solution will result in fewer LHCs per droplet. If there are no LHCs it will result in a particle containing only non-volatile solute. In case the droplet contains a single LHC, upon evaporation of solvent, it will form a single LHC coated with non-volatile solute such as salt or detergent. In order to measure the size, it is essential that the size of the particle formed from non-volatile solute be smaller than the size of coated LHC.

To measure the size of the particles it is essential to spray one particle per droplet, in this work one LHC per droplet, by adjusting concentration of LHC in solution. Figure 3–4a shows the size distribution of the FMO protein after spraying in air. The main peaks observed on spraying FMO solution correspond to 6.4 nm and 8.2 nm. First, the concentrated solution was sprayed, and then the solution was diluted to obtain one particle per droplet (see Figure 3–3). The peak at 6.4 nm was consistently obtained, even on diluting the spray solution. The 6.4 nm peak can correspond to the size of the FMO protein in air or other stray protein. Since, no contamination or other proteins have been reported from mass spectrometry for the same preparation method of FMO,[36] the 6.4 nm peak almost certainly corresponds to the FMO protein.

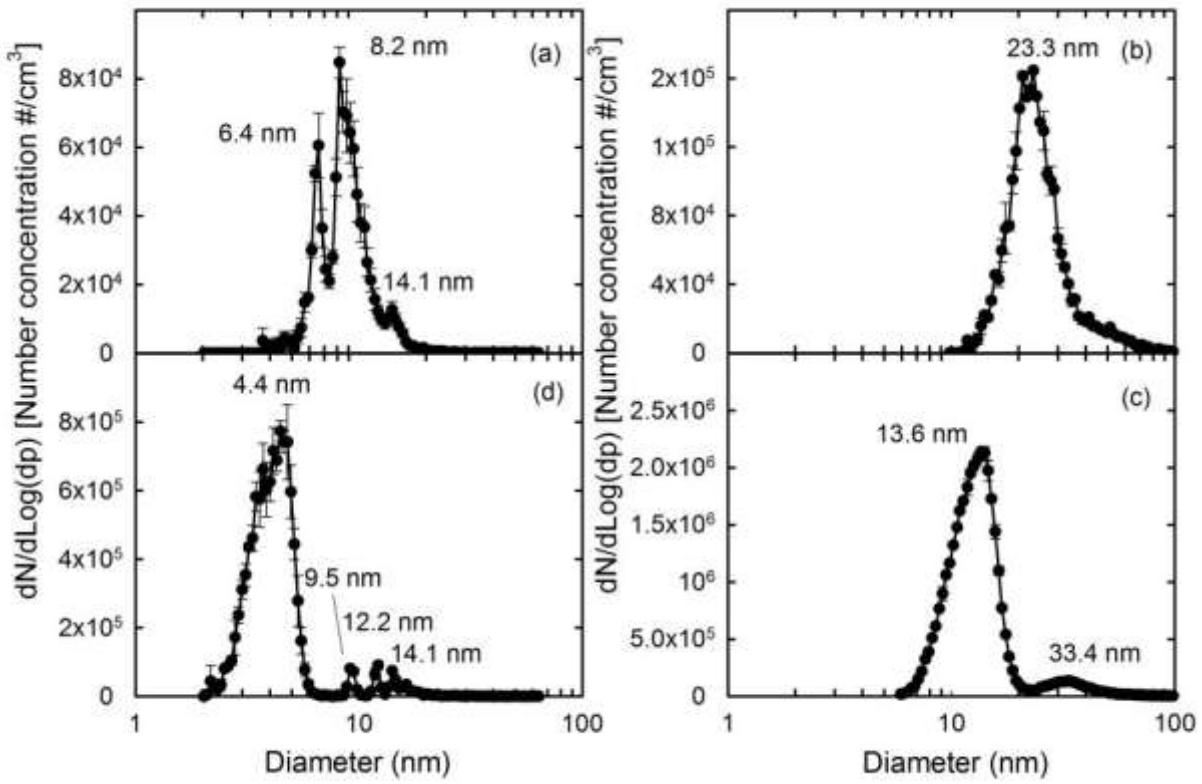

Figure 3–4: In flight size distribution measurement from electrospray-SMPS system for (a) FMO, (b) chlorosomes, (c) phycobilisome, and (d) LH2

Figure 3–1a shows the orthographic projections of the FMO protein. Although the crystal structure suggests that longest dimension of FMO protein is 8.55 nm, in top view, barring small chains, the whole of FMO fits into a circle of diameter 6.67 nm as shown in Figure 3–1a. In side view the height of FMO is 5.29 nm. Since FMO is not spherical in shape the volume average diameter along with shape correction factor needs to be considered.[13] To calculate the volume based particle size, this particle can be approximated as an ellipsoid with 6.67 nm as two major axes or a cylinder with 6.67 nm as base diameter to calculate the volume average diameter. The volume average diameter is 6.17 nm for an ellipsoid and 7.06 nm for a cylinder. Since the aspect ratio is close to 1, the shape correction factor can be ignored. The size measured corresponds well with the predicted diameter of FMO protein considering it to be an ellipsoid. The other

peaks larger than 6.4 nm correspond to aggregates of FMO, mainly because more than one FMO can also be present in the droplet. The size measured by the DLS gives a hydrodynamic diameter of 7.9±0.7 nm. The hydrodynamic size is within the limits of extreme dimensions because the size measured by DLS is the equivalent diameter of a sphere with the same viscosity. FMO protein is soluble in water and would contain water molecules on hydration. However, on spraying FMO will lose most of the water molecules. Thus, the hydrodynamic size is bigger because of hydration and this further supports the argument that aerosol measurement of 6.4 nm corresponds to single FMO particles.

The size distribution for chlorosomes has a peak at 23 nm as shown in Figure 3–4b. The size measured by AFM in previous work corresponds to 10x90x180 nm, and they are ellipsoidal in shape.[7] The droplet size generated by electrospray was 189 nm which is greater than the largest dimension of chlorosomes. The volume equivalent diameter for chlorosomes calculated from measurements by Montano, et. al. (2003)[7] is 54.5 nm, which is bigger than the peak size measured by SMPS. This implies that the chlorosomes orient inside the DMA. Particles with high aspect ratio orient inside the DMA to reduce the drag and only their projected area diameter is measured.[37] The DLS gives the hydrodynamic size of 77.9±4.1 nm. Similar results, where DLS size is larger compared to that measured by electrospray have been observed in previous works for chlorosomes.[18]

Typically, phycobillisomes are stored in a 0.8-1.0 M phosphate concentration to maintain structural stability outside of the cell. High phosphate concentration results in a solution with high conductivity (~80 mS/cm), and is beyond the operating range that results in a stable cone jet on the electrospray aerosol generator. The solution was immediately sprayed after reducing conductivity by diluting the solution four fold. A peak was obtained at 33 nm with standard

deviation of 8.5 nm as shown Figure 3–4c, which corresponds well to the literature value of the height of the phycobillisome.[34] The distribution is broad because phycobilisomes are non-spherical in shape and various orientations of phycobilisomes are possible. Different orientations will result in different resultant drag forces and hence different sizes will be obtained. On further dilution, the peak moved to 53 nm (not shown). This is probably due to agglomeration of two phycobillisomes, forming a sphere due to reduced phosphate concentration. This experiment was not reproducible due to agglomeration on diluting the solution. The non-volatile salts present in droplets that do not contain phycobillisomes are also measured as 13.6 nm salt particles. The estimated size using droplet diameter obtained from scaling laws is 17.4 nm for solution containing salts. This corresponds well with the measured size. DLS measurements could not be performed because the instrument uses a red laser (632.2 nm) which is the wavelength at which phycobilisome fluoresces.

LH2 is a membrane-bound protein and is stored in detergent solution to prevent agglomeration. 0.01% v/v Dodecyl-β Maltoside (DDM) solution was used to keep LH2 from agglomerating. The sizes of particles measured by SMPS on spraying LH2 solution are 4.4 nm, 9.5 nm, 12.2nm and 14.1 nm as shown in Figure 3–4d. The concentrated solution is sprayed initially, but high concentration of detergent and LH2 results in formation of particles that are significantly larger than the known size of LH2. The solution was diluted while maintaining the concentration of DDM above its critical micelle concentration to give one particle per droplet. However, even after obtaining one particle per droplet, the LH2 particles were still covered with detergent. Upon dilution, a significant number of electrosprayed droplets do not contain LH2 but just contain the detergent, which results in particles of size 4.4 nm as shown in Figure 3–4d. On further dilution, the size of detergent particles was reduced because each droplet will contain less

Table 3-4: Properties of solutions containing LHCs used for size distribution measurement and corresponding droplet size estimated, and size of particle measured by ES-SMPS

LHC	Concentration of other additives	Absorbance of spray solution using 2mm pathlength	Volume fraction of non-volatiles	Conductivity	Diameter of Capillary used	Flowrate	Size of droplet	Size of particle without LHC
	-		v/v	mS/cm	µm	nL/min	nm	nm
FMO	80mM Am Ac	0.35 at 808 nm	0	6.60	40	215	122	0.00
Chlorosomes	20mM Am Ac	1.85 at 747 nm	0	1.65	100	199	189	0.00
Phycobilisome	0.9M phosphate, 2mM EDTA	0.29 at 642 nm	0.010	21.35	100	199	81	17.4
LH2	50mM Am Ac, DDM 0.01% v/v	0.47 at 848 nm	0.0001	4.12	40	98	110	5.1

[a]Droplet size is calculated using scaling laws for electrospray[29]

detergent (not shown in figure). This confirms that the 4.4 nm particles are neither due to LH2 nor due to protein fragments. Since the volume concentration of DDM in solution is known, the size of particles without LH2 can be estimated knowing the droplet size. As shown in Table 3-4, this size is estimated to be 5.1 nm, which is close to measured value of 4.4 nm.

The size of LH2 measured by ES-SMPS is 9.5 nm. This size is bigger than crystallographic measurements of LH2 from similar species. The crystallographic measurement gives the height as 5 nm and diameter of 6.5 nm as shown in Figure 3–1c (PDB: 1NKZ). The size observed was bigger due to a monolayer of detergent LDAO which is ~2 nm thick[38] surrounding LH2. Only the hydrophobic sides of the cylinder will be coated with the detergent. Thus, the size of the LH2 particle in air would be 5 nm in height and 10.5 nm in diameter. The volume equivalent diameter of this cylinder is 9.4 nm. After applying shape correction for cylinders with aspect ratio of 2, the size of LH2 is estimated to be 10.2 nm. The size measured by ES-SMPS is close to the calculated value, considering the fact that it is not a perfect cylinder. The particles of size 12.2 and 14.1 nm, larger than 9.5 nm, are interpreted to be agglomerates containing multiple LH2s. Assuming that two LH2s are stacked on top of each other, a height of 10 nm and diameter of 10.5 nm is obtained, which includes the detergent layer. The volume equivalent diameter of this structure is 11.8 nm. Similarly, other larger sizes observed are agglomerates of multiple LH2. The diameter measured by DLS for LH2 is 11.3±1.1 nm. Larger diameter is measured in solution due to surfactant around LH2 and hydration. These factors will reduce the diffusion coefficient of LH2 thus increasing the measured size.

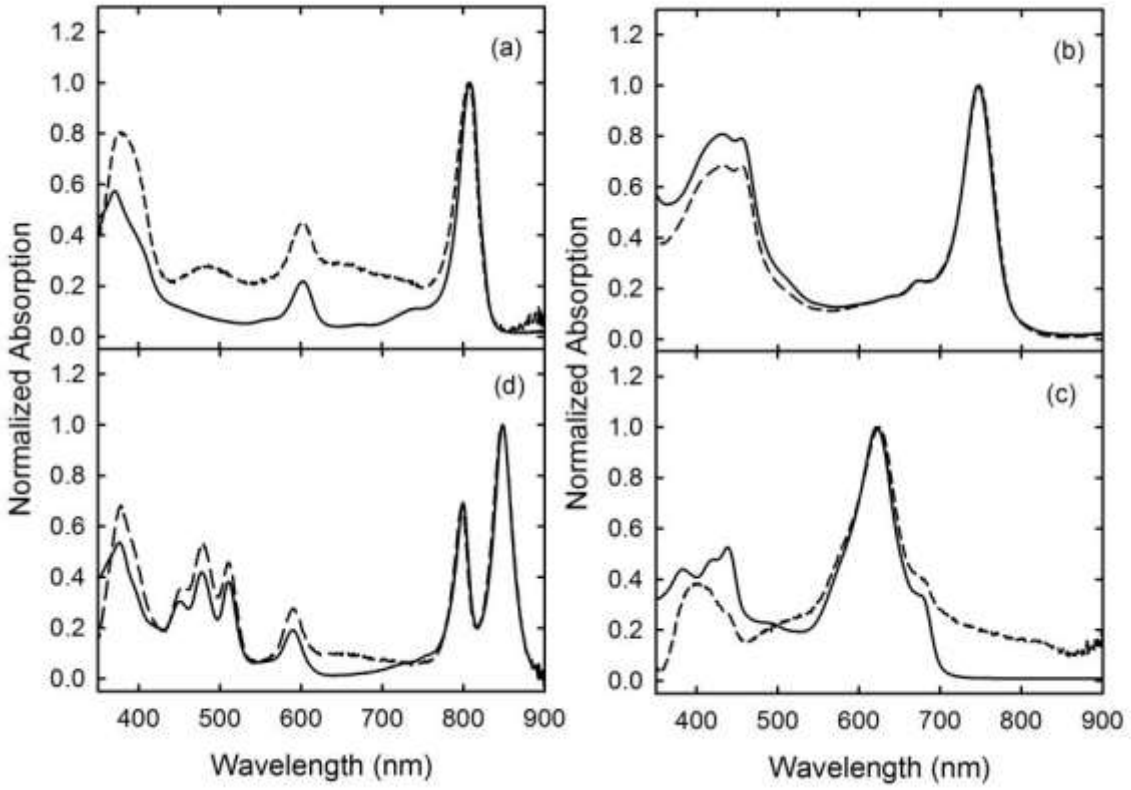

Figure 3–5: Normalized UV-visible absorption spectrum in solution (—) and on FTO slide after deposition by electrospray (--) for (a) FMO, (b) chlorosomes, (c) phycobilisome, and (d) LH2

3.4.2 UV-visible absorption and fluorescence spectra measurements

The UV-visible absorption spectra of the various LHCs are shown in Figure 3–5. The FMO protein has a characteristic absorption peak in solution at 371 nm, 602nm, and 808 nm. The FMO protein absorption spectrum was unaffected by raising the ethanol level to 10% (v/v). The deposited FMO shows the same absorption peaks as the solution sample, indicating the complex is not damaged.[39] Fluorescence emission also shows the characteristic emission peak centered at 823 nm as shown in Figure 3–6a. The fluorescence emission in solution and after deposition are identical, because the dye molecules are present inside the protein shell.

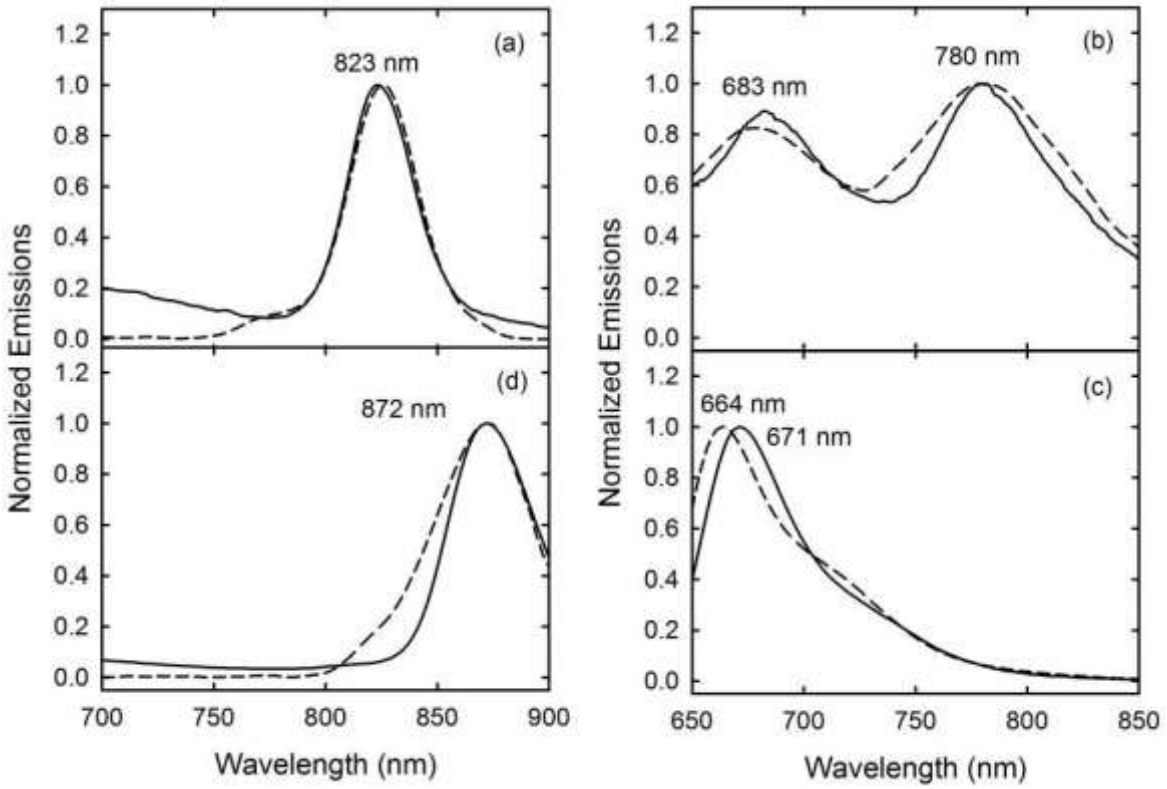

Figure 3–6: Normalized fluorescence spectra in solution (- -) and after deposition (—) by electrospray onto FTO slide (except phycobilisome which were drop coated) for (a) FMO, (b) chlorosomes, (c) phycobilisome, and (d) LH2

Chlorosomes from green sulfur bacteria have characteristic absorption peaks at 450 nm (primarily BChl *c*), 750nm (self-assembled BChl *c*).and 670nm (due to monomeric BChl *c*) as shown in Figure 3–5b. After deposition, the chlorosomes have the same characteristic peaks for absorption. Most importantly, the 670 nm peak does not appreciably rise in absorbance post-deposition, indicating that the self-assembled pigment structure inside the chlorosome is not damaged during deposition. This is mainly because the BChl *c* molecules are encapsulated in a lipid monolayer, thus isolating them from the environment. The mismatch in the spectrum at shorter wavelengths is mainly due to variation in absorption spectrum of different FTO slides. The fluorescence emission spectrum of the sample contains the characteristic 683 nm emission from monomeric BChl *c* and the 780 nm emission from assembled BChl *c* as shown in Figure 3–

6b. The monomers are more efficient at fluorescing compared to the assembled BChl *c* present in chlorosomes. Therefore, although very few monomers are present the fluorescence peaks are of similar intensity. There is narrowing of fluorescence peaks after deposition, because the proteins no longer interact with the solvent environment. The 810 nm emission from the BChl *a*-containing CsmA protein in the chlorosome is not readily visible due to redox-dependent quenching in oxygen-rich (atmospheric) conditions.[40]

The phycobilisomes require high phosphate concentration to be stable in solution. High salt concentration makes the solution highly conducting, which is beyond the envelope of conductivity for which the electrospray can be operated for deposition.[31] Although an attempt to characterize them was made by reducing conductivity on dilution, the deposition setup, which is different than characterization setup, could not be used even at that conductivity. Hence, the phycobilisomes were drop coated onto the slide. The drop-coated slide was left open to air for solvent to evaporate. On evaporation of solvent, it formed a thick sticky gel on the slide. Although the absorption spectrum of the slide has a 2 nm shift, the peak fluorescence showed a 7 nm red shift compared to the solution fluorescence as shown in Figure 3–6c. The change is absorption and fluorescence is attributed to close packing and ordering of phycobilisomes after loss of water as observed previously for rods of phycocyanin.

The LH2 sample contains a detergent to maintain the hydrophobic protein structure, thus resulting in a viscous solution. The viscous solution results in trapping of bubbles, which disrupts the electrospray cone jet. In order to reduce the viscosity and surface tension for electrospray deposition, ethanol was added to make a 10% (v/v) solution. The absorption spectra of LH2 in solution containing ethanol changed; the ratio of the peak absorption at 800nm is reduced compared to 850 nm (not shown). However, after deposition on the substrate and evaporation of

the solvent, the absorption spectrum is identical to the initial spectrum of the solution sprayed. This means that the deformation of the protein on addition of ethanol is reversible. The distortion in lower wavelengths is due to differences in absorption of the FTO glass slide. In a solution sample of LH2, the 800 nm-absorbing pigments transfer energy extremely efficiently to the 850 nm-absorbing pigments, resulting in measurable emission only from the latter pigments centered at 875 nm. As shown in Figure 3–6d, electrospray-deposited LH2 samples show an identical emission spectrum to solution samples, indicating a functioning protein complex outside of a lipid system.

3.5 Conclusions

ES-SMPS can be used to effectively and rapidly characterize LHCs. The size after aerosolizing the LHCs matches well with the hydrodynamic size measured by DLS in solution and literature reported values. However, solutions with high conductivity cannot be easily characterized or deposited by electrospray. Electrospray can be used for deposition of LHC which can be of different size, shape and protein structure without modifying the LHC or substrate. After depositing the LHCs on a FTO slide by electrospray, their absorption and fluorescence emissions are not altered, indicating that they are still capable of efficient energy capture and transfer. However, phycobilisomes, which were drop coated, showed a shift in the fluorescence emissions peak due to ordering. Electrospray deposition is a promising single-step technique for depositing LHCs for bio-hybrid solar cells. However, more work needs to be done to understand how LHCs orient after deposition. We theorize that electrospray methods can be used to deposit multiple layers of the substrate and LHC, which should transfer energy according to the FRET model.

3.6 Acknowledgements

This work was supported by a grant from the Department of Energy (DOE) project (#DOESC0001035) - Photosynthetic Antenna Research Center (PARC). The authors thank Mr. Xianglu Li for his help in purifying phycobilisomes from *Synechocystis* PCC 6803. Support from National Science Foundation - National Nanotechnology Infrastructure Network for the DLS instrument is gratefully acknowledged.

3.7 References

1. Giardi, M. T.; Koblizek, M.; Masojidek, J. Photosystem II Based Biosensors for the Detection of Pollutants. *Biosensors & Bioelectronics* **2001**, *16*, 1027-1033.

2. Badura, A.; Esper, B.; Ataka, K.; Grunwald, C.; Woll, C.; Kuhlmann, J.; Heberle, J.; Rogner, M. Light-Driven Water Splitting for (Bio-)Hydrogen Production: Photosystem 2 as the Central Part of a Bioelectrochemical Device. *Photochem Photobiol* **2006**, *82*, 1385-1390.

3. Allam, N. K.; Yen, C. W.; Near, R. D.; El-Sayed, M. A. Bacteriorhodopsin/TiO(2) Nanotube Arrays Hybrid System for Enhanced Photoelectrochemical Water Splitting. *Energy Env. Sci.* **2011**, *4*, 2909-2914.

4. Frolov, L.; Wilner, O.; Carmeli, C.; Carmeli, I. Fabrication of Oriented Multilayers of Photosystem I Proteins on Solid Surfaces by Auto-Metallization. *Adv. Mater.* **2008**, *20*, 263-266.

5. Bora, D. K.; Rozhkova, E. A.; Schrantz, K.; Wyss, P. P.; Braun, A.; Graule, T.; Constable, E. C. Functionalization of Nanostructured Hematite Thin-Film Electrodes with the Light-Harvesting Membrane Protein C-Phycocyanin Yields an Enhanced Photocurrent. *Adv. Funct. Mater.* **2012**, *22*, 490-502.

6. Modesto-Lopez, L. B.; Thimsen, E. J.; Collins, A. M.; Blankenship, R. E.; Biswas, P. Electrospray-Assisted Characterization and Deposition of Chlorosomes to Fabricate a Biomimetic Light-Harvesting Device. *Energy Env. Sci.* **2010**, *3*, 216-222.

7. Montano, G. A.; Bowen, B. P.; LaBelle, J. T.; Woodbury, N. W.; Pizziconi, V. B.; Blankenship, R. E. Characterization of Chlorobium Tepidum Chlorosomes: A Calculation of Bacteriochlorophyll *c* Per Chlorosome and Oligomer Modeling. *Biophys. J.* **2003**, *85*, 2560-2565.

8. Scheuring, S.; Reiss-Husson, F.; Engel, A.; Rigaud, J. L.; Ranck, J. L. High-Resolution AFM Topographs of Rubrivivax Gelatinosus Light-Harvesting Complex LH2. *EMBO J.* **2001**, *20*, 3029-3035.

9. Tang, K. H.; Urban, V. S.; Wen, J. Z.; Xin, Y. Y.; Blankenship, R. E. Sans Investigation of the Photosynthetic Machinery of Chloroflexus Aurantiacus. *Biophys. J.* **2010**, *99*, 2398-2407.

10. Fenna, R. E.; Matthews, B. W. Chlorophyll Arrangement in a Bacteriochlorophyll Protein from Chlorobium-Limicola. *Nature* **1975**, *258*, 573-577.

11. Schaumloffel, D.; Tholey, A. Recent Directions of Electrospray Mass Spectrometry for Elemental Speciation Analysis. *Anal. Bioanal. Chem.* **2011**, *400*, 1645-1652.

12. Stark, A.; Meyer, C.; Kraehling, T.; Jestel, G.; Marggraf, U.; Schilling, M.; Janasek, D.; Franzke, J. Electronic Coupling and Scaling Effects During Dielectric Barrier Electrospray Ionization. *Anal. Bioanal. Chem.* **2011**, *400*, 561-569.

13. Song, D. K.; Lenggoro, I. W.; Hayashi, Y.; Okuyama, K.; Kim, S. S. Changes in the Shape and Mobility of Colloidal Gold Nanorods with Electrospray and Differential Mobility Analyzer Methods. *Langmuir* **2005**, *21*, 10375-10382.

14. Kaufman, S. L.; Skogen, J. W.; Dorman, F. D.; Zarrin, F.; Lewis, K. C. Macromolecule Analysis Based on Electrophoretic Mobility in Air: Globular Proteins. *Anal. Chem.* **1996**, *68*, 1895-1904.

15. Hogan, C. J.; Biswas, P. Narrow Size Distribution Nanoparticle Production by Electrospray Processing of Ferritin. *J Aerosol Sci* **2008**, *39*, 432-440.

16. Mouradian, S.; Skogen, J. W.; Dorman, F. D.; Zarrin, F.; Kaufman, S. L.; Smith, L. M. DNA Analysis Using an Electrospray Scanning Mobility Particle Sizer. *Anal. Chem.* **1997**, *69*, 919-925.

17. Hogan, C. J.; Kettleson, E. M.; Ramaswami, B.; Chen, D. R.; Biswas, P. Charge Reduced Electrospray Size Spectrometry of Mega- and Gigadalton Complexes: Whole Viruses and Virus Fragments. *Anal. Chem.* **2006**, *78*, 844-852.

18. Tang, K. H.; Zhu, L. Y.; Urban, V. S.; Collins, A. M.; Biswas, P.; Blankenship, R. E. Temperature and Ionic Strength Effects on the Chlorosome Light-Harvesting Antenna Complex. *Langmuir* **2011**, *27*, 4816-4828.

19. Saga, Y.; Kim, T. Y.; Hisai, T.; Tamiaki, H. Assembly of Extramembranous Light-Harvesting Complexes of Green Sulfur Photosynthetic Bacterium Chlorobium Tepidum on Glass Surface by Electrostatic Layer-by-Layer Adsorption. *Thin Solid Films* **2006**, *500*, 278-282.

20. Hnilova, M.; Karaca, B. T.; Park, J.; Jia, C.; Wilson, B. R.; Sarikaya, M.; Tamerler, C. Fabrication of Hierarchical Hybrid Structures Using Bio-Enabled Layer-by-Layer Self-Assembly. *Biotechnol. Bioeng.* **2012**, *109*, 1120-30.

21. Escalante, M.; Maury, P.; Bruinink, C. M.; van der Werf, K.; Olsen, J. D.; Timney, J. A.; Huskens, J.; Hunter, C. N.; Subramaniam, V.; Otto, C. Directed Assembly of Functional Light-Harvesting Antenna Complexes onto Chemically Patterned Surfaces. *Nanotechnol* **2008**, *19*.

22. Morozov, V. N.; Morozova, T. Y. Electrospray Deposition as a Method to Fabricate Functionally Active Protein Films. *Anal. Chem.* **1999**, *71*, 1415-1420.

23. Lopez, L. B. M.; Pasteris, J. D.; Biswas, P. Sensitivity of Micro-Raman Spectrum to Crystallite Size of Electrospray-Deposited and Post-Annealed Films of Iron-Oxide Nanoparticle Suspensions. *Appl. Spectrosc.* **2009**, *63*, 627-635.

24. MacColl, R. Cyanobacterial Phycobilisomes. *J Struct Biol* **1998**, *124*, 311-334.

25. Gerola, P. D.; Olson, J. M. A New Bacteriochlorophyll Alpha-Protein Complex Associated with Chlorosomes of Green Sulfur Bacteria. *Biochim. Biophys. Acta* **1986**, *848*, 69-76.

26. Li, Y. F.; Zhou, W. L.; Blankenship, R. E.; Allen, J. P. Crystal Structure of the Bacteriochlorophyll *a* Protein from Chlorobium Tepidum. *J. Mol. Biol.* **1997**, *271*, 456-471.

27. Gall, A.; Fowler, G. J. S.; Hunter, C. N.; Robert, B. Influence of the Protein Binding Site on the Absorption Properties of the Monomeric Bacteriochlorophyll in Rhodobacter Sphaeroides LH2 Complex. *Biochem* **1997**, *36*, 16282-16287.

28. David, L.; Marx, A.; Adir, N. High-Resolution Crystal Structures of Trimeric and Rod Phycocyanin. *J. Mol. Biol.* **2011**, *405*, 201-213.

29. Chen, D. R.; Pui, D. Y. H.; Kaufman, S. L. Electrospraying of Conducting Liquids for Monodisperse Aerosol Generation in the 4 nm to 1.8 μm Range. *J. Aerosol Sci.* **1995**, *26*, 963-978.

30. Basak, S.; Chen, D. R.; Biswas, P. Electrospray of Ionic Precursor Solutions to Synthesize Iron Oxide Nanoparticles: Modified Scaling Law. *Chem. Eng. Sci.* **2007**, *62*, 1263-1268.

31. Chen, D.-R.; Pui, D. Y. H. Experimental Investigation of Scaling Laws for Electrospraying: Dielectric Constant Effect. *Aerosol Sci. Technol.* **1997**, *27*, 367-380.

32. Kim, S. H.; Mulholland, G. W.; Zachariah, M. R. Understanding Ion-Mobility and Transport Properties of Aerosol Nanowires. *J Aerosol Sci* **2007**, *38*, 823-842.

33. Tronrud, D.; Wen, J.; Gay, L.; Blankenship, R. The Structural Basis for the Difference in Absorbance Spectra for the FMO Antenna Protein from Various Green Sulfur Bacteria. *Photosynth. Res.* **2009**, *100*, 79-87.

34. Olive, J.; Ajlani, G.; Astier, C.; Recouvreur, M.; Vernotte, C. Ultrastructure and Light Adaptation of Phycobilisome Mutants of Synechocystis PCC 6803. *Biochim Biophys Acta - Bioenerg* **1997**, *1319*, 275-282.

35. Arteni, A. A.; Liu, L. N.; Aartsma, T. J.; Zhang, Y. Z.; Zhou, B. C.; Boekema, E. J. Structure and Organization of Phycobilisomes on Membranes of the Red Alga Porphyridium Cruentum. *Photosynth. Res.* **2008**, *95*, 169-174.

36. Wen, J.; Zhang, H.; Gross, M. L.; Blankenship, R. E. Native Electrospray Mass Spectrometry Reveals the Nature and Stoichiometry of Pigments in the FMO Photosynthetic Antenna Protein. *Biochem* **2011**, *50*, 3502-3511.

37. Allmaier, G.; Laschober, C.; Szymanski, W. W. Nano Es Gemma and Pdma, New Tools for the Analysis of Nanobioparticles - Protein Complexes, Lipoparticles, and Viruses. *J. Am. Soc. Mass. Spectrom.* **2008**, *19*, 1062-1068.

38. Rojas, O. J.; Stubenrauch, C.; Schulze-Schlarmann, J.; Claesson, P. M. Interactions between Nonpolar Surfaces Coated with the Nonionic Surfactant n-Dodecyl-β-D-Maltoside. *Langmuir* **2005**, *21*, 11836-11843.

39. Lakowicz, J. R.; Weber, G. Quenching of Fluorescence by Oxygen - Probe for Structural Fluctuations in Macromolecules. *Biochem* **1973**, *12*, 4161-4170.

40. vanNoort, P. I.; Zhu, Y. W.; LoBrutto, R.; Blankenship, R. E. Redox Effects on the Excited-State Lifetime in Chlorosomes and Bacteriochlorophyll *c* Oligomers. *Biophys. J.* **1997**, *72*, 316-325.

Chapter 4 Linker-Free Deposition and Adhesion of Photosystem I onto Nanostructured TiO_2 for Biohybrid Photo-electrochemical Cells

To be submitted to Langmuir, September, 2014

4.1 Abstract

Photosystem I (PSI) is an attractive sensitizer for nano-biohybrid solar cells as it has a combined light harvesting and reaction center in one protein complex; and operates at quantum yield close to one in biological systems. Using a linker-free deposition technique enabled by an electrospray system, PSI was coupled to 1D nano-structured titanium dioxide thin films to fabricate an electrode for a photo-electrochemical cell. Post deposition, the surfactant in the PSI agglomerate dissolved in the surfactant-free electrolyte; ensuring that partly hydrophobic PSI is not resuspended and stayed in contact with titanium dioxide. A maximum current density of 4.15 mA cm^{-2} was measured after 10 minutes of electrospray deposition, and this is the highest current density reported so far for PSI based photoelectrochemical cells. The high current is attributed to 1D nano-structure of titanium dioxide and orientation of the PSI onto the surface, which allows easy transfer of electrons.

Keywords

Hybrid Materials, Nanostructures, Solar Cells, photosystem I, linker-free deposition

4.2 Introduction

There is a need for renewable sources of energy to avoid increasing the carbon dioxide emissions due to enhanced use of fossil fuels to meet an ever-increasing energy demand. Solar energy can be used to generate electricity or to split water into oxygen and hydrogen which can be used as a clean fuel. In nature, sunlight is converted to chemical energy *via* photosynthesis to drive various cellular processes. Out of the wide range of protein complexes that participate in photosynthesis, Photosystem I (PSI) is a remarkable nano-photoelectric machine that operates with a quantum yield close to 1 (for $\lambda<680$ nm).[1] PSI catalyzes the plastocyanin:ferredoxin redox reaction in the presence of light and has been studied as a model system for highly efficient photochemical conversion process.[2] Cyanobacterial PSI has been resolved by X-ray crystallography at a high precision of 2.5 Å and consists of 12 protein subunits and 127 cofactors (96 Chlolorphyll *a*, 22 carotenoids, 2 phylloquinones, 3 Fe_4S_4 clusters, and 4 lipids).[3] This combination of cofactors held together by a protein scaffold makes PSI efficient at utilizing light to generate and separate the electron-hole pairs. These features make PSI attractive in improving efficiency of artificial systems for harvesting solar energy.

PSI's applicability for harvesting solar energy in artificial systems has been demonstrated in various configurations such as a photovoltaic cell,[4] artificial photosynthesis with a three electrode photoelectrochemical cell[5-12] or by in situ deposition of catalyst for hydrogen production.[13, 14] Most commonly, PSI has been deposited on gold-coated substrates by attaching it with a linker molecule to demonstrate an enhancement in the photocurrent.[5-7, 10] A linker however introduces resistance to the electron transfer, and PSI when coupled to gold degrades the performance due to formation of a Schottky barrier between gold and the semiconductor.[5] In order to avoid linkers, vacuum evaporation was used to deposit films of PSI,[8, 9] and by matching

band energies high photocurrents were obtained.[9] Using this technique, multiple layers were deposited, increasing the absorption of light. Although multiple layers of PSI are beneficial for light absorption compared to a single layer,[8] the limitations to the diffusion of an electrolyte outweights the benefits of light absorption. Instead of thick layers, a nanostructured substrate can be used to increase surface area and improve the light absorption as demonstrated by Mershin et. al.[4] However, evaporation based techniques used by earlier researchers for flat surfaces[4] may result in uneven deposition over nano-structures. Overall, there is a need for a linker-free deposition technique for nano-structured substrates, which would improve PSI's access to the electrolyte and enhance electron transfer for increased photocurrent density.

The electron separated by PSI needs to be transferred to a semiconductor for effective utilization. Titanium dioxide (TiO_2) is a stable semiconducting metal oxide which can be used as a photoanode. One dimensional (1D), single crystal titanium dioxide nanostrucutres have been demonstrated to perform well as a photoelectrode due to lower resistance to electron transfer.[15, 16] Moreover, 1D nanostructures are easier to coat with sensitizers by spraying. Using an aerosol technique, PSI agglomerates can be sprayed and deposited in a controlled manner. Electrospray atomization generates charged droplets that can be deposited in an electric field onto conducting or semi-conducting substrates. Moreover, aerosol techniques such as electrospray deposition are beneficial over solution-based techniques because they facilitate linker-free deposition[17-20] onto a nano-structured substrate. Although linker-free deposition of quantum dots via electrospray has been demonstrated,[17] for biological complexes, adhesion onto the substrate and retention of absorption needs to be demonstrated. Chlorosome antenna complexes[19] and their synthetic mimics[21] have been deposited using electrospray. Previous works have also shown that the biological light harvesting antennas retain their absorption and fluorescence.[18, 19] Chlorosomes

that were electrosprayed onto nanostructured titanium dioxide enhanced performance of solar cells,[19] but they lack a reaction center and thus acts only as a light harvesting complex. PSI, being an integrated light harvesting and photochemical conversion system, has the additional benefit of efficient splitting of electron and hole and is expected to be more efficient.[22]

The overall objective of this work is to demonstrate a linker-free attachment of PSI onto a nano-structured semiconducting surface and test its performance in a photoelectrochemical cell. In this work, electrospray deposition is used to provide two fold benefits - ability to spray onto a nano-structured surface and to deposit without a linker. First, PSI is characterized by using electrospray and DLS to confirm its size characteristics. Second, it is shown that PSI deposited onto a glass substrate retains its absorption characteristics as the native species. Third, analysis for adhesion of PSI onto surface based on critical micelle concentration on surfactant is provided. Fourth , a photoelectrochemical cell is fabricated to demonstrate the enhancements in the photocurrent in the visible and UV-visible region. Finally, the possible mechanisms for electron transfer are discussed.

4.3 Experimental methods

4.3.1 Isolation of Photosystem I

Photosystem I (PSI) trimers were isolated from HT3 cells, a genetically Photosystem II modified *Synechocystsis* sp. PCC 6803 strain.[23] In brief, Photosystem II was removed by Ni-NTA affinity chromatography, and PSI trimer and monomer were isolated using sucrose gradient ultracentrifugation similar to earlier work.[24, 25] This preparation yielded two green bands corresponding to the monomer and trimer respectively. The lower band contained the PSI trimers free from other components. Specifically, in our experiments, PSII was essentially removed by

affinity chromatography before ultracentrifugation[26] and eliminated any PSII interference during photoelectrical measurements. The purity of PSI was confirmed by measuring 77 K fluorescence, which shows the characteristic peak of PSI around 720 nm and no PSII peaks around 685 nm and 693 nm. Only PSI trimers were used for the experiment and they are referred as PSI in this paper.

4.3.2 Synthesis of Nanostructured TiO2 Films

Columnar TiO_2 nanostructured films were deposited onto tin-doped indium oxide (ITO) coated aluminosilicate glass (Delta technologies, CO) using an aerosol controlled vapor deposition (ACVD) process using a process described previously.[15] Briefly, titanium tetraisopropoxide (TTIP, 97% Sigma-Aldrich) was used as a precursor and loaded into a bubbler at 297 K. The nitrogen carrier gas was kept at a constant flow rate of 0.45 L min^{-1} through the bubbler. Additionally, a dilution flow rate (N_2) of 0.45 L min^{-1} was used. The TiO_2 formed as a result of the decomposition of the precursor, nucleates in the gas phase and forms particles. These particles are deposited onto ITO glass kept at a constant temperature of 773 K where they sinter to form columnar TiO_2 single crystal structures. The total deposition time of TiO_2 was fixed at 65 minutes. The morphology of the nanostructure titanium dioxide film was examined using field emission scanning electron. Gold sputtering of the samples was performed for 30 seconds before FESEM analysis in order to improve resolution of the images. The SEM image shows the nano-structured columns and the height of the columns was measured to be 1.6 μm.

4.3.3 Electrospray Deposition of Photosystem I

To prepare PSI for deposition, the protein was filtered using 30 kDa centrifugal filters to remove salts and glycerol, which is added for low temperature storage. The filtrate is then diluted with 0.01% v/v dodecylmaltoside (DDM) in de-ionized water (>18 MΩ). The PSI spray solution was prepared with 10% v/v ethanol and 3 mM ammonium acetate for deposition. The solution

was immediately placed into a syringe cleaned with filtered pure ethanol. Needles used for deposition had a bore of 125 μm and were tapered using the machine shop at Washington University in St. Louis. A positive potential of 7-8.5 kV with a current of 320-350 nA was applied for electrospray deposition. CO_2 sheath flow around the needle was set at 2 L min^{-1}, and it was introduced to prevent corona discharge and arcs from the needle tip to the surface.

4.3.4 Size measurement of PSI

Dynamic light scattering (DLS) was used to measure the size of PSI in solution. The DLS data was collected using a Malvern Instruments Zetasizer Nano-ZS system. The size of PSI in flight was measured by SMPS after atomization by electrospray. The Electrospray Aerosol Generator (EAG - model 3480, TSI inc., Shoreview, MN) is used to synthesize monodisperse aerosols for size characterization. Radioactive Po^{210} (5 mC activity) was used to reduce the charge on particles before they were introduced into the electrostatic classifier. An Electrostatic Classifier (TSI inc., model 3080) along with a DMA was used for size classification followed by a CPC (TSI inc., model 3776) for particle counting. Aerosol flow rates of 0.3 and sheath flow rate of 6 L min^{-1} were used. More details and schematic of setup can be found elsewhere.[18]

4.3.5 Solar Characterization of PSI-TiO_2 Films

The electrochemical measurements were made on an in-house electrochemical setup consisting of a 3-electrode electrochemical cell with an Ag/AgCl reference electrode (BASi, Inc.) and a platinum wire counter-electrode. Electrochemical performance was measured using a VersaStat 4 (Princeton Applied Research, TN) potentiostat/galavanostat. The PSI - TiO_2 electrochemical cells were tested with a 20 mM sodium ascorbate, 250 μM DCPIP and 0.1 M KCl electrolyte solution unless otherwise noted. The lamp used was a 450 W Xe arc lamp

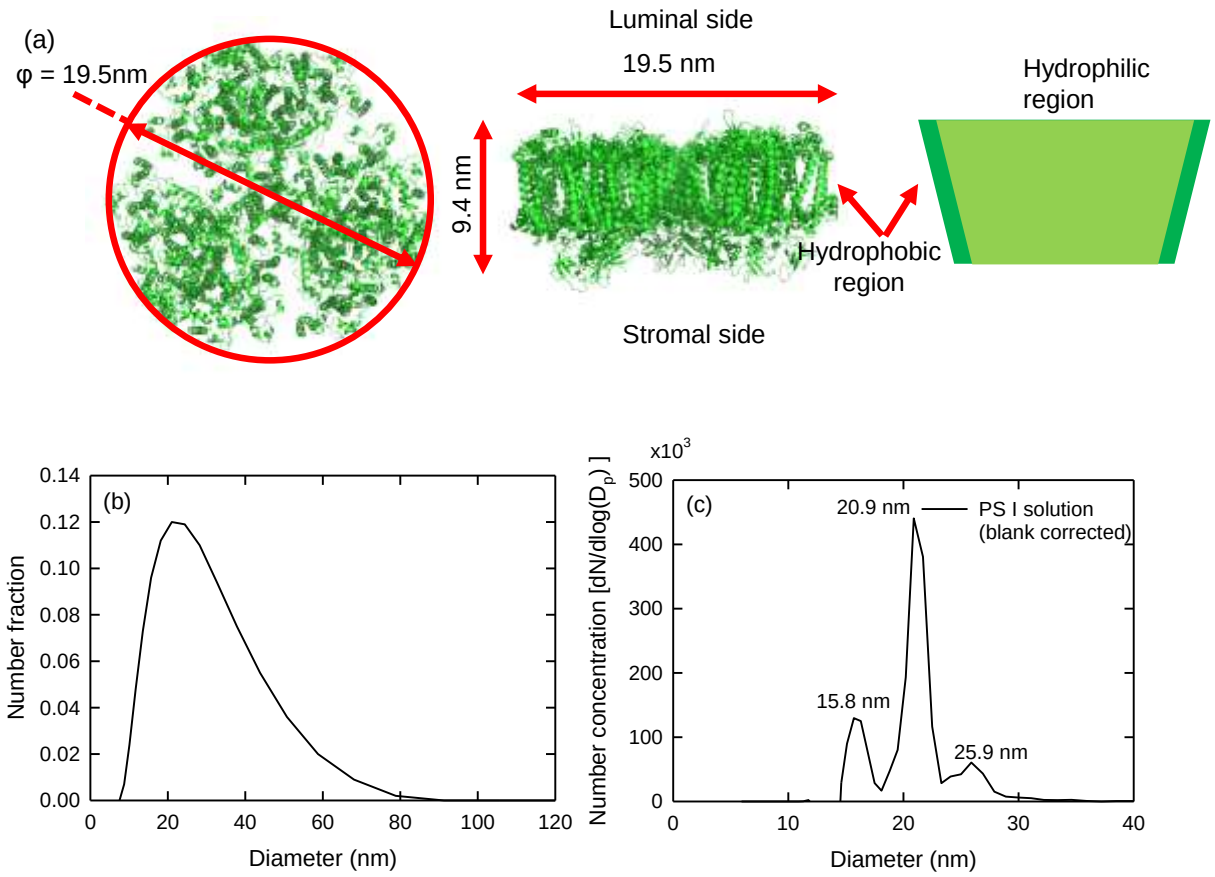

Figure 4–1: (a) Top view and side view of PSI. The hydrophobic parts on the surface have been highlighted by dark green (b) Size distribution of PSI in solution as measured by DLS and (c) Blank-corrected size distribution for the electrosprayed PSI solution obtained from scanning mobility particle sizer (SMPS).

(Newport Corporation, CA). A water filter was used to block IR wavelengths and a 400 nm cut-off filter (Newport Corporation, CA) was used to block UV wavelengths where needed.

4.4 Results and discussions

In this work, electrospray deposition was used for a linker-free attachment of PSI onto a semiconducting nanostructured titanium dioxide film to fabricate an electrode. First, the results for size characterization of PSI with dynamic light scattering and scanning mobility particle sizer are described. Second, the results for retention of absorption of PSI by different deposition

techniques after deposition on to conducting glass by electrospray are presented by comparing the absorption spectra. Finally, a PSI-based photoelectrochemical cell was characterized using linear scan voltammetry and chronoamperometry and the underlying mechanism for electron transfer is discussed.

4.4.1 PSI characterization

Figure 4–1a shows a rendering of a PSI trimer in its top and side views. Usually PSI in cyanobacteria consists of three symmetric units in top view, and is often referred to as a PSI trimer. In this paper PSI refers exclusively to the PSI trimer and is the smallest unit analyzed in this work. PSI is a membrane-bound protein and has some hydrophobic and hydrophilic parts. Thus in the process of extraction and purification of PSI in aqueous solution, dodecylmaltoside (DDM) is added to prevent it from agglomerating. Two different techniques, dynamic light scattering and electrospray atomization, have been used to measure the size of PSI in solution. Dynamic light scattering (DLS) is used to measure the size of PSI in solution and also to ascertain that they have not agglomerated in solution. Figure 4–1b shows the size distribution of PSI as measured by DLS. The mode hydrodynamic diameter measured by DLS is 21.04 nm. The effective spherical diameter for the prolate ellipsoid[27] is given by $(ab^2)^{1/3}$ and thus assuming a = 9 and b = 19.5 nm for a monomer, the volume average diameter is 15.06 nm for a PSI unit. The estimated size of PSI is lot smaller mainly because PSI is surrounded by DDM and water molecules, which reduces the diffusion of PSI. Thus the measured size is lot larger than the theoretical estimate. The size measurement verifies that the selected concentration of DDM in solution is suitable to prevent agglomeration of PSI in the solution.

A Scanning Mobility Particle Sizer (SMPS) was used to measure the mobility size distribution of PSI after aerosolization by an electrospray atomizer (Figure 4–1c). The solution

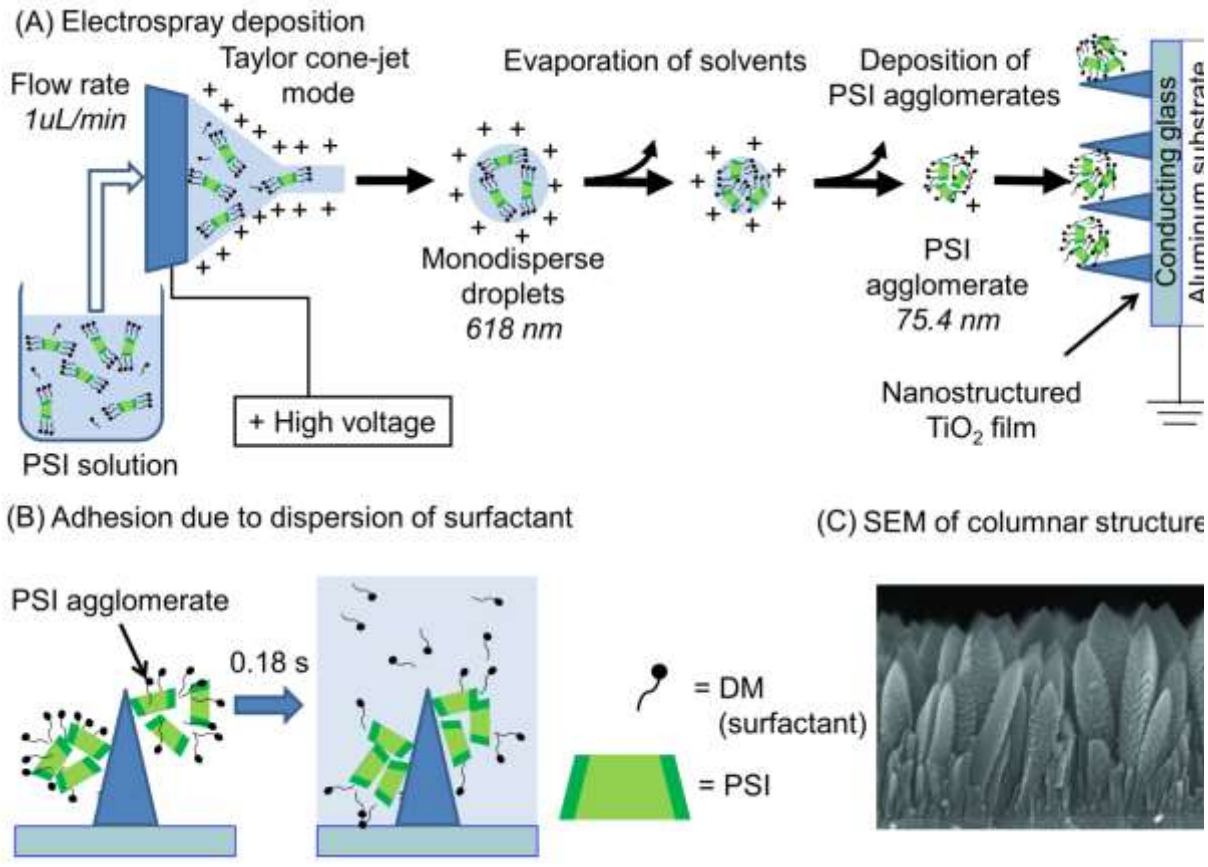

Figure 4–2. Schematic of linker-free deposition of PSI onto TiO_2. (a) Electrospray deposition of PSI onto nanostructured TiO_2 columns. (b) Adhesion of PSI due to removal of surfactant on immersion in DDM free electrolyte. (c) SEM Image of single crystal nanostructured TiO_2 columns used for deposition.

concentration used was sufficiently dilute so that either single PSI units were present in most droplets or none. If there is a single PSI inside the droplet, on evaporation of water a freely suspended charged PSI particle will be obtained. Under these conditions, this technique enables an accurate measurement of the size of PSI units with the SMPS after solvent evaporation. However if no PSI is present in the droplet then a particle formed out of DDM molecules is obtained. The size measured by SMPS for droplets which contain particles or dissolved molecules is explained in previous work.[18] In this work, the blank measurements are subtracted to get the resultant size distribution of PSI. As shown in Figure 4–1c, a peak at 15.9 nm is

obtained from the particles formed due to DDM. The other peaks at 20.9 and 25.9 nm are attributed to PSI. As PSI is not spherical, a volume average diameter for an ellipsoid is used. The effective spherical diameter for the PSI is estimated to be 15.06 nm, thus the volume of particle which consists of both the DDM and PSI, combined volume is estimated to be 19.3 nm which is close to the peak size of 20.9 nm measured by the SMPS. The difference in measured size is mainly because the SPMS measures the mobility size of PSI. There is a possibility that more than one PSI is present in a droplet. The volume average diameter for a particle consisting of two or more PSI is indicated by presence of other peaks. The size of the PSI measured using two independent techniques verifies that PSI has not agglomerated in solution.

4.4.2 Electrospray deposition of PSI

Figure 4–2a shows a schematic of the electrospray deposition setup for fabricating PSI-TiO_2 films. Table 4-1 lists the properties of the solution and the size of droplets formed. The spray solution consisting of PSI, 0.001% v/v DDM, 3mM ammonium acetate and 10% v/v ethanol is pumped through the syringe at 1 μL min^{-1}. The concentration of DDM is above the critical micelle concentration (CMC) and prevents PSI from agglomerating in solution. When the electric field is applied, monodispersed charged droplets are formed. The diameter of the droplets is estimated to be 618 nm by scaling laws.[28, 29] Based on the concentration of PSI, there are approximately 20 PSI in each droplet. These charged droplets move towards the substrate because of the electric field. The ethanol, water and ammonium acetate evaporate and leave behind charged agglomerates of PSI and DDM. Due to the electric field, the charged agglomerates deposit onto the conducting nanostructured TiO_2 (Figure 4–2c). The as deposited

Table 4-1: Solution properties and conditions for electrospray deposition of PSI.

Spray solution properties				Electrospray conditions			Properties of sprayed droplets		
Solvent	Dielectric constant of spray solution	Ammonium Acetate Concentration	Conductivity	Flow rate of spray solution	Voltage	Current	Mean droplet size[a)]	95% interval for droplet size with σ_g=1.1[b)]	95% interval for particle size[b)]
	-	[mM]	[μS cm^{-1}]	[μL min^{-1}]	[kV]	[nA]	[nm]	[nm]	-
10% Ethanol in water (v/v)	72.3	3	235	1±0.01	7-8.5	320-350	618	561.8-679.8	68.5-82.9

[a)]Using scaling law equations[12b]

[b)]Geometric standard deviation for monodisperse droplet synthesized by electrospray[12b]

structure is then immersed in a surfactant free (low concentration) electrolyte solution which is composed of 20 mM sodium ascorbate, 250 μM DCPIP and 0.1 M KCl

.

structure is then immersed in a surfactant free (low concentration) electrolyte solution which is composed of 20 mM sodium ascorbate, 250 μM DCPIP and 0.1 M KCl.

4.4.3 Linker-free adhesion and prevention of resuspension

After PSI deposition, the slide is added to electrolyte solution which does not contain DDM, which will cause DDM to dissolve into the bulk electrolyte solution. The DDM which has been deposited will diffuse into the bulk solution in form of micelles and DDM monomers. After the dissolution of DDM, the surface concentration of DDM will drop below the CMC. Below CMC the PSI may agglomerate with each other and adhere to the surface by van der Waals or hydrophobic forces on the TiO_2 surface. Thus two scenarios are possible (1) suspending PSI covered with DDM in the electrolyte solution and (2) dissolving the DDM in the electrolyte solution, leaving PSI on the surface. The conditions such as DDM concentration, solubility, and diffusion coefficient will determine which scenario is preferred.

The diffusion equation for DDM concentration can be solved to quantitatively estimate the concentration profile with time. The solution to the diffusion equation is given by,

$$c(t) = \frac{N}{A}\frac{1}{2\sqrt{\pi Dt}}\exp\left(\frac{-x^2}{4Dt}\right) \tag{4.1}$$

Where *c(t)* is the concentration of DDM at a distance *x* from surface, *t* is the time, *D* is the diffusion coefficient, *N* is the total moles of molecules and *A* is the surface area. The detailed values for the constants used are included in Table 4-2. Although initially the DDM is spread over nanostructured surface with columnar height of 1.6 μm, a suitable approximation assuming all the DDM is on surface (x=0) is made. After a certain time *t*, the concentration on surface

(x=0), will be below CMC. Since DDM monomers diffuse faster, diffusion coefficient for DDM monomers ($D = 5.4x10^{-10}$ m^2/s.[30]) is used to get an estimate for time.

$$c_{cmc} = \frac{(N / A)}{2\sqrt{\pi Dt}} \tag{4.2}$$

Solving for *t* with the constants give in Table 4-2, we get the time it will take for the surface DDM concentration to reduce below CMC. Thus the concentration below CMC would be reached in less than 0.18s. In this time, the protein complexes of PSI can also diffuse around. The root mean square distance for diffusion of PSI is given by $(2Dt)^{1/2}$. Using the diffusion coefficient of PSI estimated from the Stokes-Einstein equation and the size measured by DLS, the root mean square distance travelled is estimated to be 2.68 um. This length of diffusion is

Table 4-2: Constants used for calculation of diffusion length of PSI

Calculations for DDM	
DDM concentration	0.001% v/v
Flowrate for electrospray	1 µL/min
Deposition time for electrospray	5 min
Volume of DDM deposited	0.005 µL
Area of deposition	0.2 cm^2
CMC for DDM	0.007% v/v
Diffusion coefficient of DDM	$5.40x10^{-10}$ m^2/s
Time for peak concentration to be below CMC	0.19 s
Calculations for PSI	
Temperature	293.15 K
Size of PSI from DLS	0.022 µm
Water viscosity	8.90E-04 Pa*s
Diffusion coefficient	$2.19x10^{-11}$ m^2/s
Root mean square distance	2.87 µm

comparable to the length of the nanostructured column (1.6 μm). Moreover the diffusion lengths will be smaller for agglomerated PSI. Thus most of the PSI will remain close to the nanostructured columns, diffuse back and be adhered due to van Der Vaals and hydrophobic forces. Thus the deposited PSI agglomerates will not be resuspended into the electrolyte solution, even in the absence of a linker molecule. Figure 4–2b shows the schematic of dissolution of DDM which results in adhesion of PSI onto the surface of nanostructured TiO_2. Choosing the appropriate concentration of DDM in the original spray solution is important because at higher concentrations of DDM, it will take longer time for concentration to drop below the CMC on immersion in electrolyte. DDM concentrations above the CMC will tend to overcome other forces and resuspend the PSI in the electrolyte solution, lowering the overall performance of the cell. On the other hand, extremely low concentrations will result in agglomeration of PSI in the spray solution before spray deposition; resulting in loss of control on the deposit morphology.

4.4.4 Absorption spectrum of electrosprayed PSI

UV-vis absorption spectra were used to characterize the PSI after deposition onto a surface. The absorbance of PSI after deposition by electrospray and by drop coating onto a transparent conducting glass slide (FTO) was compared. PSI was electrosprayed in the same electrospray solution (0.001% DDM, 3 mM ammonium acetate, and 10% v/v Ethanol) and drop coated in a similar fashion to LeBlanc et al.[9] As shown in Figure 4–3, the absorption spectra of PSI after deposition by both the techniques is comparable to the solution spectra with chlorophyll peaks at 680 and 480 nm. However, the PSI deposited on the slide by drop coating dries unevenly and results in a scattering peak at 850 nm. Since small amounts of PSI are deposited by drop coating, it results in lower peak absorption and the peak at 850 nm is magnified on normalizing. The electrosprayed PSI has a much lower peak at 850 nm in comparison to the drop

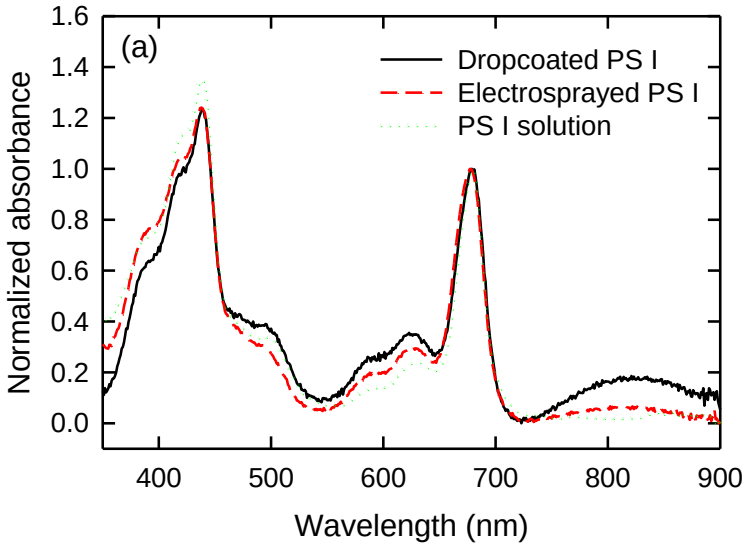

Figure 4–3. Comparison of normalized absorption spectra of PSI in solution, after deposition using electrospray, and after depositing by drop coating.

coated PSI. Significantly lower scattering is observed since a uniformly distributed deposition is obtained by electrospray. This comparison shows that the absorption spectra of PSI deposited by both drop-coating and electrospray are comparable to PSI in solution immediately after deposition as shown in Figure 4–3. After deposition, it was observed that drop-coated PSI absorbance decreased more rapidly than electrosprayed PSI, demonstrating the increased retention in absorption of the electrosprayed PSI films.

4.4.5 Characterization of photoelectrochemical cell

The performance of the photoelectrochemical cell (PEC) with the nano-biohybrid PSI-TiO_2 electrode is characterized with linear sweep voltammetry and chronoamperometry. To gain further insights into amount of PSI required to get the best performance, the peak current of the cell is measured with varying amounts of deposited PSI.

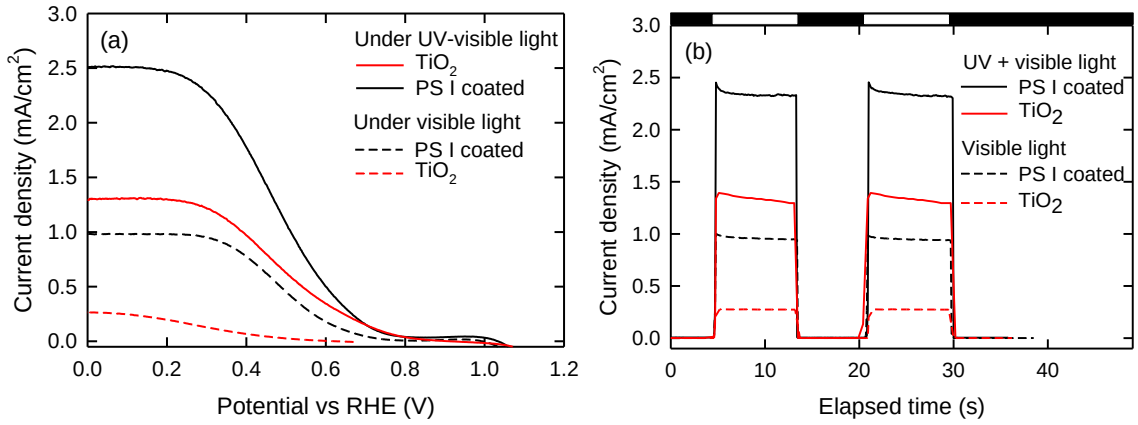

Figure 4–4. The performance of the photoelectrochemical cell under various lighting conditions with nanostructured TiO_2 and PS1 coated nanostructured TiO_2 as the working electrode by (a) linear scan voltammetry and (b) chronoamperometry. The dashed line represents the photoelectrochemical cell performance under visible light illumination only (400-900 nm), and the solid line represents the solar cell performance with UV-visible illumination (250-900 nm).

Linear sweep voltammetry & chronoamperometry data

Figure 4–4a shows the performance of the PSI based PEC for linear sweep voltammetry with applied potential (vs Ag/AgCl) varied from 0.8 V to 0 V. The current increases when the applied potential (vs Ag/AgCl) is decreased from 0.8 V to 0.3 V and is nearly constant from 0.3 V to 0 V. The results for the peak current density under various conditions are summarized in Table 4-3. The currents for PSI-TiO_2 are higher under visible light compared to the bare nanostructured TiO_2. The deposition of PSI increased light absorption in the visible region and the PSI effectively transfers electron to TiO_2. Significant enhancements in photocurrent were observed with the addition of UV light, which is absorbed by TiO_2. The addition of UV light enhanced the bare nanostructured TiO_2 photocurrent density by three-fold to 1 mA cm^{-2} and a two and a half-fold enhancement for TiO_2 with deposited PSI. The increment in photocurrent density for PSI based PEC when the incident light consisted UV component along with visible is higher compared to the bare nanostructured TiO_2 control. This is mainly attributed to PSI's

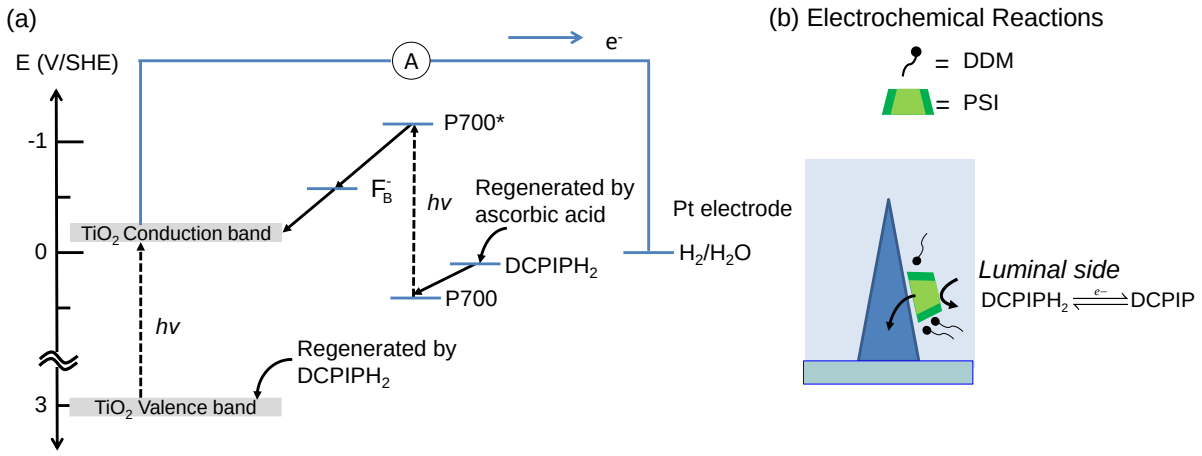

Figure 4–5: (a) The electron transfer pathway for the PSI-TiO_2 photo-electrochemical cell. (b) The schematic of reactions taking place on PSI which is deposited onto TiO2 columns.

absorption in the UV region below 400 nm. The currents measured for PSI coated nanostructured TiO_2 are higher than any other measurements reported so far for PSI based photoelectrochemical cells (Table S1). The high current density is obtained mainly due to 1D nano-structures of TiO_2, which allows more PSI to be in contact with the surface. Moreover, linker-free deposition results in effective electron transfer and orientation of PSI ensures that it is accessible to the electrolyte. Figure 4–4b shows the ON/OFF cycles in chronoamperometry measurement. The photocurrent measurements for chronoamperometry were done over 100 seconds at 0.3 V applied between reference and working electrode. There is negligible photocurrent when no light is present or under ‘OFF‘ conditions. The photocurrent response under ‘ON‘ conditions was similar for all the cycles, which implies that the photoanode shows good stability.

Electron transfer pathway

Figure 4–5a shows the electron transfer pathway in the PSI-TiO_2 photo-electrochemical cell. PSI generates a potential difference of ~0.98 V when illuminated.[14] The luminal side of PSI consists of the chlorophyll molecule P700, which is at standard reduction potential of 0.4 V.

When the P700 chlorophyll molecule is excited, denoted by P700*, the standard reduction potential is -1.25 V. However after subsequent electron transfer within PSI, the electron moves to the iron sulfur complex, F_B (E^0= -0.58 V), on the stromal side. In the natural system, ferredoxin (E^0_{redox} = -0.44 V) gets reduced at F_B[31] and acts as a shuttle to catalyze the formation of NADPH. In our system, the electron is directly injected into TiO_2 when the orientation is correct, since TiO_2 is at lower redox potential. The electron accepted by TiO_2 then flows though the ammeter and forms hydrogen at the platinum electrode. In the natural system cytochrome regenerates the hole at P700. In our system, 2, 6-dichlorophenolindophenol (DCPIP, E^0_{redox} = 0.22 V) and ascorbic acid is used. Ascorbic acid, which is in excess, reduces DCPIP to $DCPIPH_2$ and forms dehydroascorbic acid, acting as a sacrificial donor. The hole at P700 is regenerated by $DCPIPH_2$. Thus DCPIP/$DCPIPH_2$ acts as an electron shuttle between ascorbic acid and P700 in PSI. Figure 4–5b shows the orientation of PSI for electron injection and the location where reactions take place. Thus the orientation of PSI where stromal side is in contact with TiO_2 and the luminal side has access to the electrolyte results in enhanced photocurrents.

Table 4-3: Peak photocurrent densities under various lighting conditions for photo-electrochemical cells fabricated with nanostructured TiO_2 and PSI coated nanostructured TiO_2.

	Photocurrent density [mA cm^{-2}]	
Sample (lighting conditions)	without PSI	with PSI
ITO (UV+visible)	<0.001	0.05
ITO + TiO_2 (visible)[a)]	0.27	1.05
ITO + TiO_2 (UV+ visible)[b)]	1.38	2.51

[a)]Wavelength range 400-900 nm with use of UV cut-off filter [b)]Wavelength range 250-900 nm

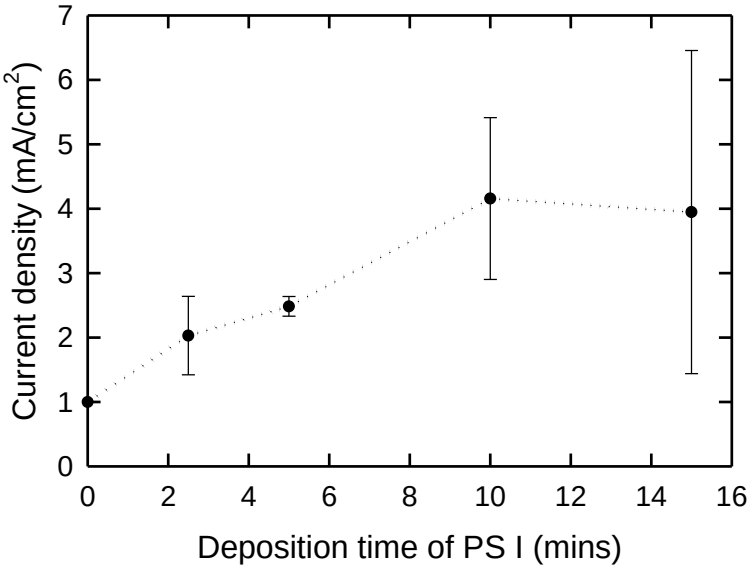

Figure 4–6: Current density for PSI coated nanostructured TiO_2 under UV-visible illumination for varying deposition times of PSI agglomerates

Effect of deposition time on current density

The previous section demonstrated that PSI-TiO_2 has enhanced photocurrent compared to nanostructured TiO_2. In order to determine the optimum amount of PSI to deposit on TiO_2, the solution was sprayed for increasing times and the slides were characterized for peak current density. Figure 4–6 shows the peak current measured for various deposition times, since the amount of PSI on the film is linearly proportional to the deposition time. All the deposition times demonstrated a higher current density than the nanostructured TiO_2 slide, represented by no deposition. For shorter deposition times of PSI, there is an increase in the current density under UV-visible light, which is mainly due to increased absorption of light by PSI. The photocurrent density of 4.15 mA cm^{-2} was observed after depositing PSI for 10 minutes, which is the highest measured photocurrent reported for a PSI system (Refer Table S1 for comparison of photocurrents). However beyond 10 minutes deposition, there is no significant increase in

current density as shown in the figure. Clearly there is an optimal deposition amount beyond which any additional PSI will not result in an increase in photo-current. The lack of increase in photocurrent density is mainly attributed to excess deposits of PSI not being in contact with nanostructured titanium dioxide. This PSI would absorb light however it would not translate to photocurrent. However, beyond 10 minutes deposition, there is no significant increase in current density as shown in the figure. Clearly, there is an optimal deposition amount beyond which any additional PSI will not result in an increase in photocurrents. The lack of increase in photocurrent density is mainly attributed to excess deposits of PSI not being in contact with nanostructured titanium dioxide, or not appropriately aligned. This PSI would absorb light, however it would not translate to photocurrent.

4.5 Conclusions

PSI was successfully deposited onto nanostructured metal oxide surfaces using electrospray without the use of linkers for attachment. PSI remain adhered to the nanostructured electrode due to removing of the DDM and due to van der Waals and hydrophobic interaction forces. These PSI sensitized titanium dioxide electrodes had a photocurrent density of 4.15 mA cm^{-2}, which is the highest reported value in the literature. The high photocurrent density is attributed to the orientation of PSI that aids in electron injection and hole regeneration from the electrolyte. There is an optimal amount of PSI that results in the highest current density (deposition time of 10 minutes). In the future, further optimization with respect to the electrolyte and redox mediator may result in an even higher current density. Using this technique of electrospray deposition, we have overcome the limitations of the existing techniques that need the use of linker molecules; or do not have control resulting in obtaining multiple layers; both of which impede electron transport. Electrospray deposition is a novel technique for fabricating

electrodes for nano-bio hybrid photoelectrochemical cells. This technique can be extended to other membrane bound proteins widening the use of other reaction centers for fabrication of more efficient solar cells.

4.6 Acknowledgements

Author V. Shah and R. Henson contributed equally to this work. This work was supported in part under the US-India Partnership to Advance Clean Energy-Research (PACE-R) for the Solar Energy Research Institute for India and the United States (SERIIUS), funded jointly by the U.S. Department of Energy (Office of Science, Office of Basic Energy Sciences, and Energy Efficiency and Renewable Energy, Solar Energy Technology Program, under Subcontract DE-AC36-08GO28308 to the National Renewable Energy Laboratory, Golden, Colorado) and the Government of India, through the Department of Science and Technology under Subcontract IUSSTF/JCERDC-SERIIUS/2012 dated 22nd Nov. 2012. Electron microscopy was performed at the Nano Research Facility (NRF) at Washington University in St. Louis, a member of the National Nanotechnology Infrastructure Network (NNIN), supported by the National Science Foundation under Grant No. ECS-0335765. H. Liu thanks Jing Jiang for technical help during PSI preparation. V. Shah thanks McDonnell International Scholars Academy for the Ph.D. fellowship at Washington University in St. Louis.

4.7 References

1. Hogewoning, S. W.; Wientjes, E.; Douwstra, P.; Trouwborst, G.; van Ieperen, W.; Croce, R.; Harbinson, J. Photosynthetic Quantum Yield Dynamics: From Photosystems to Leaves. *The Plant Cell Online* **2012**, *24*, 1921-1935.

2. Nelson, N.; Yocum, C. F. Structure and Function of Photosystems I and II. *Annu. Rev. Plant Biol.* **2006**, *57*, 521-65.

3. Jordan, P.; Fromme, P.; Witt, H. T.; Klukas, O.; Saenger, W.; Krauss, N. Three-Dimensional Structure of Cyanobacterial Photosystem I at 2.5 Å Resolution. *Nature* **2001**, *411*, 909-17.

4. Mershin, A.; Matsumoto, K.; Kaiser, L.; Yu, D.; Vaughn, M.; Nazeeruddin, M. K.; Bruce, B. D.; Graetzel, M.; Zhang, S. Self-Assembled Photosystem-I Biophotovoltaics on Nanostructured TiO_2 and ZnO. *Sci. Rep.* **2012**, *2*.

5. Frolov, L.; Wilner, O.; Carmeli, C.; Carmeli, I. Fabrication of Oriented Multilayers of Photosystem I Proteins on Solid Surfaces by Auto-Metallization. *Adv. Mater.* **2008**, *20*, 263-266.

6. Efrati, A.; Yehezkeli, O.; Tel-Vered, R.; Michaeli, D.; Nechushtai, R.; Willner, I. Electrochemical Switching of Photoelectrochemical Processes at CdS Qds and Photosystem I-Modified Electrodes. *ACS Nano* **2012**, *6*, 9258-9266.

7. Ciesielski, P. N.; Scott, A. M.; Faulkner, C. J.; Berron, B. J.; Cliffel, D. E.; Jennings, G. K. Functionalized Nanoporous Gold Leaf Electrode Films for the Immobilization of Photosystem I. *ACS Nano* **2008**, *2*, 2465-2472.

8. Ciesielski, P. N.; Faulkner, C. J.; Irwin, M. T.; Gregory, J. M.; Tolk, N. H.; Cliffel, D. E.; Jennings, G. K. Enhanced Photocurrent Production by Photosystem I Multilayer Assemblies. *Adv. Funct. Mater.* **2010**, *20*, 4048-4054.

9. LeBlanc, G.; Chen, G.; Gizzie, E. A.; Jennings, G. K.; Cliffel, D. E. Enhanced Photocurrents of Photosystem I Films on p-Doped Silicon. *Adv. Mater.* **2012**, *24*, 5959-5962.

10. Manocchi, A. K.; Baker, D. R.; Pendley, S. S.; Nguyen, K.; Hurley, M. M.; Bruce, B. D.; Sumner, J. J.; Lundgren, C. A. Photocurrent Generation from Surface Assembled Photosystem I on Alkanethiol Modified Electrodes. *Langmuir* **2013**, *29*, 2412-2419.

11. Yehezkeli, O.; Tel-Vered, R.; Michaeli, D.; Nechushtai, R.; Willner, I. Photosystem I (PSI)/Photosystem II (PSII)-Based Photo-Bioelectrochemical Cells Revealing Directional Generation of Photocurrents. *Small* **2013**, *9*, 2970-2978.

12. Darby, E.; LeBlanc, G.; Gizzie, E. A.; Winter, K. M.; Jennings, G. K.; Cliffel, D. E. Photoactive Films of Photosystem I on Transparent Reduced Graphene Oxide Electrodes. *Langmuir : the ACS journal of surfaces and colloids* **2014**, *30*, 8990-4.

13. Iwuchukwu, I. J.; Vaughn, M.; Myers, N.; O'Neill, H.; Frymier, P.; Bruce, B. D. Self-Organized Photosynthetic Nanoparticle for Cell-Free Hydrogen Production. *Nat. Nanotechnol.* **2010**, *5*, 73-79.

14. Lubner, C. E.; Grimme, R.; Bryant, D. A.; Golbeck, J. H. Wiring Photosystem I for Direct Solar Hydrogen Production. *Biochemistry* **2010**, *49*, 404-414.

15. An, W.-J.; Thimsen, E.; Biswas, P. Aerosol-Chemical Vapor Deposition Method for Synthesis of Nanostructured Metal Oxide Thin Films with Controlled Morphology. *J. Phys. Chem. Lett.* **2010**, *1*, 249-253.

16. An, W.-J.; Jiang, D. D.; Matthews, J. R.; Borrelli, N. F.; Biswas, P. Thermal Conduction Effects Impacting Morphology During Synthesis of Columnar Nanostructured TiO_2 Thin Films. *J. Mater. Chem.* **2011**, *21*, 7913-7921.

17. Zhu, L.; An, W.-J.; Springer, J. W.; Modesto-Lopez, L. B.; Gullapalli, S.; Holten, D.; Wong, M. S.; Biswas, P. Linker-Free Quantum Dot Sensitized TiO_2 Photoelectrochemical Cells. *Int. J. Hydrogen Energy* **2012**, *37*, 6422-6430.

18. Shah, V. B.; Orf, G. S.; Reisch, S.; Harrington, L. B.; Prado, M.; Blankenship, R. E.; Biswas, P. Characterization and Deposition of Various Light-Harvesting Antenna Complexes by Electrospray Atomization. *Anal. Bioanal. Chem.* **2012**, *404*, 2329-2338.

19. Modesto-Lopez, L. B.; Thimsen, E. J.; Collins, A. M.; Blankenship, R. E.; Biswas, P. Electrospray-Assisted Characterization and Deposition of Chlorosomes to Fabricate a Biomimetic Light-Harvesting Device. *Energy Env. Sci.* **2010**, *3*, 216-222.

20. Mirvakili, S. M.; Slota, J. E.; Usgaocar, A. R.; Mahmoudzadeh, A.; Jun, D.; Mirvakili, M. N.; Beatty, J. T.; Madden, J. D. W. Photoactive Electrodes Incorporating Electrosprayed Bacterial Reaction Centers. *Adv. Funct. Mater.* **2014**, *24*, 4789-4794.

21. Shah, V. B.; Biswas, P. Aerosolized Droplet Mediated Self-Assembly of Photosynthetic Pigment Analogues and Deposition onto Substrates. *ACS Nano* **2014**, *8*, 1429-1438.

22. Schubert, W.-D.; Klukas, O.; Saenger, W.; Witt, H. T.; Fromme, P.; Krauß, N. A Common Ancestor for Oxygenic and Anoxygenic Photosynthetic Systems: A Comparison Based on the Structural Model of Photosystem I. *J. Mol. Biol.* **1998**, *280*, 297-314.

23. Bricker, T. M.; Morvant, J.; Masri, N.; Sutton, H. M.; Frankel, L. K. Isolation of a Highly Active Photosystem II Preparation from Synechocystis 6803 Using a Histidine-Tagged Mutant of Cp 47. *Biochim. Biophys. Acta, Bioenerg.* **1998**, *1409*, 50-57.

24. Kruip, J.; Boekema, E. J.; Bald, D.; Boonstra, A. F.; Rogner, M. Isolation and Structural Characterization of Monomeric and Trimeric Photosystem-I Complexes (P700.Fa/Fb and

P700.Fx) from the Cyanobacterium Synechocystis PCC-6803. *J. Biol. Chem.* **1993**, *268*, 23353-23360.

25. Sun, J.; Ke, A.; Jin, P.; Chitnis, V. P.; Chitnis, P. R., Isolation and Functional Study of Photosystem I Subunits in the Cyanobacterium Synechocystis Sp. PCC 6803. In *Methods in Enzymology*, Lee, M., Ed. Academic Press: 1998; Vol. Volume 297, pp 124-139.

26. Liu, H.; Zhang, H.; Niedzwiedzki, D. M.; Prado, M.; He, G.; Gross, M. L.; Blankenship, R. E. Phycobilisomes Supply Excitations to Both Photosystems in a Megacomplex in Cyanobacteria. *Science* **2013**, *342*, 1104-1107.

27. Wang, Z.-Y.; Marx, G.; Umetsu, M.; Kobayashi, M.; Mimuro, M.; Nozawa, T. Morphology and Spectroscopy of Chlorosomes from Chlorobium Tepidum by Alcohol Treatments. *Biochim. Biophys. Acta, Bioenerg.* **1995**, *1232*, 187-196.

28. Basak, S.; Chen, D. R.; Biswas, P. Electrospray of Ionic Precursor Solutions to Synthesize Iron Oxide Nanoparticles: Modified Scaling Law. *Chem. Eng. Sci.* **2007**, *62*, 1263-1268.

29. Chen, D. R.; Pui, D. Y. H.; Kaufman, S. L. Electrospraying of Conducting Liquids for Monodisperse Aerosol Generation in the 4 nm to 1.8 μm Range. *J. Aerosol Sci.* **1995**, *26*, 963-978.

30. Horst, R.; Stanczak, P.; Stevens, R. C.; Wüthrich, K. B2-Adrenergic Receptor Solutions for Structural Biology Analyzed with Microscale NMR Diffusion Measurements. *Angew. Chem. Int. Ed.* **2013**, *52*, 331-335.

31. Díaz-Quintana, A.; Leibl, W.; Bottin, H.; Sétif, P. Electron Transfer in Photosystem I Reaction Centers Follows a Linear Pathway in Which Iron−Sulfur Cluster Fb Is the Immediate Electron Donor to Soluble Ferredoxin†. *Biochemistry* **1998**, *37*, 3429-3439.

4.8 Supporting information

Transmission electron microscopy was used to examine the deposited PSI agglomerates. The TEM characterization was done on Technai^{TM} Spirit, FEI Co. The PS1 particles were deposited on to the lacey carbon grid with electrospray. The deposited particles of PS1 were immersed in surfactant free, negative stain Nano-W® from Nanoprobes (NY, USA). Figure 4–7 shows that agglomerates in the size range of 50-100 nm were deposited. The agglomerate diameter in TEM is larger than the 75.5 nm, estimated by the volume fraction calculations. The larger size of agglomerates is attributed to directed self-assembly on the surface, resulting in thinner but larger 2 dimensional deposits.

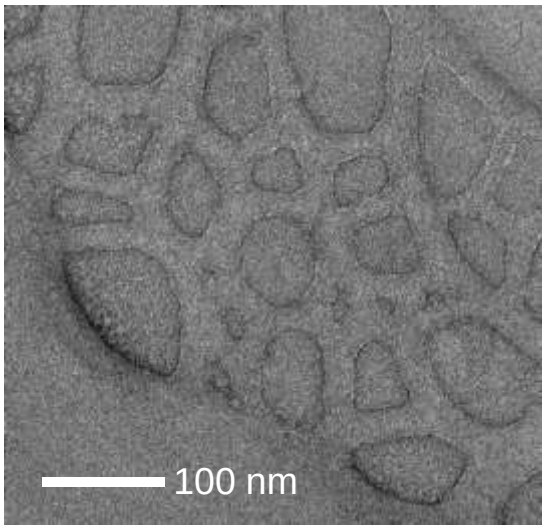

Figure 4–7: TEM image of the deposited PSI agglomerates

Table 4-4 gives a comparison of the photocurrents generated by various people for PSI based photoelectrochemical cells. Clearly the currents generated in this work are at least 3 times higher than the previously best results. The normalized currents are corrected for the difference in power, however the spectrum will be different and this comparison is only for qualitative purpose.

Table 4-4: Comparison of the best currents generated by PSI in photoelectrochemical cells

Author	Current (mA/cm^2)	Current due to PSI (mA/cm^2)	Light Source	Normalized to Arc Xenon Lamp (mA/cm2)
Shah (This work - least variance)	2.51	1.13	Arc Xenon 0.22 W/cm^2	1.13
Shah (This work - best result)	4.15	2.77	Arc Xenon 0.22 W/cm^2	2.77
Leblanc[13]	0.875	0.695	Halogen 0.19[a] W/cm^2	0.804
Mershin[8]	0.362	0.082	AM 1.5	0.287

[a]With 633 nm high pass filter

Chapter 5 Aerosolized-Droplet Mediated Self-Assembly of Photosynthetic Pigment Analogs and Deposition onto Substrates

The results reported in this chapter were published in - Shah, V. B.; Biswas, P. Aerosolized Droplet Mediated Self-Assembly of Photosynthetic Pigment Analogues and Deposition onto Substrates. ACS Nano 2014, 8, 1429-1438.

5.1 Abstract

Self-assembled photosynthetic molecules have a high extinction coefficient and a broad absorption in infrared region and these properties can be used to improve efficiency of solar cells. We have developed a single-step method for the self-assembly of synthetic chlorin molecules (analogs of native bacteriochlorophyll *c*) in aerosolized droplets, containing a single solvent and two solvents, to synthesize bio-mimetic light harvesting structures. In the single-solvent approach, assembly is promoted by a concentration driven process due to evaporation of the solvent. The peak absorbance of Zn(II) 3-(1-hydroxyethyl)-10-phenyl-13^1-oxophorbine (**1**) in methanol shifted from 646 nm to 725 nm (~80 nm shift) after assembly, which is comparable to the shift observed in naturally occurring assembly of bacteriochlorophyll *c*. Although assembly is thermodynamically favorable, the kinetics of self-assembly play an important role and this was demonstrated by varying the initial concentration of the pigment monomer. To overcome kinetic limitations, a two solvent approach using a volatile solvent (tetrahydrofuran) in which the dye is soluble and a less volatile solvent (ethanol) in which the dye is sparingly soluble, was demonstrated to be effective. The effect of molecular structure is demonstrated by spraying the sterically hindered Zn(II) 3-(1-hydroxyethyl)-10-mesityl-13^1-oxophorbine (**2**), which is an analog of **1**, under similar conditions. The results illustrate a valuable and facile aerosol based method for the formation of films of supramolecular assemblies.

Keywords: Supramolecular self-assembly, aerosol route, photosynthetic antenna, bacteriochlorophyll *c* analogs, chlorin.

5.2 Introduction

Self-assembled materials are gaining in importance due to their special properties and applications in different areas such as solar cells,[1, 2] photonics,[3, 4] organic semiconductors,[5, 6] recording media,[7] and development of biomaterials[8, 9]. Molecular self-assembly is used to synthesize new materials such as liquid crystals[10] and semi-crystalline and phase separated polymers[11]. Molecular self-assembly is defined as spontaneous assembly under equilibrium conditions to form stable aggregates; the process can entail formation of covalent[12] or non-covalent bonds.[13] Traditional synthetic procedures can be utilized to create reasonably large molecules, yet such structures typically lack order on the length scale (>10 nm) desired for many studies. On the other hand, self-assembly is attractive for formation of organized structures or molecular aggregates.[14] Molecular self-assembly takes place due to various non-covalent interactions such as van der Waals forces, hydrophobic forces, hydrogen bonds or π- orbital interactions. Molecular self-assembly is not restricted to organic materials but also can encompass inorganic materials such as polyions.[15]

Self-assembled aggregates often exhibit properties distinct from those of individual molecules. Both energy transfer and improved absorption in the near-infrared (NIR) region take place in chlorosomes, wherein bacteriochlorophyll (BChl) *c*, *d* and *e* molecules are assembled into large architectures. Chlorosomes, the light-harvesting antennas of green sulfur bacteria, serve to absorb light and funnel the resulting energy to a reaction center.[16] Efficient energy transfer takes place when individual molecules are close to each other and oriented for effective coupling of the respective transition dipole moments. The self-assembled aggregates in the chlorosomes satisfy these conditions for energy transfer. Indeed, green sulfur bacteria survive in low light conditions at 110 m below sea level by capturing and transferring the energy of all

incident photons.[17, 18] The electronic coupling of BChl *c* molecules to each other also results in a bathochromic shift in peak absorbance from 670 nm, which corresponds to Q_y band for monomers, to 749 nm for aggregates. Thus, self-assembled BChl molecules enable chlorosomes to harvest light in the NIR region of solar spectrum, which contains 26.4% of the total incident solar energy.

These special properties of light absorption and efficient energy transfer make self-assembled structures potentially attractive for applications in photovoltaics.[19] Improved performance was demonstrated when chlorosomes were incorporated in titanium dioxide based dye-sensitized solar cells.[20] In general, it is tedious to modify the native chlorosomes in size, composition, or other physicochemical attributes, to facilitate detailed experiments. Thus, there is interest in assembling synthetic analogs of the native BChls in an effort to mimic chlorosomes. BChls belongs to a class of molecules that show a characteristic bathochromically shifted absorption for aggregates, called J-aggregates (after the founder Jelley).[21] Among the various J-aggregates, derivatives of porphyrins and chlorins have been extensively studied because of their similarity to BChls and applications for harvesting solar energy. Tailored synthetic analogs also afford an opportunity, in principle, to tune the absorption spectrum to the area of interest in the solar spectrum.

Various chlorins[22-24] and porphyrins[25] have been assembled in solution and the effects of molecular structure and substituents have been studied extensively. Self-assembled aggregates of chromophores are formed by hydrophobic interactions,[26, 27] interaction with nonpolar solvents[28], evaporating solvent[19, 29] or dispersive halogen interactions[30]. The solution-based assembly of various tetrapyrrole macrocycles has been reviewed by Miyatake and Tamiaki.[31] One of the drawbacks of solution-based methods is the difficulty in controlling the final size of the

aggregate. In this regard, the rate of assembly is often faster than the time scale for mixing, making it difficult to control the growth of aggregates.[32] The size of the aggregate determines the spectral properties such as extinction coefficient and wavelength of absorption, which are critical for light harvesting. Hence controlling the size is important for the final application. One approach to control the size of aggregates entails formation as an emulsion using detergents[26] or using amphiphilic molecules[33]. However, in all such methods, transferring the aggregates to a surface is difficult. Since deposition on a surface is essential for numerous fundamental studies as well as device applications, evaporative self-assembly has been used to form self-assembled architectures by spin coating.[19, 29] This evaporative technique offers little or no control over the size of aggregates and is typically restricted to use with smooth surfaces. Other approaches rely on formation of Langmuir-Blodgett films[34] when amphiphilic molecules are available, or covalent chemical synthesis with building block chromophores via stepwise[35] or polymerization[36] methods.

Aerosol-based methods for synthesis are readily scalable and often entail only a single step fabrication process. This approach affords a number of advantages over most other methods of assembly. Particles formed after aerosolization can readily be deposited to form thin films. Moreover, using aerosol techniques, the contact of a solvent with the substrate can be avoided, thereby enabling deposition of multiple layers without the risk of washing out preceding layers.[20] The first work to attain nanostructured ordering using aerosols involved the synthesis of mesoporous silica particles by Brinker et al.[37] Since then, aerosol-based self-assembly has been widely used to synthesize mesoporous structures.[38-41] Although a wide range of mesoscopic structures has been synthesized by aerosol routes, to our knowledge, supramolecular self-assembly in aerosolized droplets has heretofore not been reported. Some mass spectrometric

studies demonstrate evidence of stable molecular aggregates formed by electrospray,[42, 43] but such aggregates have not been isolated or characterized by UV-visible absorption spectroscopy. Moreover, in order to use the aerosol technique, detailed understanding of the underlying mechanism of assembly is required.

Here, self-assembly is explored in aerosolized droplets with chlorin molecules 1 and 2 (Chart 5-1), which are analogs of natural photosynthetic dye bacteriochlorophyll *c*. Two different approaches, using a single solvent and two solvents, for molecular self-assembly in aerosolized droplets are examined. The underlying mechanism for assembly, which is different from spray drying, is also elucidated. The applicability of the method to assemble different types of molecules is demonstrated with both the single and two solvent approaches.

5.3 Methods

Various experimental techniques and characterization techniques used to assembled the dyes molecules in this work are summarized in following sections.

5.3.1 Spray Solution Composition and Characterization

The molecular structures of the dyes used in this work are shown in Chart 5-1. The dyes have a keto group, a hydroxyl group, and a metal center which are required for self-assembly.[22] The dye molecules were dissolved in either methanol or a mixture of ethanol and tetrahydrofuran (Et-THF). Anhydrous ethanol (200 proof from Sigma-Adrich, St. Louis, MO), THF (inhibitor free, Cromasolv ® plus, Sigma-Adrich), and methanol (Cromasolv ®, Simga-Adrich) were used for the experiments. On dissolution in solvent either methanol or Et-THF, these dyes show a characteristic Q_y absorption at 646 nm for **1** and 648 nm for **2**. The UV-visible absorption of the spray solution and the deposits is measured on a UV-visible spectrophotometer (Cary 100,

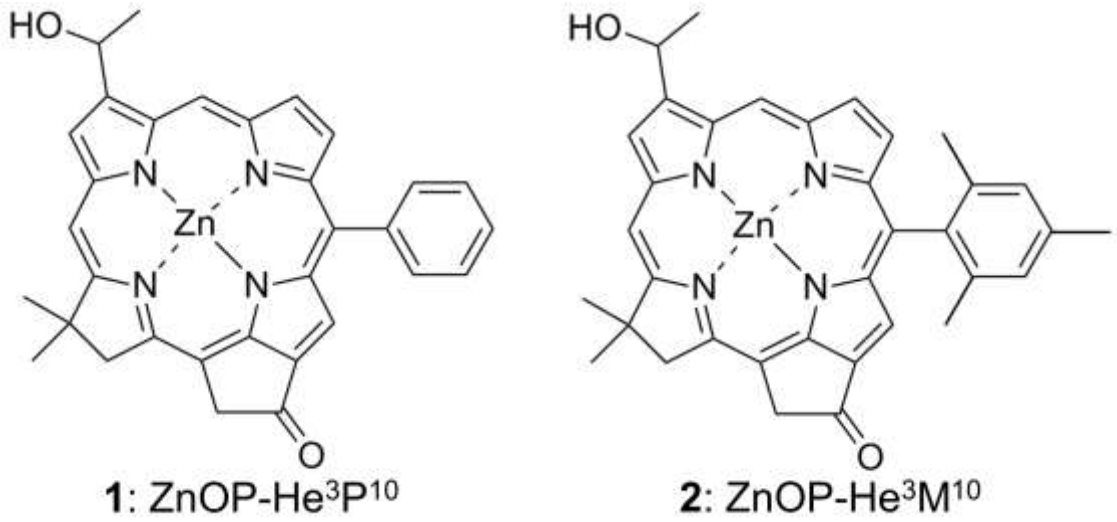

Chart 5-1: Molecular structure of Zinc chlorins (**1**, **2**), with self-assembling properties

Agilent Technologies, Santa Clara, CA). The absorbance of the dye molecules in solution at the Q_y band is converted to concentration using extinction coefficient (ε=74 $mM^{-1}cm^{-1}$) of the natural dye – Bacteriochlorphyll *c*. The dissolved dye molecules are present as monomers in the solution before spraying as evidenced by the absence of an aggregate peak in the absorption spectrum. Ammonium acetate is added to make the solution conducting for electrospray atomization and it also acts as a buffer. Conductivity of the spray solution is measured using a digital conductivity meter (Dip cell, Pt plate surface, Model 1054, Amber Science Inc., OR, USA). Since methanol is highly conducting, a lower ammonium acetate concentration of 5 mM employed for methanol compared to 10 mM for ethanol-THF.

5.3.2 Electrospray atomization

Figure 5–1 shows the schematic of a laboratory electrospray setup for synthesizing and depositing the self-assembled structures. The spray solution is pumped through a tapered needle with an inner diameter of 125 μm attached to a syringe. High voltage (4-4.5 kV) is applied between the needle and a grounded substrate to form a cone jet. The spray is delivered onto a

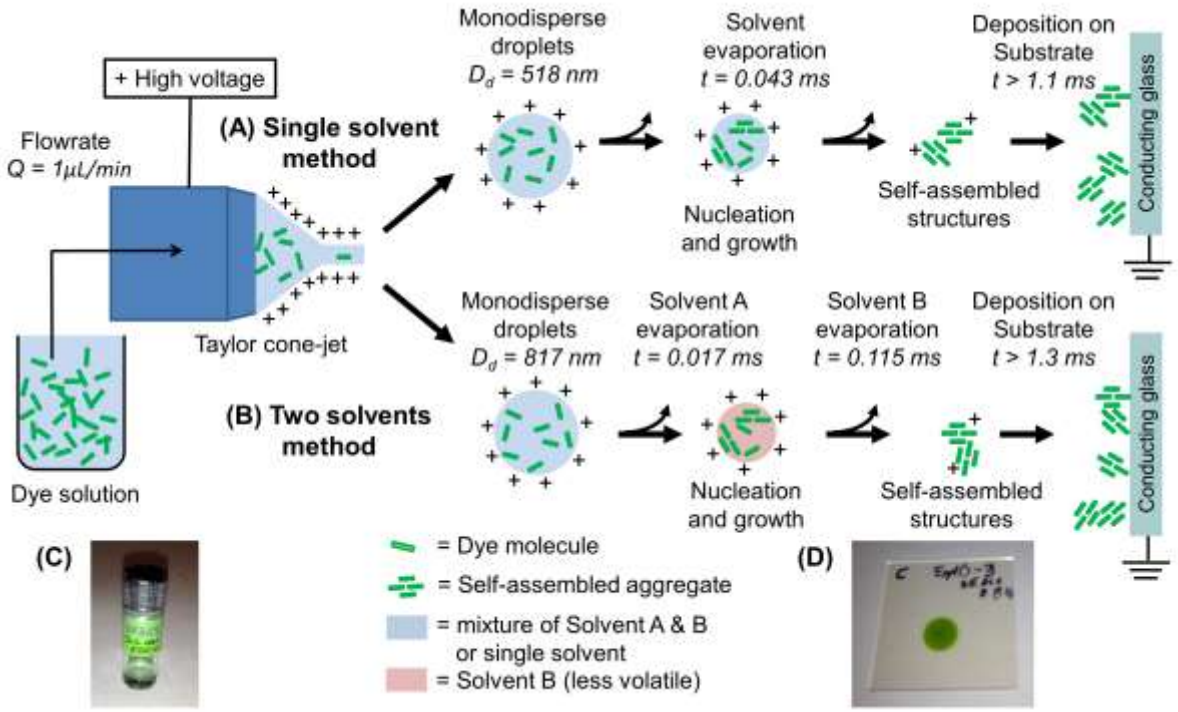

Figure 5–1: Schematic of the electrospray deposition system and proposed mechanisms for self-assembly of chlorin molecules in a droplet by (a) the single-solvent and (b) the two-solvent method in which solvent A is more volatile than solvent B. (c) Image of a spray solution of **1** prepared by dissolution in ethanol-THF. (d) Image of a conducting glass substrate after electrospray deposition of **1**.

substrate, transparent conducting fluorine doped tin oxide (FTO), placed at a distance of 10 mm from the tip of needle. The cone jet is visually monitored using a digital optical microscope (QX5, Digital Blue, Atlanta, GA, USA). The current is monitored with an ammeter (6485 Picoammeter, Keithley, Cleveland, OH) to ensure operation in cone jet mode. The scaling law equations are used to calculate the size of droplet sprayed based on the solution flow rate, conductivity and dielectric constant.[44, 45] Ammonium acetate decomposes and escapes into surrounding air before deposition of the dye molecules. Thus ammonium acetate does not hamper assembly.

5.3.3 Characterization of the deposit

The self-assembled structures are deposited on glass slides coated with fluorine doped tin oxide (FTO) to improve conductivity. After deposition, the slides are immediately characterized for the UV-vis absorption spectra.

5.4 Results and discussion

On aerosolizing a solution containing the dye molecules, a droplet with a known concentration (or number of monomers) is obtained. As the solvent evaporates, the concentration increases in the droplet, eventually reaching thermodynamically favorable conditions for self-assembly. By controlling the concentration of dye molecules in the solution, the location (or time) in flight at which self-assembly takes place can be varied. The nucleation rate is also an important parameter that determines whether self-assembly takes place before the solvent evaporates. The nucleation rate is a function of dye molecule concentration. The interplay of these various time scales is described in detail in the following sections.

The size of the assembled structures synthesized by the aerosol technique is hard to probe in-flight, because of short time scales (~1 ms) and small size of the self-assembled structures (<50 nm). Hence the self-assembled structures are characterized after deposition onto a substrate. Since the self-assembled structures are made up of organic molecules, imaging with TEM or characterization by X-Ray diffraction does not give insightful results. However, these photosynthetic molecules have a special property that the peak absorption of self-assembled structures shifts because of the excitonic interactions. These set of photosynthetic molecules whose absorption is red shifted on assembly are called J-aggregates. Hence the self-assembled structures and their size are analyzed by measuring the change in peak absorption by an UV-visible spectrophotometer.

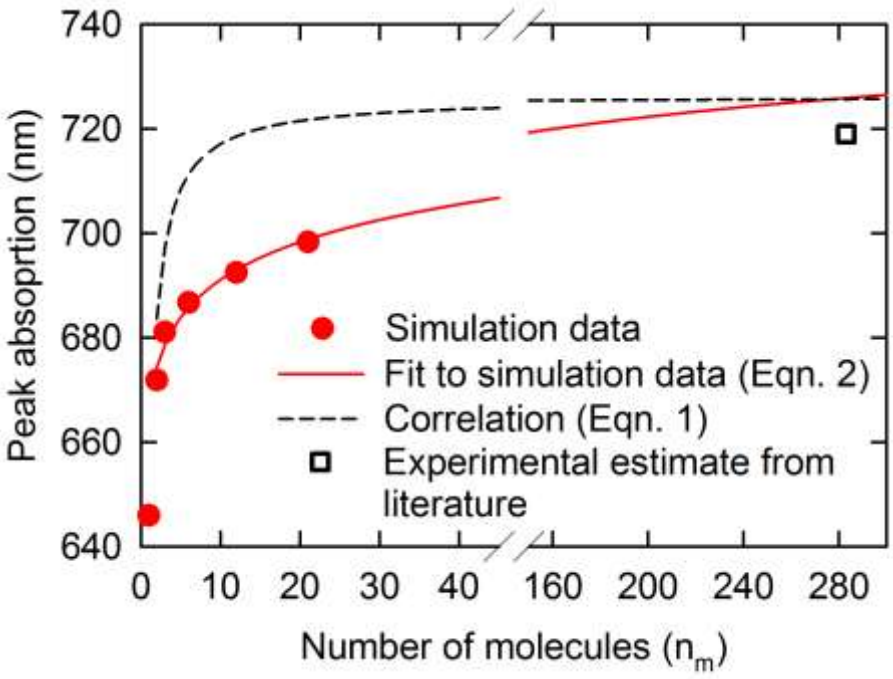

Figure 5–2: A comparison of the simulation data taken from Roden et. al.[48] to a simplistic correlation [Eqn. (5.1)] for change in peak absorption wavelength with increasing number of molecules present in the self-assembled structure. The experimental estimate is for chlorosomes of *Chloroflexus aurantiacus* which consists of self-assembled BChl *c* resulting in 73 nm shift in spectra.[47]

The shift in spectra as function of size is explained first as it is used to analyze the self-assembly results. A single solvent approach to assemble dye molecules is then discussed. To overcome the kinetic limitations of nucleation over a wider range of initial concentrations of dye molecules and to change the size of the self-assembled structure, a two solvent approach is then described. The detailed conditions for the experiments are listed in Table 5-1.

5.4.1 Shift in absorption spectra

There is a sharp shift in the absorption peak of the self-assembled molecules of J-aggregates in comparison to monomers due to excitonic interactions. It should be noted that a random aggregation that would result in an ordinary spray drying process will not result in the formation of J-aggregates. For these self-assembled structures, as the number of dye molecules increases, the peak absorption is more red-shifted as shown in Figure 5–2. However when large

number of molecules are present the shift gets saturated. The shift due to a large number of self-assembled molecules is commonly observed in J-aggregates. However there is limited experimental data for correlating size with a shift in peak absorption.[46] For linear one dimensional self-assembled aggregate with circular boundary conditions, the energy of electronic transition and the physical size are related[47]

$$\begin{aligned} & E_{n_m} = E_\infty - \left(E_\infty - E_1\right)/n_m \\ & \because E = hc/\lambda \\ & 1/\lambda_{n_m} = 1/\lambda_\infty - \left(1/\lambda_\infty - 1/\lambda_{n_m}\right)/n_m \end{aligned} \tag{5.1}$$

where, E_{n_m} is the transition energy of an aggregate consisting of n_m number of molecules, E_1 is the transition energy of an isolated molecule, and E_∞ is the transition energy of an infinite chain. The transition energy can be converted to peak absorption wavelength (λ) as a function of number of molecules and is shown in Figure 5–2. This equation is compared to simulation of absorption spectra by Roden et. al.[48] for linear chains of molecules with -0.15eV interaction potential at 0 K. Since the correlation fails to capture the shift at less number of molecules, hence the simulation data is used for analysis. The simulation data by Roden et. al.[48] is fitted with an equation to aid analysis when large number of molecules are present in self-assembled structure. The resulting equation for $n_m \geq 2$ is

$$\lambda_p = 10.41 ln\left(n_m\right) + 667.15 \tag{5.2}$$

where n_m is the number of molecules and λ_p is the peak absorption wavelength in nm. As shown in the figure, the correlation overestimates the shift compared to simulation. The shift in absorption given by equation (5.2) may be oversimplistic, however due to lack of knowledge of

the self-assembled structure of **1** or **2**, it is used to explain the results under the assumption that peak shifts remain the same at 293K, the temperature at which measurements are made.

For these molecules the shift is dependent on the interaction distance, orientation and dipole strength. A protein network or external factors would be required to force the interaction of dyes in different orientations apart from the thermodynamically favorable structures. Since there are no external factors, hence only one thermodynamically favorable structure is assumed to be formed using techniques described in this work.

5.4.2 Single solvent method

In the single solvent method, a dye is dissolved in methanol (solvent) and the solution is then atomized by electrospray. An electrospray atomization methodology is used because monodisperse droplets in the small sizes are readily produced. Furthermore, the droplets are charged and the charge is transferred to the self-assembled structures. These charged assembled structures are then readily deposited onto the substrate or desired surface using the electric field. After atomization, the solvent evaporates and the droplet is supersaturated with the dye molecules. This promotes nucleation into self-assembled structures as shown in Figure 5–1a. However there are certain conditions (lower initial concentrations) where the dye molecules do not assemble due to kinetic reasons. In order to study the kinetics in detail, the initial concentration of **1** in the spray-solution was varied from 8.8 μM to 20.2 μM . The kinetics of self-assembly is analyzed by comparing the time constants for evaporation, nucleation and the time available for nucleation. The time available for nucleation is the time to complete solvent evaporation after the droplet attains a critical saturation ratio.

Table 5-1: Properties of spray solution, electrospray conditions for the spray-solution and various properties of the sprayed droplet

Properties of spray solution					Electrospray conditions			Properties of sprayed droplets				
Solvent	Dielectric constant of spray solution	Dye concentration range	Concentration of ammonium acetate	Conductivity	Flowrate of spray solution	Voltage	Current	Mean droplet size[a]	95% interval for droplet size with σ_g=1.1[b]	Average number of dye molecules per droplet	Time of flight[c]	Evaporation time
	-	μM	mM	μS/cm	μL/min	kV	nA	nm	nm	-	ms	ms
Methanol	33±0.5	8.8-20.2	5	322±2	1±0.01	4.75	260	518±4	428 -626	1190	>1.38	0.043
Ethanol-THF (5:4)	15.7±1.0	13.5-43.9	10	53.4±0.4	1±0.01	4.3	130	817±21	675 - 988	4650	>1.10	0.115[d]

[a]Using scaling law equations.
[b]Geometric standard deviation for monodisperse droplet
[c]Assuming constant size of the droplet and charge. Actual times will be much larger than the ones estimated for constant size and charge.
[d]Using equation for scaling laws of electrosrpay and assuming Fuchs correction factor to be one. For ethanol-THF mixture sequential evaporation of solvents is assumed because THF is highly volatile. The heat transfer effects have been taken into account by using the equation for droplet cooling.[49]

Using the scaling laws for electrospray,[45, 50] the diameter of the droplet is estimated to be 518 nm. The size of the droplets decreases with time due to evaporation of the solvent. The time taken for complete evaporation of solvent (τ_e) is

$$\tau_e = \frac{R\rho_d d_i^{\,2} T_d}{8 D_v M p_d} \propto d_i^{\,2} \ , \tag{5.3}$$

where R is the universal gas constant, ρ_d is the density of the solvent, d_i is the initial droplet diameter, T_d is the temperature of the droplet, D_v is the diffusion coefficient of the vapor, M is the molecular weight, p_d is the partial pressure of the solvent vapors. Using this equation, the estimated time for evaporation of a methanol droplet of diamter 518 nm is 43 μs . The estimated time for the droplet to reach the substrate at a distance of 10 mm due to electrostatic force without evaporation is >1.3 ms. Hence the selected distance between the electrospray capillary needle and substrate ensures complete evaporation of the solvent before the dyes are deposited onto the substrate. Thus, the thermodynamic criteria of supersaturation is reached for all our selected experimental conditions (as the droplet evaporation time is much smaller than the transit time to the deposition substrate).

As the droplet shrinks in size due to evaporation, the concentration of the dye inside the droplet (c) increases with time. Beyond the equilibrium concentration (c_e), the solution gets supersaturated. The relation between the saturation ratio and droplet size is given as

$$S = \frac{c}{c_e} = \frac{c_i}{c_e}\frac{d_i^{\,3}}{d^3}, \tag{5.4}$$

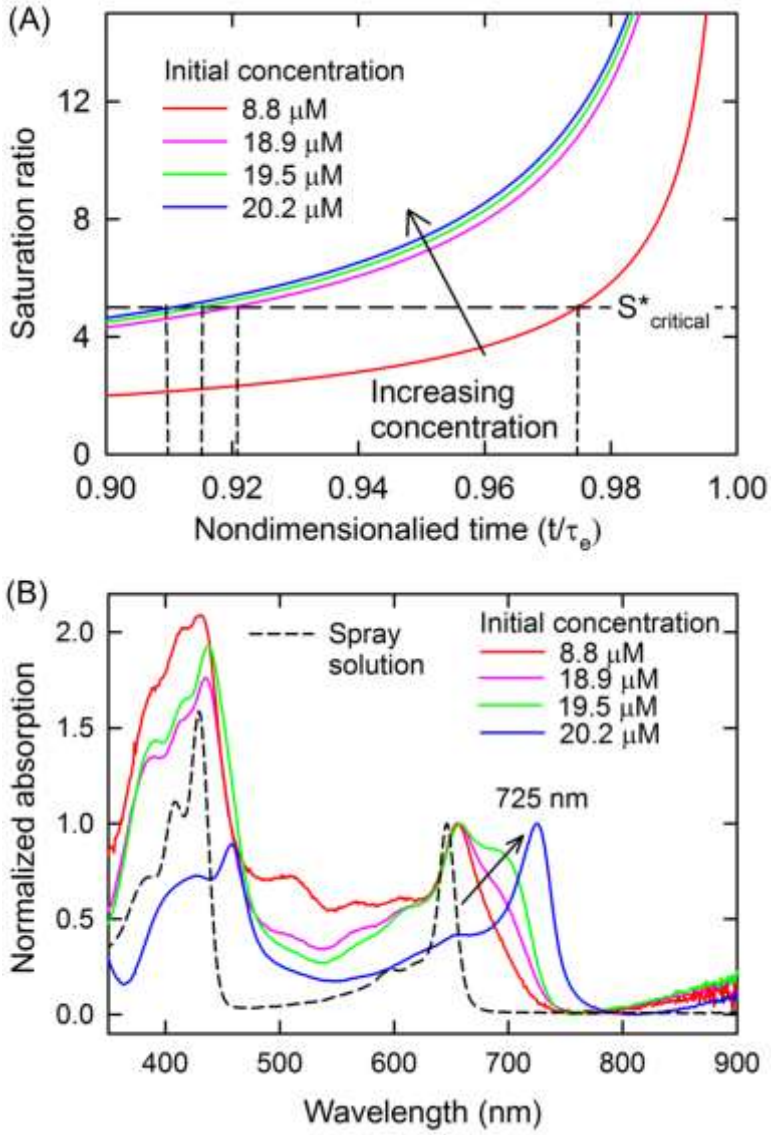

Figure 5–3: (a) Change in saturation ratio inside the evaporating droplet as a function of non-dimensionalized time (b) A comparison of the normalized UV-vis absorption spectrum after deposition at various initial concentration of **1** in spray solution (*colored solid lines*) to its spray solution in methanol (*black broken line*)

where c_i is the initial concentration, d_i is the initial diameter of the droplet and d is the droplet diameter at time t. The size of the evaporating droplet at any time using eqn. (5.3) is given as,

$$d(t)/d_i = (1 - t/\tau_e)^{1/2} \tag{5.5}$$

Using this expression, the saturation ratio inside the droplet as a function of time is given by

$$S = \frac{c_i}{c_e(1-t/\tau_e)^{3/2}} \ . \tag{5.6}$$

Figure 5–3a shows the variation of saturation ratio with time for different initial concentrations. Higher initial concentrations result in higher saturation ratios at any given time. As the solvent evaporates, resulting high saturation ratios promote nucleation of the dye molecules and separation of phases. The change in free energy for phase separation is given by,

$$\Delta G = 4\pi r^2\gamma + \frac{4}{3}\pi r^3 \Delta g_v \tag{5.7}$$

where γ is the surface energy, r is the radius of the assembled nuclei and Δg_v is the difference in free energy in assembled phase to monomers in solution. Δg_v is a function of saturation ratio (S) and is given by,

$$\Delta g_v = -\frac{kT \ln S}{\Omega} \tag{5.8}$$

where, k is the Boltzmann constant, T is the temperature and Ω is the molecular volume. When the saturation ratio is greater than one, Δg_v is negative. At saturation ratio (S) greater than the critical saturation ratio (S^*), the change in free energy will be negative and hence the nucleation into self-assembled structures will be favored. Critical saturation ratio (S*) is the value of S when the nucleation rate is greater than 1 nucleation/second inside the droplet. Thus irrespective of the initial concentration, thermodynamically, nucleation is expected to take place inside the droplets once the critical saturation ratio is exceeded. However this is contrary to some of the experimental observations. Figure 5–3b shows the effect of initial concentration on the absorption spectra of the deposited aggregates. The shift in peak absorption and the spectra

Table 5-2: Values of the constants for **1** for estimating the time delay for nucleation

Constant	Value
Molecular volume (v_0)	0.5×10^{-27} m^3
Surface energy (σ)	0.03 J/m^2
Diffusion coefficient (D)	1.00×10^{-9} m^2/s
Equilibrium solubility (c_e)	1.81×10^{22} $\#/m^3$
Saturation ratio (S)	40
Temperature[a] (T)	268 K
Delay time (τ_d)	35.9 μs

[a]Steady state temperature for evaporating droplet of methanol with diameter 518 nm

varies with the initial concentration, which means that assembly does not take place for all the cases. In order to understand the reasons, the kinetics of nucleation of self-assembled structures are analyzed.

The nucleation into self-assembled structure takes finite time after the critical saturation ratio is reached i.e. there is a delay before nucleation takes place. The delay time for nucleation (τ_d) is given by following equation[51],

$$t_d = \frac{32}{\pi^2} \frac{v_0 \sigma^2}{\gamma^* (kT)^2 D c_e S (\ln S)^3} \tag{5.9}$$

where v_0 is the molecular volume of dye, σ is the surface energy of the self-assembled material, γ^* is the accommodation coefficient in solution which is ~ 1, k is Boltzmann constant, T is the temperature, D is the monomer diffusion coefficient in the solvent , c_e is the equilibrium solubility and S is the saturation ratio. At a critical saturation ratio (S^*), the time delay for nucleation will be constant irrespective of the initial concentration. Assuming the values of parameters listed in Table 5-2 for **1**, the delay is estimated to be 35.9 μs . The estimated time

delay is of the order of evaporation time of solvent. t_d can be normalized by the evaporation time for the droplet to give a delay time constant

$$\tau_d = t_d / \tau_e \tag{5.10}$$

The dimensionless time available when S is greater than S* before the solvent completely evaporates is

$$\tau_a = t_a / \tau_e = 1 - t^* / \tau_e \tag{5.11}$$

where t^* is the time at which droplet reaches S^*. Thus for assembly to take place the delay time for nucleation should be less than the time available before the solvent from the droplet completely evaporates i.e. $\tau_d < \tau_a$. If the time available is less than the delay time for nucleation, the dyes will nucleate into clusters smaller than stable nuclei or result in random aggregation.

Since the exact value of c_e and other constants is not known, Figure 5–3a shows the qualitative relation between the delay in nucleation time and the time available for nucleation depending on the initial concentration. Figure 5–3b shows the experimental results for assembly with the change in initial concentration. The molecules at low concentration, corresponding to 8.8 μM, result in a 10 nm shift in the absorption peak which indicates the formation of unstructured (amorphous-like) aggregates without any long range order. Since at low concentration there is insignificant time for nucleation, random aggregation of the dye molecules takes place as evaporation proceeds to completion. This random agglomeration is similar to an uncontrolled spray drying process. On increasing the monomer concentration to 18.9 μM and 19.5 μM, the dyes give rise to intermediate size clusters resulting in a shoulder at 690–710 nm. The dyes at these concentrations reach the critical saturation ratio and form clusters. However

due to solvent evaporation their growth into stable nuclei is incomplete. On increasing the concentration to 20.2 μM, self-assembled structures give rise to a sharp, bathochromically shifted peak at 725 nm. As shown in the figure, in this case there is enough time for the monomers to nucleate into self-assembled structures since $\tau_a > \tau_d$. Thus to form self-assembled structures using single solvent assembly, the solvent should be selected such that $\tau_a > \tau_d$. Using a single solvent method, the saturation ratio cannot be changed independently of the droplet size (ref. equation (5.4)). Moreover, in the single solvent method the maximum concentration is limited by the solubility of the dye in the solvent. Hence for some molecules which require very high saturation ratio to assemble, the condition of $\tau_d < \tau_a$ may not be satisfied for certain droplet sizes.

5.4.3 Two Solvent Method

A two solvent combination is used to overcome the kinetic limitations and the dependence of saturation ratio on the droplet size for a single solvent. In the two solvents method, solvent A that easily dissolves the dye molecules is selected such that it is more volatile than solvent B in which the dye is sparingly soluble. Figure 5–1b shows the proposed mechanism for self-assembly with the two solvents. Tetrahydrofuran (THF) which dissolves the dye is selected as solvent A and ethanol (Et) in which the dye is sparingly soluble is selected as solvent B. THF being volatile evaporates first, supersaturating the ethanol droplets with the dye molecules. In this case, the solution is supersaturated due to evaporation of volatile solvent - THF. Hence the saturation ratio is dependent on the solvent composition and not on the droplet size. After the ethanol solution is supersaturated, the dye molecules nucleate into self-assembled structures. Over time ethanol completely evaporates and the charged aggregate of the dye is deposited on the substrate due to electrostatic force.

In the single solvent method, the dye is selected such that it is sparingly soluble, so that it will nucleate at high saturation ratio. In contrast, in the two solvent method the solvent in which the dye is highly soluble is mixed with the solvent in which the dye is sparingly soluble. Thus a higher initial concentration of dye in the spray solution can be attained, which is not possible with the single solvent method. A high initial concentration translates to a higher saturation ratio in the sprayed droplet after evaporation of the volatile solvent A (THF). The longer time available for nucleation due to lower volatility of ethanol and higher saturation ratio which ensures shorter delay time for nucleation, both help satisfy the condition $\tau_a > \tau_d$. Thus on using a two solvent method, the kinetic limitations to the assembly process are eliminated. Since there are no kinetic limitations and saturation ratio can be independently controlled, the size of self-assembled structure could be altered to change the absorbance spectra. In order to study the size dependence with supersaturation, experiments at different initial concentration from 13.5 to 43.9 μM in et-THF were conducted. The results for the size dependence of concentration were analyzed by the classical nucleation theory.

Mono-dispersed droplets of 817 nm diameter are electrosprayed. After the droplet is sprayed the solvents start evaporating. The estimated time for evaporation of ethanol-THF droplets of 817nm diameter is 115 μs . The time for evaporation is much shorter than >1.1ms taken to traverse the distance between needle and substrate without solvent evaporation. Thus the solvents evaporate before deposition. The volatile solvent THF evaporates first, supersaturating the ethanol solution. The saturation ratio can be expressed as

$$S = \frac{mc_i}{c_e} \ , \tag{5.12}$$

where m is the enhancement in concentration due to evaporation of solvent, c_i is the initial concentration and c_e is the equilibrium concentration. The dye molecules nucleate, after the saturation ratio crosses the critical value. Since there are two solvents, the solvent with lower volatility ensures sufficient time for nucleation and the nucleation is not limited by kinetics. The size of nuclei (d_p^*) by classical nucleation theory is given as,

$$d_p^* = \frac{4\sigma v_m}{kT \ln S}, \tag{5.13}$$

where σ is the surface energy, v_m is the molecular volume and S is the saturation ratio. Thus the number of molecules (n_m) in the nuclei is given by,

$$n_m = \frac{\pi}{6}\left(\frac{4\sigma v_m^{2/3}}{kT \ln S}\right)^3 \tag{5.14}$$

On varying the initial concentration in the spray solution, different saturation ratios can be attained. Substituting equation (5.12) in equation (5.14) gives the relation between number of molecules in the self-assembled structure and the initial concentration,

$$n_m = \frac{k_1}{\left(\ln c_i - \ln k_2\right)^3} \tag{5.15}$$

where $k_1 = \frac{\pi}{6}\left(\frac{4\sigma v_m^{2/3}}{kT}\right)^3$ and $k_2 = \frac{c_e}{m}$ are the new constants.

Figure 5–4a shows the shift in absorption spectra at various initial concentrations from 13.5 to 43.9 μM on the self-assembly of **1**. The peak shift for these concentrations and the

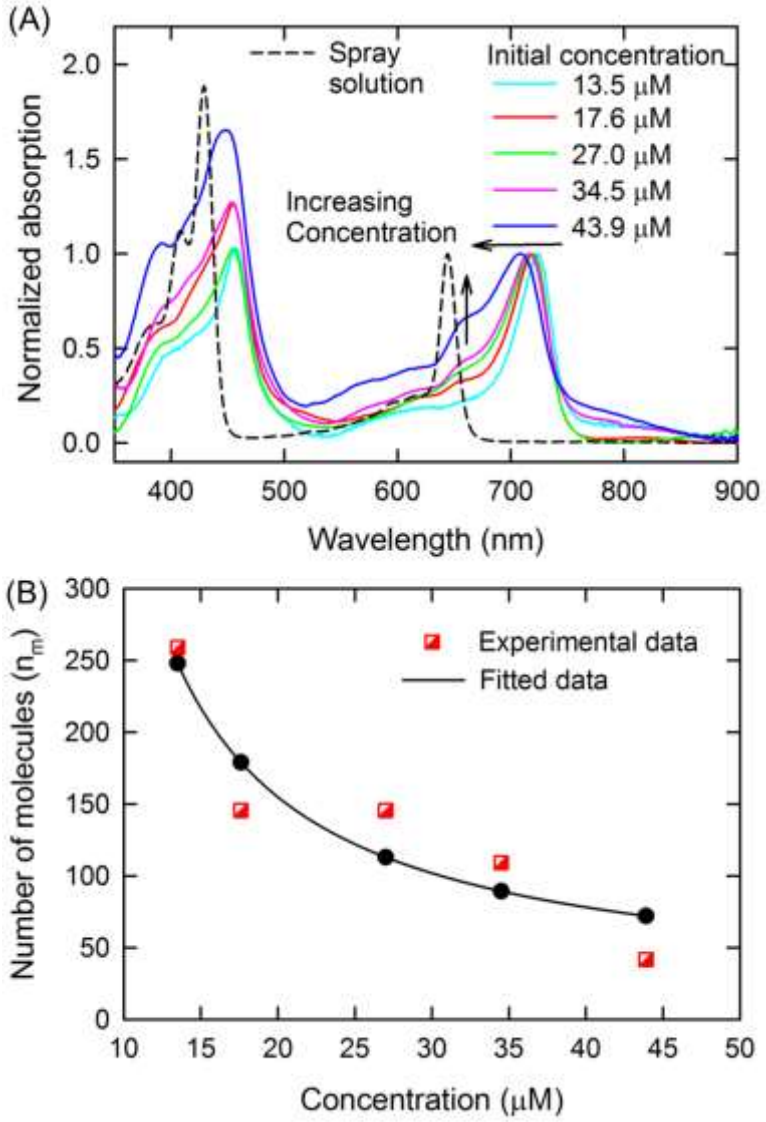

Figure 5–4: (a) A comparison of the normalized UV-vis absorption spectrum after deposition at various monomer concentration of **1** in spray solution (*colored solid lines*) compared to spray solution in ethanol-THF (*black broken line*) (b) The data for shift in absorption due to different initial concentrations summarized in Table 5-3 and the fitted curve after optimizing constants in eqn. (5.15)

number of molecules present in the self-assembled structure estimated using eqn. (5.2) are both summarized in Table 5-3. At the higher concentrations, the peak corresponding to the aggregate is less red-shifted, and at lower concentrations the aggregate peak is more red-shifted (bathochromically shifted). In order to establish a quantitative relationship between initial concentration and the number of molecules, equation (5.15) is a fit to the experimental data listed

in Table 5-3. Since the saturation ratio has to be greater than one, k_2 should be less than minimum initial concentration (<13.5 μM). The parameters k_1 and k_2 from equation (5.15) are

Table 5-3: Experimental results using two solvent method for the self-assembly of **1**

Concentration	Peak wavelength	Shift in absorption[a] (Δλ)	Number of molecules[b]
μM	nm	Nm	-
13.5	725	81	259
17.6	719	75	145
27	719	75	145
34.5	716	72	109
43.9	706	62	41

[a]Calculated for peak monomer absorption of **1** as 644 nm
[b]Calculated using the fitting equation (5.2) plotted in Figure 5–5

fitted using the *nlinfit* function in MATLAB® to the number of molecules and the initial concentration data in the table. As shown in Figure 5–4b, a good fit to the experimental data is obtained. The values obtained from fitting correspond to k_1 = 3079 ±2643 and k_2 = 1.33 ± 0.95. Using k_1 = 3079 and assuming the molecular volume to be ~0.5 nm^3, the estimated value of surface energy is 0.027 N/m. The surface energy is less than the values for the organic molecules reported in literature, which is in the range of 0.08-0.16 N/m. Lower than literature values for surface energy could be because the reported values are with respect to vacuum, however the molecules of **1** are in contact with ethanol. The other reason for lower estimate for surface energy could be due to heterogeneous nucleation at the air-liquid interface. Using k_2 the saturation ratios are estimated to be in range of 10.1 to 32.9, for the concentrations used in this study. The variation between the fitted data and the experimental data is due to possible differences in the shape of self-assembled structures or the simulated spectra. The number of molecules in each aggregate (Table 5-1) are less than the total dye molecules in each droplet (Table 5-3), thus implying that there are multiple centers of nucleation. This also clearly

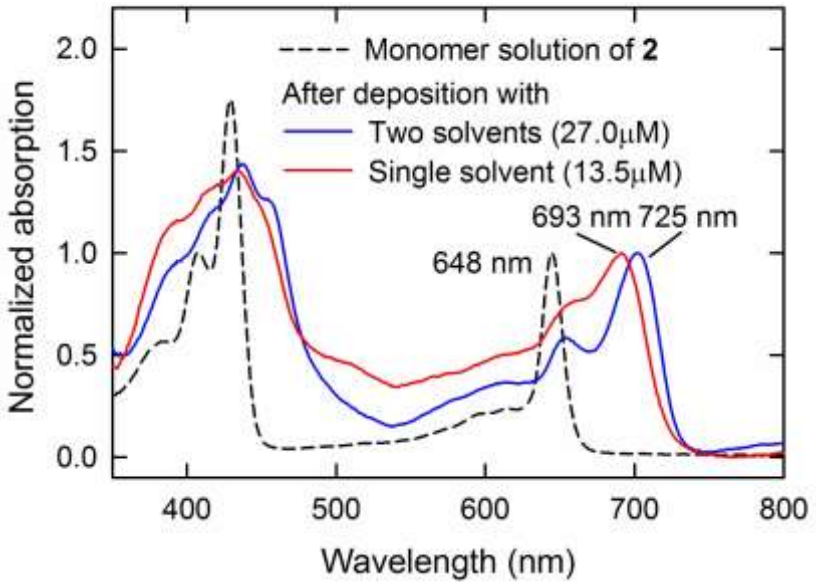

Figure 5–5: Self-assembly results using **2** which is analogous to **1** using single solvent and two solvent methods

illustrates that the self-assembly is different from purely spray drying which does not require any thermodynamic driving force and results in randomly oriented molecules.

Fig. 5 shows the spectra of the deposits sprayed at 13.5 μM concentration using methanol as solvent and 27.0 μM concentration using ethanol-THF as solvents. This molecule has similar characteristics to that of **1**, except for the substituent group. The shifts observed correspond to 693 nm for single solvent method and 725 nm for two solvent method, as shown in Fig. 5. Clearly, both the methods can be used to assemble **2**. Thus the aerosol based molecular assembly technique can be used for other self-assembling molecules.

5.5 Conclusions

Supramolecular assembly in an aerosolized droplet has been demonstrated for the first time in this work. Self assembly that resulted in formation of J-aggregates was successfully

promoted due to the strict control of droplet size using an electrohydrodynamic atomization process. By self-assembling bacteriochlorophyll *c* analogs, synthetic mimics of light harvesting antennas were synthesized and also deposited as films. This aerosol based method is a novel technique to synthesize and deposit self-assembled structures in one step. Using the aerosol technique, higher control over deposition and the size of the self-assembled structures can be exercised; in contrast to a simple spray drying process. In the single solvent method, although assembly is thermodynamically favored, kinetics of nucleation are important for eventual assembly. These kinetic limitations on the time available for assembly due to evaporation of the droplet in a single solvent method, can be overcome by using two solvents. On using two solvents, further control over the size of nuclei of the self-assembled structure was demonstrated. Similar control using solution based methods has not been possible because of difficulties in controlling nucleation which takes place on short time scales. The study of these two cases (single solvent and two solvent methods) suffices to explain most of the practical solvent combinations and their effects on the mechanism of assembly. The self-assembled structures, especially of porphyrin derivatives, can be used for a wide range of applications such as light harvesting in up conversion systems, solar cells and/or for synthesizing metal organic frameworks. A wide range of molecules so far assembled using solution techniques could be assembled and deposited with greater control using the aerosol technique.

5.6 Acknowledgments

This work was supported by the Photosynthetic Antenna Research Center (PARC), an Energy Frontier Research Center funded by the U.S. Department of Energy, Office of Science, Office of Basic Energy Sciences under Award Number DE-SC0001035. V. Shah thanks McDonnell International Scholars Academy for the fellowship to pursue Ph.D. at Washington

University in St. Louis. The authors thank Prof. Dewey Holten for stimulating discussions and Joseph Springer for help with spectroscopy and sample preparations. The authors also thank Prof. Jonathan Lindsey and Olga Mass, from North Carolina State University, for providing the *de novo* synthesized dye molecules.

5.7 References

1. Peet, J.; Heeger, A. J.; Bazan, G. C. "Plastic" Solar Cells: Self-Assembly of Bulk Heterojunction Nanomaterials by Spontaneous Phase Separation. *Acc. Chem. Res.* **2009**, *42*, 1700-1708.

2. Tange, R.; Inai, K.; Sagawa, T.; Yoshikawa, S. Application of Self-Assembling Photosynthetic Dye for Organic Photovoltaics. *J. Mater. Res.* **2011**, *26*, 306-310.

3. Fiorini, C.; Charra, F. Self-Assembly: Mastering Photonic Processes at Nanoscale. *Opto-Electronics Review* **2010**, *18*, 376-383.

4. Tam, J. M.; Tam, J. O.; Murthy, A.; Ingram, D. R.; Ma, L. L.; Travis, K.; Johnston, K. P.; Sokolov, K. V. Controlled Assembly of Biodegradable Plasmonic Nanoclusters for near-Infrared Imaging and Therapeutic Applications. *ACS Nano* **2010**, *4*, 2178-2184.

5. Kim, D. H.; Lee, D. Y.; Lee, H. S.; Lee, W. H.; Kim, Y. H.; Han, J. I.; Cho, K. High-Mobility Organic Transistors Based on Single-Crystalline Microribbons of Triisopropylisilylethynl Pentacene Via Solution-Phase Self-Assembly. *Adv. Mater.* **2007**, *19*, 678-682.

6. Palmer, R. E.; Robinson, A. P. G.; Guo, Q. How Nanoscience Translates into Technology: The Case of Self-Assembled Monolayers, Electron-Beam Writing, and Carbon Nanomembranes. *ACS Nano* **2013**, *7*, 6416-6421.

7. Lee, C.; Meteer, J.; Narayanan, V.; Kan, E. Self-Assembly of Metal Nanocrystals on Ultrathin Oxide for Nonvolatile Memory Applications. *J. Electron. Mater.* **2005**, *34*, 1-11.

8. Zhang, S. Fabrication of Novel Biomaterials through Molecular Self-Assembly. *Nat. Biotechnol.* **2003**, *21*, 1171-1178.

9. Hirose, T.; Maeno, Y.; Himeda, Y. Photocatalytic Carbon Dioxide Photoreduction by Co(Bpy)(3)(2+) Sensitized by Ru(Bpy)(3)(2+) Fixed to Cation Exchange Polymer. *Journal of Molecular Catalysis a-Chemical* **2003**, *193*, 27-32.

10. Schmidt-Mende, L.; Fechtenkotter, A.; Mullen, K.; Moons, E.; Friend, R. H.; MacKenzie, J. D. Self-Organized Discotic Liquid Crystals for High-Efficiency Organic Photovoltaics. *Science* **2001**, *293*, 1119-1122.

11. De Rosa, C.; Park, C.; Thomas, E. L.; Lotz, B. Microdomain Patterns from Directional Eutectic Solidification and Epitaxy. *Nature* **2000**, *405*, 433-437.

12. Lindsey, J. S. Self-Assembly in Synthetic Routes to Molecular Devices. Biological Principles and Chemical Perspectives: A Review. *New J. Chem.* **1991**, *15*, 153-180.

13. Whitesides, G. M.; Mathias, J. P.; Seto, C. T. Molecular Self-Assembly and Nanochemistry - a Chemical Strategy for the Synthesis of Nanostructures. *Science* **1991**, *254*, 1312-1319.

14. Whitesides, G. M.; Grzybowski, B. Self-Assembly at All Scales. *Science* **2002**, *295*, 2418-2421.

15. Miras, H. N.; Wilson, E. F.; Cronin, L. Unravelling the Complexities of Inorganic and Supramolecular Self-Assembly in Solution with Electrospray and Cryospray Mass Spectrometry. *Chem. Commun.* **2009**, 1297-1311.

16. Frigaard, N.-U.; Bryant, D., Chlorosomes: Antenna Organelles in Photosynthetic Green Bacteria. In *Complex Intracellular Structures in Prokaryotes*, Shively, J., Ed. Springer Berlin / Heidelberg: 2006; Vol. 2, pp 79-114.

17. Overmann, J.; Cypionka, H.; Pfennig, N. An Extremely Low-Light-Adapted Phototrophic Sulfur Bacterium from the Black-Sea. *Limnol. Oceanogr.* **1992**, *37*, 150-155.

18. Blankenship, R. E. *Molecular Mechanisms of Photosynthesis*. Blackwell Science: 2002.

19. Huijser, A.; Marek, P. L.; Savenije, T. J.; Siebbeles, L. D. A.; Scherer, T.; Hauschild, R.; Szmytkowski, J. d.; Kalt, H.; Hahn, H.; Balaban, T. S. Photosensitization of TiO_2 and SnO_2 by Artificial Self-Assembling Mimics of the Natural Chlorosomal Bacteriochlorophylls. *J. Phys. Chem. C* **2007**, *111*, 11726-11733.

20. Modesto-Lopez, L. B.; Thimsen, E. J.; Collins, A. M.; Blankenship, R. E.; Biswas, P. Electrospray-Assisted Characterization and Deposition of Chlorosomes to Fabricate a Biomimetic Light-Harvesting Device. *Energy Env. Sci.* **2010**, *3*, 216-222.

21. Jelley, E. E. Spectral Absorption and Fluorescence of Dyes in the Molecular State. *Nature* **1936**, *138*, 1009-1010.

22. Mass, O.; Pandithavidana, D. R.; Ptaszek, M.; Santiago, K.; Springer, J. W.; Jiao, J.; Tang, Q.; Kirmaier, C.; Bocian, D. F.; Holten, D.; Lindsey, J. S. De Novo Synthesis and Properties of Analogues of the Self-Assembling Chlorosomal Bacteriochlorophylls. *New J. Chem.* **2011**, *35*, 2671-2690.

23. Huber, V.; Katterle, M.; Lysetska, M.; Würthner, F. Reversible Self-Organization of Semisynthetic Zinc Chlorins into Well-Defined Rod Antennae. *Angew. Chem. Int. Ed.* **2005**, *44*, 3147-3151.

24. Roger, C.; Muller, M. G.; Lysetska, M.; Miloslavina, Y.; Holzwarth, A. R.; Wurthner, F. Efficient Energy Transfer from Peripheral Chromophores to the Self-Assembled Zinc Chlorin Rod Antenna: A Bioinspired Light-Harvesting System to Bridge the "Green Gap". *J. Am. Chem. Soc.* **2006**, *128*, 6542-6543.

25. Balaban, T. S. Tailoring Porphyrins and Chlorins for Self-Assembly in Biomimetic Artificial Antenna Systems. *Acc. Chem. Res.* **2005**, *38*, 612-623.

26. Miyatake, T.; Tamiaki, H.; Holzwarth, A. R.; Schaffner, K. Self-Assembly of Synthetic Zinc Chlorins in Aqueous Microheterogeneous Media to an Artificial Supramolecular Light-Harvesting Device. *Helv. Chim. Acta* **1999**, *82*, 797-810.

27. Shahar, C.; Baram, J.; Tidhar, Y.; Weissman, H.; Cohen, S. R.; Pinkas, I.; Rybtchinski, B. Self-Assembly of Light-Harvesting Crystalline Nanosheets in Aqueous Media. *ACS Nano* **2013**, *7*, 3547-56.

28. Miyatake, T.; Tamiaki, H.; Holzwarth, A. R.; Schaffner, K. Artificial Light-Harvesting Antennae: Singlet Excitation Energy Transfer from Zinc Chlorin Aggregate to Bacteriochlorin in Homogeneous Hexane Solution. *Photochem. Photobiol.* **1999**, *69*, 448-456.

29. Misawa, K.; Ono, H.; Minoshima, K.; Kobayashi, T. New Fabrication Method for Highly Oriented J-Aggregates Dispersed in Polymer-Films. *Appl. Phys. Lett.* **1993**, *63*, 577-579.

30. Mayerhoffer, U.; Wurthner, F. Halogen-Arene Interactions Assist in Self-Assembly of Dyes. *Angew. Chem.-Int. Edit.* **2012**, *51*, 5615-5619.

31. Miyatake, T.; Tamiaki, H. Self-Aggregates of Natural Chlorophylls and Their Synthetic Analogues in Aqueous Media for Making Light-Harvesting Systems. *Coord. Chem. Rev.* **2010**, *254*, 2593-2602.

32. Horn, D.; Rieger, J. Organic Nanoparticles in the Aqueous Phase—Theory, Experiment, and Use. *Angew. Chem. Int. Ed.* **2001**, *40*, 4330-4361.

33. Numata, M.; Kinoshita, D.; Taniguchi, N.; Tamiaki, H.; Ohta, A. Self-Assembly of Amphiphilic Molecules in Droplet Compartments: An Approach toward Discrete Submicrometer-Sized One-Dimensional Structures. *Angew. Chem. Int. Ed.* **2012**, *51*, 1844-1848.

34. Mobius, D.; Kuhn, H. Energy-Transfer in Monolayers with Cyanine Dye Sheibe Aggregates. *J. Appl. Phys.* **1988**, *64*, 5138-5141.

35. Jiao, J.; Anariba, F.; Tiznado, H.; Schmidt, I.; Lindsey, J. S.; Zaera, F.; Bocian, D. F. Stepwise Formation and Characterization of Covalently Linked Multiporphyrin-Imide Architectures on Si(100). *J. Am. Chem. Soc.* **2006**, *128*, 6965-6974.

36. Liu, Z.; Schmidt, I.; Thamyongkit, P.; Loewe, R. S.; Syomin, D.; Diers, J. R.; Zhao, Q.; Misra, V.; Lindsey, J. S.; Bocian, D. F. Synthesis and Film-Forming Properties of Ethynylporphyrins. *Chem. Mater.* **2005**, *17*, 3728-3742.

37. Lu, Y. F.; Fan, H. Y.; Stump, A.; Ward, T. L.; Rieker, T.; Brinker, C. J. Aerosol-Assisted Self-Assembly of Mesostructured Spherical Nanoparticles. *Nature* **1999**, *398*, 223-226.

38. Moon, J. H.; Yi, G. R.; Yang, S. M.; Pine, D. J.; Bin Park, S. Electrospray-Assisted Fabrication of Uniform Photonic Balls. *Adv. Mater.* **2004**, *16*, 605-609.

39. Lee, S. Y.; Gradon, L.; Janeczko, S.; Iskandar, F.; Okuyama, K. Formation of Highly Ordered Nanostructures by Drying Micrometer Colloidal Droplets. *ACS Nano* **2010**, *4*, 4717-4724.

40. Wang, W. N.; Park, J.; Biswas, P. Rapid Synthesis of Nanostructured Cu-TiO_2-SiO_2 Composites for CO_2 Photoreduction by Evaporation Driven Self-Assembly. *Catal. Sci. Technol.* **2011**, *1*, 593-600.

41. Wu, C.; Lee, D.; Zachariah, M. R. Aerosol-Based Self-Assembly of Nanoparticles into Solid or Hollow Mesospheres. *Langmuir* **2010**, *26*, 4327-4330.

42. Langley, G. J.; Hecquet, E.; Morris, I. P.; Hamilton, D. G. Direct Observation of Associative Behaviour by Electrospray Ionization: Self-Assembly - Fact or Fiction? *Rapid Commun. Mass Spectrom.* **1997**, *11*, 165-170.

43. Alcalde, E.; Mesquida, N.; Fernandez, I.; Giralt, E. Novel Charged 1(4) Azolophanes: Associative Behaviour Revealed by Electrospray Ionization. *Rapid Commun. Mass Spectrom.* **2000**, *14*, 1014-1016.

44. Chen, D. R.; Pui, D. Y. H.; Kaufman, S. L. Electrospraying of Conducting Liquids for Monodisperse Aerosol Generation in the 4 nm to 1.8 μm Range. *J. Aerosol Sci.* **1995**, *26*, 963-978.

45. Basak, S.; Chen, D. R.; Biswas, P. Electrospray of Ionic Precursor Solutions to Synthesize Iron Oxide Nanoparticles: Modified Scaling Law. *Chem. Eng. Sci.* **2007**, *62*, 1263-1268.

46. Novoderezhkin, V.; Taisova, A.; Fetisova, Z. G. Unit Building Block of the Oligomeric Chlorosomal Antenna of the Green Photosynthetic Bacterium Chloroflexus Aurantiacus: Modeling of Nonlinear Optical Spectra. *Chem. Phys. Lett.* **2001**, *335*, 234-240.

47. Muenter, A. A.; Brumbaugh, D. V.; Apolito, J.; Horn, L. A.; Spano, F. C.; Mukamel, S. Size Dependence of Excited-State Dynamics for J-Aggregates at Silver Bromide Interfaces. *J. Phys. Chem.* **1992**, *96*, 2783-2790.

48. Roden, J.; Strunz, W. T.; Eisfeld, A. Spectral Properties of Molecular Oligomers. A Non-Markovian Quantum State Diffusion Approach. *Int. J. Mod Phys B* **2010**, *24*, 5060-5067.

49. Hinds, W. C. *Aerosol Technology: Properties, Behavior, and Measurement of Airborne Particles*. Second edition ed.; John Wiley & Sons, Inc.: New York, 1999.

50. Chen, D.-R.; Pui, D. Y. H. Experimental Investigation of Scaling Laws for Electrospraying: Dielectric Constant Effect. *Aerosol Sci. Technol.* **1997**, *27*, 367-380.

51. Kashchiev, D. *Nucleation*. Elsevier Science: 2000.

Chapter 6 Supramolecular self-assembly of BChl *c* molecules in aerosolized droplets to synthesize biomimetic chlorosomes

To be submitted to Langmuir, September, 2014

6.1 Abstract

Unique properties of chlorosomes, arising out of the self-assembled BChl *c* structure, have made them attractive for use in solar cells. In this work, we have demonstrated the self-assembly of BChl *c* in aerosolized droplets to mimic naturally occurring chlorosomes, and deposited them. We compare results for two different techniques, one using a single-solvent and the other using two-solvent, and demonstrate the superiority of the two-solvent technique. Results showed that the self-assembled BChl *c* fluoresced at 780 nm, even when solutions with different initial concentration were sprayed. The assembly of BChl *c* in the presence of lipids and carotenes was found to encourage assembly of BChl *c*. The absorption peak was at 750 nm and the fluorescence peak was at 790 nm, which were both red shifted in comparison to cases where lipids and carotenes were not present. Finally the deposited films were characterized by grazing incidence small-angle X-ray scattering (GISAXS) and the 2D X-ray scattering pattern of the mimics sample clearly indicated the distinct lamellar structure found in chlorosomes. GISAXS particle size fitting analysis suggested that the film was composed of nanometer sized particles, confirming our hypothesis that the self-assembled structures formed in flight after solvent evaporation from the sprayed droplets. The results of this work provide additional insight into self-assembly in aerosolized droplets, which can be used for assembling a wide range of molecules.

Keywords:

Self-assembly, Bacteriochlorophyll c, electrospray atomization, chlorosome

6.2 Introduction

Chlorosomes, present in green sulphur bacteria, are one of the biggest and most efficient light harvesting antennas in nature. Chlorosomes consist of self-assembled dye molecules (Bacteriochlorophyll (BChl) *c/d/e*). They have minimal or no protein network,[1, 2] and hence have the highest dye density among natural light-harvesting complexes. Self-assembled structures contain other molecules, such as carotenoids, for photo-protection. Carotenoids also extend the absorption spectrum by absorbing light in the visible region and transferring energy to BChl *c*. The light energy absorbed by self-assembled dye molecules is transferred to a baseplate and then to the Fenna-Mathew-Olson protein complex by the Foster resonance energy transfer process. Thus chlorosomes, which are made up of BChl *c* molecules, can capture almost all incident photons and transfer excitons efficiently to the baseplate and subsequently to a reaction center.[3]

Self-assembled structures, unlike bulk materials which are only realized by covalent or ionic bond synthesis, have different properties. For example, the self-assembled BChl c in chlorosomes results in a red-shift in the absorption peak, allowing bacteria to absorb in the NIR region. Moreover, the energy absorbed is delocalized over the self-assembled structure, and hence can be transferred to the baseplate. Thus for chlorosomes to function, it is essential that BChl *c* be self-assembled. These properties of chlorosomes make them attractive for extending the absorption spectrum in dye sensitized solar cells. Chlorosomes extracted from naturally occurring organisms have been used as antennas for solar cells to improve their light absorption and efficiency.[4] However the natural light-harvesting antennas cannot be easily tuned with respect to their size, absorption spectra or composition. In addition, it is cumbersome to extract the light-harvesting antennas from living organisms. In order to control the size, absorption

spectra and composition of the chlorosomes, mimics need to be synthesized. Moreover self-assembled aggregates are of interest for biomimetic solar cells.[5, 6]

Self-assembled structures of various dyes have been synthesized and studied, yet BChl c is of interest because of its peculiar properties. A wide range of research has focused on fabricating synthetic self-assembled BChl *c* agglomerates to form mimics of chlorosomes.[7-13] Most of these works use either organic solvents[12, 13] or aqueous solutions.[8, 9, 11] Although there are a wide range of solution based techniques, aerosol based methods have not been used for supramolecular self-assembly of BChl *c*. Assembly of bacteriochlorophyll analogs was demonstrated in aerosolized droplets for the first time by Shah and Biswas.[14] However, the BChl *c* molecule is much larger than the bacteriochlorophyll analogues due to the long hydrocarbon tail, and it is not clear how these steric factors will affect assembly. Moreover, in comparison to synthetic analogs, naturally occurring BChl *c* and their self-assembled structures have been extremely well characterized. Thus, it should be feasible to analyze BChl *c* assembled via aerosol technique and compare it with material fabricated by using solvents. In addition, there are limited studies examining the effect of carotenoids and lipids on the self-assembly process,[15] although self-assembled BChl *c* is present along with carotenoids and lipids in chlorosomes.

The overall objective of this work is to assemble BChl *c* using an aerosol-based technique to mimic chlorosomes and to understand various factors that affect assembly in the droplet. First, the effect of droplet size and concentration on assembly is analyzed. Second, single-solvent and two-solvent techniques for assembly with electrospray are compared. Third, the assembly of BChl *c* in presence of other molecules, such as lipids and carotenes, is demonstrated. Finally, the grazing incidence small angle scattering results for the self-assembled structure are presented.

6.3 Methods

6.3.1 Extraction and purification of pure BChl *c*

The green sulphur bacterium *Chlorobaculum tepidum* was grown anaerobically and photoautotrophically at 40 °C for 3 days in a 13 L carboy irradiated with incandescent bulbs with a total photon flux of 100 μmol-$m^{-2}s^{-1}$. The liquid growth medium has been described previously.[16] Cells were harvested via centrifugation at 6,000 × g for 15 minutes. To facilitate faster purification of pigment, whole cells were used instead of isolated photosynthetic complexes. In a 50 mL Corning tube, 5 g of wet-packed cells were broken via the addition of 20 mL of a HPLC-grade 7:2 acetone-methanol mixture and thorough vortexing. The solution was then centrifuged at 6,000 × g for 15 minutes. The clear, green supernatant was removed and dried under a gentle stream of nitrogen gas. The dry green film was re-dissolved in 500 μL of HPLC-grade methanol. 100 μL aliquots were injected into an Agilent 1100 series HPLC equipped with an Agilent Zorbax C-18 reverse-phase analytical column equilibrated at 20 °C. The elution was performed using a static solvent mixture of HPLC-grade 60:36:4 acetonitrile-methanol-tetrahydrofuran pumped at 1.5 mL min^{-1}. The four main BChl *c* peaks (corresponding to pigments with identical absorption spectra, differing only in the alkyl substituents at the C-8 and C-12 positions) were collected, pooled, and dried under a gentle stream of nitrogen gas.[17]

6.3.2 Solution preparation for BChl *c*

BChl *c* has a keto group, a hydroxyl group, and a metal center, all of which are required for self-assembly.[18] The dried BChl *c* was dissolved in either methanol or ethanol:methanol solution (1:1 v/v). Anhydrous ethanol (200 proof, Sigma-Adrich, St. Louis, MO) and methanol (Cromasolv ®, Simga-Adrich) were used for the experiments. When dissolved in solvent, either methanol or methanol-ethanol, these dyes show a characteristic Q_y absorption at 667 nm. The UV-visible absorption of the spray solution and the deposits was measured on a UV-visible

spectrophotometer (Cary 100, Agilent Technologies, Santa Clara, CA). The absorbance of the dye molecules in solution at the Q_y band was converted to concentration using the extinction coefficient (ε=74 $mM^{-1}cm^{-1}$) of BChl *c*. The dissolved dye molecules were present as monomers in the solution before spraying, as evidenced by the absence of an aggregate peak in the absorption spectrum. Ammonium acetate was added to make the solution conductive for electrospray atomization. Conductivity of the spray solution is measured using a digital conductivity meter (Dip cell, Pt plate surface, Model 1054, Amber Science Inc., OR, USA). The conductivity of the solution was adjusted by adding ammonium acetate. In order to maintain the same droplet size, 5mM Ammonium acetate was used in Methanol and 8mM ammonium acetate was used for solution in ethanol:methanol to adjust conductivities.

6.3.3 Crude BChl *c* purification

A 'crude' BChl *c* solution containing most of the important chlorosome components was produced, starting with purified chlorosome antenna complexes instead of whole cells. The chlorosomes were purified using a previous method.[9] The purified chlorosome solution was ultracentrifuged at 266,000 × g for 2 hr, and the aqueous supernatant was discarded. The chlorosomes were disrupted and dissolved by adding 20 mL of HPLC-grade 7:2 acetone-methanol to the pellet, followed by thorough vortexing. The solution was then dried under a gentle stream of nitrogen. Using purified chlorosomes as a starting material ensured that the remaining dry film contained only chlorosome pigments (including BChl *c*, BChl *a*, chlorobactene, and β-carotene) and chlorosome lipids.

6.3.4 Electrospray Atomization

Figure 6–1 is a schematic of the laboratory electrospray setup for synthesizing and depositing the self-assembled structures. The spray solution is pumped through a tapered needle

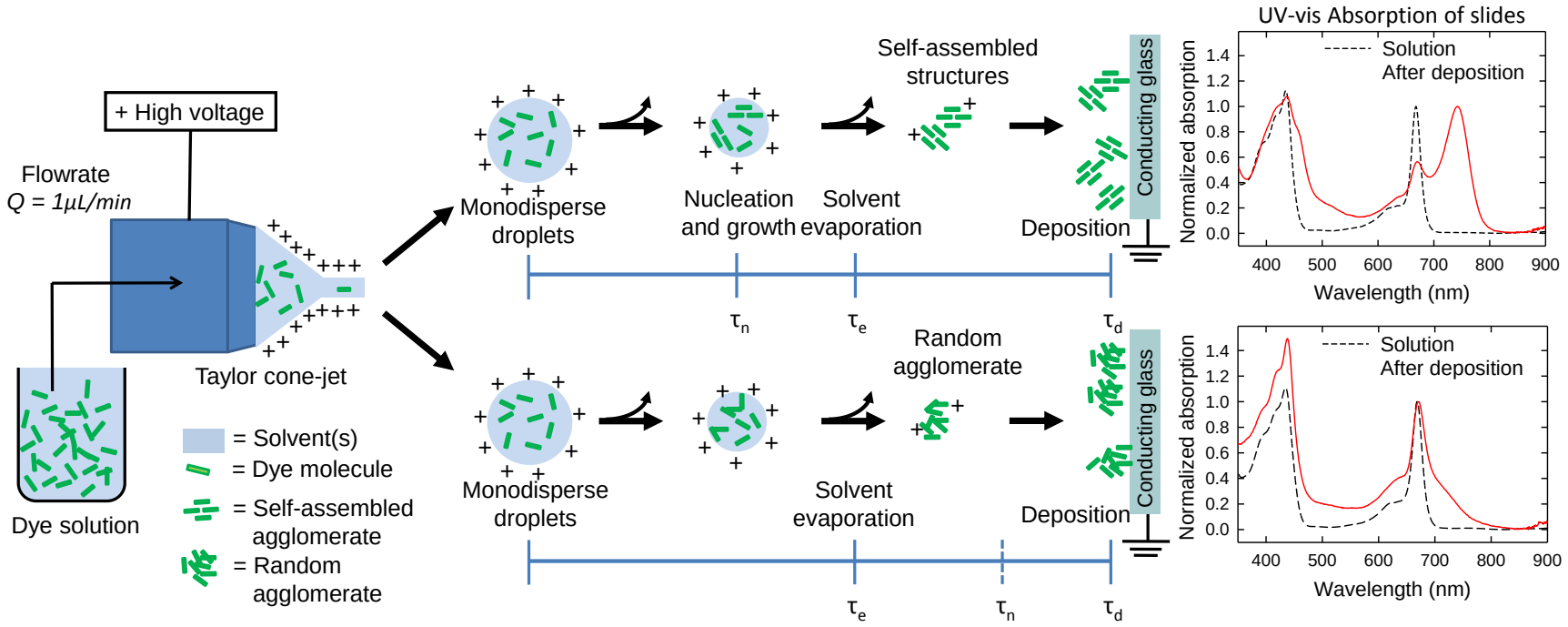

Figure 6–1: Two extreme cases, complete assembly and no assembly, arising when BChl *c* solution is electrosprayed

with an inner diameter of 125 μm, attached to a syringe. High voltage (4-4.5 kV) is applied between the needle and a grounded substrate to form a cone jet. The spray is delivered onto a substrate of transparent conducting fluorine doped tin oxide (FTO) placed 10 mm from the tip of the needle. The cone jet is visually monitored using a digital optical microscope (QX5, Digital Blue, Atlanta, GA, USA). The current is monitored with an ammeter (6485 Picoammeter, Keithley, Cleveland, OH) to ensure operation in cone jet mode. The scaling law equations are used to calculate the size of sprayed droplet, based on the solution flow rate, conductivity and dielectric constant.[19, 20] Ammonium acetate decomposes and escapes into surrounding air before deposition of the dye molecules, so ammonium acetate does not hamper assembly. Table 6-1 lists the detailed conditions for electrospray deposition.

6.3.5 Characterization of the Deposit

The self-assembled structures were deposited on to FTO slides. After deposition, the UV-vis absorption spectra of the slides were measured. Fluorescence emission spectra were obtained in a manner similar to that used by Modesto-Lopez et al.[4] A custom fluorometer setup was employed (Photon Technology International, NJ), consisting of a Xe excitation lamp, excitation monochromator, emission monochromator, signal chopper, lock-in amplifier and avalanche photodiode detector. FTO slides containing electrospray-deposited self-assemblies were mounted using a custom slide holder in the sample compartment at a 45-60° angle to the incident light to maximize the absorption cross-section. Bandpass and long-pass filters eliminated second-order diffraction and scattering from the FTO slide. BChl *c* samples were excited using 430 nm light, while the crude BChl *c* (with carotenes and lipids) samples were excited by 400, 440 and 550 nm light. Comparison of absolute fluorescence efficiency could not be accomplished due to the

Table 6-1: Electrospray deposition conditions

Properties of spray solution					Electrospray conditions			Properties of sprayed droplets				
Solvent	Dielectric constant of spray solution	Dye concentration range	Concentration of ammonium acetate	Conductivity	Flowrate of spray solution	Voltage	Current	Mean droplet size[a]	95% interval for droplet size with σ_g=1.1[b]	Average number of dye molecules per droplet	Time of flight[c]	Evaporation time
	-	μM	mM	μS/cm	μL/min	kV	nA	nm	nm	-	ms	ms
Methanol	33±0.5	8.8-20.2	5	322±2	1±0.01	4.75	260	518±4	428 -626	1190	>1.38	0.043
Ethanol-THF (5:4)	15.7±1.0	13.5-43.9	10	53.4±0.4	1±0.01	4.3	130	817±21	675 - 988	4650	>1.10	0.115[d]

[a]Using scaling law equations.
[b]Geometric standard deviation for monodisperse droplet
[c]Assuming constant size of the droplet and charge. Actual times will be much larger than the ones estimated for constant size and charge.
[d]Using equation for scaling laws of electrosrpay and assuming Fuchs correction factor to be one. For ethanol-THF mixture sequential evaporation of solvents is assumed because THF is highly volatile. The heat transfer effects have been taken into account by using the equation for droplet cooling.[21]

variability of slide orientation during measurement and differences in deposition areas across samples.

6.3.6 Grazing Incidence Small Angle Scattering experiments

Single crystal silicon substrates with electrospray deposited BChl *c* films were mounted on the sample stage at APS Sector 12-ID-B, Argonne National Labs. X-ray energy of 14 keV and a sample-to-detector distance of 2 m was used to detect the films. A range of X-ray incidence angles were tested to optimize the GISAXS scattering signal for various deposition times and subsequent layer thicknesses. For an electrospray deposition time of 20 min, an incidence angle of 0.12° was selected as the best scattering angle. All data analysis was performed with the Igor Pro® program (V. 6.34A, WaveMetrics, Inc., Oregon). To analyze the 2D GISAXS data, horizontal line-cuts were made along the in-plane direction of either the Yoneda wing or the strong scattering signal, attributed to the silicon substrate surface. Data reduction was performed using the GISAXShop v4.5 macro made available at APS Sector 12-ID-B. The GISAXS particle size evolution in each sample was obtained by fitting the reduced 1D images with the polydisperse sphere model and Schultz size distribution function, which includes a structure factor for particle interactions. In addition to horizontal line-cuts used for analyzing the BChl *c* aggregate size, out-of-plane GISAXS vertical line-cuts were also made at $2\theta_f = 0.25°$.

6.4 Results and discussion

This work utilizes electrospray atomization and deposition to synthesize self-assembled structures of BChl *c*. BChl *c* dissolved in a solvent or a combination of solvents is electrosprayed to form monodisperse droplets. Figure 6–1 shows the two extreme possibilities arising from spraying a solution of BChl *c*: complete assembly or no assembly. The assembly of the dyes,

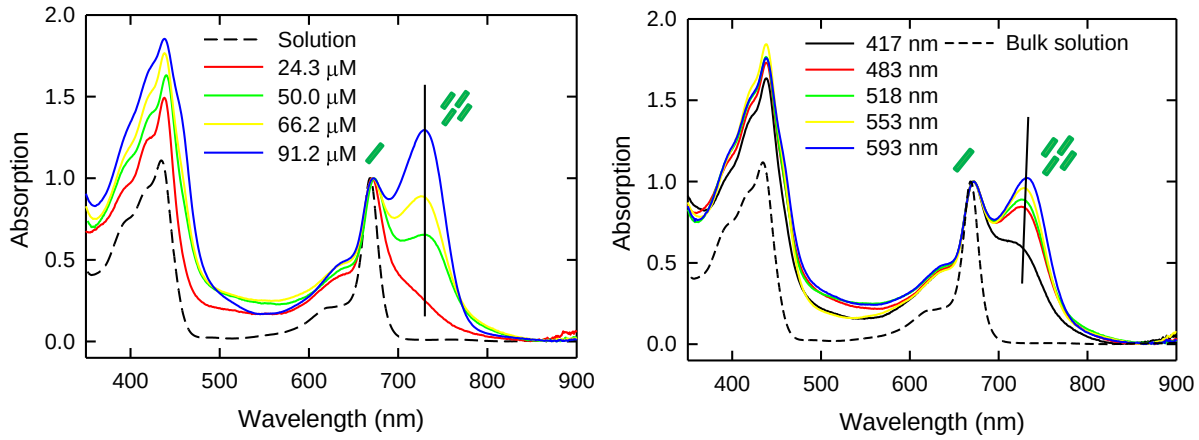

Figure 6–2: (a) The effect of different initial concentrations on the assembly and (b) the effect of droplet size on assembly. Increasing concentration or droplet size has a similar effect on assembly of BChl *c* molecules

although thermodynamically favorable, depends on time delay for nucleation (τ_n).[14] If there is enough time for nucleation, i.e. the droplet doesn't evaporate, which depends on the properties of the dye and solvent, the dye molecules will assemble. When the dye molecules assemble, the UV-vis absorption peak of the self-assembled structure shifts, which is not the case for molecules that have not assembled. The characteristic shift in UV-visible absorption on assembly has been used to analyze BChl *c* deposits. Although self-assembly with a single solvent and two solvents have been demonstrated by Shah and Biswas,[22] this work gives a robust analysis for self-assembly by comparing the effect of droplet size and demonstrating the benefits of using two solvents over a single solvent. First, we present the results for assembly of BChl *c* with a single solvent, then make a detailed comparison for the effect of droplet size and initial concentration on assembly with single solvent methanol. The results for assembly with single-solvent technique are compared with a two solvent technique for the same concentration range and droplet size. The results for BChl *c* assembly in the presence of various chlorosomal molecules are also described. Finally, to prove that the assembly takes place in droplets and to analyze the self-assembled structure, the film was characterized by GISAXS.

6.4.1 Single solvent based assembly of BChl c: effect of initial concentration and droplet size

For the single-solvent technique, the effects on assembly due to the initial concentration and droplet size are presented. The concentration in the solution was increased from 24.3 μM to 91.2 μM, and the absorption spectrum of the slides is measured after deposition. Figure 6–2a shows the effect of different initial concentrations on the assembly when the droplet size was kept constant at 0.518 μm. The peak absorption for deposits sprayed at initial concentration of 24.3 μM is at 671 nm, which corresponds to randomly oriented monomeric molecules. At low concentration, there is no assembly because nucleation does not take place before the solvent evaporates, as described in the previous section. At higher initial concentrations, a peak is observed at 730 nm, which corresponds to assembled molecules.

The droplet size effect was studied by increasing the size of sprayed droplets from 0.417 μm to 0.593 μm, keeping the BChl *c* concentration constant at 66.2 μM (Figure 6–2b). When the droplet size is small, a shoulder is observed at 726 nm corresponding to the absorption of self-assembled structures. As the droplet size increases, the assembly peak also grows in intensity. The results show that increasing droplet size has a similar effect as concentration on self-assembly. The assembly of the molecules is mainly dependent on nucleation of the self-assembled structures. The critical supersaturation needs to be crossed in solution for nucleation to take place. The supersaturation (S) inside the droplet is given by following equation:

$$S = \frac{c(t)}{c_e} = \frac{c_i}{c_e}\frac{d_i^3}{d(t)^3}, \tag{6.1}$$

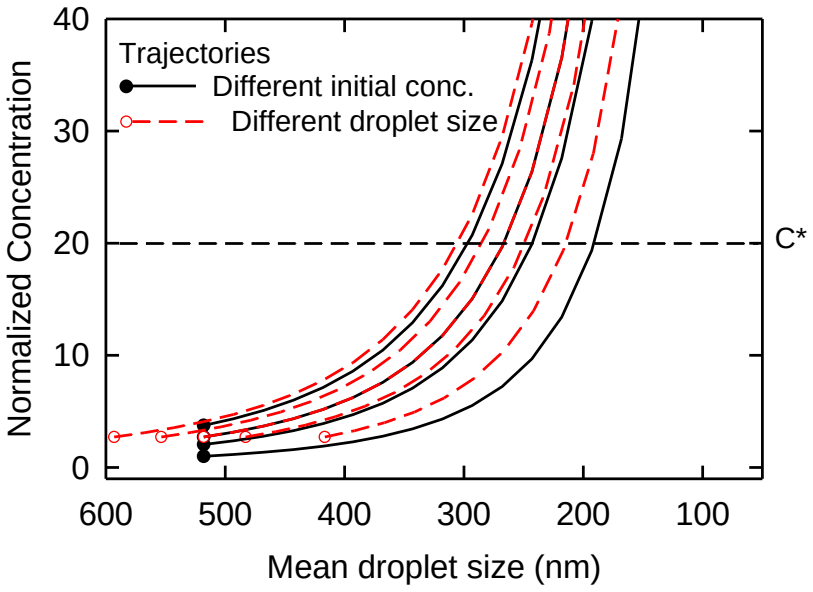

Figure 6–3: Variation in droplet size and concentration due to evaporation for different initial conditions. Red hollow circles are the initial conditions for same concentration and different droplet sizes while black solid circles are the initial conditions for the same droplet size and different initial concentrations. The UV-vis spectra for these conditions are shown in Fig. 1.

where *c(t)* is the concentration at time t, c_i is the initial concentration, c_e is the equilibrium concentration, d_i is the initial diameter of the droplet and d (t) is the droplet diameter at time t. Thus the concentration and the droplet size are related to each other. As the solvent evaporates, the size and concentration inside each droplet changes. Figure 6–3 shows the concentration and droplet size at various times. Different initial conditions result in different starting points. For example, the same c_i results in points representing initial conditions parallel to the y-axis, and the same droplet size results in points representing initial conditions parallel to x-axis. We can plot the normalized concentration and the droplet size as shown in . The figure highlights the relationship between the effect of droplet size and initial concentration. If there is enough time for molecules to nucleate, all the droplets reach critical supersaturation and then assemble. Thus,

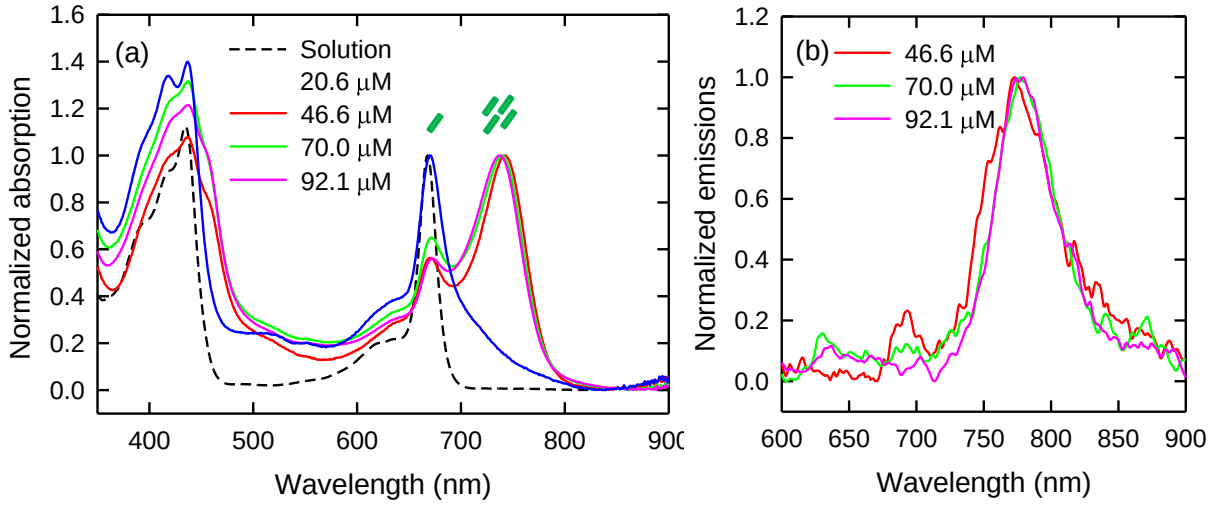

Figure 6–4: Effect of concentration on (a) absorption spectrum of the self-assembled molecules and (b) fluorescence emission from the self-assembled molecules exicted at 430 nm.

for small droplets or lower initial concentrations, no assembly is observed, while for larger droplets or higher initial concentration complete assembly is observed.

Interestingly, partial assembly was observed in some cases, even though nucleation had taken place. This can be explained by looking at the actual size distribution of the droplets, which is log normal with a mean size of 0.518 μm and geometric standard deviation of 1.1. Thus there are droplets from 0.428 to 0.626 μm, which spans the complete range studied in this work. The spread in size distribution results in a band in the plot of droplet size and concentration space. The partial assembly is observed primarily because there are some droplets with no assembly and some with assembly. This ratio will vary as the initial concentration or droplet size increases. The ratio will change as the droplet size increases, and beyond a certain size, there would be no effect due to droplet size.

6.4.2 Comparison of single-solvent and two-solvent based assembly of BChl c

The two-solvent technique allows for higher concentrations in solution and also avoids kinetic limitations due to vaporization of the solvent.[22] In this work, the two-solvent and single-solvent techniques are compared by keeping the droplet size constant. Metanol:Ethanol (1:1 v/v) was used as solvent and the concentration in the solvent was varied from ~ 20.6 to 92 μM for the two-solvent technique. Figure 6–4a shows the results for the two-solvent technique, which are compared with the results from the single-solvent technique shown in Figure 6–2a. As described in the previous section, at a low initial concentration of 20.6 μM a kinetic limitation similar to single-solvent technique is observed. This is because concentrations are too low and there is not enough time for nucleation after supersaturation is reached. At higher concentrations, from 46 μM to 92 μM, complete assembly is observed, as shown in Figure 6–4a. In contrast to two-solvent technique, when single-solvent technique was used the assembly peak grows as the concentration is increased, however complete assembly was not observed. It should be noted that the peak for the two-solvent technique is normalized with respect to the assembly peak in comparison to the single solvent synthesis where it is normalized to the monomer peak after deposition, because there is a higher number of molecules have not assembled. The comparison clearly indicates that the two-solvent technique allows for longer time for nucleation, and hence more molecules assemble. In order to check the quality of self-assembled structures, fluorescence was measured immediately after deposition. Figure 6–4b shows fluorescence measured for all cases, and the peak emission wavelength is in the range of 770 - 780nm for all the initial concentrations.

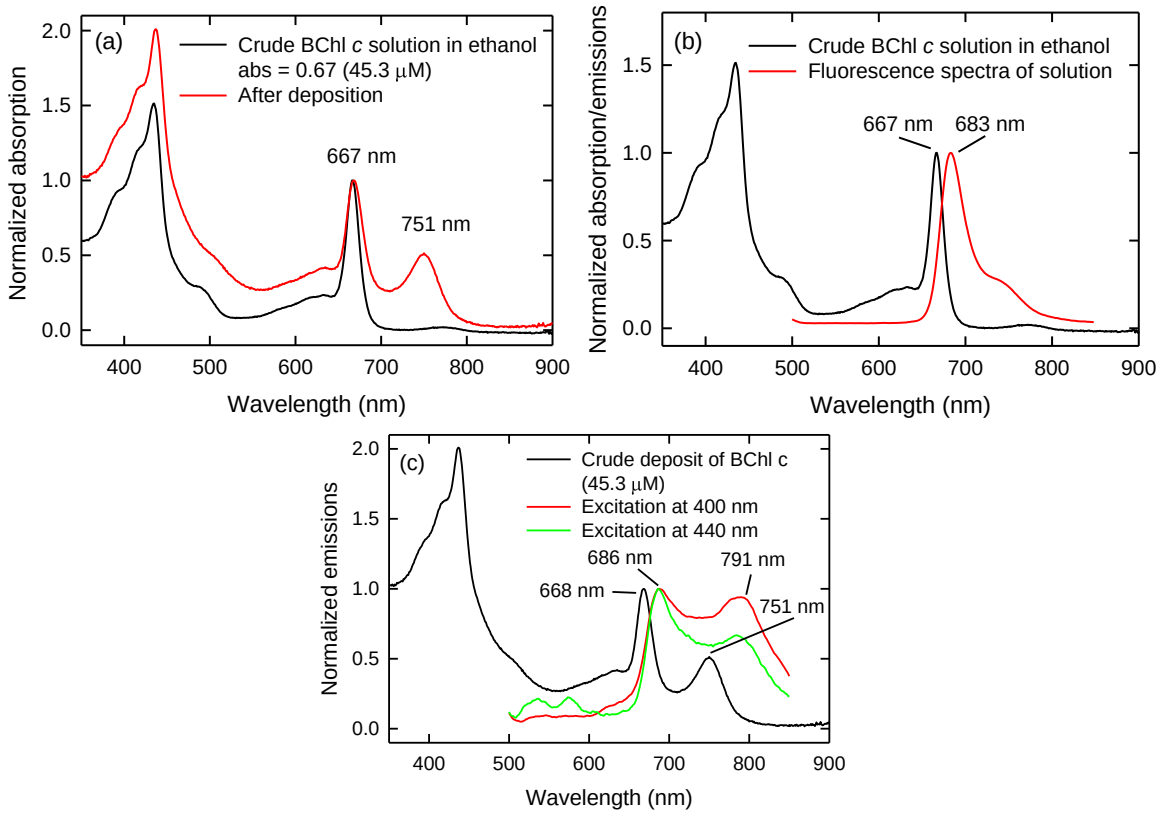

Figure 6–5: (a) Absorption spectrum of the BChl *c* deposited by using electrospray in comparison with the solution spectrum (b) Comparison of the emission spectrum of the 'crude' BChl *c* solution with the absorption spectrum (c) Normalized emissions from the deposit of crude BChl *c* solution in comparions with the absorption spectrum.

6.4.3 Assembly of BChl *c* with other chlorosomal components

In addition to BChl *c*, the chlorosomes contain other molecules such as carotenes, lipids and other proteins.[23] Thus BChl *c* is assembled in the presence of other molecules by the aerosol technique. In order to keep the constituent composition of the molecules the same, the chlorosomes were broken up by the addition of ethanol. The resulting solution had the same composition as the chlorosomes. Figure 6–5a shows the absorption spectrum of the solution, which has absorption for carotene at 550 nm. The solution was made conductive by addition of ammonium acetate and was electrosprayed. The droplet size was 654 nm, and the concentration for BChl *c* was 50.8 μM. Pure BChl *c* did not assemble at the same concentration (not shown in

the figure) when sprayed in ethanol. This result shows that the cellular components catalyzed the assembly of BChl *c*. Klinger et. al.[15] also observed that carotenoids and lipids both increase the self-assembly of BChl *c* in solution due to hydrophobic interactions.

Figure 6–5a compares the absorption spectra of the spray solution and the deposit. The sprayed solution assembled and showed an absorption peak at 751 nm which is more red shifted than for normal agglomerates. In solution, it has been observed that on addition of carotenoids, the absorption for self-assembled structures is further red shifted,[15] which is similar to observations in this work. The peak absorbance in the self-assembled region corresponds to absorption in chlorosomes. However, there are monomers in the deposit as seen from absorption at 668 nm, indicating that assembly is not complete than that seen in the Klinger et. al. study[8] where the chlorosome components were dissolved in aqueous buffer, or the cases when pure BChl *c* was assembled.

Figure 6–5b shows the emission spectrum of the deposit in comparison to the absorption spectrum in which both the monomers and the agglomerates fluoresce. After deposition, the monomers fluoresce at 686 nm, and the assembled structures fluoresce at 791 nm. The monomer emission is slightly red shifted in comparison to that of the monomers from the solution (Figure 6–5c). Since the absorption is at 751 nm, the fluorescence from the self-assembled structure in the presence of other molecules is also more shifted than that of self-assembled structures synthesized from pure BChl *c*. The fluorescence results are similar to that of chlorosomes which were deposited by electrospray.[24] A smaller Stokes shift is observed for monomers than that of the self-assembled structures. When the sample was excited at 400 nm, a prominent fluorescence peak from the agglomerates was observed. However the agglomerate fluorescence peak was of lower intensity when excited at 440 nm, which is mainly attributed to difference in absorption.

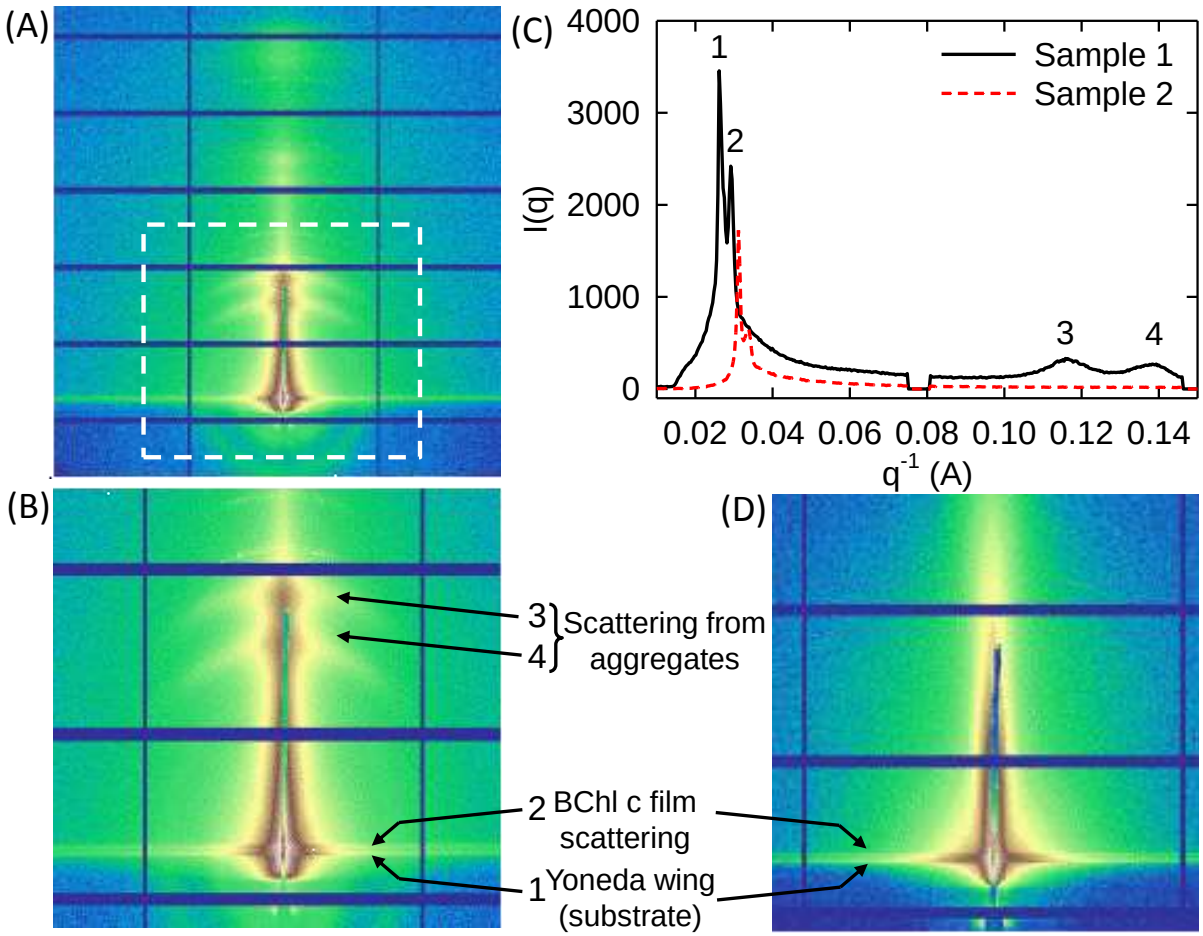

Figure 6–6: Two samples were characterized by GISAXS. (a) GISAXS scattering pattern for sample 1 showing lamellar scattering pattern and (b) a zoomed in scattering pattern for sample 1. (c) Vertical line cut to compare the various peaks obtained with samples. (d) GISAXS pattern for sample 2, which does not show lamellar scattering pattern.

The slides were also excited at 500 nm to selectively excite carotenes; however, no emissions were observed. This could be due to the lack of energy transfer, due to a low concentration of carotenes or the oxidation of carotenes. Figure 6–5c shows the fluorescence spectrum for the crude solution of BChl *c*, which is characteristic of the monomeric BChl *c*. The peak is less Stokes shifted than the deposited one; however, no emission corresponding to the agglomerate is observed. This control study verifies that the emission observed at 791 nm comes from the self-assembled agglomerate. This work demonstrates that it is possible to assemble BChl *c* in the

presence of other components to realize multicomponent self-assembly and obtain optical properties comparable to natural systems.

6.4.4 GISAXS characterization of self-assembled structures

GISAXS was used to probe the internal structure of the self-assembled BChl c. GISAXS measurements can provide several pieces of information to contribute to our knowledge of BChl *c* ordering and stacking. The scattering results are presented for 'sample 1' - the self-assembled structures formed on spraying 67.6 μM BChl *c* solution in methanol into 0.75 μm droplets. The resulting self-assembled structures had a peak absorption at 745 nm, which is similar to that of chlorosomes. Figure 6–6a shows the 2D X-ray scattering pattern of the self-assembled structure. Figure 6–6b is a magnified view to help clearly indicate the features in the scattering pattern. There are two strong horizontal scattering patterns, which correspond to the Yoneda wing (or substrate scattering), marked by '1', and the scattering from the film layer atop the substrate, marked by '2'. There are two arcs above the film and also substrate scattering, marked by '3' & '4' respectively which are characteristic of lamellar structures in chlorosomes observed using other techniques. Figure 6–6c is obtained by a vertical line-cut of the 2D X-ray scattering pattern. The vertical line-cut provides two important pieces of information: the BChl *c* layer thickness and radial cylindrical spacing of the heterogeneous electrosprayed BChl *c* mixture. Using the peak location along the 1D wave vector from the vertical line-cut, two characteristic lengths are estimated to be 2.27 nm and 2.72 nm. Extensive cryo-electron microscopy and small angle X-ray scattering experiments have been performed to investigate self-ordering of the BChls and have shown that wild type chlorosomes have the lamellar stacking with spacing of ~ 2.1 nm.[25-27] Thus the measured values for biomimetic aggregates deposited on slide matches well with spacing in literature for chlorosomes. Chlorosomes consist of BChl *c* molecules with

slightly different side chains, which results in BChl *c* structures heterogeneous in nature due to differences in side chain orientations and chemistries.[28] The additional prominent arc indicating a radius of 2.72 nm for lamellar structure could be attributed to heterogeneity of the BChl *c* side groups or different stacking pattern. Further scattering arcs indicate that there are lamellar structures with larger diameter, which could be attributed to assembly of the molecules around the cylindrical core of radius 2.27 nm or 2.1 nm. The vertical line cut was also used to determine the deposited layer thickness using the following relationship:

$$\frac{2\pi}{q_2 - q_1}, \tag{6.2}$$

where q_2 and q_1 correspond to the wave vectors (in $Å^{-1}$) of the film and substrate diffraction peak positions, respectively. The film thickness was calculated at 209 nm using equation (6.2). The horizontal line-cut from the 1D GISAXS reduction analysis can be fitted to provide information on the larger BChl *c* agglomerate size generated after the evaporation of solvents in electrospray deposition. The horizontal line cut fitting resulted in particle diameters of 31.6 nm, which indicates that assembly took place in droplets and not after deposition. It should be noted that this characteristic lamellar pattern was not always obtained. On some occasions a typical scattering pattern (Figure 6–6d) of the self-assembled structures were obtained, mainly because of the particulate nature of the film. This indicates that lamellar structure are formed under certain conditions, and would require further investigation.

6.5 Conclusions

The aerosol based self-assembly technique can be used to assemble BChl *c* in its ‘pure’and ‘crude’ form. The solvent, droplet size and the concentration all play important roles in the assembly. However, the two-solvent synthesis is better than the single solvent for the same

droplet size. The difference in fluorescence of crude and pure self-assembled BChl *c* reflects the differences in absorption spectra. GISAXS analysis shows that the lamellar structure formed in natural chlorosomes can be reproduced using this technique. Moreover GISAXS also establishes that the particles are formed in flight, since they retain their particulate nature in the film. This is the first work where the films deposited by electrospray have been characterized by GISAXS. This technique of electrospray deposition will allow a detailed study of various chlorosome components such as carotenes, quinones, and lipids, and their interaction with bacteriochlorophyll *c* molecules. The effect of assembly on the structure and fluorescence of the assembled structures could be studied in detail. Although in this work the fluorescence was observed at 778 nm, in the future, it would be interesting to see if there is a significant difference in fluorescence spectra as observed for the absorption peaks. The fluorescence of the deposited material suggests that this technique could be used for fabrication of a device wherein the self-assembled structures can act as antennas.

6.6 Acknowledgments

This work was supported by the Photosynthetic Antenna Research Center (PARC), an Energy Frontier Research Center funded by the U.S. Department of Energy, Office of Science, Office of Basic Energy Sciences under Award Number DE-SC0001035. V. Shah thanks the McDonnell International Scholars Academy for a fellowship to pursue the Ph.D. at Washington University in St. Louis.

6.7 References

1. Blankenship, R. E.; Olson, J. M.; Miller, M., Anoxygenic Photosynthetic Bacteria. Blankenship, R. E.; Madigan, M. T.; Bauer, C. E., Eds. Kluwer Academic Publishers, The Netherlands: 1995; pp 399–435.

2. Orf, G.; Blankenship, R. Chlorosome Antenna Complexes from Green Photosynthetic Bacteria. *Photosynth. Res.* **2013**, *116*, 315-331.

3. Frigaard, N.-U.; Bryant, D., Chlorosomes: Antenna Organelles in Photosynthetic Green Bacteria. In *Complex Intracellular Structures in Prokaryotes*, Shively, J., Ed. Springer Berlin / Heidelberg: 2006; Vol. 2, pp 79-114.

4. Modesto-Lopez, L. B.; Thimsen, E. J.; Collins, A. M.; Blankenship, R. E.; Biswas, P. Electrospray-Assisted Characterization and Deposition of Chlorosomes to Fabricate a Biomimetic Light-Harvesting Device. *Energy Env. Sci.* **2010**, *3*, 216-222.

5. Marek, P. L.; Hahn, H.; Balaban, T. S. On the Way to Biomimetic Dye Aggregate Solar Cells. *Energy Env. Sci.* **2011**, *4*, 2366-2378.

6. McHale, J. L. Hierarchal Light-Harvesting Aggregates and Their Potential for Solar Energy Applications. *J Phys Chem Lett* **2012**, *3*, 587-597.

7. Saga, Y.; Saiki, T.; Takahashi, N.; Shibata, Y.; Tamiaki, H. Scrambled Self-Assembly of Bacteriochlorophylls *c* and *e* in Aqueous Triton X-100 Micelles. *Photochem. Photobiol.* **2014**, *90*, 552-559.

8. Uehara, K.; Mimuro, M.; Ozaki, Y.; Olson, J. M. The Formation and Characterization of the in-Vitro Polymeric Aggregates of Bacteriochlorophyll *c* Homologs from Chlorobium Limicola in Aqueous Suspension in the Presence of Monogalactosyl Diglyceride. *Photosynth. Res.* **1994**, *41*, 235-243.

9. vanNoort, P. I.; Zhu, Y. W.; LoBrutto, R.; Blankenship, R. E. Redox Effects on the Excited-State Lifetime in Chlorosomes and Bacteriochlorophyll *c* Oligomers. *Biophys. J.* **1997**, *72*, 316-325.

10. Saga, Y.; Akai, S.; Miyatake, T.; Tamiaki, H. Self-Assembly of Natural Light-Harvesting Bacteriochlorophylls of Green Sulfur Photosynthetic Bacteria in Silicate Capsules as Stable Models of Chlorosomes. *Bioconjugate Chem.* **2006**, *17*, 988-994.

11. Miyatake, T.; Tamiaki, H. Self-Aggregates of Natural Chlorophylls and Their Synthetic Analogues in Aqueous Media for Making Light-Harvesting Systems. *Coord. Chem. Rev.* **2010**, *254*, 2593-2602.

12. Brune, D. C.; Nozawa, T.; Blankenship, R. E. Antenna Organization in Green Photosynthetic Bacteria. 1. Oligomeric Bacteriochlorophyll *c* as a Model for the 740 nm Absorbing Bacteriochlorophyll *c* in Chloroflexus Aurantiacus Chlorosomes. *Biochemistry* **1987**, *26*, 8644-8652.

13. Balaban, T. S.; Leitich, J.; Holzwarth, A. R.; Schaffner, K. Autocatalyzed Self-Aggregation of (3^1R)-[Et,Et]Bacteriochlorophyll c_F Molecules in Nonpolar Solvents. Analysis of the Kinetics. *J. Phys. Chem. B* **2000**, *104*, 1362-1372.

14. Shah, V. B.; Biswas, P. Aerosolized Droplet Mediated Self-Assembly of Photosynthetic Pigment Analogues and Deposition onto Substrates. *ACS Nano* **2014**.

15. Klinger, P.; Arellano, J. B.; Vácha, F.; Hála, J.; Pšenčík, J. Effect of Carotenoids and Monogalactosyl Diglyceride on Bacteriochlorophyll *c* Aggregates in Aqueous Buffer: Implications for the Self-Assembly of Chlorosomes. *Photochem. Photobiol.* **2004**, *80*, 572-578.

16. Gerola, P. D.; Olson, J. M. A New Bacteriochlorophyll *a* Protein Complex Associated with Chlorosomes of Green Sulfur Bacteria. *Biochimica et Biophysica Acta (BBA)-Bioenergetics* **1986**, *848*, 69-76.

17. Orf, G. S.; Tank, M.; Vogl, K.; Niedzwiedzki, D. M.; Bryant, D. A.; Blankenship, R. E. Spectroscopic Insights into the Decreased Efficiency of Chlorosomes Containing Bacteriochlorophyll *f*. *Biochimica et Biophysica Acta (BBA)-Bioenergetics* **2013**, *1827*, 493-501.

18. Mass, O.; Pandithavidana, D. R.; Ptaszek, M.; Santiago, K.; Springer, J. W.; Jiao, J.; Tang, Q.; Kirmaier, C.; Bocian, D. F.; Holten, D.; Lindsey, J. S. De Novo Synthesis and Properties of Analogues of the Self-Assembling Chlorosomal Bacteriochlorophylls. *New J. Chem.* **2011**, *35*, 2671-2690.

19. Chen, D. R.; Pui, D. Y. H.; Kaufman, S. L. Electrospraying of Conducting Liquids for Monodisperse Aerosol Generation in the 4 nm to 1.8 μm Range. *J. Aerosol Sci.* **1995**, *26*, 963-978.

20. Basak, S.; Chen, D. R.; Biswas, P. Electrospray of Ionic Precursor Solutions to Synthesize Iron Oxide Nanoparticles: Modified Scaling Law. *Chem. Eng. Sci.* **2007**, *62*, 1263-1268.

21. Hinds, W. C. *Aerosol Technology: Properties, Behavior, and Measurement of Airborne Particles*. Second edition ed.; John Wiley & Sons, Inc.: New York, 1999.

22. Shah, V. B.; Biswas, P. Aerosolized Droplet Mediated Self-Assembly of Photosynthetic Pigment Analogues and Deposition onto Substrates. *ACS Nano* **2014**, *8*, 1429-1438.

23. Arellano, J. B.; Psencik, J.; Borrego, C. M.; Ma, Y.-Z.; Guyoneaud, R.; Garcia-Gil, J.; Gillbro, T. Effect of Carotenoid Biosynthesis Inhibition on the Chlorosome Organization in Chlorobium Phaeobacteroides Strain CL1401. *Photochem. Photobiol.* **2000**, *71*, 715-723.

24. Shah, V. B.; Orf, G. S.; Reisch, S.; Harrington, L. B.; Prado, M.; Blankenship, R. E.; Biswas, P. Characterization and Deposition of Various Light-Harvesting Antenna Complexes by Electrospray Atomization. *Anal. Bioanal. Chem.* **2012**, *404*, 2329-2338.

25. Ganapathy, S.; Oostergetel, G. T.; Wawrzyniak, P. K.; Reus, M.; Gomez Maqueo Chew, A.; Buda, F.; Boekema, E. J.; Bryant, D. A.; Holzwarth, A. R.; de Groot, H. J. M. Alternating Syn-Anti Bacteriochlorophylls Form Concentric Helical Nanotubes in Chlorosomes. *Proceedings of the National Academy of Sciences* **2009**.

26. Pšenčík, J.; Ikonen, T. P.; Laurinmäki, P.; Merckel, M. C.; Butcher, S. J.; Serimaa, R. E.; Tuma, R. Lamellar Organization of Pigments in Chlorosomes, the Light Harvesting Complexes of Green Photosynthetic Bacteria. *Biophys. J.* **2004**, *87*, 1165-1172.

27. Ikonen, T. P.; Li, H.; Pšenčík, J.; Laurinmäki, P. A.; Butcher, S. J.; Frigaard, N. U.; Serimaa, R. E.; Bryant, D. A.; Tuma, R. X-Ray Scattering and Electron Cryomicroscopy Study on the Effect of Carotenoid Biosynthesis to the Structure of Chlorobium Tepidum Chlorosomes. *Biophys. J.* **2007**, *93*, 620-628.

28. Ganapathy, S.; Oostergetel, G. T.; Reus, M.; Tsukatani, Y.; Gomez Maqueo Chew, A.; Buda, F.; Bryant, D. A.; Holzwarth, A. R.; de Groot, H. J. M. Structural Variability in Wild-Type and BchQ BchR Mutant Chlorosomes of the Green Sulfur Bacterium Chlorobaculum Tepidum. *Biochemistry* **2012**, *51*, 4488-4498.

Chapter 7 Conclusions and future work

7.1 Conclusions

Although utilizing efficient sensitizers for improving efficiency of titanium dioxide solar cell has been challenging, this work has improved the fundamental understanding of the directed self-assembly and self-assembly in aerosolized droplets. The major conclusions from this study are summarized below:

1. The morphology of the film generated by ACVD can be simulated for short times. Spread index can be used as an objective indicator for the morphology of the film. Sintering rate, which can be controlled by changing the substrate temperature, is an important parameter that affects the morphology of the film. Apart from sintering, deposition rate also plays an important role in determining the morphology of the film. Although the sintering model developed is better than previous models while retaining computational simplicity, the model needs to be improved to match the experimental results.
2. Biological LHCs can be electrospray deposited and they retain their light absorption and fluorescence properties. Thus the technique of electrospray deposition can be used for fabrication of solar cells.
3. PSI was successfully deposited onto the nanostructured metal oxide surfaces using electrospray, without the use of linkers for attachment. On exposure to electrolyte PSI was reoriented and adhered to the nanostructure due to hydrophobic forces. The orientation of the PSI, where stromal and luminal side are not in contact with TiO_2 allowing easy access to the electrolyte, gives the highest photocurrent for PSI based photo-electrochemical cell.
4. Supramolecular assembly in an aerosolized droplet has been demonstrated for the first time in this work. In the single solvent method, although assembly is thermodynamically favored, kinetics of nucleation are important for eventual assembly. These kinetic limitations on the

time available for assembly due to evaporation of the droplet in a single solvent method, can be overcome by using two solvents. On using two solvents, further control over the size of nuclei of the self-assembled structure was demonstrated.

5. The assembly of BChl *c* in pure and 'crude' form is demonstrated. The solvent composition, droplet size and the concentration all play an important role in self-assembly in an aerosolized droplet. However, two solvent is better than single solvent for the same droplet size. GISAXS analysis establishes that the particles are formed in flight and retain the particulate nature in the film. GISAXS also helps in identifying the lamellar structures which are similar to the ones present in chlorosomes, thus mimicking them.

7.2 Future work

The existing work opens up wide array of research questions and topics. These research questions are listed as follows:

1. The ACVD simulation can be improved by using a better model for the estimation of the particle size which also integrates the flow field. A better sintering model that takes into account non-spherical particles, surface energies and crystal structure into account would be needed for better simulations.
2. PSI based solar cells can be developed to measure the efficiency with two electrode cell. Additional experiments should be done to establish the pathway for electron transfer. The technique of directed assembly can be used to fabricate PSII based solar cells for water splitting. This technique can be used to spray other membrane bound reaction centers, thus broadening the absorption spectrum.

3. The self-assembly of artificial analogs shows that kinetics can play and important role inside an evaporating droplet. This technique can be used for synthesis of other self-assembled materials in droplet such as metal organic frameworks. The self-assembly work could be extended to verify if the aggregates are reduced or oxidized in the process of electrospray deposition. Moreover, assembly of the excited molecules is more favorable and this area may be explored in detail by shining light on to sprayed droplets.
4. Self-assembled structures of BChl *c* can be characterized by GISAX scattering and diffraction. BChl *c* constituents can be modified such that only single molecule is allowed to assemble, or assemble in presence of lipids and compare the scattering pattern with that of chlorosomes.
5. The energy balance based approach for electrospray can be improved to understand the voltage requirement for various setup and designs.

Appendix A Simple trimodal model for evolution of multicomponent aerosol dynamics

A.1 Abstract

A computationally simple model which incorporates nucleation, condensation, and particle growth by collisions of three discrete sized, non-spherical particles is presented. The model is extended to incorporate multiple components which are usually encountered in combustion and atmospheric environments. As there are only three discrete sizes that represent the entire distribution (for simplicity), different ways of apportioning the particles into these modes are described. No significant difference between the various apportionment methods is observed at sufficiently long time scales. The model predictions are in good agreement with those of previously developed Nodal General Dynamic Equation (NGDE) and sectional approaches. The trimodal model is used to simulate a multicomponent system for lead capture using nanostructured sorbents. Good agreement between the model and experimental results for the capture of lead species is obtained.

Keywords: Trimodal model, Multicomponent, Apportioning, Combustion Aerosols, Sorbent Capture

A.2 Introduction

There are numerous models to predict aerosol growth dynamics ranging from simplistic lognormal to the more accurate discrete-sectional models. In combustion systems and various aerosol reactors wherein nanoparticles are synthesized, there is a need to also track the shape or morphology of the resultant particles. This added dimension complicates the aerosol models, and thus several simpler approaches have been proposed. Kruis, *et. al.*[1] developed a simple monodisperse model to predict particle growth, however accounting for the morphology using a fractal representation. Their model was computationally efficient and also showed good agreement with the more detailed two dimensional sectional model predictions.[2] However, the monodisperse model does not reflect the polydisperse character when particle generation and growth occur simultaneously, as in many aerosol reactor systems. To overcome this problem of the monodisperse model, Jeong & Choi[3] proposed an extension to the monodisperse model[1] by using a bimodal monodisperse approach, and obtained reasonable agreement with more accurate models when new particle generation exists.

In many combustion systems, there are multiple components present that result in particle formation. Furthermore, nanostructured sorbents have been proposed to scavenge metallic vapor species to promote condensational growth and chemi-sorption that results in particles that are larger in size and effectively captured.[4-6] Similarly, multicomponent growth processes are also encountered in synthesis of nanocomposites and in atmospheric aerosol processes. Pirjola *et. al.*[7] developed a four modal model to describe aerosol growth dynamics for atmospheric aerosol processes. They assumed log normal distribution to apportion the masses and numbers to large modes. While several analytical[8-10] and numerical[11, 12] approaches of multicomponent aerosol growth dynamics have been extensively studied, the models are computationally expensive. The

bimodal model[3] is computationally simple; however it has only two modes and therefore it is not possible to extend the model for multiple components, which is the subject of this paper.

In the present paper, a computationally simple trimodal monodisperse model for single and multicomponent aerosol formation and growth is proposed. This model incorporates an additional mode for nucleating particles compared to bimodal model. The model is then generalized for "*m*" components. Due to the simplicity of the use of only three modes, the apportionment of the particles is an important factor, and is examined in this paper. This model is used to simulate a toxic metal capture process using sorbents. The simulation results of the proposed model are compared to that of more detailed models, such as the NGDE (Nodal General Dynamic Equation) and discrete sectional methods.

A.3 Model equations

Jeong & Choi[3] developed the bimodal monodisperse model to describe the growth of non-spherical particles. The two sizes selected were that of the nucleation and accumulation mode, and they derived four equations to predict growth dynamics of non-spherical particles. They assumed that the monomer (molecular size) was the nucleated particle, that is, there was no nucleation barrier. In the present model, three modes (trimodal monodisperse) consisting of the monomer, nucleation and accumulation mode are used. The equations are described for a single component, and then generalized for a multi-component system.

A.3.1 Single component model

Figure A–1 is a schematic representation of the trimodal monodisperse model for the single component particle formation and growth system. Mode 0, 1 and 2 represent the monomer, nucleation and accumulation mode, respectively. For single component particle

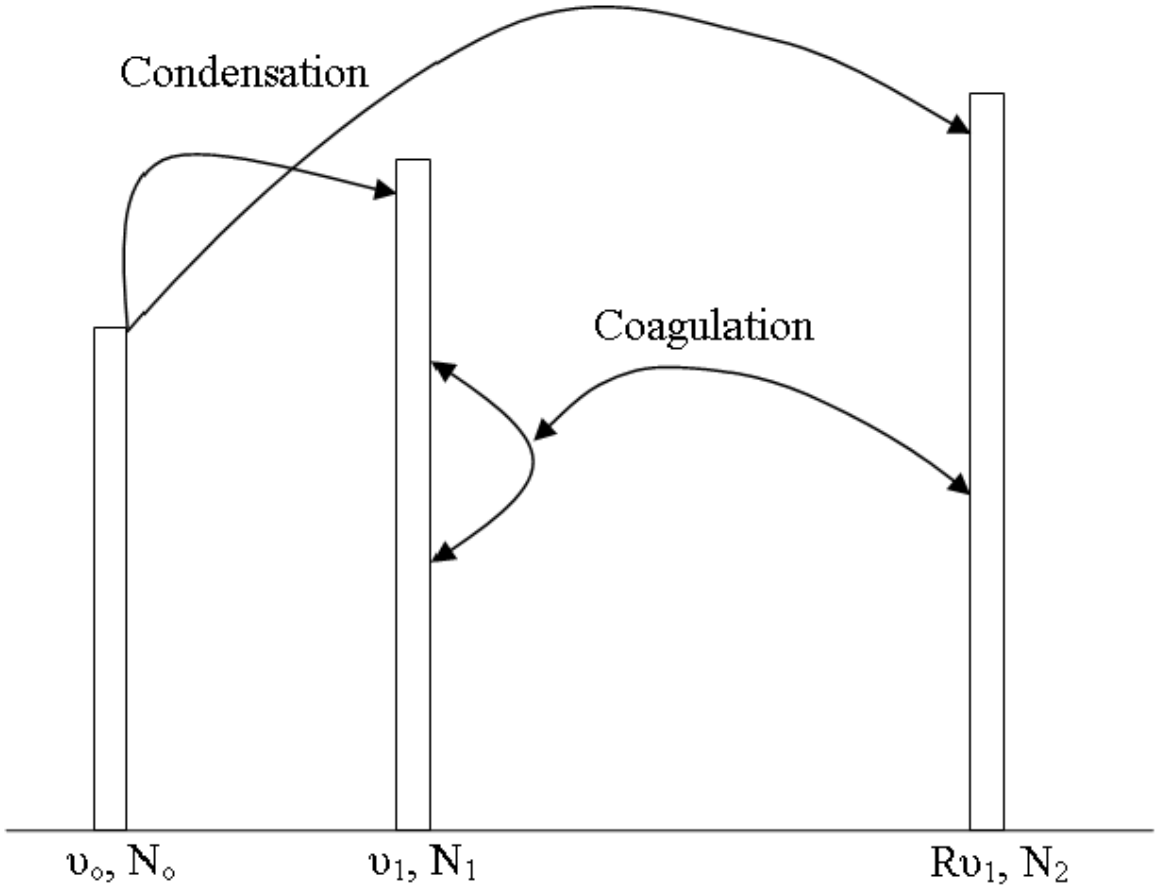

Figure A–1: Schematic diagram of the trimodal monodisperse model illustrating the nucleation, condensation and coagulation pathways.

growth, the derivation of the governing equations is very similar to that proposed by Jeong and Choi.[3] One difference is that the condensation pathway is now accounted for as illustrated in Figure A–1. The monomer balance equation is

$$\frac{dN_o}{dt} = I_o - K_1^o N_o N_1 - K_2^o N_o N_2 - J^* \frac{\upsilon^*}{\upsilon_o} \tag{A.1}$$

where I_o is monomer generation rate, J^* is nucleation rate of the critical cluster, υ^* is volume of the critical cluster, υ_o is monomer volume, N_i is the number concentration of mode i and K^o_i is the modified Fuchs-Sutugin condensation coefficient between monomer and mode i.

In the present model, the volume of mode 1 is fixed at υ_1. Therefore, only the number concentration equation is required for mode 1. The volume of particles in mode 1 is selected such that $\upsilon_1 \geq \upsilon^*$ (when nucleation has occurred). Since J^* is the nucleation rate of the critical cluster, υ^*, the rate of increase of υ_1 sized particles is expressed as $J^* \upsilon^* / \upsilon_1$. The condensation pathway can change the volume of mode 1. To simplify the model, the number concentration equation is modified to satisfy the mass balance condition. The number concentration equation of mode 1 is thus,

$$\frac{dN_1}{dt} = J^* \frac{\upsilon^*}{\upsilon_1} - \frac{1}{2}\beta_{11} N_1^2 \frac{r}{r-1} - \beta_{12} N_1 N_2 + \frac{\upsilon_o}{\upsilon_1} K_1 N_o N_1 \tag{A.2}$$

where β_{ij} is coagulation coefficient between mode i and j, and r is equal to ratio of mode 2 volume to mode 1 volume as shown in Fig. 1.

For mode 2, using a similar approach of the previous study,[3] total number concentration, volume and area are described as

$$\frac{dN_2}{dt} = \frac{1}{2}\beta_{11} N_1^2 \frac{1}{r-1} - \frac{1}{2}\beta_{22} N_2^2 \tag{A.3}$$

$$\frac{dV_2}{dt} = \frac{1}{2}\beta_{11} N_1^2 \frac{r}{r-1}\upsilon_1 + \beta_{12} N_1 N_2 \upsilon_1 + K_2 N_o N_2 \upsilon_o \tag{A.4}$$

$$\frac{dA_2}{dt} = \frac{1}{2}\beta_{11} N_1^2 \frac{r}{r-1} a_1 + \beta_{12} N_1 N_2 a_1 + K_2 N_o N_2 a_o - \frac{1}{\tau}\left(A_2 - N_2 a_{2s}\right) \tag{A.5}$$

where N_2, V_2 and A_2 are total number concentration, volume and area of mode 2, respectively, a_o, a_1 are the surface area of mode 0 and mode 1 and a_{2s} is the surface area when volume of mode 2 is completely fused. The collision cross section is used for calculating the collision frequency for mode 2 to account for the fractal shape of the particles. The radius of collision cross section is r_{2c}

$= r_2\ r^{1/Df}$.[1] This allows us to incorporate formation of fractal particles in the process. In this study, D_f is taken as 1.8 for diffusion limited growth of aerosol particle.[13]

The rate of total volume change is given by

$$\frac{dV_t}{dt} = \frac{d}{dt}\left(V_o + V_1 + V_2\right) = \upsilon_o \frac{dN_0}{dt} + \upsilon_1 \frac{dN_1}{dt} + \frac{dV_2}{dt} = I_o \upsilon_o \tag{A.6}$$

As shown in Eq. (A.6), the rate of total volume change is equal to the rate of monomer volume generation. Thus the model approach satisfies the mass conservation condition. Furthermore, the present model reduces to the bimodal monodisperse model, when mode 1 is not present and the monomer is a stable particle.

A.3.2 Two component model

Figure A–2 shows the schematic representation of the two component model with two monomer modes (one for each component), two nucleation modes and one accumulation mode. The monomer and nucleation mode volume is determined as described earlier for the single component model. The subscript "*o*" denotes the monomer and subscript 1 and 2 denote the components 1 and 2, respectively. The monomer balance expressions are

$$\frac{dN_{o1}}{dt} = I_{o1} - J_1^* \frac{\upsilon_1^*}{\upsilon_{o1}} - K_1^{o1} N_{o1} N_1 - K_2^{o1} N_{o1} N_2 - K_3^{o1} N_{o1} N_3 \tag{A.7}$$

$$\frac{dN_{o2}}{dt} = I_{o2} - J_2^* \frac{\upsilon_2^*}{\upsilon_{o2}} - K_1^{o2} N_{o2} N_1 - K_2^{o2} N_{o2} N_2 - K_3^{o2} N_{o2} N_3 \tag{A.8}$$

where, $K^{oi}_{\ j}$ means that condensation coefficient between i component monomer and j mode. For mode 1 (nucleation mode of component 1) the number concentration equation is given by

$$\frac{dN_1}{dt} = J_1^* \frac{\upsilon_1^*}{\upsilon_1} - \frac{1}{2}\beta_{11}N_1^2 \frac{R_1}{R_1 - 1} - \frac{1}{2}\beta_{12}N_1N_2 \frac{\upsilon_2}{\upsilon_1(R_1 - 1)} - \beta_{13}N_1N_3 + \frac{\upsilon_{o1}}{\upsilon_1}K_1^{o1}N_{o1}N_1 + \frac{\upsilon_{o2}}{\upsilon_1}K_1^{o2}N_{o2}N_1 \quad \text{(A.9)}$$

where, $R_i = \upsilon_3/\upsilon_i$. The first term on the right hand side represents nucleation, the second, third and fourth terms coagulation, and the fifth and sixth term represent condensation and heterogeneous condensation. The coagulation terms are similar to the single component model, with an additional term that accounts for coagulation between the two nucleation modes of the different components (as illustrated in Figure A–3). When coagulation takes place, the mode 1 number concentration is reduced by one unit and increased by $1-\upsilon_2/(R_1-1)\upsilon_1$ units and mode 3 increases

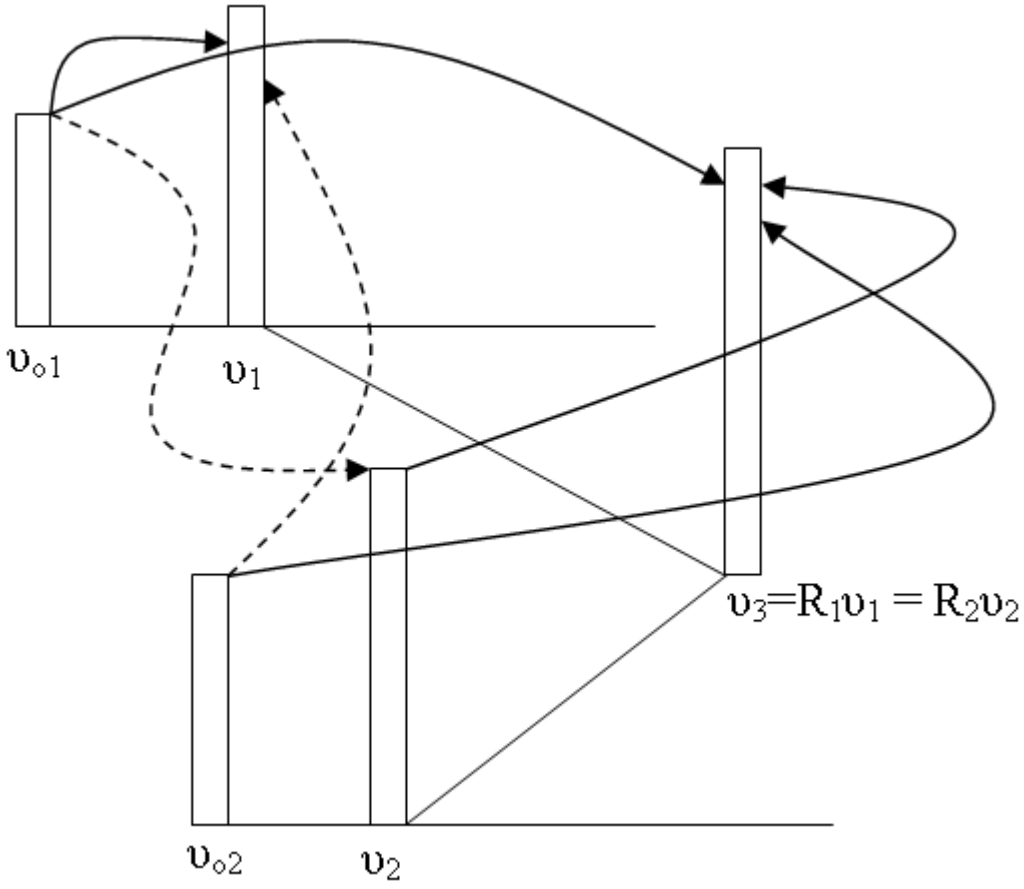

Figure A–2: Illustration of the two component trimdoal monodisperse model.

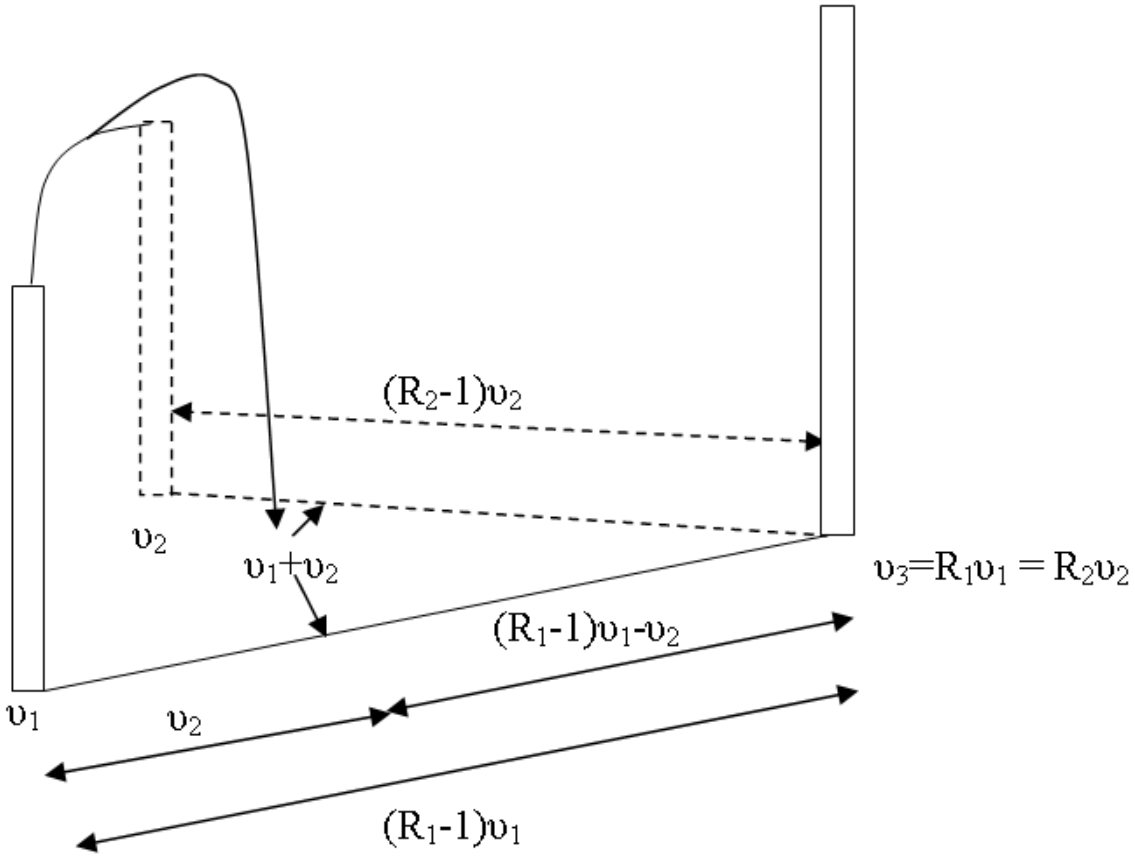

Figure A–3: Representation of coagulation between the nucleation modes of the two components.

$\upsilon_2/(R_1\text{-}1)\upsilon_1$. Similarly, for mode 2,

$$\frac{dN_2}{dt} = J_2^* \frac{\upsilon_2^*}{\upsilon_2} - \frac{1}{2}\beta_{22}N_2^2\frac{R_2}{R_2-1} - \frac{1}{2}\beta_{12}N_1N_2\frac{\upsilon_1}{\upsilon_2(R_2-1)} - \beta_{23}N_2N_3 + \frac{\upsilon_{o1}}{\upsilon_2}K_2^{o1}N_{o1}N_2 + \frac{\upsilon_{o2}}{\upsilon_2}K_2^{o2}N_{o2}N_2 \quad \text{(A.10)}$$

For the accumulation mode, as in the single component case, equations for number concentration, volume and area are given by

$$\frac{dN_3}{dt} = \frac{1}{2}\beta_{11}N_1^2\frac{1}{R_1-1} + \frac{1}{2}\beta_{22}N_2^2\frac{1}{R_2-1} - \frac{1}{2}\beta_{33}N_3^2 + \frac{1}{2}\left(\beta_{12}N_1N_2\frac{\upsilon_2}{\upsilon_1(R_1-1)} + \beta_{12}N_1N_2\frac{\upsilon_1}{\upsilon_2(R_2-1)}\right) \quad \text{(A.11)}$$

$$\frac{dV_3}{dt} = \frac{1}{2}\beta_{11}N_1^2\frac{R_1}{R_1-1}\upsilon_1 + \frac{1}{2}\beta_{12}N_1N_2\frac{\upsilon_2}{(R_1-1)} + \beta_{13}N_1N_3\upsilon_1 + \frac{1}{2}\beta_{22}N_2^2\frac{R_2}{R_2-1}\upsilon_2 + \frac{1}{2}\beta_{12}N_1N_2\frac{\upsilon_1}{(R_2-1)} + \beta_{23}N_2N_3\upsilon_2 + K_3^{o1}N_{o1}N_3\upsilon_{o1} + K_3^{o2}N_{o2}N_3\upsilon_{o2} \quad \text{(A.12)}$$

$$\frac{dA_3}{dt} = \frac{1}{2}\beta_{11}N_1^2\frac{R_1}{R_1-1}a_1 + \frac{1}{2}\beta_{12}N_1N_2\frac{\upsilon_2 a_1}{(R_1-1)\upsilon_1} + \beta_{13}N_1N_3a_1 + \frac{1}{2}\beta_{22}N_2^2\frac{R_2}{R_2-1}a_2 + \frac{1}{2}\beta_{12}N_1N_2\frac{\upsilon_1 a_2}{(R_2-1)\upsilon_2} + \beta_{23}N_2N_3a_2 + K_3^{o1}N_{o1}N_3a_{o1} + K_3^{o2}N_{o2}N_3a_{o2} - \frac{1}{\tau_{eff}}\left(A_3 - N_3a_{3s}\right) \quad \text{(A.13)}$$

where τ_{eff} is the effective characteristic sintering time. Using the derived equations, the mass conservation relation is satisfied as

$$\frac{dV_t}{dt} = \frac{d\left(V_{o1}+V_{o2}+V_1+V_2+V_3\right)}{dt} = I_{o1}\upsilon_{o1} + I_o\upsilon_{o2} \quad \text{(A.14)}$$

A.3.3 Generalization: m-component model

In many combustion environments, there are multiple components present, for example, the various trace metallic species in an incinerator or coal combustion system. Figure A–4 illustrates the schematic diagram representing a *m*-component model. In the present model, every component is assumed to have a monomer and nucleation mode. One combined accumulation mode is assumed to be present. Therefore, for the m-component model, there are m monomer modes, *m* nucleation modes and one accumulation mode, and hence, a total of 2*m*+1 modes are considered. Similar to the derivations described in the previous sections, the equations for the general m-component model are readily derived. Monomer balance of the *i*-th component can be expressed as

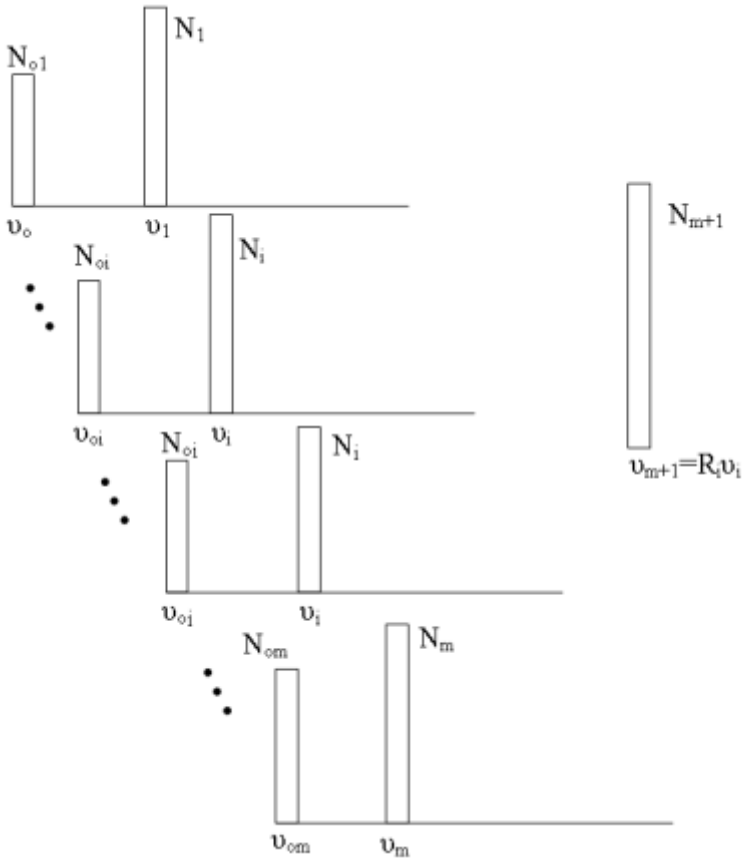

Figure A–4: Representation of the general m-component model with a total of 2m+1 modes: m monomer modes, m nucleation modes and one accumulation mode.

$$\frac{dN_{oi}}{dt} = I_{oi} - J_i^* \frac{\upsilon_i^*}{\upsilon_{oi}} - \sum_{j=1}^{m+1} K_j^{oi} N_{oi} N_j \tag{A.15}$$

The number concentration representing the nucleation mode of *i*-th component is given by

$$\begin{aligned}\frac{dN_i}{dt} &= J_i^* \frac{\upsilon_i^*}{\upsilon_1} + \sum_{j=1}^{m} \frac{\upsilon_{oj}}{\upsilon_i} K_i^{oj} N_{oj} N_i - \sum_{i=1}^{m} \frac{1}{2} \beta_{i,i} N_i^2 \frac{R_i}{R_i - 1} \\ &- \sum_{j=1}^{m} \frac{1}{2} \beta_{i,j} N_i N_j \frac{\upsilon_j}{\upsilon_i (R_i - 1)} - \beta_{i,m+1} N_i N_{m+1}\end{aligned} \tag{A.16}$$

The accumulation mode equations are given by,

$$\frac{dN_{m+1}}{dt} = \sum_{i}^{m} \frac{1}{2} \beta_{i,i} N_i^2 \frac{1}{R_i - 1} + \sum_{i=1}^{m} \sum_{j \neq i}^{m} \frac{1}{2} \beta_{i,j} N_i N_j \frac{\upsilon_j}{\upsilon_i (R_i - 1)} - \frac{1}{2} \beta_{m+1,m+1} N_{m+1}^2 \tag{A.17}$$

$$\begin{aligned}\frac{dV_{m+1}}{dt} &= \sum_{i=1}^{m} \frac{1}{2} \beta_{ii} N_i^2 \frac{R_i}{R_i - 1} \upsilon_i + \sum_{i=1}^{m} \beta_{i,m+1} N_i N_{m+1} \upsilon_i + \sum_{i=1}^{m} \sum_{j \neq i}^{m} \frac{1}{2} \beta_{i,j} N_i N_j \frac{\upsilon_j}{R_i - 1} \\ &+ \sum_{i}^{m} K_{m+1}^{oi} N_{oi} N_{m+1} \upsilon_{oi}\end{aligned} \tag{A.18}$$

$$\begin{aligned}\frac{dA_{m+1}}{dt} &= \sum_{i=1}^{m} \frac{1}{2} \beta_{ii} N_i^2 \frac{R_i}{R_i - 1} a_i + \sum_{i=1}^{m} \beta_{i,m+1} N_i N_{m+1} a_i + \sum_{i=1}^{m} \sum_{j \neq i}^{m} \frac{1}{2} \beta_{i,j} N_i N_j \frac{\upsilon_j}{(R_i - 1)\upsilon_i} a_i \\ &+ \sum_{i}^{m} K_{m+1}^{oi} N_{oi} N_{m+1} a_{oi} - \frac{1}{\tau_{eff}} (A_{m+1} - N_{m+1} a_{(m+1)s})\end{aligned} \tag{A.19}$$

The overall mass conservation is again satisfied

$$\frac{dV_t}{dt} = \frac{d}{dt}\left(\sum_{i=1}^{m} V_{oi} + \sum_{i=1}^{m} V_i + V_{m+1} \right) = \sum_{i=1}^{m} I_{oi} \upsilon_{oi} \tag{A.20}$$

A.3.4 Apportioning of particles into different modes

In the trimodal model, the size distribution is represented by three discrete sizes or modes. As the particles grow by dynamic mechanisms, they may not belong to any of these modes. Thus, they need to be apportioned among the existing modes. The newly formed particle can be arbitrarily put into the next mode or split it into two modes bracketing the particle.

However, it is important to conserve the mass (or total volume) as the apportionment is done. In a general case, if there are 'n' modes, 'n-1' parameters can be conserved. For example, the following can be conserved: 'v^2' for light scattering, 'area' for sintering, number or collisions, or any other chosen integral property. Three different approaches are discussed – no apportionment (where the particles are included in the next larger mode), conservation of mass and number (as done by Jeong & Choi[3]) and conservation of total collision rates (due to the importance of collisional growth of particles in high number concentration environments, this work).

No apportionment

One way to accommodate the intermediate size particles is to put the total volume of particles in to the next mode. As total volume has to be conserved, the number concentration in the larger mode is arbitrarily altered. Although the subsequent dynamics (such as collision rates) of particles in the new mode are going to be different from the actual values, this method is simple and easy to implement.

Apportioning by conserving total volume and number

Jeong & Choi[3] apportioned the particles into adjacent modal nodes by conserving total volume and number.

$$N_{app} = f_1 N_{app} + f_2 N_{app} \tag{A.21}$$

$$v_{app} N_{app} = v_1 f_1 N_{app} + v_2 f_2 N_{app} \tag{A.22}$$

where f_i denotes the fraction of particles that go into ith mode. If there is a large particle then most of its volume (mass) will go into the larger mode, and if there is a smaller particle most of the apportioned volume will go into the smaller mode. Unlike the previous method with no

apportionment, the particles are split in such a way to better ensure that the initial particle properties and apportioned particle properties are similar.

Apportioning by conserving total volume and collision rates

The total volume of particles is split between two modes while conserving the total number of collisions the particles would have undergone, and the new particles will undergo. This will result in same number of collisions as the parent particle and will be more representative of the rate of growth in processes where collisional growth is dominant. The following methodology is used to split a particle between mode 1 and 2

$$\beta(v_{app}, v_i) N_{app} N_i = \beta(v_1, v_i) N_{app} f_1^i N_i + \beta(v_2, v_i) N_{app} f_2^i N_i \tag{A.23}$$

$$v_{app} = v_1 f_1^i + v_2 f_2^i \tag{A.24}$$

where i is the mode with which the particle to be apportioned collides, f_1 and f_2 denote the number fraction that go into each mode. Equation (A.23) conserves the total number of collisions, while (A.24) conserves the total volume. These can be solved simultaneously to give the number concentration in each mode. Collision of v_{app} with ith mode yields values of f_1^i and f_2^i. A volume weighted average is used to ensure that large number of collisions by small volume particles are same as few collisions by large particles.

$$f_1 = \frac{\sum_i f_1^i N_i v_i}{\sum_i N_1 v_i} \tag{A.25}$$

$$\& \quad f_2 = \frac{\sum_i f_2^i N_i v_i}{\sum_i N_1 v_i} \tag{A.26}$$

A.3.5 Numerical Approach

The resultant trimodal model consists of simultaneous first order differential equations. To solve these simultaneous equations, the Euler method was used. The time step was reduced until the solution was 0.1% of the absolute value for the two selected time steps. In single component aerosol, the growth of aluminum particles was considered. Initially saturated Al vapor is nucleated and growth, the classical homogeneous nucleation theory was adopted.[14] In multi-component aerosol, the PbO removal using SiO_2 sorbent was considered. Initial precursor concentration, nucleation rate and flame temperature were given from other literatures.[5, 15]

A.4 Results and discussion

A numerical approach was used to solve the various model equations for both single and multicomponent aerosol generation. First, the results of the various apportionment methods are discussed. This followed by comparing the results of the trimodal model to those from two more accurate models, the NGDE[16] and the discrete-sectional[15] models. The application studied was that of toxic metal capture by sorbents, and two important parameters were the monomer concentration and nucleation rate.

A.4.1 Comparison of various methods of apportionment

Different ways of apportioning as mentioned in section 2.4 were tested on a TiO_2 synthesis system as described by Thimsen & Biswas, 2007.[17] This system was chosen because it is a high temperature system that results in large number concentrations, thus resulting in collisional growth. The precursor used was titanium tetra isopropoxide (TTIP), which reacted at a constant temperature of 2000K, with initial concentration of TTIP of 0.56M and residence time

of 590 μs. The decomposition of TTIP was assumed to be a first order process with decomposition rate constant of $3.96\times10^{5}\exp(-70.5KJ/RT)$.[18]

The maximum difference (~25%) between the "no apportionment" case and the various apportionment methods discussed above is observed at 2.6 μs for number concentrations in the largest mode. The error then goes down consistently and quickly drops below 5% at 5 μs for the number concentration in mode 2. The number concentration in mode 1 also shows a maximum error of (~25%) at 6 μs and then the error drops to less than 5% at 31 μs. The error between the apportionment method of Jeong & Choi, 2003[3] and the one proposed in this work is always less than 5%, and becomes even smaller at longer simulation times. The variation in the predicted radius is always less than 1% for all three methods of apportionment. At longer times and very high initial number concentrations, all the simplistic modal models behave like monodisperse model simulations after some time of simulation; hence there is no variation in the predicted results.

Simulations were also conducted by arbitrarily increasing and decreasing the concentrations, and the total simulation time. The time at which the peak deviation was observed varied; however, there was not much difference between the different apportionment methods. In summary, apportionment methods are thus going to be important for short time predictions, and for the production of very fine sized particles. Such systems include those where, for example, accurate control of arrival particle size is necessary.[17, 19] It should also be noted that in a system at low temperature the difference will be valid at time scales longer than this.

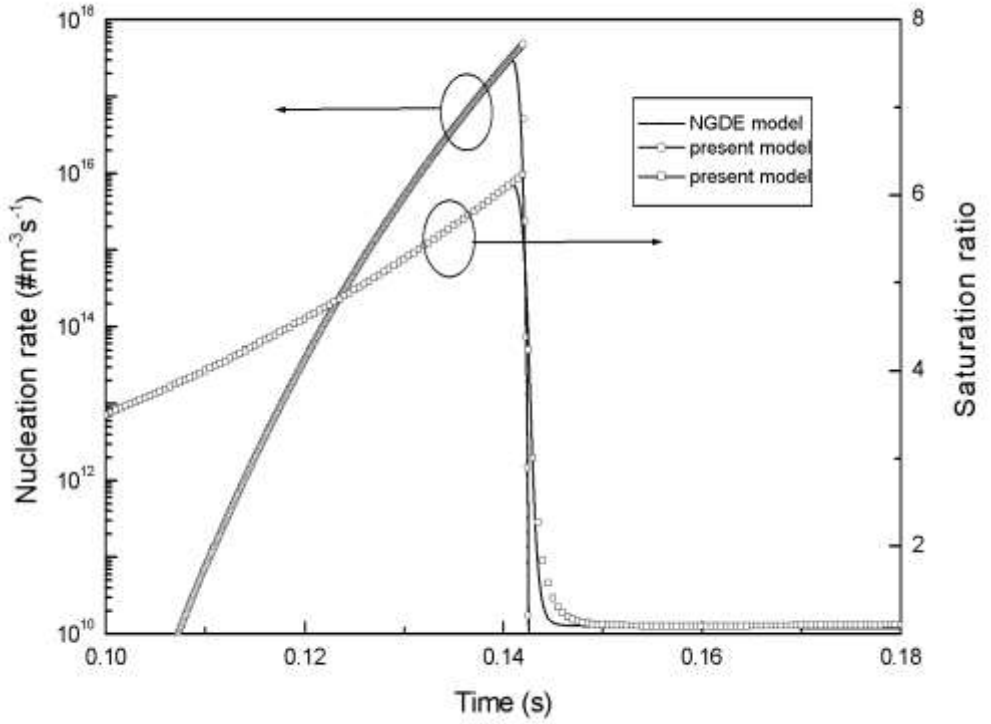

Figure A–5: Comparison of nucleation rate and saturation ratio of aluminum vapor as a function of time predicted by the current model and the NGDE method.

A.4.2 Single component aerosol

Aluminum particle formation and growth was used as the system to be studied. Saturated Aluminum vapor at 1800K traverses the condenser with a cooling rate of 1100K/s. The nucleation rate and saturation ratio are compared to predictions of the NGDE model reported in a previous study.[16] The apportionment method of Jeong & Choi, 2003[3] was used in all the following simulations.

Figure A–5 shows the nucleation rate and the saturation ratio as function of time. As the temperature decreases, the saturation ratio increases due to a decrease in the saturation vapor pressure. Nucleation is initiated when the saturation ratio attains a critical value. Following this, the monomer vapor is consumed by nucleation and condensation. As the monomer concentration

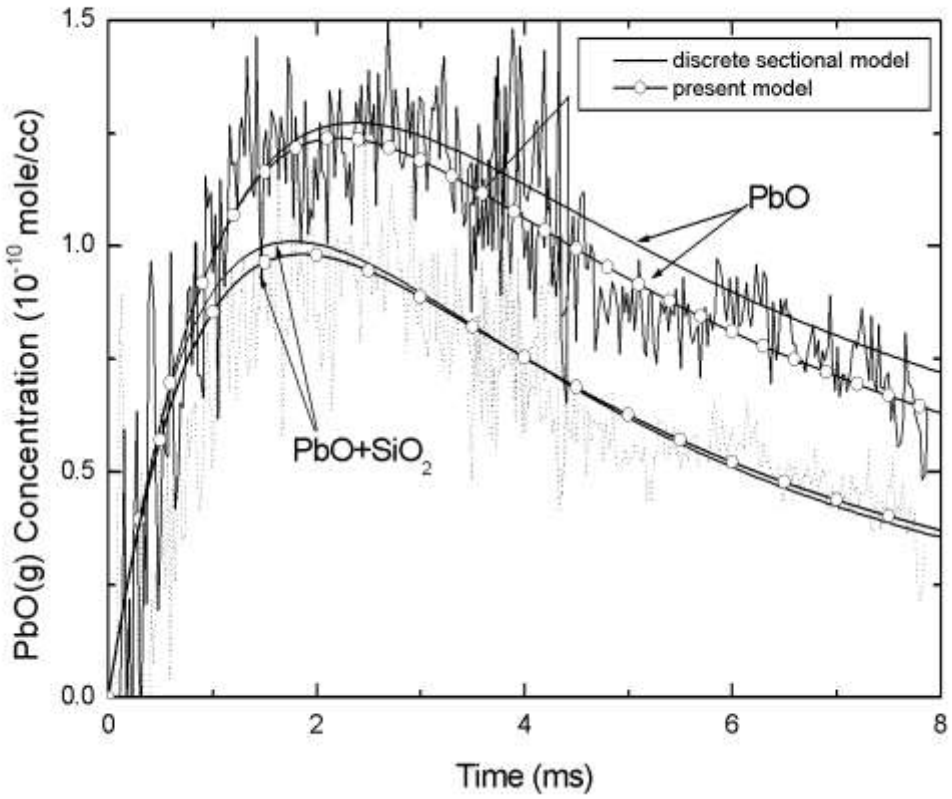

Figure A–6: Comparison of PbO (g) concentration as a function of time; predicted by the current model and the discrete-sectional method.

decreases, nucleation rate and saturation ratio also decrease after reaching a maximum value. The present model predictions are in good agreement with those of a 42 node NGDE model.

A.4.3 Multi-component aerosol

To test the model for a multicomponent system, lead species capture by injection of vapor phase silica sorbent precursor is studied. The model predictions are compared to both experimental simulation results of a discrete-sectional model. The various parametric conditions and detailed experimental procedure are described in other works.[5, 15]

Figure A–6 shows the PbO vapor concentration as function of residence time in the high temperature zones of the premixed flame aerosol reactor. The PbO vapor concentration increases

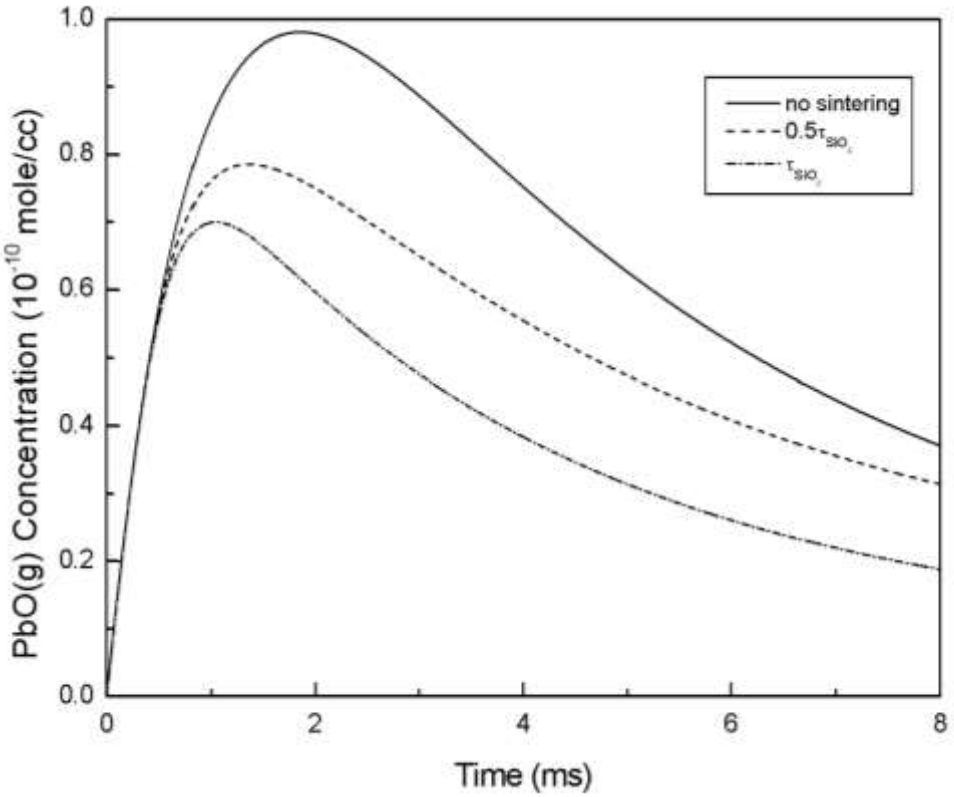

Figure A–7: Variation of PbO (g) concentration as a function of time predicted by the current model with different sintering time.

by a chemical decomposition reaction of the feed, and decreases downstream as the lead oxide vapors undergo nucleation and condensation. With a silicon precursor that results in formation of SiO_2 particles, the PbO vapor concentration has an additional removal pathway (chemisorptions on surface on silica particles) and decreases more rapidly. The present model describes these phenomena accurately and the predicted results are in good agreement with the discrete sectional method and experimental measurement. The trimodal model requires 7 equations to be solved for this case and hence is computationally simpler compared to discrete-sectional model.

To determine the particle morphology effect, sintering is considered. The discrete sectional model[15] assumed spherical particles, and results in Figure A–6 are for instantaneous sintering conditions. In reality, the particles form aggregates, and this is the preferred mode for

the silica sorbent as the larger surface area promotes scavenging of the lead oxide vapor. Figure A–7 shows the PbO vapor concentration as function of residence time accounting for sintering (using a characteristic sintering time for the silica particles). The characteristic time for sintering of silica is taken from Kingery *et al.*, 1960[20]

$$\tau_s = 6.5\times10^{-13} d_p \exp(83000/T) \tag{A.27}$$

As shown in Figure A–7, the PbO vapor concentration is much lower when sintering is considered. The agglomerates of silica particles have a larger surface area than a sphere having the same volume. Therefore, PbO vapor condenses more rapidly onto the larger surface area silica particles.

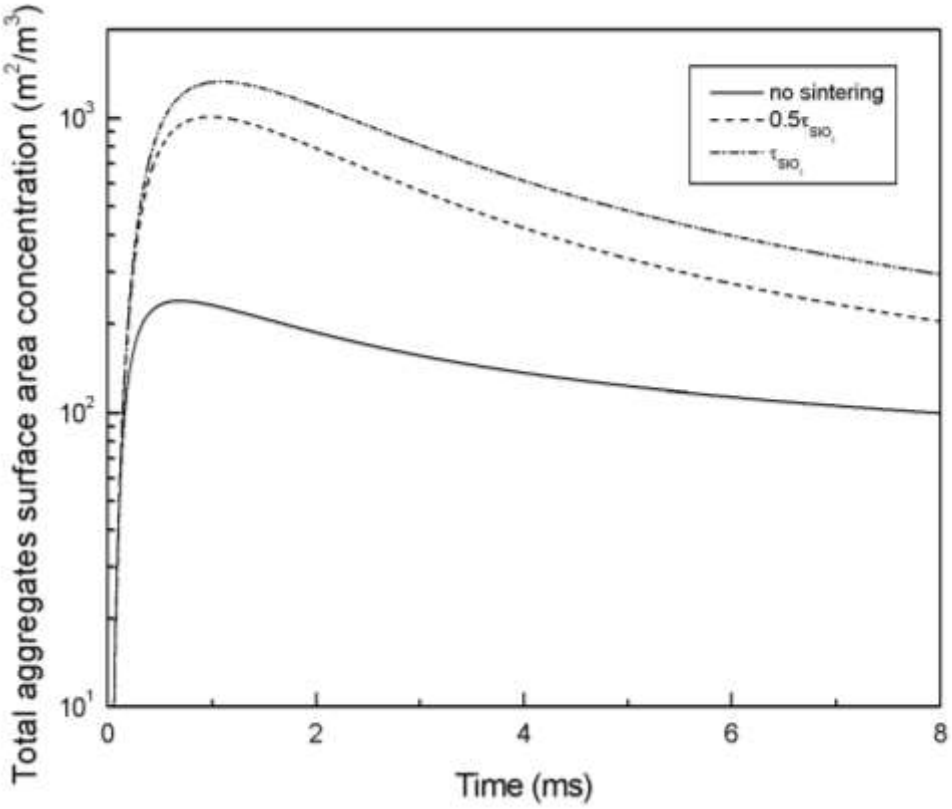

Figure A–8: Variation of total aggregates surface area concentration as a function of time predicted by the current model with different sintering time.

The model can also be used to conduct parametric studies. Sintering rate expressions for lead –silica composite particles are not available in the literature. Simulations are conducted for a range of values of characteristic sintering time. Figure A–7 shows the PbO vapor concentration and Figure A–8 the total particle surface area variation as function of time for a range of characteristic sintering times. As the characteristic sintering time decreases, the total particle surface area increases and PbO vapor concentration decreases more rapidly due to more rapid condensation. Models such as these can also be used to design sorbent processes for capture of heavy metal species. For example, the minimum sorbent precursor feed rate necessary to obtain a sufficiently large agglomerate size that suppresses nucleation of the lead oxide vapor, and is readily captured in particle control devices can be evaluated.

A.5 Conclusions

A computationally inexpensive trimodal monodisperse model generalized for "*m*" multi-component species is developed in this study. The model is consistent and satisfies overall mass balance of the various species. Various apportionment models were examined and no significant difference was observed for the simulated conditions. Such models can find application in high temperature aerosol formation systems encountered in combustion and nanostructured materials synthesis. The model equations were solved for both a single component (Al particle formation) and multicomponent system (lead species capture using silica sorbents). The results were compared to those of more accurate models previously developed in the literature, and good agreement was obtained. The model could account for non-spherical shapes, and parametric studies to examine the impact on lead species capture by silica particles undergoing sintering at different rates was compared. The model developed in this work can be used for optimization

studies of various processes. For example, optimization of sorbent injection processes for heavy metals capture can be conducted.

A.6 Acknowledgements

One author (Sang Bok Kim) acknowledges partial support through a grant from the Brain Korea 21 program of the Ministry of Education. The work was also partially supported by the Stifel and Quinette Jens Endowment at Washington University in St. Louis; and the McDonnell Academy Global Energy and Environmental Partnership (MAGEEP, http://mageep.wustl.edu)

A.7 References

1. Kruis, F. E.; Kusters, K. A.; Pratsinis, S. E.; Scarlett, B. A Simple Model for the Evolution of the Characteristics of Aggregate Particles Undergoing Coagulation and Sintering. *Aerosol Sci. Technol.* **1993**, *19*, 514-526.

2. Xiong, Y.; Pratsinis, S. E. Formation of Agglomerate Particles by Coagulation and Sintering—Part I. A Two-Dimensional Solution of the Population Balance Equation. *J. Aerosol Sci.* **1993**, *24*, 283-300.

3. Jeong, J. I.; Choi, M. A Simple Bimodal Model for the Evolution of Non-Spherical Particles Undergoing Nucleation, Coagulation and Coalescence. *J. Aerosol Sci.* **2003**, *34*, 965-976.

4. Owens, T. M.; Biswas, P. Vapor Phase Sorbent Precursors for Toxic Metal Emissions Control from Combustors. *Industrial & Engineering Chemistry Research* **1996**, *35*, 792-798.

5. Biswas, P.; Zachariah, M. R. In Situ Immobilization of Lead Species in Combustion Environments by Injection of Gas Phase Silica Sorbent Precursors. *Environ. Sci. Technol.* **1997**, *31*, 2455-2463.

6. Lee, M. H.; Cho, K.; Shah, A. P.; Biswas, P. Nanostructured Sorbents for Capture of Cadmium Species in Combustion Environments. *Environ. Sci. Technol.* **2005**, *39*, 8481-8489.

7. Pirjola, L.; Tsyro, S.; Tarrason, L.; Kulmala, M. A Monodisperse Aerosol Dynamics Module, a Promising Candidate for Use in Long-Range Transport Models: Box Model Tests. *Journal of Geophysical Research: Atmospheres* **2003**, *108*, 4258.

8. Kim, Y. P.; Seinfeld, J. H. Simulation of Multicomponent Aerosol Condensation by the Moving Sectional Method. *J. Colloid Interface Sci.* **1990**, *135*, 185-199.

9. Katoshevski, D.; Seinfeld, J. H. Analytical–Numerical Solution of the Multicomponent Aerosol General Dynamic Equation—with Coagulation. *Aerosol Sci. Technol.* **1997**, *27*, 550-556.

10. Katoshevski, D.; Seinfeld, J. H. Analytical Solution of the Multicomponent Aerosol General Dynamic Equation―without Coagulation. *Aerosol Sci. Technol.* **1997**, *27*, 541-549.

11. Gelbard, F.; Seinfeld, J. H. Simulation of Multicomponent Aerosol Dynamics. *J. Colloid Interface Sci.* **1980**, *78*, 485.

12. Kim, Y. P.; Seinfeld, J. H. Simulation of Multicomponent Aerosol Dynamics. *J. Colloid Interface Sci.* **1992**, *149*, 425-449.

13. Sorensen, C. M.; Cai, J.; Lu, N. Light-Scattering Measurements of Monomer Size, Monomers Per Aggregate, and Fractal Dimension for Soot Aggregates in Flames. *Appl. Optics* **1992**, *31*, 6547-6557.

14. Friedlander, S. K. *Smoke, Dust, and Haze: Fundamental of Aerosol Dynamics*. Second ed.; Oxford University Press: New York, 2000.

15. Wu, C. Y.; Biswas, P. Study of Numerical Diffusion in a Discrete-Sectional Model and Its Application to Aerosol Dynamics Simulation. *Aerosol Sci. Technol.* **1998**, *29*, 359-378.

16. Prakash, A.; Bapat, A. P.; Zachariah, M. R. A Simple Numerical Algorithm and Software for Solution of Nucleation, Surface Growth, and Coagulation Problems. *Aerosol Sci. Technol.* **2003**, *37*, 892-898.

17. Thimsen, E.; Biswas, P. Nanostructured Photoactive Films Synthesized by a Flame Aerosol Reactor. *AlChE J.* **2007**, *53*, 1727-1735.

18. Okuyama, K.; Ushio, R.; Kousaka, Y.; Flagan, R. C.; Seinfeld, J. H. Particle Generation in a Chemical Vapor-Deposition Process with Seed Particles. *AlChE J.* **1990**, *36*, 409-419.

19. An, W.-J.; Thimsen, E.; Biswas, P. Aerosol-Chemical Vapor Deposition Method for Synthesis of Nanostructured Metal Oxide Thin Films with Controlled Morphology. *J. Phys. Chem. Lett.* **2010**, *1*, 249-253.

20. Kingery, W. D. *Introduction to Ceramics*. Wiley: 1960.

Appendix B An improved computationally simple simulation of multi-particle geometric sintering

To be submitted to Aerosol Science and Technology, September, 2014

B.1 Abstract

In this work a multi-particle geometric sintering (MPGS) model is developed which is computationally simple and hence can be used to simulate the sintering of large number of particles. A novel approach to compute the volume of the sintering particles enables implementation with existing sintering equations based on neck radius. The results from MPGS model are compared to the estimates from Koch and Friedlander model for predicting the normalized surface area. The MPGS model is then applied to test cases of linear agglomerates and fractal agglomerates to study the effect of number of particles in the cluster. The surface area decrease has been shown to be dependent on the number particles in the agglomerate in contrast to Koch and Friedlander model. Finally the model is applied to a film of particles to study the effect of sintering on the morphology.

B.2 Introduction

The gas phase synthesis of particle agglomerates or aggregates has diverse applications such as sorbents,[1] fillers[2] or catalysts.[3] The applications of these particle agglomerates or aggregates depend upon physical properties such as surface area, primary particle size, agglomerate size and electrical conductivity. Sintering rate is a key factor in high temperature processes that determines the physical properties of aggregates. Aggregates are often deposited to form films with very high surface area or low thermal conductivity.[2] To improve the properties of film, they are annealed or particles are deposited at high temperature to encourage sintering. Along with other properties, sintering due to the thermal treatment also changes the morphology. There have been many studies to establish models and determine parameters for sintering.[4] Using these models for simulating particle sintering will improve capabilities to estimate the final properties of various agglomerates and films synthesized by various high temperature processes.

The most widely used model for sintering is the Koch and Friedlander model.[5] The model approximates a neck radius expression as an exponential decay in surface area, the simplified expressions enables easy incorporation in aerosol models which simulate sintering. However, the model does not allow tracking properties other than surface area, thus limiting the applications of the model for multiple particles, especially in films. To simulate the sintering of a large number of particles deposited to form a film, a physically accurate yet computationally simple multi-particle sintering model is required. Simplified models[6, 7] for multi-particle sintering track all the parameters, however the physics of sintering are not represented correctly. For example, Kulkarni and Biswas[7] assume that one particle grows small and while another grows big with time with a net reduction in the surface area. Different approaches for simulating multi-particle

sintering have been developed such as molecular dynamics,[8] and surface energy reduction.[9, 10] However, these simulations are computationally intensive and hence cumbersome to apply to a large number of particles present in a film.

A model based on neck radius would give accurate depiction of physics and also allow tracking of each particle in the simulation. Accurate expressions for sintering rate based on neck radius are available for various mass transport mechanisms such as molecular diffusion, surface diffusion, volume diffusion, viscous flow, and evaporation condensation.[11-13] These expressions have been used for simulating the sintering of two particles which are equal[14] or unequal[15] in size. However, there are very few cases where two particles exist, most scenarios require simulation of sintering with multiple particles. In spite of the simplicity of the neck radius based model, the applications have been limited due to lack of suitable sintering model for multiple particles.

The overall objective of this work is to simulate multi-particle geometric sintering (MPGS) to accurately estimate the properties of sintering particles in a film using a simple neck radius based expression. The first objective is to compare the surface area of a sintering agglomerate from our MPGS model with the Koch and Friedlander model. The second objective is to study the effect of the number of particles on sintering rate for linear and fractal agglomerates. The third objective is to simulate sintering of a large number of deposited particles (~5000), which is possible because of the computational simplicity of the model.

B.3 Model formulation and simulation conditions for mutli-particle sintering

The MPGS model is an extension of a two particle geometric sintering model.[15, 16] Hence the two particle geometric sintering model will be described first, followed by the algorithm to extend it to multiple particles.

B.3.1 Two particle geometric sintering model

Consider two particles that are in contact with each other at time $t = 0$ as shown in Figure B–1a. Let their initial volume be V_1^0 and V_2^0, thus the initial diameter of the two particles d_{s1} and d_{s2} is given by equations

$$d_1^0 = \frac{6}{\pi}\left(V_1^0\right)^{1/3} \text{ and } d_2^0 = \frac{6}{\pi}\left(V_2^0\right)^{1/3}. \tag{B.1}$$

At any time t, let d_1 and d_2 be the diameter of particles. As the particles start sintering, the particles start fusing with each other. In this model it is assumed that the particles remain spherical through the process of sintering. Thus the overlap volume between the particles projected onto a plane surface is shown in Figure B–1a as the shaded area. This overlap volume comprises of the spherical caps which are denoted by O_{12} and O_{21}. Let h_1 and h_2 denote the heights of the spherical caps O_{12} and O_{21} respectively, and the neck diameter of the spherical caps be X_{12}. By using simple geometrical considerations the neck diameter can be expressed as

$$X_{12} = d_2\sqrt{1-(1-h_2)^2} = d_1\sqrt{1-(1-h_1)^2}\,. \tag{B.2}$$

Since the volume of particle 1 is conserved,

$$V_1 = \frac{\pi}{6}d_1^3 - O_{12} = V_1^0, \tag{B.3}$$

where O_{12} denotes the volume of spherical cap of particle 1 intercepted by particle 2.The volume of spherical cap of particle 1 intercepted by 2 can be expressed as

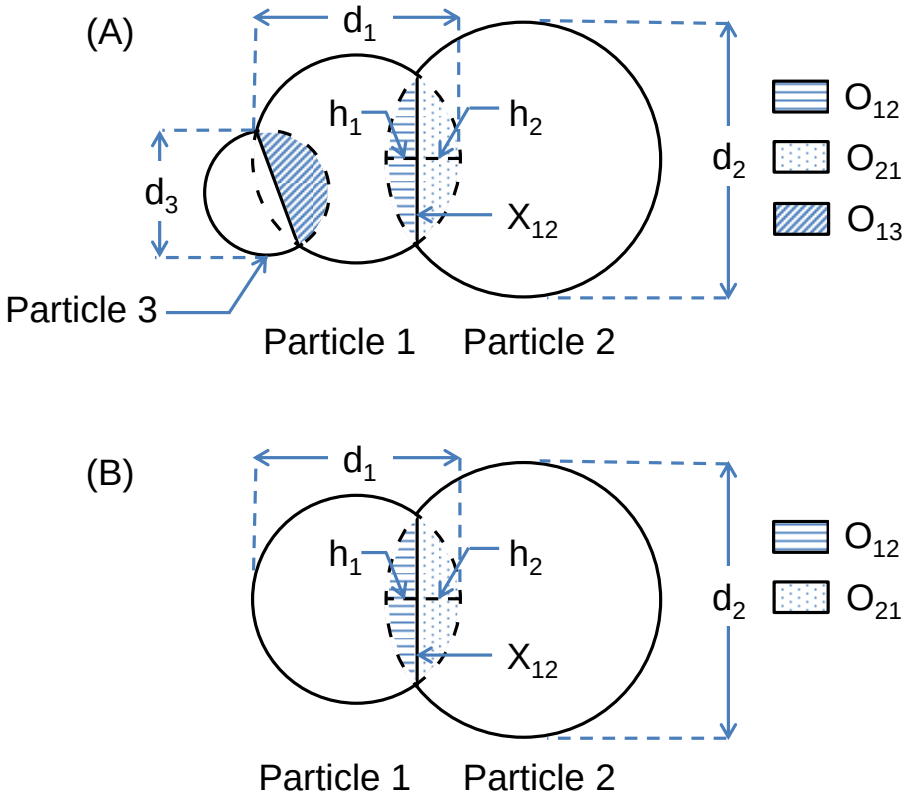

Figure B–1: A 2D schematic of (a) two particles and (b) three particles namely 1, 2 and 3 sintering with d_1, d_2 and d_3 as their diameters respectively. These particles are sintering and the overlapping volumes from a neck diameter X_{12} and X_{13}. The volume of spherical caps

$$O_{12} = \pi h_1^2 \left(\frac{d_1}{2} - \frac{h_1}{3} \right). \tag{B.4}$$

By using the expression of sintering rate we get a relation between neck diameter X_{12} and diameter of particles $d_1$and d_2,

$$X^m d^n = At\,, \tag{B.5}$$

where A is dependent on temperature and mechanism for sintering. Thus we can solve for all the unknowns at any time using these equations and knowing the initial volume of sintering

particles. The distance between particle centers is given by D_{12}, by geometrical considerations we get,

$$D_{12} = d_1/2 + d_2/2 - h_1 - h_2 . \tag{B.6}$$

The distance between particles will keep on decreasing throughout the process of sintering and go to zero when the particles have fully sintered or coalesced.

B.3.2 Multi-particle geometric sintering model

For simplicity, consider the three particles as shown in Figure B–1. In contrast to two particle sintering explained in previous section, the diameter of a sintering particle changes due to more than one particle which are in contact with it. For example, in this case the diameter of particle 1 changes due to sintering to both particle 2 and particle 3. In the case where multiple particles are in contact, two particles are selected at a time, then the two particle sintering model[15] is applied after modifying the initial volume of the particle used in equation (B.4) to include the changes in volume due to other particles. For illustration the particles 1 and 2 are selected first. To conserve the mass or volume (since density is usually constant) of the system, an apparent initial volume of the particle V_1^{0n} is defined. The apparent initial volume is the volume of the particle if it had been sintering only to the selected particle. Thus for particle 1, the apparent initial volume is the initial volume of particle 1 and the volume of spherical caps intercepted by particle 1 except the spherical cap of particle 2, that is

$$V_1^{0n} = \left(V_1^0 + \sum_{j \neq 2} O_{1j} \right) \tag{B.7}$$

Using apparent initial volume ensures that the volume is conserved in the process of sintering with multiple particles. Similarly for particle 2 apparent initial volume is,

$$V_2^{0n} = \left(V_2^0 + \sum_{k \neq 1} O_{2k} \right) \tag{B.8}$$

Equations (B.7) and (B.8) for apparent initial volume simplifies to initial volume of particle for two particle sintering case, since the volume of other spherical caps intercepted is zero. By conservation of volume, apparent initial volume is equated to the volume at any time t

$$V_1 = \frac{\pi}{6} d_1^3 - O_{12} = V_1^{0n} . \tag{B.9}$$

The apparent initial volume needs to be computed at each time step to account for the changing volume of spherical caps intercepted. Thus at each time step the diameter d_1 obtained from equation (B.7) and equation (B.5) will give the neck diameter X at various times. Other parameters such as the distance between particles and the diameters can be found from the neck diameter and the diameter of particles. The two particle sintering model is then applied to all the particles pairwise, and all the particles are rearranged according to the new distance between them obtained from equation (B.6). In case of film, the particles in contact with the surface are rearranged first, followed by rearrangement of other particles on top of them based on the distance between.

In case the distance between any two particles is zero, the sintering is complete and the two particles are merged at the time. In this case, after sometime say the particles 1 and 2 are merged to give a new particle of combined volume. All the particles which were in contact with particles 1 or 2 are in contact with just one new particle. The time step is then increased and procedure for sintering is continuously repeated by selecting particles pairwise and rearranging particles. In the process of iterations, the time step is chosen to be less than the sintering time constant.

B.4 Characterization of aggregates and deposits

All the aggregates are characterized for their surface area and fractal dimension. Surface area is calculated at each time step with the analytical expression for area of sphere or the spherical caps. The area is then summed up over all the particles in the aggregate or film. The fractal dimension of the particles is measured by fitting the number of primary particles within a particular distance based on the equation,

$$N_p = Br^{D_f} \tag{B.10}$$

where N_p is the number of particles, r is the radius, D_f is the fractal dimension and B is a constant. For fractal dimension calculations all the primary particles are assumed to be spherical to simplify computation.

Table B-1: List of simulations performed in the study

Set	Objective	Figure	Radius of particle
I	To simulate the change in surface area and fractal dimension of an agglomerate using MPGS model	Figure B–2	4nm
II	To observe the change in surface area due to varying number of particles in agglomerate of same fractal dimension with MPGS compared with Koch and Friedlander model	Figure B–3	10 nm
III	To observe the change in surface area due to varying fractal dimension for same number of primary particles	Figure B–4	4 nm
IV	To demonstrate simulation of annealing of large number of deposited particles	Figure B–5	4 nm

B.5 Simulation conditions for sintering

The simulation plan for the current work is described in Table B-1. Depending on the dominant mechanism the expression for sintering will change. The sintering mechanism used in this work is over all diffusion and the expression for neck radius is,

$$X^2 = \frac{64\gamma D\Omega}{kTd_1}t \tag{B.11}$$

where D is the diffusion coefficient, T is the temperature, k is the Boltzmann constant and γ is the surface tension. In this work all the particles in simulations are assumed to be of titanium dioxide. The values for the various properties used are summarized in Table B-2. The results are compared to Koch and Friedlander model and the time constant used is the time for neck radius to reach 0.83 of diameter for two particles.[16]

Table B-2: Values for the parameters used for the simulation of sintering

Quantity	Value
Material	Titanium dioxide
Expression for diffusion	$10.86\times10^{-2}exp\left(-323KJ/RT\right)$
Transport mechanism for sintering	Over all diffusion
Temperature	1173K
Omega	1.57E-29 m^3
Gamma	0.6 K/m^2
Radius	4 nm
Sintering time constant for 4 nm particles	0.21s

B.6 Results and discussion

The results are divided into four sections. First, sintering of an agglomerate of the fractal dimension of 1.74 is simulated using the MPGS model and the change in surface area, the fractal dimension, and the morphology are shown. Second, the change in surface area using both MPGSM and KFM model are compared for sintering of linear chain of particles with varying

number of particles. Third section shows a comparison of decrease in normalized surface area of various fractal aggregates with same number of primary particles. Fourth section shows an application of the mutli-particle sintering model that simulates the change in morphology due to annealing on the deposited particles of TiO_2.

B.6.1 Change in fractal dimension and surface area for an agglomerate

Figure B–2 shows the change in normalized surface area and the fractal dimension of the agglomerate with an initial fractal dimension of 1.74. The agglomerate consists of 30 primary particles which are 4 nm in radius and they are sintering at 1173 K. Figure B–2a shows the aggregate over the time of sintering with the initial agglomerate on the left and final compact aggregate on the right. The figure enables visualization of change in shape and size of the aggregate. According to MPGS model the surface area of the agglomerate decreases over time as the sintering takes place, however the decrease is much slower than the estimation by the Koch and Friedlander model. As expected the fractal dimension of the agglomerate increases from 1.74 to 2.6, and over long period of time should reach 3.0. However the method used for determining fractal dimension increase results in fractal dimension not monotonically increasing or smooth. To determine fractal dimension successive circles are drawn and the number of particles inside each circle is fitted to the equation (B.10). The successive circles are multiples of radius of primary particles, since it is the characteristic size. As the size of aggregate reduces due to sintering, the number of circles get reduced and a jump in fractal dimension is observed. Moreover as the mass in the last circle decreases due to sintering, the error in fitting increases and the fractal dimension decreases before the jump. However if the cluster were significantly larger than the radius of particle, these jumps would have been subtle.

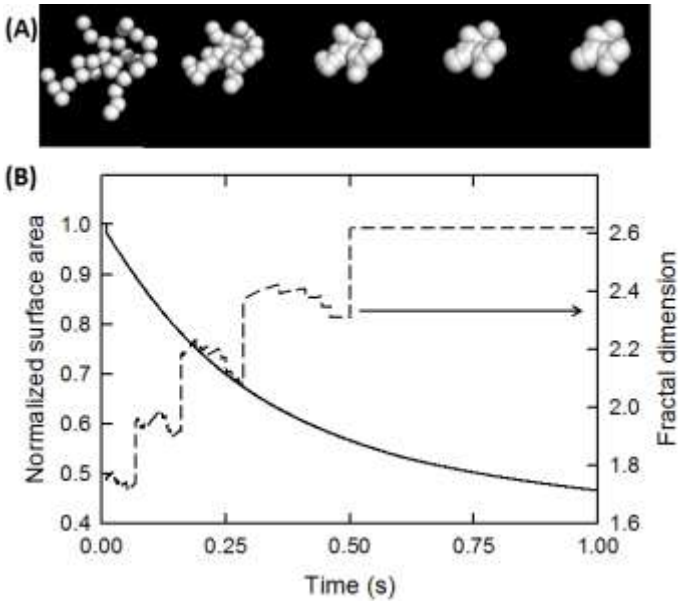

Figure B–2: (A) Change in shape of a 30 particle agglomerate due to sintering at 1173K (B) The change in normalized surface area and fractal dimension due to sintering of same agglomerate with initial fractal dimension of 1.74.

B.6.2 Sintering of linear chains

Figure B–3 shows the rate of decrease in normalized surface area of linear chain of agglomerates with varying number of particles. Linear chains consisting of 2 to 8 particles of 10 nm radius undergo sintering at 1173 K. The change in normalized surface area for different number of particles in the linear chain is compared between the MPGS model and the Koch and Friedlander model. The decrease in normalized surface area is strongly dependent on the number of particles present in the chain using the MPGS model. Fastest decrease in area is for 2 particles because the sintering is not slowed down by increase in size due to other particles in contact. Since the sintering rate decreases as the particles size increases, 2 particle sintering is the fastest. As the number of particles increase, the time taken for sintering increases, reducing the net rate of surface area decrease. Thus, the normalized surface area as simulated by MPGS model is different based on the number of particles present in the chain. In contrast, the decrease in normalized surface area with Koch and Friedlander model is fast and independent of the number

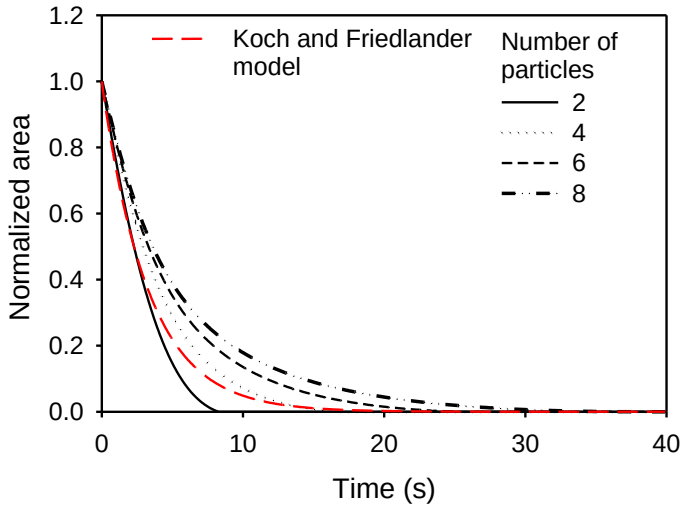

Figure B–3: Comparison of MPGS model with KFM for varying number of particles in agglomerate ($D_f = 1$) sintering at 1173K.

of particles present. This lack of dependence on number of particles is due to the first order decrease in surface area. Hence, the MPGS model is more versatile and better at estimating properties of multiple sintering particles which depend on the number of particles present in agglomerate.

B.6.3 Change in surface area of particles with wide range of fractal dimension

Figure B–4 shows the effect of configuration of the particles on the decrease in normalized surface area. The configuration is varied by generating 15 different agglomerates which have range of fractal dimension varying from 1.0 to 2.0 and varying radius of agglomerates keeping the number of primary particles constant. The primary particles were varied from 5 to 35 and the normalized surface area of the particles were tracked over time. The primary particles in this simulation have radius of 4 nm and sinter at 1173 K. As shown in the figure, lesser the number of particles faster is the decrease in normalized surface area which is consistent with the previous results for linear chain ($D_f = 1$). Moreover the decrease in surface area does not depend on the orientation or the number of neighbor of each particle during the

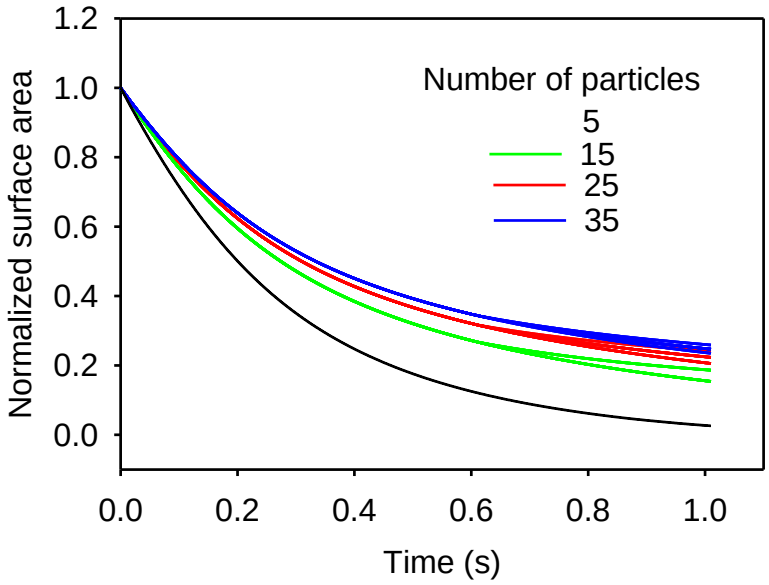

Figure B–4: Decrease in normalized surface area as a function of the number of particles in the initial agglomerate. The agglomerate consists of 4 nm particles sintering at 1173K.

initial time of sintering. The normalized surface area decrease for initial time ~1 s, that is 3 time constants, is same irrespective of the fractal dimension. There are subtle differences at longer times because the particles are too close to each other. This shows that under the assumption that particles remain spherical the change in surface area is not strongly dependent on the arrangement of particles.

B.6.4 Annealing of a large number of particles deposited to form film

Figure B–5 shows the application of the MGPS model by simulating annealing of large number of particles deposited to form a film. The simplicity of the model enables the application for large number of particles with reasonable accuracy. Figure B–5a shows the initial deposit and Figure B–5b shows the final simulated image of the annealed particles. The decrease in surface area is as shown in Figure B–5c. A significant change in the properties of the film takes place in the first time constant of sintering, after which the change is subtle. The information of the

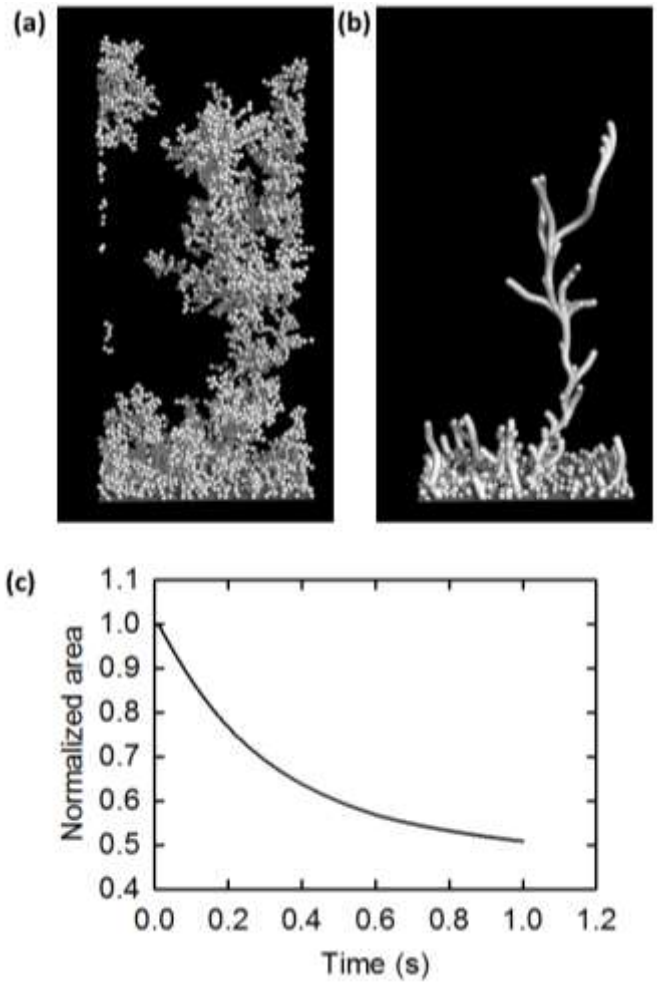

Figure B–5: Change in morphology due to annealing of deposited titanium dioxide particles (a) 5000 particles of radius 4 nm deposited by diffusion to form a film (b) The film after annealing at 1173K for 1 sec (c) The change in surface area over 1 second.

location of each particle and its neighbors is stored while implementing the MPGS models, enabling visualization of the deposit after annealing. This visualization wouldn't have been possible using Koch and Friedlander model since only the area of the agglomerate is tracked. This sintering model can be extended to estimate other physical parameters such as electrical conductivity, since all the parameters such as interface area and height are known.

B.7 Conclusions

The MPGS model could be used to simulate sintering of wide range of agglomerates in gas phase or after deposition. In this work the model has been implemented with sintering expression for over all diffusion of molecules, however the other sintering expressions could be could be used to account for different material properties. The MPGS model enables more quantitative analysis of sintering agglomerate such as fractal dimension of the agglomerate in the process of sintering since the properties and location of all the particles are stored. Using MPGS model it is observed that the surface area decrease of a linear chain of particles is dependent on the number of particles unlike the behavior predicted by KF model. Moreover, at shorter time scale, the decrease in surface area is not dependent on the fractal number or arrangement, but on the total number of particles in agglomerate. Since the MPGS model uses an analytical technique for calculation of spherical caps, instead of computational technique, this model can be used for simulation of large number of particles.

B.8 Acknowledgements

This work was supported by the Photosynthetic Antenna Research Center (PARC), an Energy Frontier Research Center funded by the U.S. Department of Energy, Office of Science, Office of Basic Energy Sciences under Award Number DE-SC0001035. VBS thanks McDonnell International Scholars Academy for the fellowship to pursue Ph.D. at Washington University in St. Louis. Author thanks Gerard Lakin, Tandeep Chadha and Dr. Weining Wang for reviewing the manuscript.

B.9 Nomenclature

A = factor dependent on the mechanism of sintering

d = diameter (nm)

D = diffusion coefficient

D_f = fractal dimension

D_{ij} = distance between two particles

h = height of the spherical cap

k = Boltzmann constant

N_p = number of particles

O_{ij} = overlap volume between i and j, with the volume closer to particle 1

r = radius

t = time

T = temperature

V = volume of the spherical particle (nm^3)

X = neck diameter

γ = surface energy

Ω = volume of molecule

B.10 References

1. Owens, T. M.; Biswas, P. Vapor Phase Sorbent Precursors for Toxic Metal Emissions Control from Combustors. *Industrial & Engineering Chemistry Research* **1996**, *35*, 792-798.

2. Ulrich, G. D. Flame Synthesis of File Particles. *Chemical & Engineering News* **1984**, *62*, 22-29.

3. Schimmoeller, B.; Pratsinis, S. E.; Baiker, A. Flame Aerosol Synthesis of Metal Oxide Catalysts with Unprecedented Structural and Catalytic Properties. *ChemCatChem* **2011**, *3*, 1234-1256.

4. Seto, T.; Shimada, M.; Okuyama, K. Evaluation of Sintering on Nanometer-Sized Titania Using Aerosol Method. *Aerosol Sci. Technol.* **1995**, *23*, 183-200.

5. Koch, W.; Friedlander, S. K. The Effect of Particle Coalescence on the Surface Area of a Coagulating Aerosol. *J. Colloid Interface Sci.* **1990**, *140*, 419-427.

6. Yang, G. X.; Biswas, P. Computer Simulation of the Aggregation and Sintering Restructuring of Fractal-Like Clusters Containing Limited Numbers of Primary Particles. *J. Colloid Interface Sci.* **1999**, *211*, 142-150.

7. Kulkarni, P.; Biswas, P. Morphology of Nanostructured Films for Environmental Applications: Simulation of Simultaneous Sintering and Growth. *J. Nanopart. Res.* **2003**, *5*, 259-268.

8. Raut, J. S.; Bhagat, R. B.; Fichthorn, K. A. Sintering of Aluminum Nanoparticles: A Molecular Dynamics Study. *Nanostruct. Mater.* **1998**, *10*, 837-851.

9. Ch'ng, H. N.; Pan, J. Sintering of Particles of Different Sizes. *Acta Mater.* **2007**, *55*, 813-824.

10. Eggersdorfer, M. L.; Kadau, D.; Herrmann, H. J.; Pratsinis, S. E. Multiparticle Sintering Dynamics: From Fractal-Like Aggregates to Compact Structures. *Langmuir* **2011**, *27*, 6358-6367.

11. Astier, M.; Vergnon, P. Determination of the Diffusion Coefficients from Sintering Data of Ultrafine Oxide Particles. *J. Solid State Chem.* **1976**, *19*, 67-73.

12. Frenkel, J. Viscous Flow of Crystalline Bodies under the Action of Surface Tension. *J. Phys* **1945**, *9*, 385-391.

13. Coblenz, W. S.; Dynys, J. M.; Cannon, R. M.; Coble, R. L., Initial State Solid State Sintering Models.A Critical Analysis and Assessment. In *Sintering Processes*, Kuczynski, G. C., Ed. Plenum Press: NewYork, 1980; pp 141–157.

14. Cho, K.; Biswas, P. Sintering Rates for Pristine and Doped Titanium Dioxide Determined Using a Tandem Differential Mobility Analyzer System. *Aerosol Sci. Technol.* **2006**, *40*, 309-319.

15. Xie, H. A Geometrical Model for Coalescing Aerosol Particles. *J. Aerosol Sci.* **2008**, *39*, 277-285.

16. Cho, K.; Biswas, P. A Geometrical Sintering Model (GSM) to Predict Surface Area Change. *J. Aerosol Sci.* **2006**, *37*, 1378-1387.

Appendix C Maximum and minimum flow rate at an applied potential for an electrospray

To be submitted to Aerosol Science and Technology, June, 2014

C.1 Introduction

Electrosprays have applications in various areas such as Mass spectrometers, Satellite propulsion, material synthesis, analytical instrumentation, and printing to name a few. One of the open questions for electrospray is the estimation of maximum or minimum flow rate. In this section an analysis is provided for estimating the maximum flow rate that can be obtained in electrospray system. Each electrospray is a unique system in terms of setup, applied voltage, electric field at the needle and the solvents used. The minimum flow rate and the maximum flow rate for the electrospray haven't been well defined. Although there are some estimates they are not robust. Chen *et. al.*[1] reports that product of flow rate (Q) and conductivity (k) is constant. However that is for a specific system keeping most of the parameters constant. There is little

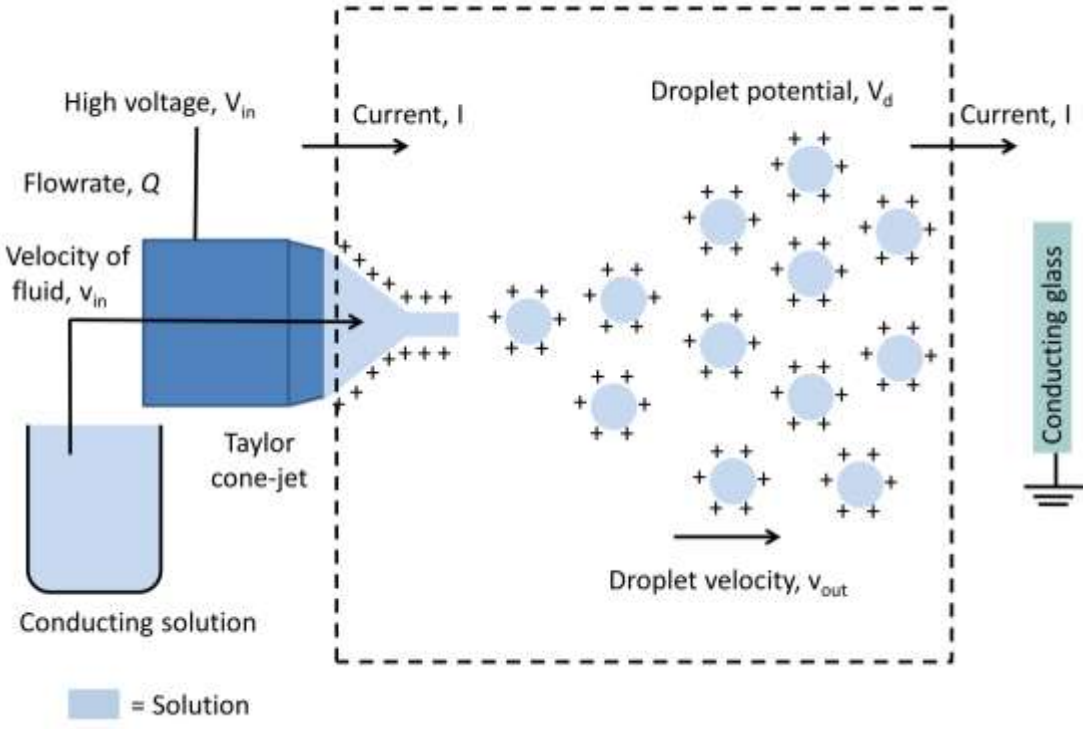

Figure C–1: Schematic for energy balance on dotted box to gain insight into working of electrospray

knowledge about the effect of solution parameters and the system on the maximum flow rate.

One of the key technique is to apply energy balance to the electrospray system. Although energy balance has been applied to the electrospray system, this analysis is different since a size distribution for the droplets formed is assumed and balance is applied globally. In this work we present a new set of dimensionless number for estimating the flow rate in electrospray, under certain assumptions.

C.2 Analysis

Figure C–1 shows the schematic of an electrospray system. Assuming the spray current for the system is I and solution which is at high voltage V_{in}, the power applied is IV_{in}. The total power supplied is electric and kinetic, given by

$$P_{in} = IV_{in} + \frac{1}{2} Q\rho \left(\frac{Q}{A} \right)^2 \tag{C.1}$$

Ignoring the input in kinetic power and substituting the scaling law equation for the current (I) gives,

$$P_{in} = f(\kappa) \left(\frac{\gamma K Q}{\kappa} \right)^{1/2} V_{in} \tag{C.2}$$

Assuming that there is no evaporation of the solvent, the power output will be in form of surface energy, kinetic energy and electric energy. Assuming the solution dissociates from the high voltage to form a droplets at potential V_d and velocity v_{out}.

$$P_{out} = \gamma AN + \frac{1}{2} Q\rho v_{out}^2 + IV_d \tag{C.3}$$

where γ is the surface tension of solution, N is the number of sprayed droplets per unit time, and *A* is the area of droplet.

$$P_{out} = \gamma N \int \pi d_p{}^2 f(d_p) dd_p + \frac{1}{2} Q \rho v_{out}^2 + IV_d \tag{C.4}$$

The synthesized droplets are assumed to have a size distribution where $f(d_p)$ is the fraction of droplets of size d_p. The kinetic energy of the droplets and the electrical power, due to finite potential of each droplet, out of the system has been assumed to be small compared to surface tension.

$$P_{out} = \gamma N \int \pi d_p{}^2 f(d_p) dd_p \tag{C.5}$$

$$N = \frac{Q}{V} \tag{C.6}$$

where V is the volume of each droplet.

$$N = \frac{Q}{\int \frac{\pi}{6} d_p{}^3 f(d_p) dd_p} \tag{C.7}$$

$$P_{req} = 6\gamma Q \frac{\int f(d_p) d_p{}^2 dd_p}{\int f(d_p) d_p{}^3 dd_p} \tag{C.8}$$

For ease of analysis the droplets formed by electrospray are assumed to have a lognormal size distribution with a geometric mean $d_{\bar{1}}$ and standard deviation of σ_g given by,

$$f(d_p) = \frac{1}{\sqrt{2\pi} d_p \ln \sigma_g} \exp\left(-\frac{\left(\ln d_p - \ln d_{\bar{1}} \right)^2}{2\left(\ln \sigma_g \right)^2} \right) \tag{C.9}$$

The derivation also holds true if the droplet distribution is not log-normal. Using Hatch-Choate equations:

$$P_{req} = 6\gamma Q \frac{\bar{d_2}^2}{\bar{d_3}^3} = 6\gamma Q \frac{\bar{d_1}^2 \exp\left(\frac{4}{2}\ln^2 \sigma_g\right)}{\bar{d_1}^3 \exp\left(\frac{9}{2}\ln^2 \sigma_g\right)} = \frac{6\gamma Q}{\bar{d_1} \exp\left(\frac{5}{2}\ln^2 \sigma_g\right)} \tag{C.10}$$

$$P_{req} = \frac{6\gamma Q}{\bar{d_1} \exp\left(\frac{5}{2}\ln^2 \sigma_g\right)} \tag{C.11}$$

Under the Taylor cone-jet mode, if the flow rate of the liquid is constant, the size of the droplets formed should also be the same. Substituting the scaling law equation for diameter of droplet, we get

$$P_{req} = \frac{6\gamma Q}{g(\kappa)(\kappa Q / K)^{1/3} \exp\left(\frac{5}{2}\ln^2 \sigma_g\right)} \tag{C.12}$$

The power supplied should be more than or equal to the power consumed. This gives,

$$P_{in} = f(\kappa)\left(\frac{\gamma K Q}{\kappa}\right)^{1/2} V_{in} \geq P_{req} \tag{C.13}$$

$$P_{in} = f(\kappa)\left(\frac{\gamma K Q}{\kappa}\right)^{1/2} V_{in} \geq P_{req} \tag{C.14}$$

$$f(\kappa)\left(\frac{\gamma K Q}{\kappa}\right)^{1/2} V_{in} \geq \frac{6\gamma Q}{g(\kappa)(\kappa Q / K)^{1/3} \exp\left(\frac{5}{2}\ln^2 \sigma_g\right)} \tag{C.15}$$

$$V_{in} \geq \frac{6\kappa^{1/6}\gamma^{1/2}Q^{1/6}}{f(\kappa)g(\kappa)K^{1/6} \exp\left(\frac{5}{2}\ln^2 \sigma_g\right)} \tag{C.16}$$

$$V_{in} \geq \frac{6}{f(\kappa)g(\kappa)\exp\left(\frac{5}{2}\ln^2\sigma_g\right)}\left(\frac{\kappa Q\gamma^3}{K}\right)^{1/6} \quad \text{(C.17)}$$

Equation (C.17) also gives the dependence of the applied voltage on dielectric constant, flow rate and the conductivity, which is extremely small. Thus the only factor that strongly affects voltage is square root of surface tension.

C.3 Discussion

This section describes the Equation (C.17) for various cases.

C.3.1 Relation between V_{in} (applied voltage) and σ_g (standard deviation) at constant Q

In the cone-jet mode when we keep all the conditions same, we have a region of stability over which we can increase the voltage. This is reflected by decrease in standard deviation. The term $\exp\left(\frac{5}{2}\ln^2\sigma_g\right)$ is a monotonically increasing function of σ_g, thus power required decreases as σ_g increases. The range of applied voltage will depend on the minimum and maximum value of standard deviation $\sigma_{g\_\min} = 1 < \sigma_g < \sigma_{g\_\max}$. As long as the solution parameters are kept constant, the voltage applied can be reduced and this will increase the standard deviation of the droplets synthesized till $\sigma_{g\_\max}$ is reached, which will give a necessary condition for onset potential.

The maximum standard deviation requirement also explains the reason for hysteresis observed in the cone-jet mode. The conejet is extremely unstable as the droplets are synthesized have a high standard deviation. Thus increasing the instability by decreasing applied voltage is

preferred. However if we are increasing the applied voltage, we need to get to a region which has higher stability.

C.3.2 Relation between Q (flow rate) and σ_g (standard deviation) at constant V_{in}

Equation (C.17) also reinforces the previous observation that on decreasing flow rate at constant applied voltage results in smaller standard deviation. At a constant applied potential V_{in}, a minimum flow rate of $Q_{\min}$ will be reached when the standard deviation will assume the lowest value of 1 (for monodisperse droplets).

$$V_{in} = \frac{6}{f(\kappa)g(\kappa)}\left(\frac{\kappa Q_{\min}\gamma^3}{K}\right)^{1/6} \tag{C.18}$$

Thus we obtain a scaling equation for the electrospray at a fixed applied voltage. Assuming standard deviation as 1, Equation (C.18) gives the voltage that has to be applied to obtain a cone jet at $Q_{\min}$. $Q_{\min}$ can be independently changed with V_{in}. If the $V_{in}' < V_{in}$ is applied, $Q_{\min}' < Q_{\min}$ can be obtained. Thus $Q_{\min}$ has to be defined at a fixed potential, which hasn't been done in any work so far. The results from this equation can also be interpreted as if we increase the flow rate at same applied potential then we increase the standard deviation of the sprayed droplets.

C.4 Conclusions

This equation, which has been derived under certain assumptions, gives the pathway to design the flow rate for the electrospray and also an estimate of the proportionality constants and an estimate of the onset voltage. This analysis is independent of the system e.g. the electrospray could be dipped in another solution (liquid-liquid system) or any interface (vacuum). This equation also explains that higher applied voltage will allow larger flow rates, as long as a single

cone jet is present. Moreover the current analysis will also enable generation of monodisperse droplets are various flow rates resulting in more applications for electrospray.

C.5 References

1. Chen, D.-R.; Pui, D. Y. H. Experimental Investigation of Scaling Laws for Electrospraying: Dielectric Constant Effect. *Aerosol Sci. Technol.* **1997**, *27*, 367-380.

Curriculum Vitae

Curriculum Vitae

Vivek Shah

Email: vivekshah@wustl.edu

ACADEMIC BACKGROUND

Ph. D., Energy, Environment and Chemical Engg., Washington University in St. Louis, 2014
SunEdison Corporate Fellow
Advisor: Prof. Pratim Biswas
M. S., Chemical Engineering, IIT Bombay, Mumbai, India, 2009
B. S., Chemical Engineering, IIT Bombay, Mumbai, India, 2009

AWARDS AND ACHIEVEMENTS

- Doctoral Student Research Award, Washington University in St. Louis, 2014
- Awarded fellowship for five years to pursue Ph.D. by McDonnell International Scholar's Academy at Washington University in St. Louis, *2009-14*
- Awarded beam time at Argonne National Labs, 2013
- Awarded PARC travel grant to Oak Ridge National Labs, 2013
- AAAR travel grant, Portland, Oregon, 2013
- Best poster award AAAR, Portland, Oregon, 2010
- Recipient of Forest and Patricia McGrath Endowed Scholarship, *2009-10*

JOURNAL PUBLICATIONS

1. Shah, V. B., and P. Biswas, "Aerosolized Droplet Mediated Self-Assembly of Photosynthetic Pigment Analogues and Deposition onto Substrates". *ACS Nano 2014.*
2. Shah, V. B., Orf, G. S., Reisch, S., Harrington, L. B., Prado, M., Blankenship, R. E., and P. Biswas, "Characterization and deposition of various light-harvesting antenna complexes by electrospray atomization". *Analytical and Bioanalytical Chemistry 2012, 404, 2329-2338.*
3. Shah, V. B., Ferris C., Orf, G. S., Lakin, G., Lee, B., Blankenship, R. E., and P. Biswas, "Supramolecular self-assembly of BChl c molecules in aerosolized droplets to synthesize mimics of chlorosomes". *To be submitted to Photochemistry and Photobiology, September, 2014.*
4. Shah, V. B., and P. Biswas, "Computationally simple multi-particle geometric sintering model". *To be submitted to Aerosol Science and Technology, September, 2014.*

5. Shah, V. B., Henson, W. R., Chadha, T. S., Lakin, G., Liu, H., Blankenship, R. E., and P. Biswas, "Directed Assembly of Photosystem I onto Nanostructured TiO_2 for Biohybrid Photo-electrochemical Cell". *To be submitted to Langmuir, September, 2014.*
6. Shah, V.B., and P. Biswas, "Estimating minimum flow rate for electrospray at an applied potential". *To be submitted to Aerosol Science and Technology, September, 2014.*

OTHER ARTICLES

1. P. Biswas, An, W.-J., and V. B. Shah, "Single-crystal semiconductor thin films for biohybrid photovoltaic devices", SPIE Newsroom – Alternate and solar energy, 2012.

CONFERENCE PRESENTATIONS

1. Lakin, G., Shah, V. B., Orf, G., Blankenship, R.E., and P. Biswas "A Collision-Based Model for the Kinetics of Bacteriochlorophyll *c* Self-Assembly in Methanol-Water Solution", American Association for Aerosol Research, Portland, Sept-October 2013.
2. Shah V. B. and Biswas P., "Supramolecular Self-assembly of Chlorins in an Aerosolized Droplet to Synthesize Biomimetic Antennas", MRS fall meeting, San Francisco, April 1-5, 2013
3. Biswas, P., An, W.-J., and V.B. Shah, "One step process to synthesize single crystal semiconductor thin films to fabricate bio-hybrid and bio-mimetic solar PV devices", SPIE optics + photonics, San Diego, August 2012
4. Shah V. B., Springer J., Mass O., Lindsey J., Holten D., and Biswas P, "Aerosol techniques for self-assembling dyes into light harvesting complexes" PARC All hands meeting, St. Louis, July 2012
5. Mass, O., Springer, J., and V. B. Shah, "Synthetic Chlorosomal -Type Antenna**",** DOE PARC review meeting, Washington DC, March 2012
6. Shah, V. B., Springer, J., Holten, D., and P. Biswas, "Self-Assembled Antenna Complexes via Electrospray Deposition of Synthetic analogs of Bacteriochlorophyll c", PARC All hands meeting, St. Louis, June 2011.
7. Shah V. B., An, W.-J., and P. Biswas, "Brownian Dynamics Simulation and Multiparticle Sintering to Predict Morphology of Nanostructured Thin Films Synthesized by ACVD and FLAR Processes", American Association of Aerosol Research, Orlando, October 2011.

CONFERENCE POSTERS

1. Shah, V. B., and P. Biswas "Computationally Efficient Multi-particle Sintering Model", American Association for Aerosol Research, Portland, October 2013.
2. Shah, V. B., and P. Biswas "Supramolecular Self-assembly of Photosynthetic Dyes in Aerosolized Droplets", American Association for Aerosol Research, Portland, October 2013.
3. Henson, W.R., Shah, V.B., Lakin, G., Chadha, T.S., Liu, H., Blankenship, R. E., and P. Biswas "Production and performance of a Photosystem I-based solar cell using nano-

columnar TiO_2" IEEE 39th Photovoltaic Specialists Conference (PVSC), Tampa, June 2013.

4. Shah, V.B., Lakin, G., Orf, G.S., Blankenship, R. E., and P. Biswas "Biomimetic approach to synthesize sensitizers for hybrid solar cells", IEEE 39th Photovoltaic Specialists Conference (PVSC), Tampa, June 2013.
5. Shah, V.B., Chadha T., and P. Biswas, "Aerosols for addressing energy and environmental problems", McDonnell Global Energy and Environment Partnership, Mumbai, December 2012.
6. Shah V. B., Springer J., Mass O., Lindsey J., Holten D. and Biswas P, "Supramolecular Self-assembly of Chlorins by Aerosol Route", McDonnell Global Energy and Environment Partnership, Mumbai, December 2012.
7. Shah, V.B., Springer, J., Wang, W., Holten, D., and P. Biswas, "Self-assembly of Chlorins in aerosol droplets for synthetizing biomimetic antennas", DOE - PARC review meeting, Washington DC, March 2012.
8. Shah, V.B., Springer, J., Wang, W., Holten, D., and P. Biswas, "Self assembly of Chlorins in Aerosol Droplets for Use in Solar Energy Applications", American Association for Aerosol Research, Orlando, October 2011.
9. Shah, V. B., Ray, R., An, W.-J., and P. Biswas, "Simulation to predict the morphology of nanostructured TiO_2 thin films for solar energy application", American Association for Aerosol Research, Portland, October 2010.
10. Shah, V.B., Ray, R., An, W.-J., and P. Biswas, "Synthesis of TiO_2 Thin Films by ACVD and Their Application to Light-Harvesting Devices", PARC meeting, St. Louis, June 2010.

MENTORED

Rohit Ray (undergraduate student) 2010, Sean Reisch (undergraduate student) 2011, Jenna Lin (high school) 2012, Ryo Nakanishi (visiting scholar, Nagoya University) 2012, Chloe Ferris (undergraduate student) 2013, Ray Henson (Graduate Student) 2013, and Shalinee (Graduate student) 2014.